2013

Experimental and numerical investigation of dynamic rocking foundation behavior

Jacob Nathan Phipps
Iowa State University

Recommended Citation

Phipps, Jacob Nathan, "Experimental and numerical investigation of dynamic rocking foundation behavior" (2013). *Graduate Theses and Dissertations*. 13615.
https://lib.dr.iastate.edu/etd/13615

Experimental and numerical investigation of dynamic rocking foundation behavior

by

Jacob Nathan Phipps

A thesis submitted to the graduate faculty

in partial fulfillment of the requirements for the degree of

MASTER OF SCIENCE

Major: Civil Engineering (Structural Engineering)

Program of Study Committee:
Jeramy Ashlock, Co-major Professor
Sri Sritharan, Co-major Professor
Charles Jahren

Iowa State University

Ames, Iowa

2013

DEDICATION

This work is dedicated to my wife, Morgan Phipps.

TABLE OF CONTENTS

LIST OF FIGURES

LIST OF TABLES

ACKNOWLEDGEMENTS

I would like to take this opportunity to express my thanks to those who helped me with various aspects of the research and writing of this thesis. Thanks to Dr. Jeramy C. Ashlock and Dr. Sri Sritharan for guidance, patience, and support throughout the research process. I am grateful for their encouragement, for challenging me to pursue innovative research, and for establishing the standard of excellence in their own contributions to academia by which I measure my own work. I would also like to thank Dr. Charles T. Jahren for his efforts and contributions to this research work by serving on my committee.

This thesis greatly benefitted from the help and support of my officemates Mohammad Fotouhi-Ardakani, Theodore “Ted" Bechtum, and Shibin Lin. I am thankful for Mohammad's technical expertise as well as the time he spent helping me run tests for this research. I was fortunate not only to have him as a resource throughout my graduate education, but also for his friendship outside the office. I am indebted to Ted for his help with running tests and for providing much of the programming framework required for the data acquisition of this research.

I wish to thank Douglas Wood, Dr. Sriram Aaleti, Jessica Heine, and Grant Schmitz for the insight and labor they provided toward the assembly of the rocking experiments conducted in this research.

Thanks to my colleagues Nicholas Decker and Michael Shimkus. I couldn't imagine going through graduate school with a better set of friends. I am grateful to have shared with them all the triumphs and defeats that graduate school offers.

A special “thank you" belongs to my father, James “Jamie" Phipps. It is safe to say that this research could not have been possible without the effort from Jamie. He sacrificed a great deal of his time and offered valuable construction expertise toward the building of the experiments herein. Thank you also to his employer, Steven W. Hay of Hay Construction Services, Inc. of Marshalltown, Iowa, for their donation of some of the equipment and materials used in the construction of these experiments.

Lastly, and most importantly, thanks to my wife, Morgan. I owe a huge debt of gratitude to her for allowing me to spend countless hours on research and coursework over the years. She has been a pillar of support to me throughout graduate school, and I deeply appreciate the sacrifices she has made on my behalf.

ABSTRACT

Soil-structure interaction problems have long been a focus of researchers over a wide array of applications. Presented in this thesis are experiments and analyses of small-strain soil-structure vibration problems and large-strain soil-structure rocking behavior. A literature review is presented regarding the relevant bodies of work for both topics followed by two experimental investigations. The first is an investigation of multi-modal, small-strain vibrations of field-scale surface foundations on a natural cohesive soil deposit. For this investigation, the physical aspects of the soil-structure vibrating system, the excitation system, the measurement system, the measurement approach, numerical modeling, and comparison with experimental results are presented. The validity and efficiency of a hybrid-mode vertical-eccentric test is demonstrated via its equivalence to separate modal vertical and lateral-rocking tests. Critical insights from numerous past centrifuge scaled-model studies are verified and extended to this field-scale study. The second is an experimental investigation of large-strain rocking of a field-scale surface foundation resting on a cohesive soil deposit. The physical aspects of the soil-structure rocking system, the measurement system, the various actions imposed on the physical system, and a discussion of the experimental results are presented. The results of the field investigation show that energy may be dissipated at the soil-structure interface by means of soil hysteresis through moment-rotation and horizontal force-horizontal displacement. Rounding of the soil surface was observed due to yielding and plastic deformation of the soil from increased rotational strains. Yielding soil also introduced nonlinearity into the response of the soil-foundation system, which directly influenced the period. Lastly, an analytical model was developed to satisfactorily simulate dynamic properties of a rocking system from quasi-static experimentation.

CHAPTER 1

INTRODUCTION

1.1 Overview

Research on mechanistic approaches to better understanding and predicting the behavior of dynamic soil-structure interaction has been ongoing since at least the 1930s. The constant attention paid to this topic through the years by researchers may be attributed to the wide range of affected applications such as the design of machine foundations and seismic design of buildings and civil structures. In the United States, increasing consideration is currently being paid to the topic in response to an aging infrastructure, especially with regard to the retrofit of existing structures and the construction of new structures. In terms of structural analysis, the predictable engineering properties of structural materials have resulted in mechanical models that can predict dynamic response with sufficient accuracy. Greater difficulty exists in accurately predicting the dynamic behavior of structures interacting with soil. When evaluated as a building material in a mechanical sense, the engineering properties of soil can vary widely from season to season and location to location. Even locally, a wide range of soil conditions may be present at a given site. This is because soil is a heterogeneous, nonlinearly inelastic material whose engineering properties are governed by several parameters including strain history, void ratio, moisture content, and state of stress at a given point. The advent and evolution of computational technology has emboldened researchers to attempt to integrate many of these soil parameters into more advanced dynamic analyses to more accurately model soil behavior and soil-structure interaction.

1.2 Small-Strain Vibrating Footing

Many experimental centrifuge investigations by previous researchers have been performed with dynamic loading on small-scale foundations supported by prepared soil specimens. These studies have been pursued with the goal of characterizing modal dynamic responses of various foundation systems subjected to small-amplitude vibrations. The high level of parametric control in a laboratory environment is convenient when studying soil-structure interaction problems. These studies were accompanied by theoretical investigations to develop improved three-dimensional continuum models to more accurately capture the observed experimental dynamic responses.

Three-dimensional continuum models such as elastic half-spaces have been popular analytical tools used to represent soil media for a variety of dynamic soil-structure problems. Elastic half-spaces are typically characterized by soil parameters, such as shear modulus, soil density, and Poisson's ratio as well as contact pressure distribution from the supported foundation. The previous centrifuge studies utilized the half-space approach to parametrically fit shear moduli of theoretical modal responses with experimental modal responses based on defined soil parameters and contact stress distribution assumptions. Limitations of the half-space were observed for multi-modal responses of surface footings, which led to the development of a method for relating vertical and lateral-rocking responses through modification of the impedance matrix. Thus far, the modification of the impedance matrix approach has been limited to centrifuge experiments of scale-model foundations in laboratory environments.

As mentioned, the dynamic response of surface footings vibrating on soil is dependent upon the properties of the soil. Natural soil deposits are exposed to seasonal variations in moisture and temperature, which can dramatically impact the dynamic response of the soil or the foundation-soil system. With a wide range of soil types tested in a controlled laboratory environment, it would be useful to test the dynamic vibration response of field-scale footings on a natural soil deposit over a wide range of moisture and temperature conditions to study how seasonal changes impact the dynamic response.

1.3 Large-Strain Rocking Footing

The topic of rocking foundations has been a heavily investigated issue in recent years. There are certainly advantages to studying soil-structure seismic design with the aim of improving performance of structural systems. The premise of allowing shallow foundations to rock in order to dissipate energy through plastic deformation of the soil, rather than the design of plastic hinges within the structural elements, is one of the primary issues that researchers are studying. Researchers (e.g. Gajan et al. 2005, Kutter et al. 2006, Gajan et al. 2008, etc.) have performed centrifuge testing on shallow rocking foundations in order to evaluate the dynamic response and energy dissipation of rocking foundations on soil. These investigators have developed nonlinear analytical models using finite elements to predict the dynamic response and energy dissipation of rocking foundations. These analytical models are cumbersome for the use of designers and may or may not be quantitatively accurate. Thus far, only centrifuge testing of scale model foundations have been examined.

1.4 Scope of Research

For small-strain vibration of surface footings, experimental techniques will be developed to study field-scale surface foundation vibration problems for dynamic loading on a natural soil deposit. Dynamic loading will aim to engage vertical and coupled lateral-rocking vibration responses of the surface footing. Observed behavior from previous centrifuge studies of other investigators will be verified for field-scale experiments. The first field-scale calibration of the Impedance Modification Factor (IMF) approach, which relates vertical and lateral-rocking responses through modification of the impedance matrix, will be performed for field-scale experiments. The small-strain vibration experiments of a field-scale footing will be performed over a span of seven months to observe seasonal variations in the dynamic response.

For large-strain foundation rocking, experimental techniques will be developed to study the dynamic response of a field-scale surface footing. The foundation response due to various types of loading will be studied. A hydraulic mass shaker will be employed to provide dynamic forced vibrations to the rocking system. A quick-release “snap” mechanism will be used to set the system into free vibration for larger levels of strain. A hydraulic jack will be used for quasi-static cyclic loading of the system for even greater levels of strain. Instrumentation, such as accelerometers and string potentiometers, will be used to capture the dynamic and quasi-static rotational and translational displacements of the rocking system. Experimental results will be presented and analyzed. Results from this investigation will be compared with the findings from scale model centrifuge tests by previous researchers. An analytical model will be presented in order to more simply predict dynamic rocking responses from quasi-static experimental results.

1.5 Thesis Layout

The topics of small-strain foundation vibrations and large strain soil-structure interaction due to foundation rocking will be considered in the ensuing chapters. A literature review will be presented regarding the relevant bodies of work for both topics followed by two separate experimental investigations. The first will be an experimental investigation of multi-modal, small-strain vibrations of field-scale surface foundations resting on a natural cohesive soil deposit. This investigation will present the physical aspects of the soil-structure vibrating system, the excitation system, the measurement system, the measurement approach, and a discussion of experimental results. Various theoretical models will be used to describe the observed dynamic behavior. The second will be an experimental investigation of large strain rocking of a field-scale surface foundation resting on a natural cohesive soil deposit. This investigation will present the physical aspects of the soil-structure rocking system, the measurement system, the various actions imposed on the physical system, a discussion of the experimental results, and an analytical model to predict dynamic properties of a rocking system from quasi-static experiments. These investigations will be followed by a summary of the conclusions that were elucidated from the experimental results.

CHAPTER 2

LITERATURE REVIEW

2.1 Previous Small Strain Dynamic Soil-Structure Interaction Research

Since at least the 1930s, researchers have actively investigated small strain dynamic soil-structure interaction problems and generated new advances in experimental methods and mathematical models. Their aim has been to develop soil models that accurately predict physical behavior based on relevant soil parameters. In light of dramatic advances in computational technology over the decades, researchers have been able to attempt the integration, and parametric variation, of many of these soil parameters into more advanced dynamic analyses and modeling of structures interacting with soil. A brief history of this endeavor is detailed below.

Researchers began by describing various modes of small strain vibration of soil-foundation systems by using half-space models as an approximation of soil. Reissner (1936, 1937) modeled small strain dynamic soil-structure interaction of a massless, flexible circular foundation resting on an elastic semi-infinite half-space. In Reissner's work, a uniform contact stress distribution was assumed under the footing, resulting in a mixed boundary value problem. Later, Sung (1953) and Quinlan (1953) studied the effects of variation in the contact pressure distributions beneath vertically oscillating footings.

To develop a method for analysis of vibration modes of soil-foundation systems, an understanding of the force-displacement relationship at the soil-foundation interface is necessary. Stiffness is the term usually reserved by the structural or geotechnical engineer to relate static force and displacement for structural or soil materials, respectively. In the dynamic case of soil, where stiffness and damping are frequency dependent, the term impedance is used in place of stiffness. The impedance matrix is complex-valued and symmetric for the different modes of vibration. The real part of impedance coefficients describes the stiffness of the system while the imaginary part represents damping within the system. An overview of the many attempts to define impedance matrices for various soil-foundation systems will be presented herein.

Richart and Whitman (1967) developed lumped parameter models for circular rigid foundations resting on the surface of a homogeneous elastic half-space in the 1950s and 1960s. These models constituted a mass, spring, and dashpot analog which replaced a single mode of vibration of a foundation on soil as illustrated in Figure 1.

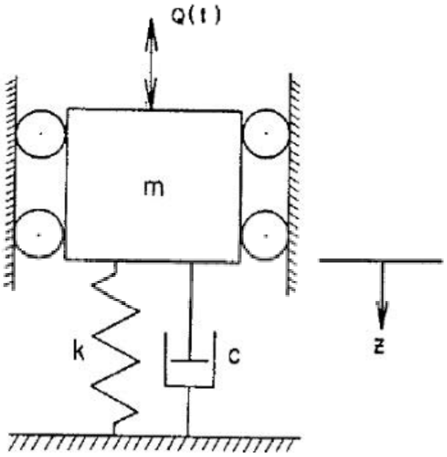

Figure 1. Mass-spring-dashpot system (from Richart and Whitman 1967).

The purpose of Richart and Whitman's work was to compare the results of model footing vibration tests with homogeneous, isotropic, elastic semi-infinite half-space solutions and to evaluate the applicability of the theoretical methods for design purposes. They used a rotating-mass mechanical vibrator to set circular footings into steady-state vibration. The vibration modes that resulted were vertical translation, torsional oscillation, and coupled lateral-rocking as shown in Figure 2.

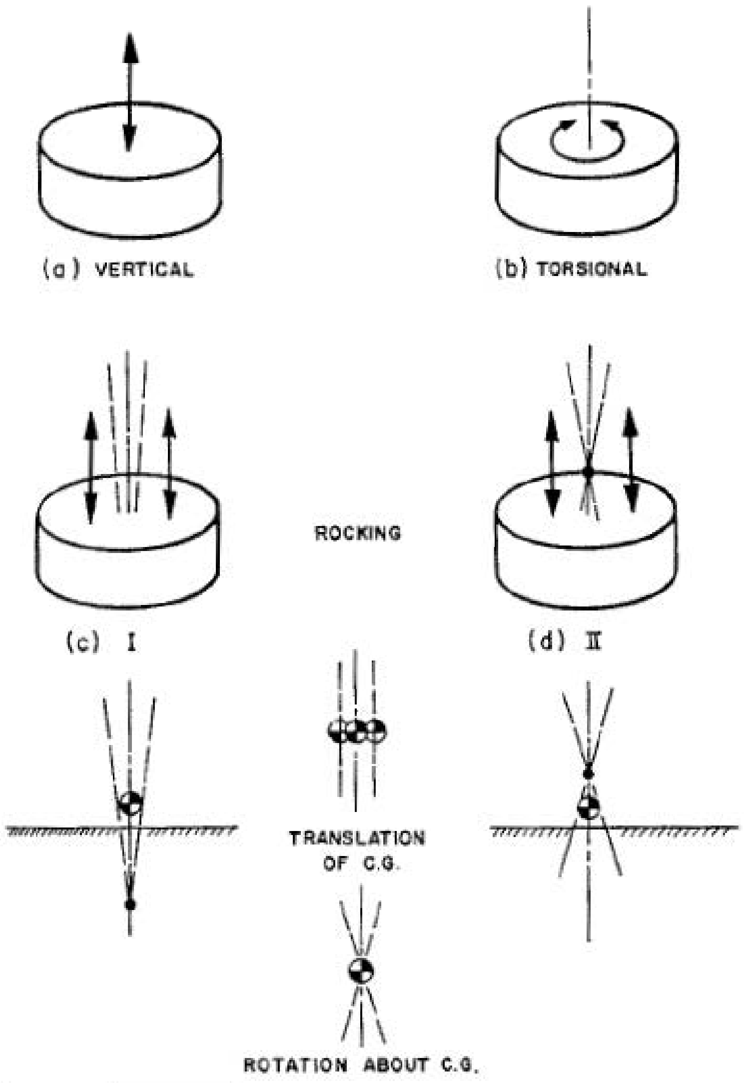

Figure 2. Modes of vibration of model footings (from Richart and Whitman 1967).

Magnitudes of motion were on the order of a few thousandths of an inch in linear translation or a few hundredths of a radian in rotational oscillations. Thus, at small strain levels, the soil response was approximately elastic and a theoretical elastic medium was assumed for the supporting soil. The top of Figure 3 shows typical theoretical vertical displacement oscillation responses versus normalized frequency for various assumed pressure distributions. The bottom of Figure 3 shows the effect of Poisson’s ratio on the theoretical vertical oscillation response curves. As can be seen in this figure, the footing’s dynamic response is quite sensitive to the pressure distribution and soil properties.

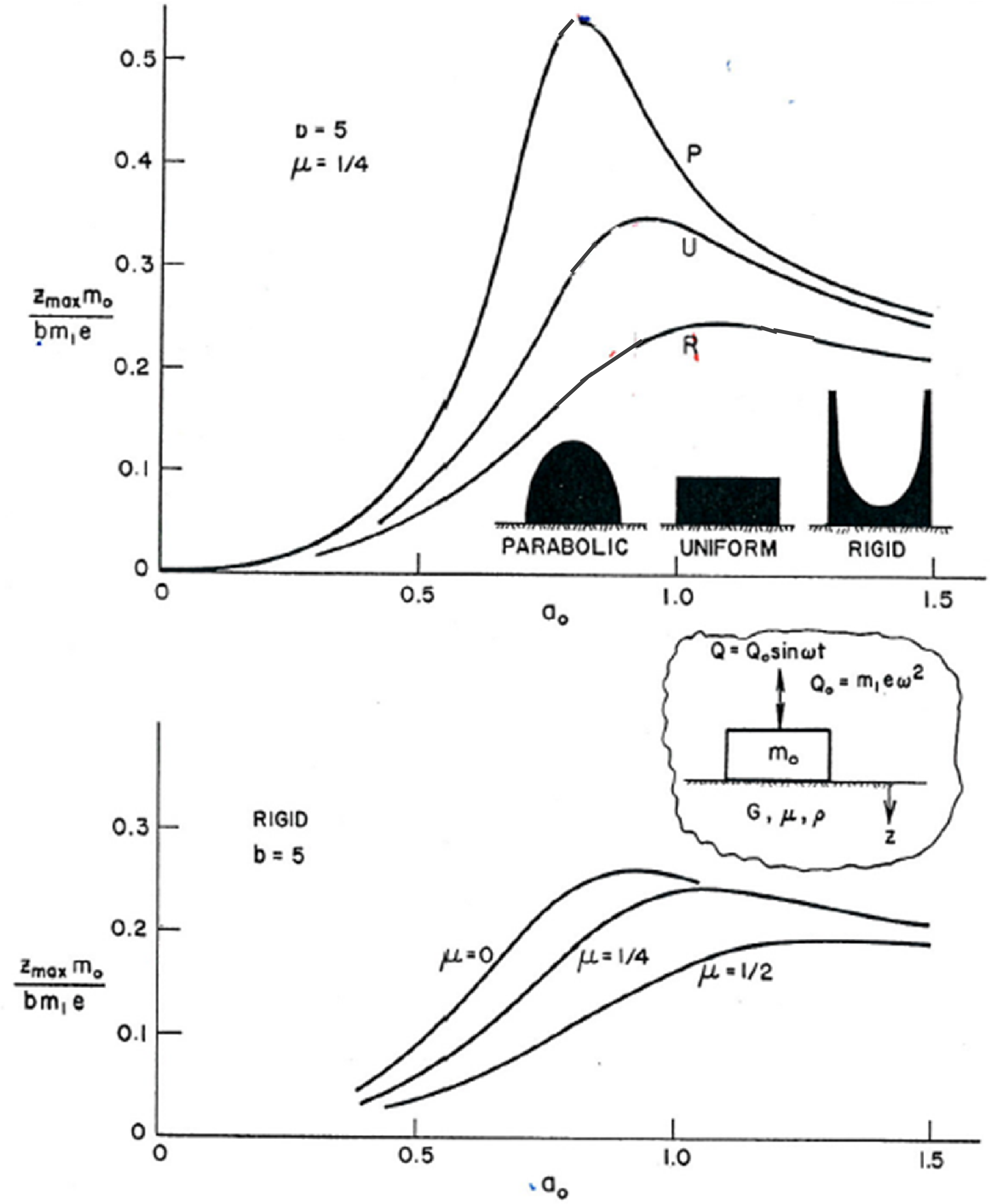

Figure 3. Effect of pressure distribution and Poisson's ratio on theoretical response curves for vertical footing motion (from Richart and Whitman 1967).

Figure 4 illustrates pressure distributions beneath a footing for working stress levels up to failure. Richart and Whitman explained that failure of soil near the footing edges progressed toward the center of the footing as increasing dynamic load was added to static load (Figure 4b), thus reducing

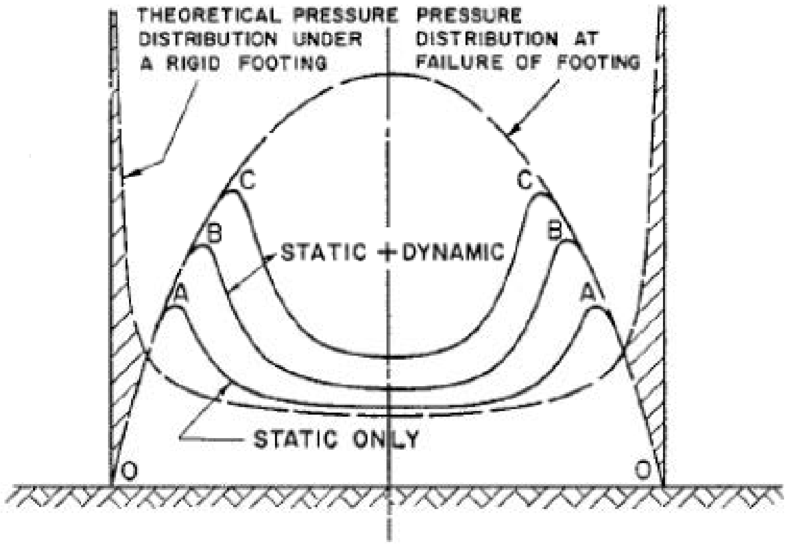

(a) DISTRIBUTION OF TOTAL LOAD

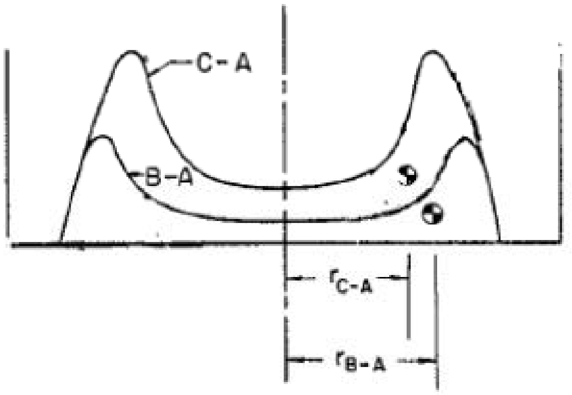

(b) REDUCTION OF THE EFFECTIVE RADIUS

Figure 4. Variation of pressure distribution by increasing the dynamic load (from Richart and Whitman 1967).

the effective radius by shifting the centroid of half the pressure distribution nearer the axis of the footing. The authors noted that the amplitude of motion increased as the total load upon a base increased, and the response curve began to be more like that for a uniform or parabolic stress distribution rather than for a rigid base distribution. The effect of the change of pressure distribution from Figure 3 shows that the frequency of vibration at which the maximum amplitude of motion occurred was reduced from a rigid to a parabolic stress distribution.

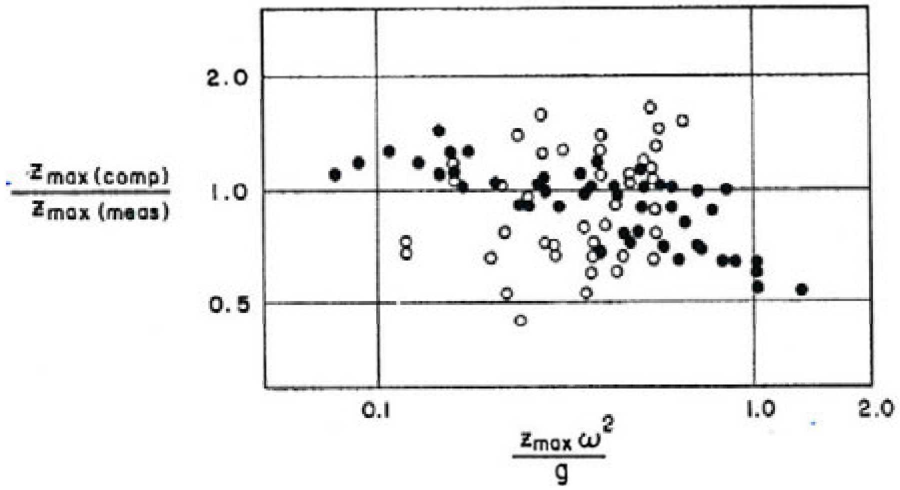

Figure 5. Ratio of computed to measured vertical amplitude vs. ratio of maximum footing acceleration to gravity – summary of tests (from Richart and Whitman 1967).

Richart and Whitman summarized test results of vertical oscillation from two different test sites in Figure 5. The ordinate of Figure 5 is a ratio of the maximum computed amplitude to maximum measured amplitude, where the abscissa represents the ratio of maximum vertical acceleration of the footing to the acceleration of gravity, which is also a normalized measure of the excitation frequency ω. The authors noted that throughout the vertical oscillation test program, the theoretical prediction of the maximum amplitude of oscillation was within a factor of two of the measured amplitude indicating that the theory did not sufficiently capture the mechanics of the soil-structure interaction problem.

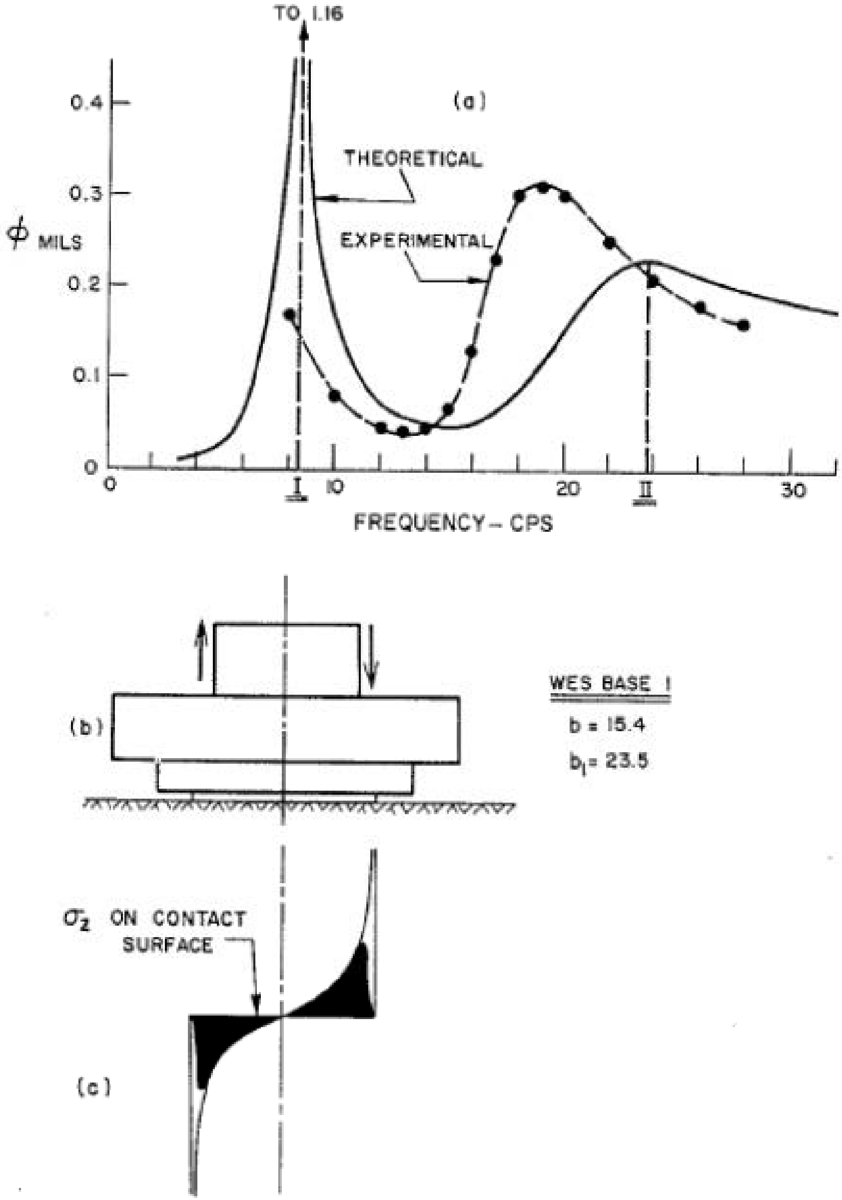

Figure 6. Rocking and sliding – WES Base 1 (from Richart and Whitman 1967).

Figure 6 shows the theoretical response curve for the rotational motion of the footing about its center of gravity and the dashed curve represents a test obtained from the rocking and sliding study of Richart and Whitman. The authors commented on their inability to attain the first experimental peak (Figure 6a) due to limitations in frequency range of the mechanical oscillator. They noted that the second theoretical peak was higher in frequency and lower in amplitude than what was exhibited experimentally. Their explanation of this result was through the differences in the theoretically singular and actual truncated vertical contact pressure distributions beneath a footing under pure rocking, as illustrated in Figure 6c. Recalling Figure 3 and Figure 4, the shaded distribution in Figure 6c would result in higher amplitudes at lower frequencies.

Richart and Whitman argued that the effects of the inertia of the soil and the loss of energy through radiation of elastic waves from the footing base were correctly accounted for in the theory of a rigid base resting upon an elastic half-space. The authors cautioned that while the elastic half-space solution provided good estimates of amplitudes of motion for small strain vibrations, nonlinear effects may cause large differences between theory and experimental results for larger motions.

Novak (1970) explained that the half-space solution was an attractive theory to apply because it takes into account soil properties that can be clearly defined such as shear modulus, Poisson's ratio, and density of the soil. A further benefit of the half-space solution was that the mathematics had been well established (Reissner, 1936, 1937). Novak studied the elastic half-space solution for vibrating foundations and evaluated the results with comparison to field experiments. His comparison was based on the changes in natural frequencies of footings with foundation base size; the dynamic magnification of forced vibrations in the resonance range; the nonlinear character of the foundation response; and the effect of embedment on footings.

Novak investigated the effect of footing embedment since one of the assumptions of the theoretical solution was that the vibrating body rested on the surface of the half-space. Realistically, most footings are embedded to some degree. The effect of footing embedment from Novak's study can be seen in Figures 7 - 9. Figure 7 shows response curves of vertical excitation on a footing surrounded by an air gap and various heights of undisturbed soil or compacted fill material.

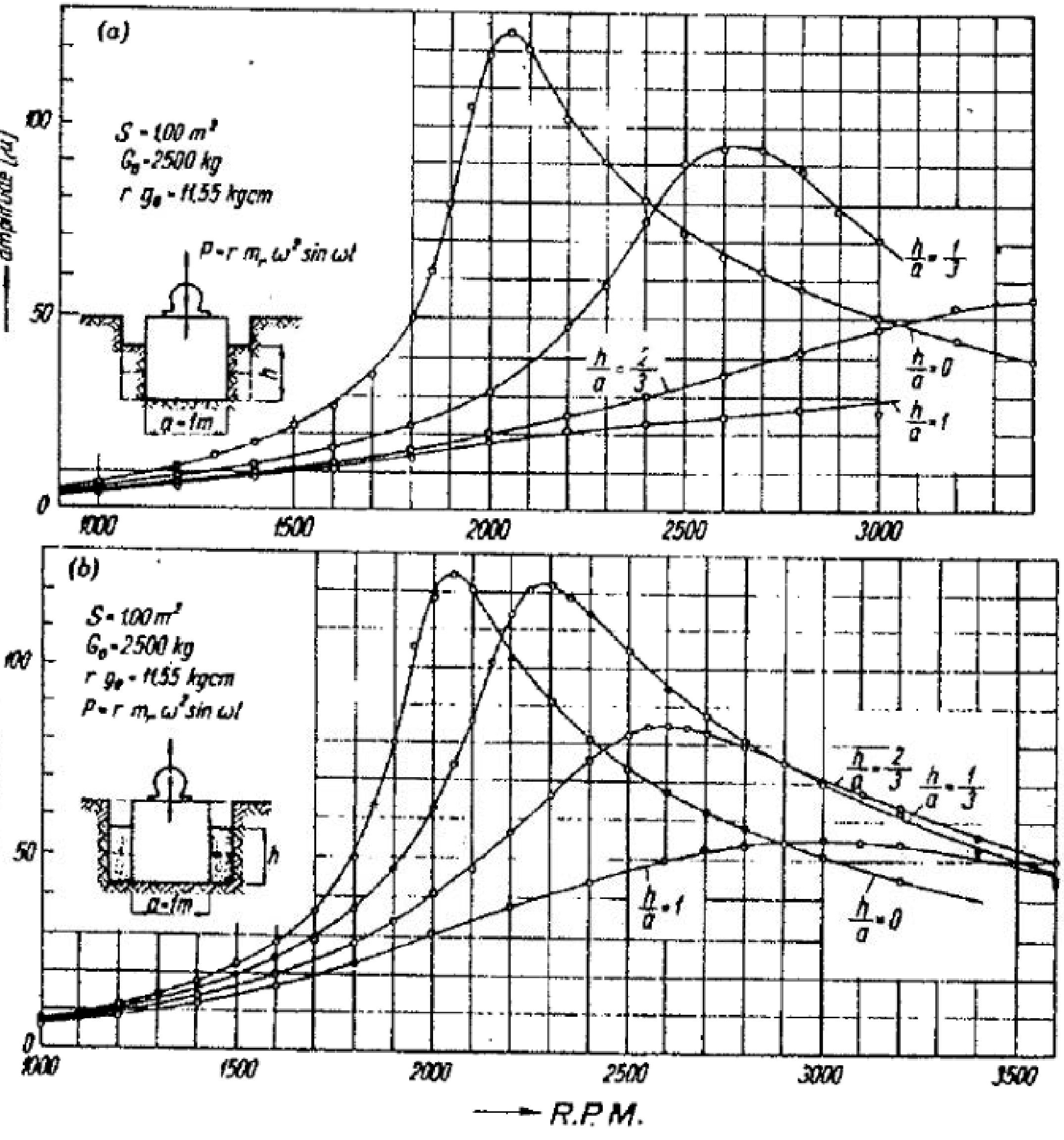

Figure 7. Resonance curves of vertical vibrations of a concrete foundation with different heights of contact with: (a) undisturbed soil; (b) compacted fill material, at same magnitude of exciting forces (from Novak 1970).

As shown from the responses of Figure 7, even conditions with compacted fill material can greatly affect the response due to vertical vibrations. Novak described the response of the footings with compacted fill material as being dependent on the embedment depth of the footing and the relative density of the fill material.

Figure 8 compares foundation responses with vertical and horizontal excitations due to the same excitation intensities, but with different contact conditions. In terms of peak response amplitude, the footings with an air gap had the highest amplitude of response at the lowest frequency. The conditions where the footing was embedded next to undisturbed soil had the lowest amplitude of response at the highest frequency. The response of the footing embedment condition with compacted fill material fell somewhere between the air gap and undisturbed soil conditions, depending on the relative density of the compacted fill.

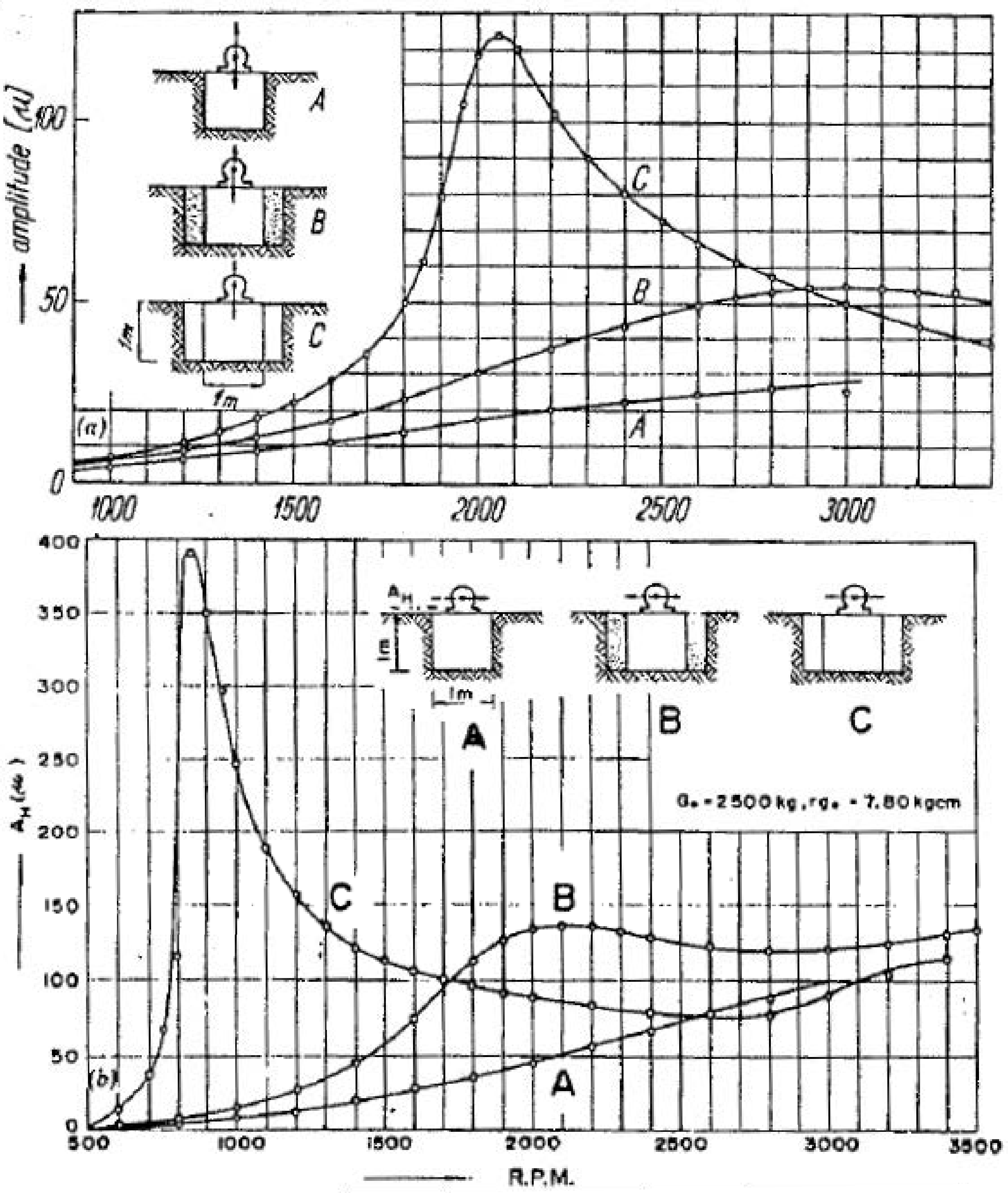

Figure 8. Comparison of foundation response to: (a) vertical; (b) horizontal excitations with various types of contact between sides and surrounding soil, at same excitation intensities (from Novak 1970).

Figure 9 shows the response of embedded footings subjected to the same horizontal excitation, but at different eccentricities. Again, similar results were obtained for the horizontal excitation case where the air gap condition produced the greatest response amplitude at the lowest frequency.

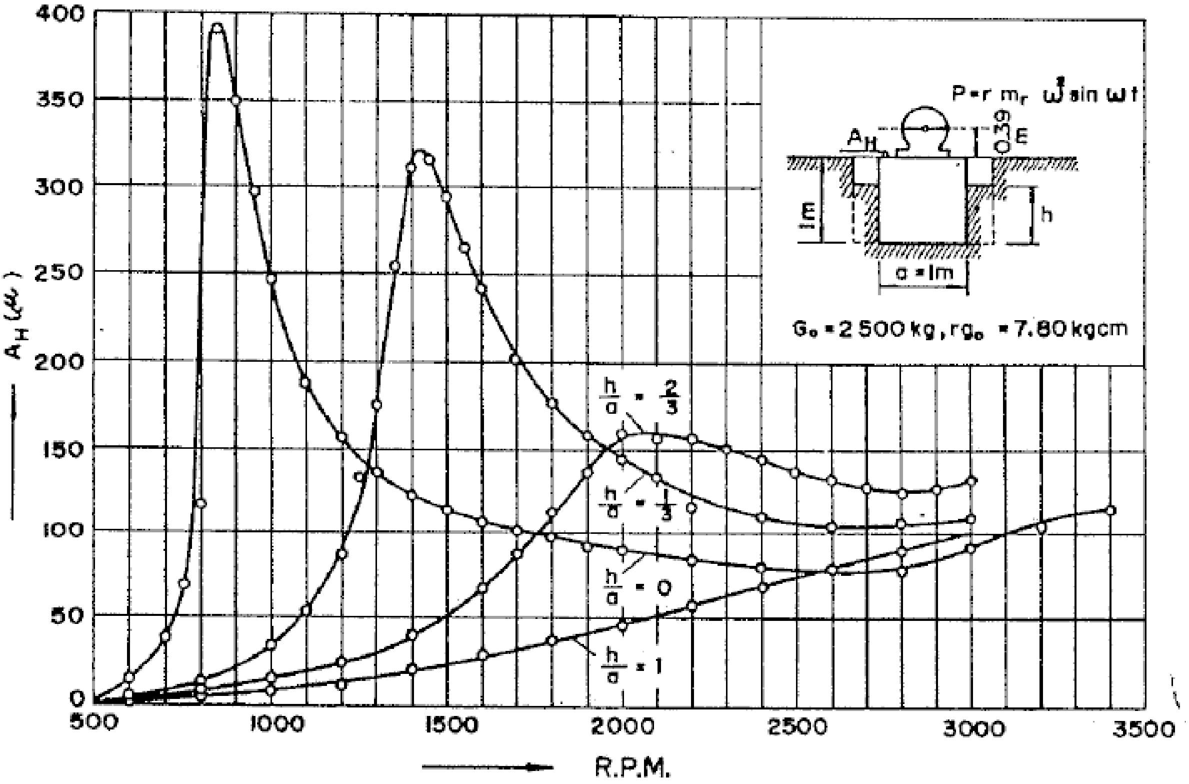

Figure 9. Resonance curves of horizontal vibrations of concrete foundation with different heights of contact with surrounding undisturbed soil, at same excitation intensities as Figure 8 (from Novak 1970).

Novak studied variations in natural frequencies with the foundation base size at constant static contact pressure under the base. Figure 10 shows results from previous experiments along with Novak's results of vertically vibrating rigid foundations compared against half-space theoretical results. A similar comparison is made in Figure 11 for foundations having a constant weight (mass) and different base areas.

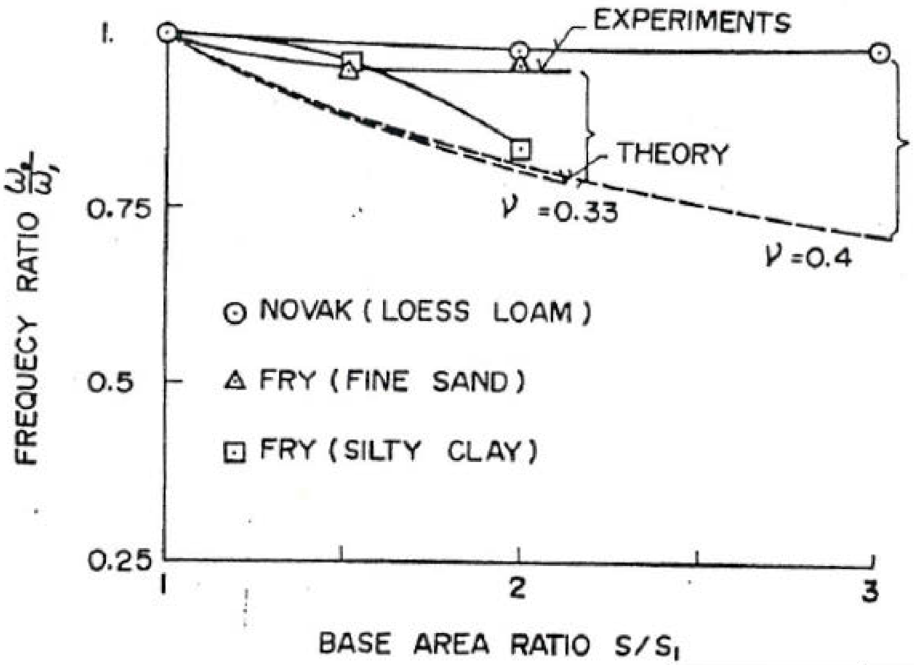

Figure 10. Relative variations of natural frequencies with foundation base area at constant static contact pressure (rigid foundations vibrating vertically, from Novak 1970).

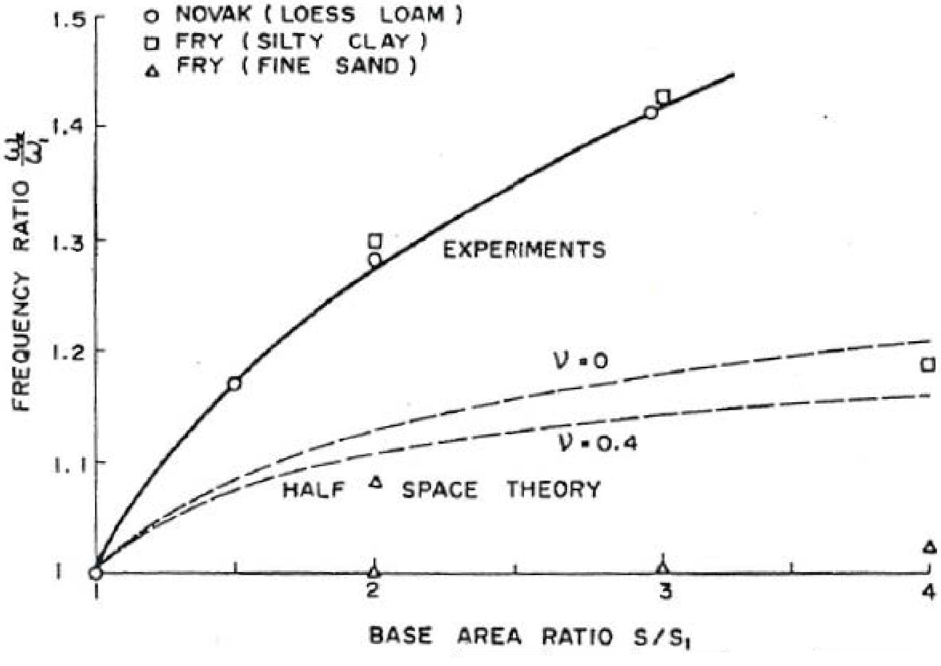

Figure 11. Relative variations of natural frequencies with foundation base area at constant foundation weight (rigid foundations vibrating vertically, from Novak 1970).

As can be seen in both Figures 10 and 11, the experimental results deviated from theoretical behavior. In Figure 11, the observed changes in frequency ratio with base area were much greater than the theoretical ones. The author noted that the test foundations produced results that varied with foundation base size as if situated on an elastic stratum rather than an elastic half-space. As the footing sizes increased, the half-space theory became a less attractive theoretical approximation. Novak concluded his findings by explaining that the theoretical half-space solution provided a good qualitative picture of the experimental footing response, but didn't quantitatively capture the experimental vibration response.

With time, Luco and Westmann (1971) were able to take advantage of increasing computational power by expanding the library of impedance functions for circular footings over a wider frequency range. Up to this point in history, impedance functions for footings resting on a homogeneous, elastic half-space had only been calculated for a very limited low-frequency range. Luco and Westmann presented numerical results of circular footing dynamic compliances for a significantly wider range of frequencies. Their work also went beyond the consideration of contact stresses and surface displacements for the vertical mode of vibration and included torsional, rocking, horizontal, and coupled vibrations as well. Fredholm integral equations were used to derive the surface displacements for a range of frequencies and Poisson's ratios. In addition, Luco, Wong, and Trifunac (1975) expressed the importance of not only accurate identification of impedance matrices in the response calculation of rigid embedded foundations, but also the necessity of forces induced by incident seismic waves. The authors illustrated that foundation input motions (external driving forces from incoming seismic waves) were equally important to the frequency dependent impedance in the force-deformation relationship. Previously, researchers had been making the assumption that the free field seismic motion was equal to the foundation input motion for simplification. This assumption failed when accounting for rocking and torsional components of motion present with horizontal and vertical translations.

The work by Crouse, Liang, and Martin (1985) further explored the impedance matrix. One interesting observation was that negative imaginary parts of the complex valued impedance coefficient indicated negative damping. Negative imaginary parts could also result from experimental error in the measurement of foundation response and may actually have no real significance. The authors considered the formulation of off-diagonal terms of impedance matrices for partially embedded shallow foundations and evaluated their effect on the modes of vibration by comparing responses of field experiments. Many researchers had previously neglected the off-diagonal terms of the impedance matrix, claiming they had little effect in dynamic response. The conclusion of Crouse, Liang, and Martin was that the effect of the off-diagonal terms of the impedance matrix had little influence on the dynamic response of surface footings. The influence of the off-diagonal terms becomes more significant as embedment depth increases.

Wong and Luco (1985) further expanded the library of impedance functions for layered soil profiles resting on an elastic half-space, as shown in Figure 12.

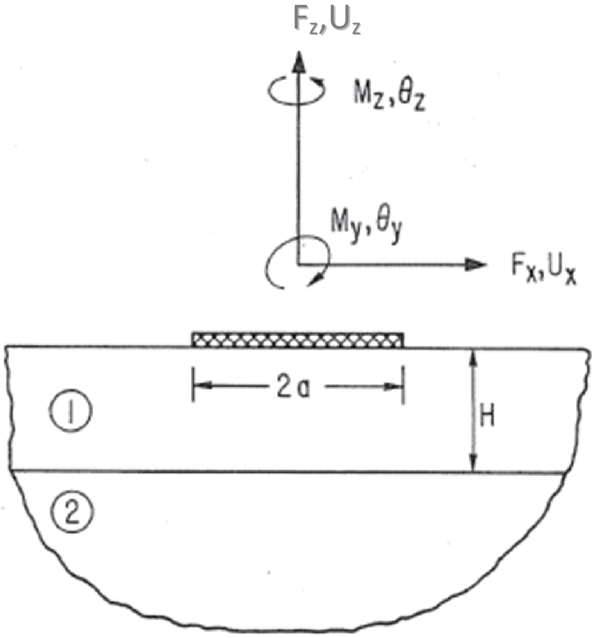

Figure 12. Description of the model (from Wong and Luco 1985).

Their work pointed out that a tabular reference for impedance functions of a number of foundation geometries and soil characteristics would be convenient due to the cumbersome numerical integration approaches to the solution of mixed boundary-value problems. Highly complex and time consuming computer analyses were required to calculate these impedance functions. Wong and Luco presented tables of impedance functions for a rigid massless square foundation resting on two types of layered viscoelastic soil models. One of the viscoelastic models had a layer with constant shear wave velocity overlying a half-space, while the other model had a linearly varying shear wave velocity distribution for the upper layer, as depicted in Figure 13.

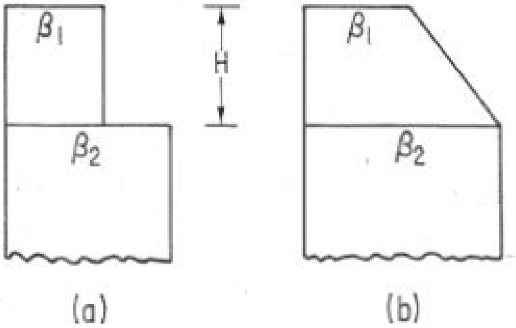

Figure 13. Shear wave velocity distribution of viscoelastic layer (from Wong and Luco 1985).

Impedance functions were reported for horizontal, coupling, rocking, vertical, and torsional modes of vibration. The library of tabulated impedances continued to grow with embedded square foundations through the work of Luco and Mita (1987). Velestos and Wei (1971) and Luco and Mita (1987) tabulated impedances for circular surface foundations, while Wong and Luco (1978) presented impedances for rectangular foundations resting on a uniform half-space.

As mentioned previously, the lumped parameter models of the 1950s and 1960s were simple and convenient for use by practitioners, but the circular shape of the footings limited the accuracy of the models for real world situations. Dobry and Gazetas (1986) provided a collection of different analyses carried out over many different foundation shapes. Researchers in the past had attempted to use equivalent circular footings with the lumped parameter single degree-of-freedom models for the more common square, rectangular, or strip footings with limited success. Important results from Dobry and Gazetas included confirmation that both frequency and foundation shape may significantly affect the dynamic stiffness and damping coefficients. Their paper presented several different foundation shapes with an emphasis on machine foundations. They demonstrated that the method used to compute dynamic stiffness and radiation damping via an equivalent circular footing approach can cause large errors since impedance coefficients are frequency- and shape- dependent.

The work of Crouse, Hushmand, Luco, and Wong (1990) considered experimental vibration-response data from two different foundation systems in different parts of California. The experimental data was then used to compute experimental impedance functions. One of the two foundations considered was a square slab with corner piers embedded in a moderately stiff alluvial deposit while the other was a rectangular slab resting directly on softer deposits, as shown in Figure 14.

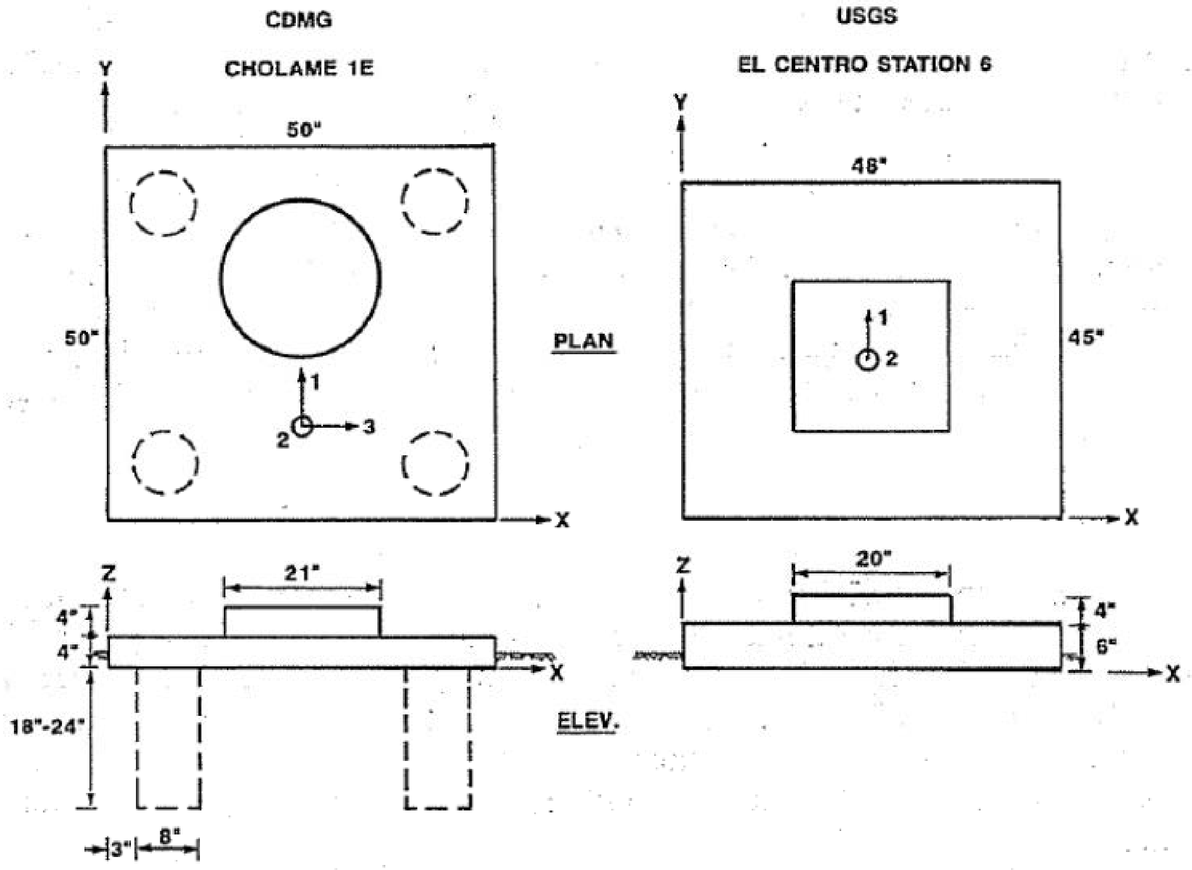

Figure 14. Foundations at Cholame 1E and Station 6; Numbered arrows indicate locations and directions of applied shaker forces (from Crouse et al. 1990).

The experimental impedance functions were compared against theoretical ones. The theoretical impedance functions predicted for the rectangular slab were consistent with the experimental ones, but significant differences were observed in the square foundation with corner piers. The differences between theoretical and experimental impedance functions were hypothesized to be due to overestimation of shear-wave velocities of the top layers of soil directly underneath the foundations.

Gazetas (1991) gave a comprehensive overview of soil-structure interaction problems. He stated that impedance functions depend solely on frequency due to the influence that frequency exerts on inertia. The complex impedance function reflects two types of damping in the system. The first type of damping is energy that is carried by waves spreading away from the foundation, or radiation damping. The second type of damping results from hysteretic action of the soil material. Gazetas stated that the off-diagonal terms of the impedance matrix are likely negligible for surface footings (as noted in Crouse et al. 1985), but could play a bigger role when foundations are embedded in soil since the soil surrounding the foundation would add resistance to the system.

The work by Luco and Wong (1992) discussed an in situ approach for the determination of dynamic soil properties, such as shear-wave velocities, material damping ratios, and Poisson's ratios from forced vibration tests. This in situ approach was made possible by the ability to conduct highly accurate harmonic forced vibration tests of foundations over a wide frequency range; efficient techniques to calculate the dynamic response of foundations resting on a layered, slightly dissipative half-space; and techniques to minimize the difference between theoretical and experimental results, such as the difference of the sum of squares approach. In most harmonic forced vibration tests, the applied force was proportional to the frequency squared and the response at low frequencies was quite small and may fall below the noise level of the instrumentation. The material damping in the soil was best identified by its effect on the imaginary parts of the impedance functions at low frequencies.

Luco and Wong made the observation that impedance functions depend on the elastic and dissipative characteristics of the soil and on the known geometry of the foundation, but not on its inertial properties or on the location of the external forces acting on the foundation.

Svinkin (2002) provided a method to obtain complete time-domain vibration records for the design of impact machine foundations. The method was able to predict vibrations of surrounding soil, structures, and equipment while considering the heterogeneity and variability of soil and structural properties, especially under nonuniform and complicated soil conditions. Compression, shear, and surface waves are generated by foundations for impact machines, with surface waves accounting for about 70% of the total vibration energy near the ground surface. Svinkin investigated the shape of contact area, concluding that foundation dimensions have a negligible effect on the amplitudes of ground vibrations at distances more than 10-25 m from the source of vibration for frequencies below 32 Hz.

Pak and Ashlock (2000) introduced Impedance Modification Factors to help bring analytical frameworks for characterizing dynamic behavior of surface foundations on sandy soils to more closely agree with physical soil-foundation behavior. The test set up consisted of square high-strength aluminum scale-model foundations on a prepared sand medium in a geotechnical centrifuge. Some of the major sources of difficulty in capturing vibratory characteristics of foundations on granular soils were complex stress-strain relationships under cyclic loading and spatially inhomogeneous stress conditions. The dynamic lateral load problem was more complicated than the dynamic vertical one due to the lack of symmetry in motion, the coupling of the translational and rotational response, and other higher order contact phenomena. Load cells and accelerometers were used to capture the applied force and resulting motion of the foundations. A Fourier analyzer was used to generate random excitations, process the analog response time history signals with averaging and windowing, and determine the frequency response functions for the forced vibration problems. A homogeneous half-space theoretical model was examined against the vertical vibration experimental data and an equivalent homogeneous shear modulus was determined by using impedance functions from a rigorous boundary element solution. The same equivalent homogeneous half-space model was then used to predict the lateral response. This yielded a theoretical lateral-rocking response similar in shape to the experimental one, but the peak frequencies were noticeably different. The authors demonstrated that an equivalent homogeneous shear modulus for the lateral-rocking case would need to be about 30% less than that for the vertical vibration case. Pak and Ashlock argued that the characterization of a soil deposit via two dramatically different shear moduli was not a rational solution for general multi-directional loading cases. The differences in shear moduli could be attributed to the following discrepancies: (1) the theoretically singular contact stresses at the footing edges while the experimental ones are more likely saddle-shaped (similar to those shown in Figure 4 and Figure 6); (2) the shear modulus of a uniform sand is known to increase with depth, contrary to the homogeneous assumption; and (3) an increase in confining pressure immediately under the footing leading to a locally stiffened soil modulus which is not accounted for by the homogeneous half-space theory. These observations led to the development of impedance modification factors (IMF) to improve the agreement between theoretical and experimental foundation responses.

Pak et al. (2010) performed dynamic load tests on scale model surface foundations, as shown in Figure 15, and measured the vertical, horizontal, and rocking responses. They proved that the multi-modal surface foundation response under vertical eccentric loading was equivalent to that of a combination of both the vertical centric and horizontal centric tests (Figure 16a equivalent to Figure 18a and Figure 17a equivalent to Figure 18b). Since all three modes of vibration could be delivered in a single test, the cumulative effects of load history inherent in soil-structure interaction of separate modal tests could be greatly reduced.

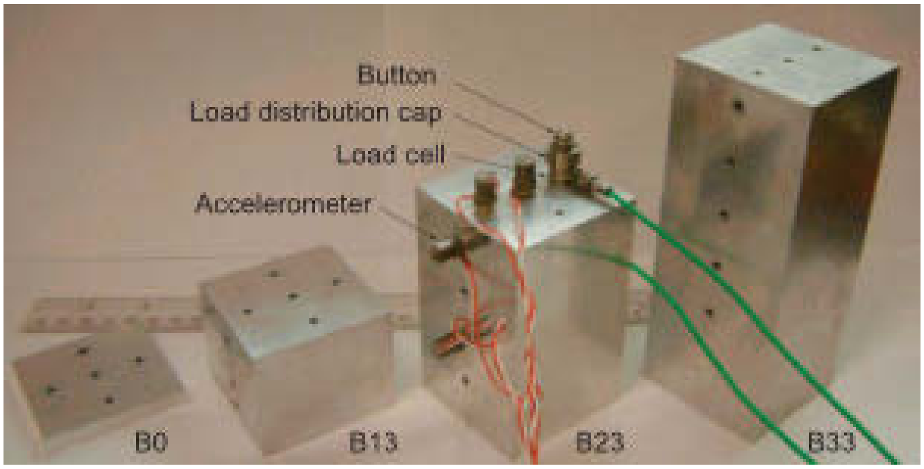

Figure 15. Scale model footings and instrumentation (from Pak et al. 2010).

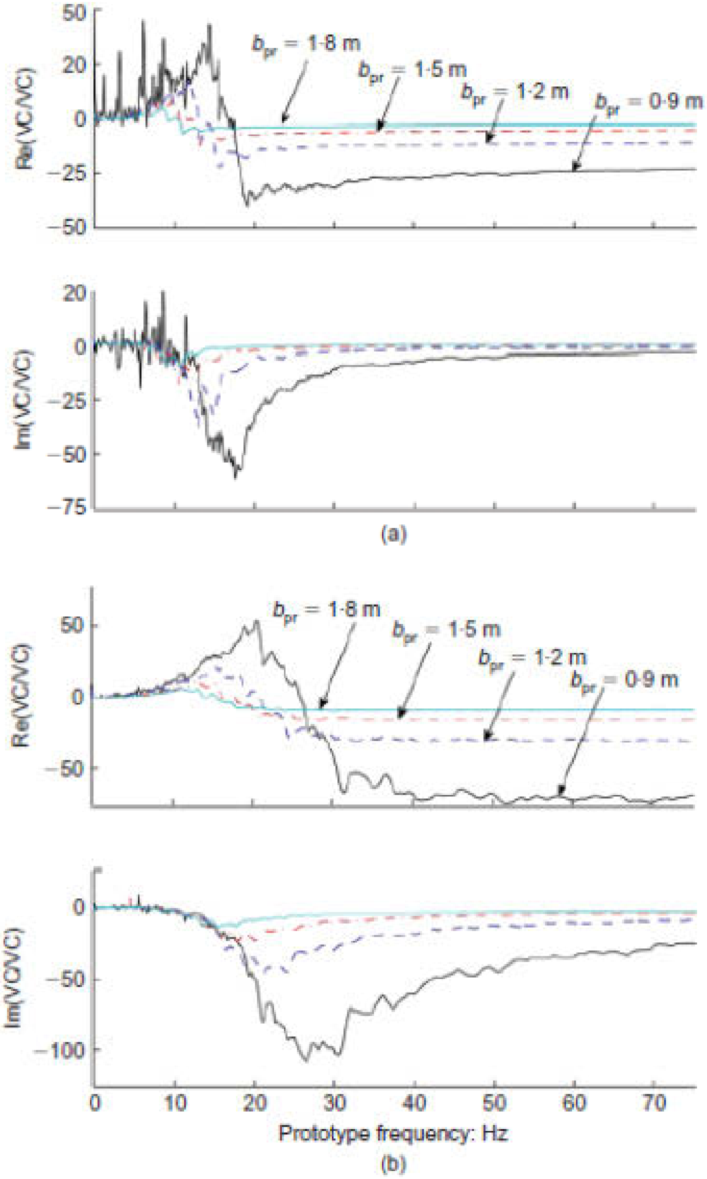

Figure 16. Representative VC/VC prototype-scaled accelerances (mm/s^2/kN) in vertical-centric tests for (a) footing B33 and (b) footing B13 at 33, 44, 55, and 66g (from Pak et al. 2010).

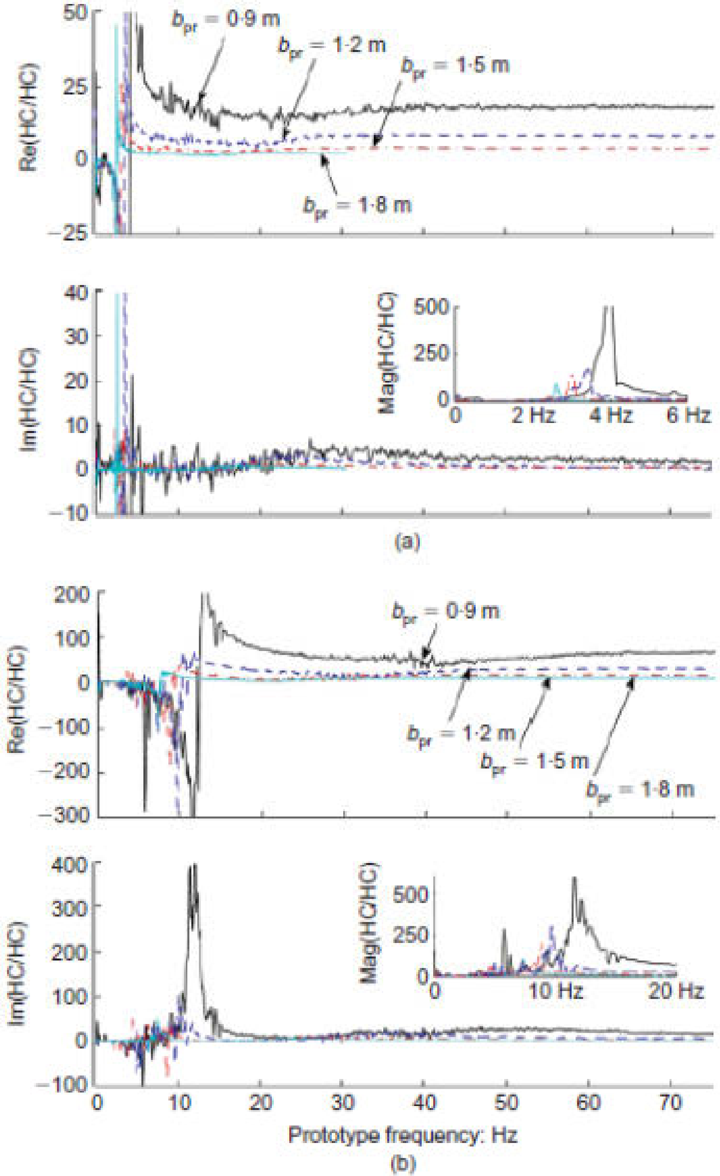

Figure 17. Representative HC/HC prototype-scaled accelerances (mm/s^2/kN) for laterally mounted accelerometer (hole 3) in HC tests of (a) footing B33 and (b) footing B13 at 33, 44, 55, and 66g with close-ups of fundamental peaks (from Pak et al. 2010).

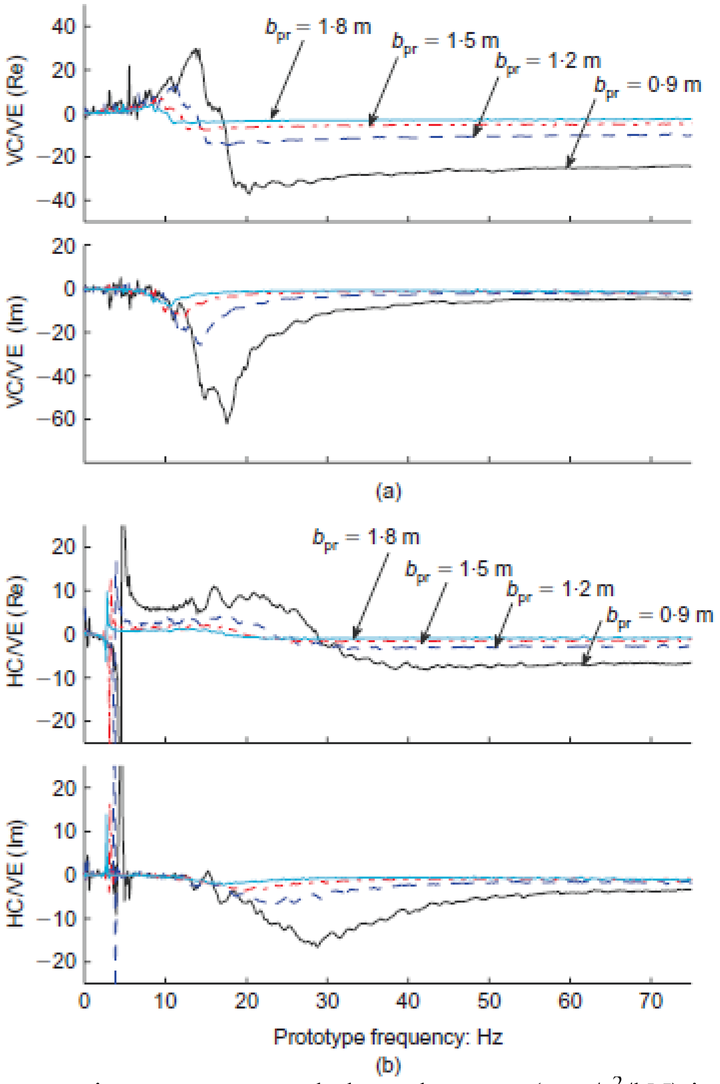

Figure 18. Representative prototype-scaled accelerances (mm/s^2/kN) in vertical-eccentric tests of footing B33 at 33, 44, 55, and 66g: (a) VC/VE and (b) HC/VE (from Pak et al. 2010).

The findings of Pak and Ashlock (2000) and Pak, Ashlock, Kurahashi, and Soudkhah (2010) from centrifuge scale-model tests serve as a basis for the field-scale vibration study presented in Chapter 3.

2.2 Previous Large Strain Dynamic Foundation Rocking Research

The seminal work of Housner (1963) forms the basis for large strain dynamic foundation rocking research. Housner first studied the counter-intuitive ability of slender looking structures to withstand strong motion earthquakes while more stable looking structures toppled under similar conditions. Interest of this topic was piqued from the good seismic performance of slender elevated water tanks versus more stable looking elevated water tanks during Chilean earthquakes in 1960. The more slender water tanks resulted in much less damage than their less slender counterparts. Interestingly, this phenomenon was also observed in graveyards where tall slender stone pillars were able to survive strong ground motions. Housner's investigation to explain this behavior examined rigid blocks resting on a rigid base and subjected to constant, horizontal acceleration, a single sine pulse, and an earthquake type excitation. Important properties of the rigid block included the weight, moment of inertia about the rotation point, and the location of the center of gravity at a distance from the base and side, as shown in Figure 19.

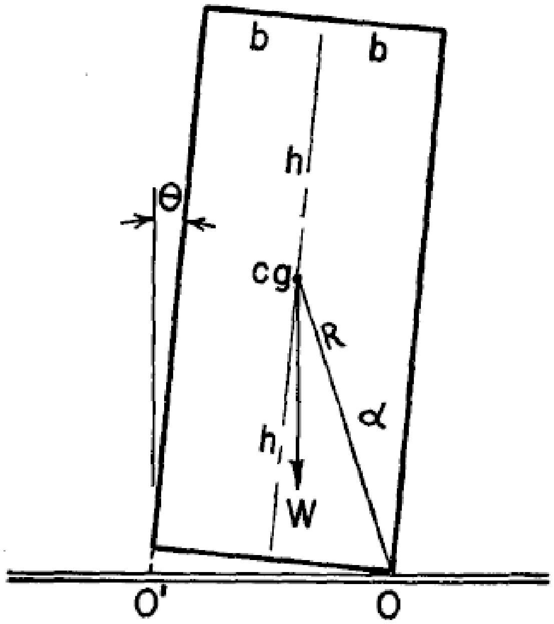

Figure 19. Model of a rocking block (from Housner 1963).

Through free vibration equations of motion for the rigid block, Housner illustrated that the period of a structure was strongly dependent upon the initial angle of rotation. It can be seen from Figure 20 that large initial rotations near unity produced a much longer period than that of smaller initial rotations.

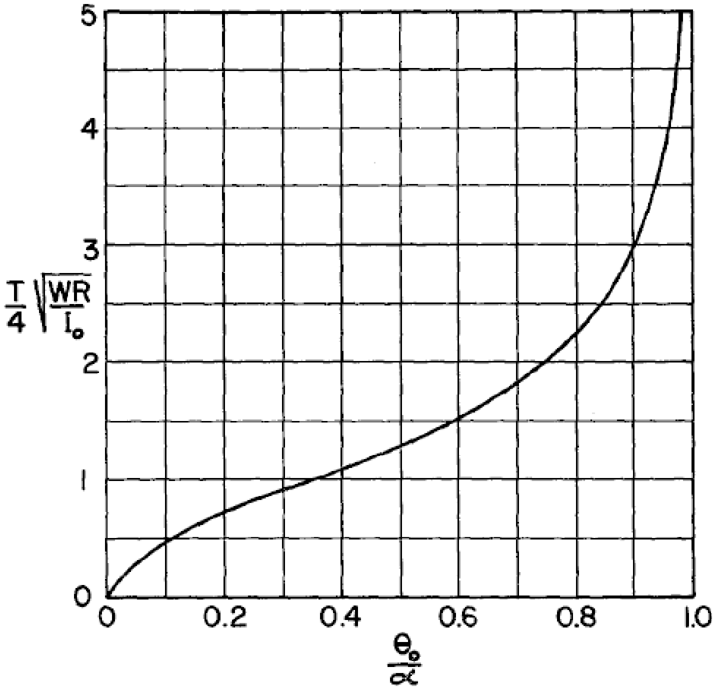

Figure 20. Period T of a rocking block with initial rotation amplitude θ_0 (from Housner 1963).

Housner assumed negligible energy loss at impacts of rocking and that friction was sufficient to prevent sliding from occurring, so the period remained constant and θ_0 was restored through each half cycle. In reality, energy was lost through rocking impacts. Housner explained that once during each half-cycle there would be an increment decrease in the energy of vibration due to the rocking impacts, thus the period through each half cycle would be longer than that which preceded it. The amplitude of rotation (φ_n) was affected through n impacts for a given constant reduction of energy due to impact r, as shown in Figure 21. The figure illustrates how larger initial rotations experienced a more severe degradation of amplitude than that of smaller initial rotations. Another observation was that as the number of impacts increased, the frequency of oscillation approached an infinite value.

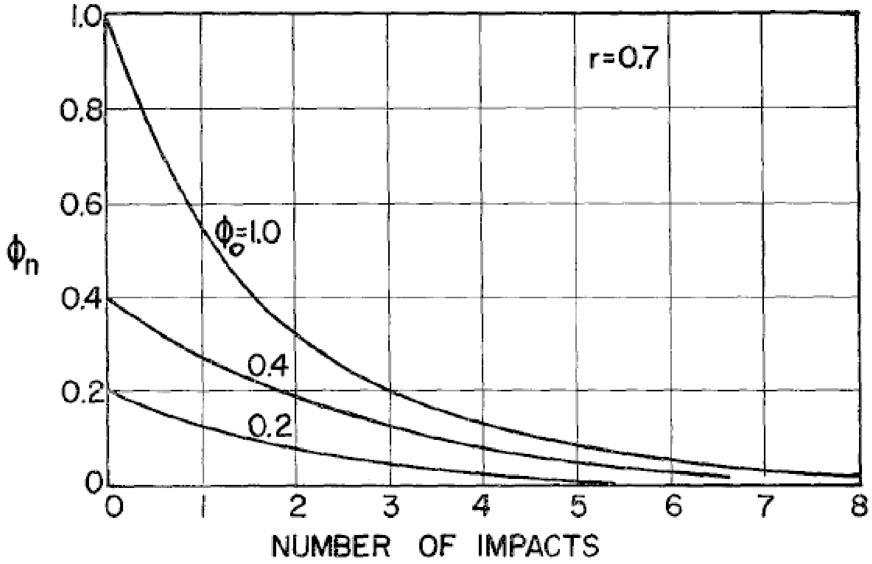

Figure 21. Amplitude φ_n subsequent to *n*-th impact (from Housner 1963).

Through this study, Housner was able to compare the energy input against the energy required to overturn a structure. If the energy input was computed from a velocity response spectrum, the only geometric input affecting stability against overturning was the distance from the center of rotation to the center of gravity, *R*, as shown in Figure 19. As *R* increased, so did the stability against overturning. This conclusion revealed a scale effect where the larger of two geometrically proportional blocks was more stable than the smaller block.

Many authors have extended Housner's work to a myriad of different applications. The particular application for the large strain dynamic soil-structure rocking of the present study is related to the work of Gajan et al. (2005), who explored the use of soil as an energy dissipation mechanism to reduce shaking demands on structures supported on shallow foundations. Gajan et al. performed a series of tests on shear wall footings on a large centrifuge to study the nonlinear load-deformation characteristics during cyclic and earthquake loading. They studied parametric variations of footing dimensions, depth of embedment, wall weight, initial static vertical factor of safety, soil density, and soil type to examine the overall rocking response. Two types of soil were tested; dry sand (relative density, D_r = 80 and 60%) and saturated clay (uniformity coefficient, C_u = 100 kPa).

Figure 22 shows the different test setups and instrumentation used for the vertical push, dynamic loading, and slow cyclic lateral push tests. Bearing capacity was estimated for each series of tests by performing at least one concentric vertical push test. Dynamic loading was applied to the models by shaking the base of the soil container with a gradually increasing cosine displacement time history. Accelerations and displacements were recorded at different positions on the footing and wall. Slow cyclic lateral push tests used an actuator to push on the wall at different heights. Displacements were measured by two horizontal and two vertical linear potentiometers attached on the wall, and forces were measured by a load-cell attached to the actuator.

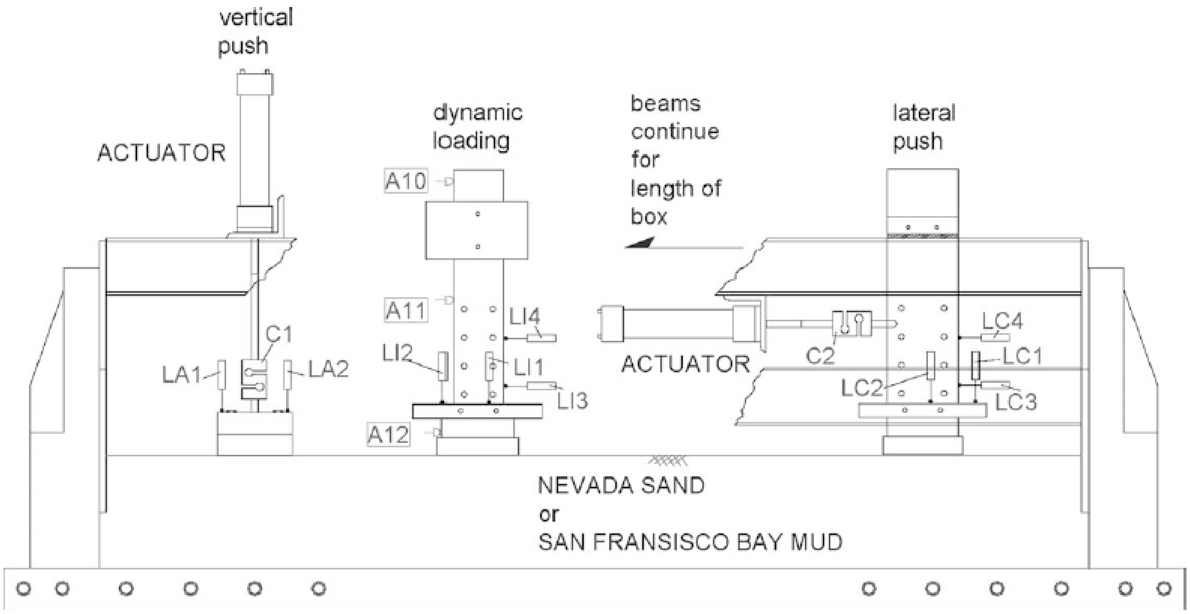

Figure 22. Model container and experimental setup with instrumentation for vertical push, slow cyclic lateral push, and dynamic loading tests (from Gajan et al. 2005).

For slow cyclic lateral tests, the measured forces and displacements were used to calculate the resultant forces and displacements at the base center reference point of the footing by equilibrium equations and rigid body translation and rotation. The additional moment caused by the self-weight of the structure moving through a lateral displacement (P-delta effect) was also included. For dynamic tests, the interfacial forces and displacements of the footing were obtained by combining the accelerometer and displacement transducer measurements by considering the equation of motion of the rigid body shear wall.

Figure 23 and Figure 24 show results for a slow cyclic lateral test on sand and clay, respectively. These moment-rotation hysteresis loops indicated a significant amount of energy dissipation at the footing-soil interface. As shown in these figures, the moment capacity did not appear to reduce with the number of cycles, but a degradation of rotational stiffness was observed with increasing amplitude of rotation. These figures illustrate the large amount of permanent footing settlement that accumulates through each cycle of testing. Footing settlement on this order of magnitude develops significant internal strains within the supported structural system. The cost of allowing soil to dissipate energy is large permanent deformations of the soil and the potential for increased internal strains within the supported structure.

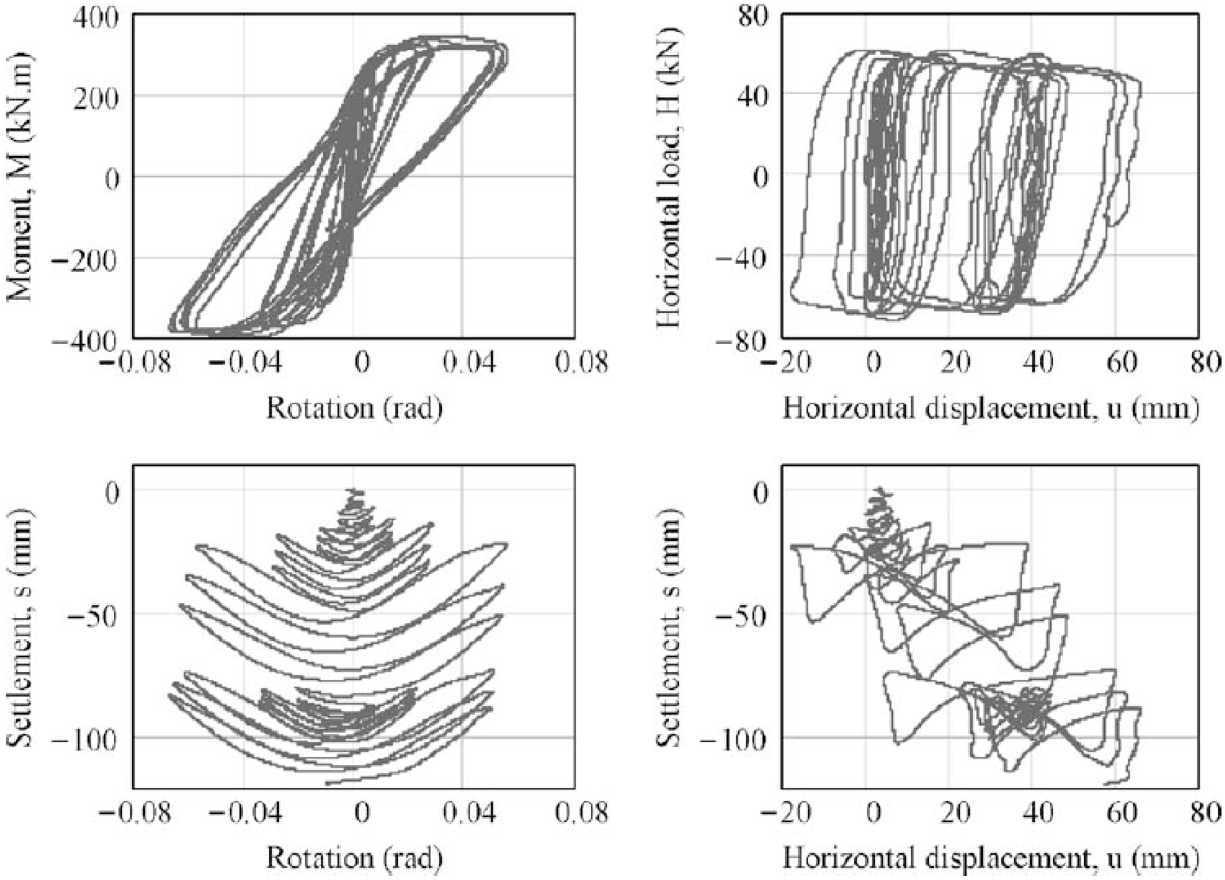

Figure 23. Slow cyclic lateral push test; sand (D_r = 80%), footing length = 2.8 m, width = 0.65 m, embedment = 0.0 m, FS = 6.7, lateral load height = 4.9 m (forces and displacements are at the base center point of the footing) (from Gajan et al. 2005).

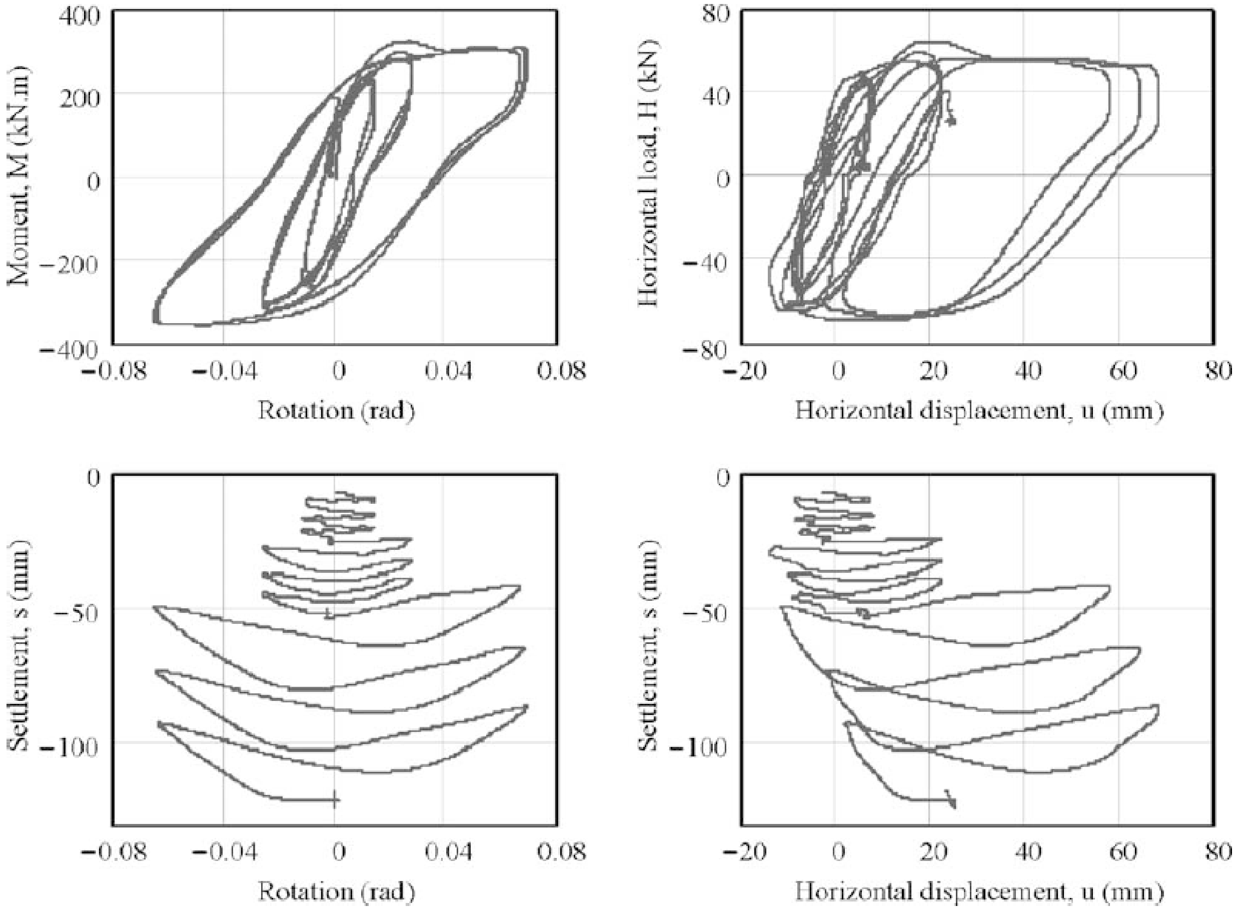

Figure 24. Slow cyclic lateral push test; clay (C_u = 100 kPa), footing length = 2.7 m, width = 0.65 m, embedment = 0.0 m, FS = 3.0, lateral load height = 4.6 m (forces and displacements are at the base center point of the footing) (from Gajan et al. 2005).

The settlement-rotation relationship tracked the accumulation of permanent settlement beneath the footing. The figures also depict the uplift behavior of the footing associated with larger rotation amplitudes. As the footing lost contact with the soil, a gap formed on one side and caused yielding on the other. This gap formation and yielding caused rounding of the soil surface and a nonlinear moment-rotation relationship as shown in the figures. The horizontal load-sliding relationship did not show any degradation in horizontal stiffness with number of cycles or amplitude of displacement. The settlement-sliding relationship shows the coupled behavior of sliding and uplift and the closing of the gap formation upon unloading.

Figure 25 shows dynamic test results for a footing on sand. Similar to the slow cyclic lateral push tests, the moment-rotation relationship exhibited a reduction in rotational stiffness with increasing rotation, though dynamic loading produced a peak rotation less than the slow cyclic lateral push loading. The settlement-rotation relationship indicated that the dynamic tests did not produce significant uplift, but significant amounts of permanent settlement accumulated like the tests on clay.

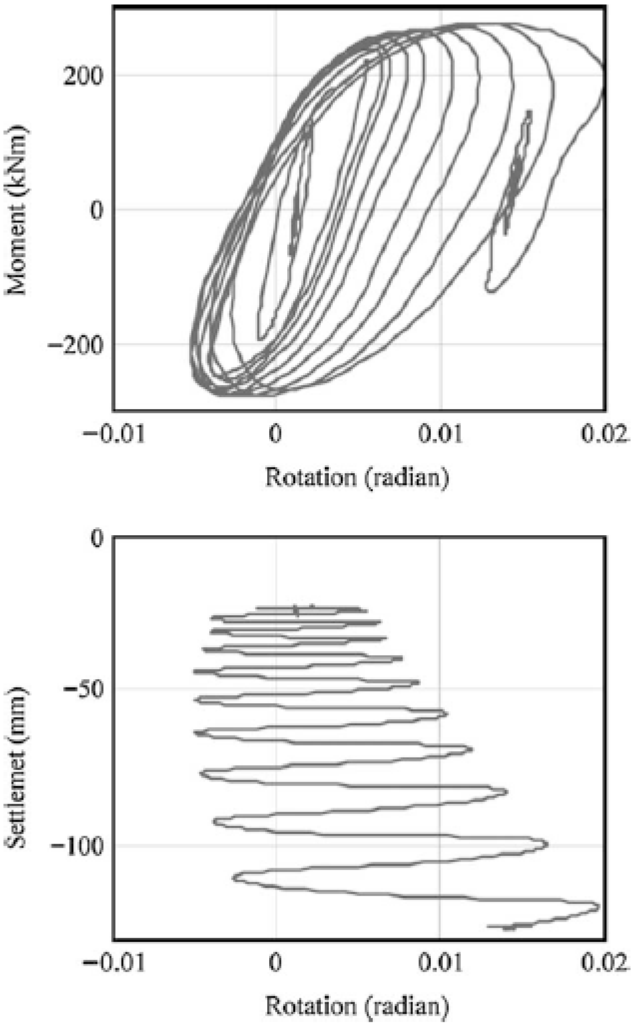

Figure 25. Results of dynamic test with base shaking: sand (D_r = 80%), footing length = 2.84 m, width = 0.65 m, embedment = 0.0 m, FS = 5.3 (from Gajan et al. 2005).

To compare the soil behavior from the dynamic tests with seismic shaking to that of the quasi-static cyclic tests, the dynamic moment-rotation backbone curve connecting the extreme points of each cycle in Figure 25 was superimposed over a portion of the slow cyclic test from Figure 23 as shown in Figure 26.

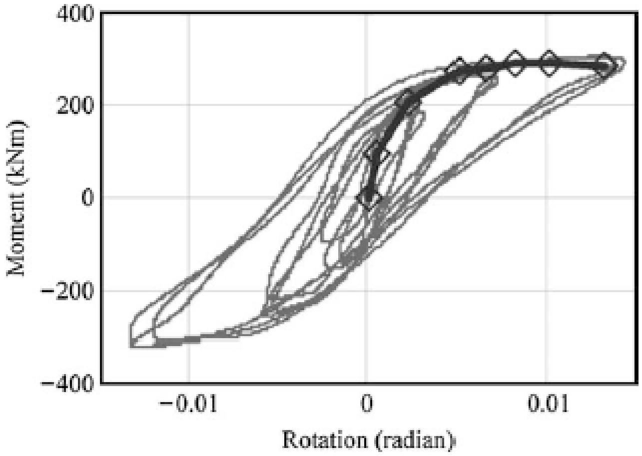

Figure 26. Comparison of dynamic data trend line with slow-cyclic moment-rotation plot: sand, D_r = 80%, L = 2.84 m, B = 0.65 m, D = 0.0 m (from Gajan et al. 2005).

Figure 26 shows that the moment-rotation behavior held close agreement between slow cyclic and dynamic tests and that slow cyclic tests may be appropriate for simulating moment-rotation behavior in dynamic events.

Gajan et al. (2005) presented experimental results of rotational stiffness degradation behavior in terms of a mean rotational stiffness at a given rotation for a foundation rocking on sand, which is shown in Figure 27. In their study, the factor of safety against vertical bearing capacity failure, FS_V, was a parameter of interest, as it affects the moment capacity and shape of the moment-rotation relationship.

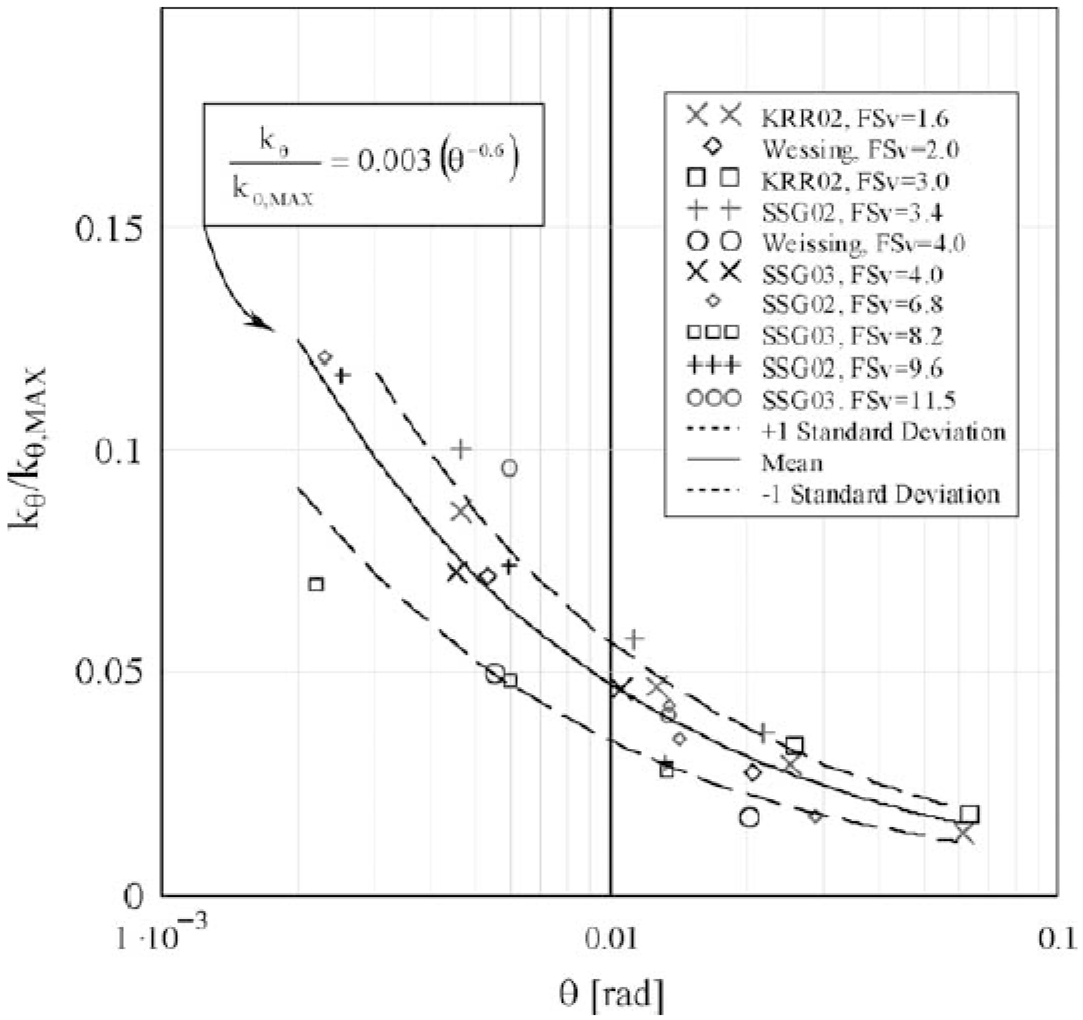

Figure 27. Rotational stiffness degradation as a result of foundation rocking: test results on sand for various initial static vertical factors of safety, FS_v (from Gajan et al. 2005).

The rounding of the footing-soil interface was verified by casting plaster in the structures' footprint and measured by a computer measuring machine following some of the tests. A free body diagram shown in Figure 28 illustrates forces and deformations leading to the rounded soil surface.

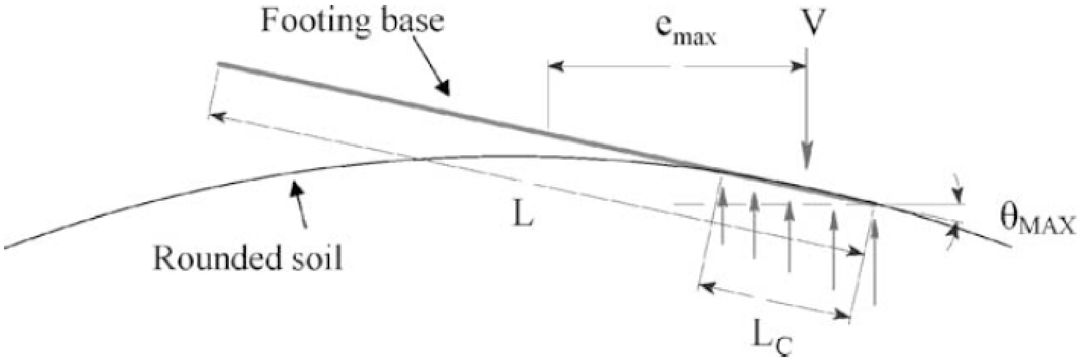

Figure 28. Illustration of the geometry and contact of the rigid footing with deformed soil surface (from Gajan et al. 2005).

As the footing is uplifted, the contact area decreases, which leads to an increase in bearing stress and consequently deforms the soil surface. The nonlinear bearing stress resultant changes location as the footing rotates and dictates the moment-rotation behavior.

While the work of Gajan et al. (2005) confirmed that soil has the capacity to dissipate large amounts of energy through rocking, the observed permanent deformations led to the structurally undesirable softening of the building system.

The work of Kutter et al. (2006) was an extension of Gajan et al. (2005) and previous research that commenced in the early 2000s at the University of California - Davis and University of California - Irvine. The previous research focused on centrifuge and analytical modeling studies of nonlinear load-deformation behavior of shallow foundations. Kutter et al. (2006) focused on the development of numerical tools for modeling nonlinear rocking behavior and predicting associated foundation and building settlements, and validating these tools against available experimental data. The two numerical tools described in this study were a nonlinear Winkler-type framework for modeling the soil-structure interaction using nonlinear springs and dashpots with gapping elements, and a single-element “macro-model” based on plasticity theory.

Kutter et al. (2006) presented summaries of the centrifuge model experiments performed as part of their work on both sand and clay soils. The majority of the centrifuge tests were performed at an acceleration level of 20g in order to make stresses in the model equal to stresses in the prototype. Three types of loading were applied to the models: dynamic loading, slow cyclic lateral loading, and axial loading. Dynamic loading was provided by a programmable shake table to apply various ground motions and recorded earthquake acceleration histories to the base of the soil container. Slow cyclic lateral loading used a hydraulic actuator to apply sinusoidal displacements to shear walls. Axial loading used the same hydraulic actuator to apply cyclic or monotonic vertical loading to the model footings. Parameters of interest in this study were vertical factor of safety of the footing against bearing capacity failure, footing embedment, soil density, soil type, and the height of the building.

The types of model structures tested in this study were either double shear walls or single shear walls. The double wall configuration provided a stand-alone laterally stable structure, with out of plane tilting caused by dynamic events. The single wall configuration was laterally braced on each side of the wall by Teflon points to ensure planar motion while minimizing resistance from friction.

The soil for the sand tests was prepared by pluviating sand through air from a controlled height. Relative densities were calibrated from the pluviating method, and friction angles were back-calculated from vertical load tests using the conventional bearing-capacity equation. In clay tests, clay layers were placed and consolidated in the centrifuge prior to testing. Soil strengths of the clay tests were determined using a variety of different methods, but their ultimate recommendation was to use shear strength values by back-calculating from the conventional bearing-capacity equation.

Instrumentation used for the tests included both accelerometers and linear potentiometers in dynamic tests. Accelerometers were not used in slow cyclic tests. For dynamic events, accelerometers were attached both vertically and horizontally in the direction of shaking on the shaker manifold, in the sand layer, and on the building model. Kutter et al. (2006) double integrated the acceleration signals to determine dynamic displacement time histories. Four linear potentiometers were used for each single shear wall footing (two horizontal and two vertical). While only three linear potentiometers were required to define planar motion of the wall, the fourth served as a measurement redundancy. A load cell recorded applied actuator loads on the walls. Results of force-displacement and rocking motion relationships from a single shear wall footing test subjected to slow lateral cyclic loading are presented in Figure 29.

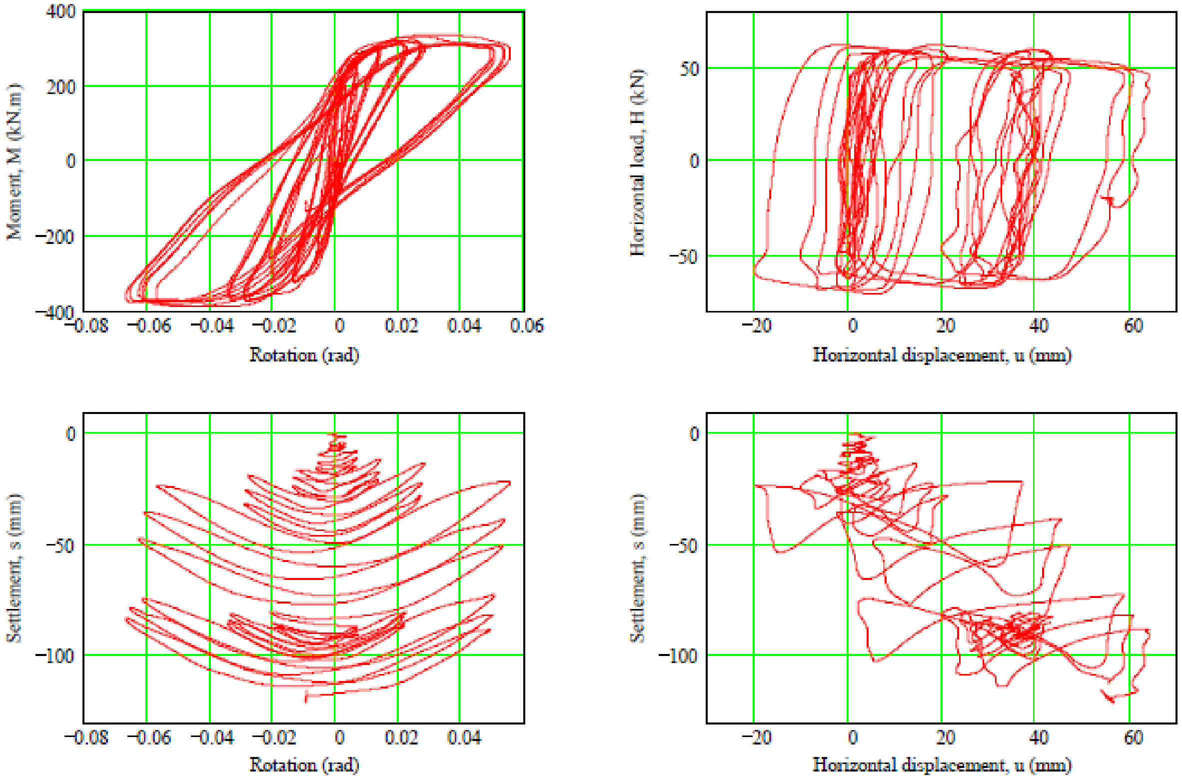

Figure 29. Data from test SSG02, test#3a, FS = 6.7, embedment = 0.0m, load height = 4.9m, footing length = 2.84m (from Kutter et al. 2006).

From their program of centrifuge tests, some notable conclusions were that soil (sand and clay) beneath a shallow footing had great potential to dissipate large amounts of energy during dynamic loading. Moment-rotation relationships indicated moment resistance did not significantly decay with rotational amplitude or number of cycles, and that backbone moment-rotation and hysteresis curves were similar for dynamic and slow cyclic loading tests. A drawback of using soil to dissipate energy was that footings may experience permanent deformations in the form of settlement, sliding, and rotation. These permanent deformations continued to accumulate as the number of loading cycles progressed. The footing shown in Figure 29 exhibited as much as 3 to 14 mm of settlement per cycle. Also, footings with a greater factor of safety against bearing capacity failure exhibited less settlement deformations under dynamic loading than those with smaller factors of safety.

Kutter et al. (2006) developed numerical tools for the modeling of soil-foundation interaction. One of the tools presented was a beam-on-nonlinear-Winkler-foundation (BNWF) model. The BNWF model was based on Winkler's (1867) pioneering work of representing the soil medium as a system of discrete, closely spaced independent linear elastic springs as a representation of the physical soil medium. Variations of Winkler's general method have been used in a wide variety of geotechnical applications. Nonlinear spring models have been used for application to the highly nonlinear rocking problem, but there is no widely accepted analytical procedure for developing static, cyclic, and dynamic spring resistance curves from experimental data.

Kutter et al. (2006) attempted to analyze and identify the important parameters of nonlinear spring-type models used in BNWF approaches that would reasonably capture system response for performance-based design methodologies. The investigators implemented the BNWF model in the OpenSees platform to carry out the study. These BNWF models were used to simulate the centrifuge tests described above as well as experimental datasets from other researchers. An example of these comparisons is shown in Figure 30.

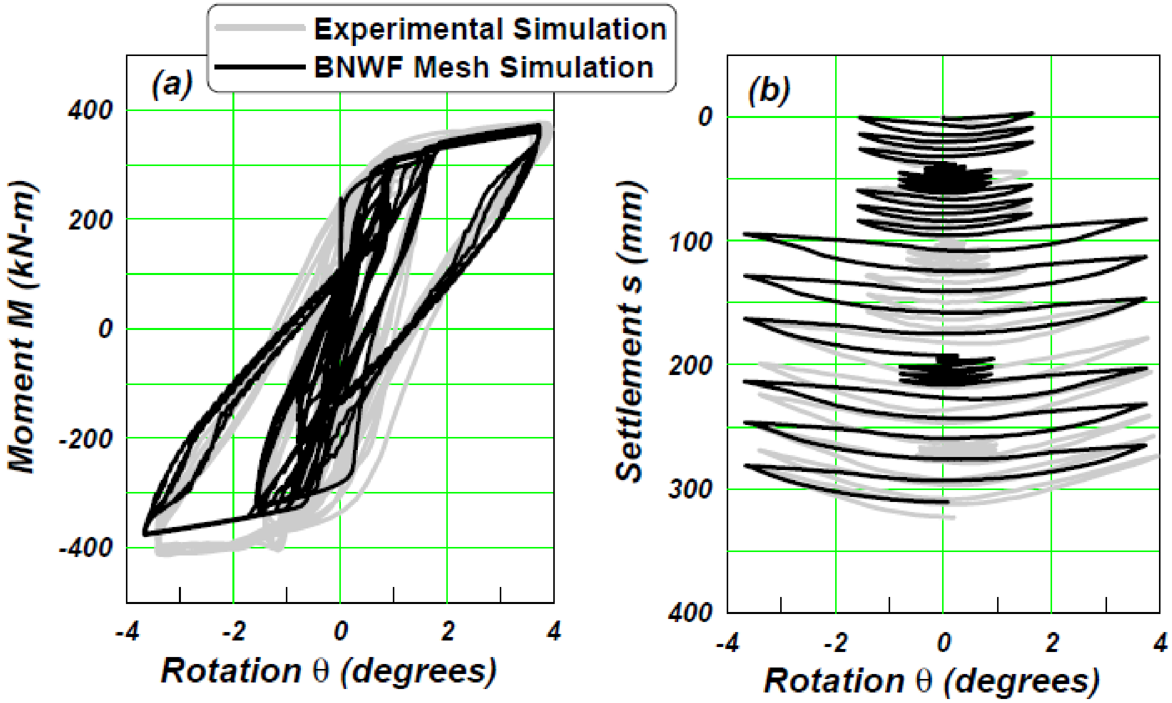

Figure 30. Comparison of experimental and numerical simulation of rocking shallow foundation: (a) moment-rotation response and (b) settlement-rotation response. Experimental dataset: KRR02-S21 (Parameters: centrifuge, sand, small footing, $FS_V = 3.0$) (from Kutter et al. 2006).

Numerical sensitivity studies were performed by varying parameters of the BNWF model. Parameters under investigation included bearing-capacity distribution and magnitude, spring stiffness, spring tension capacity, and distribution of springs. With regard to moment-rotation and settlement-rotation relationships, one of the most critical parameters affecting simulations was discovered to be the selection of bearing-pressure distribution and magnitude. Parabolic bearing-pressure distributions resulted in more reasonable comparisons for footings on sands, while inverse parabolic distributions gave more reasonable comparisons for footings on clays. The parabolic sensitivity analysis is shown in Figure 31.

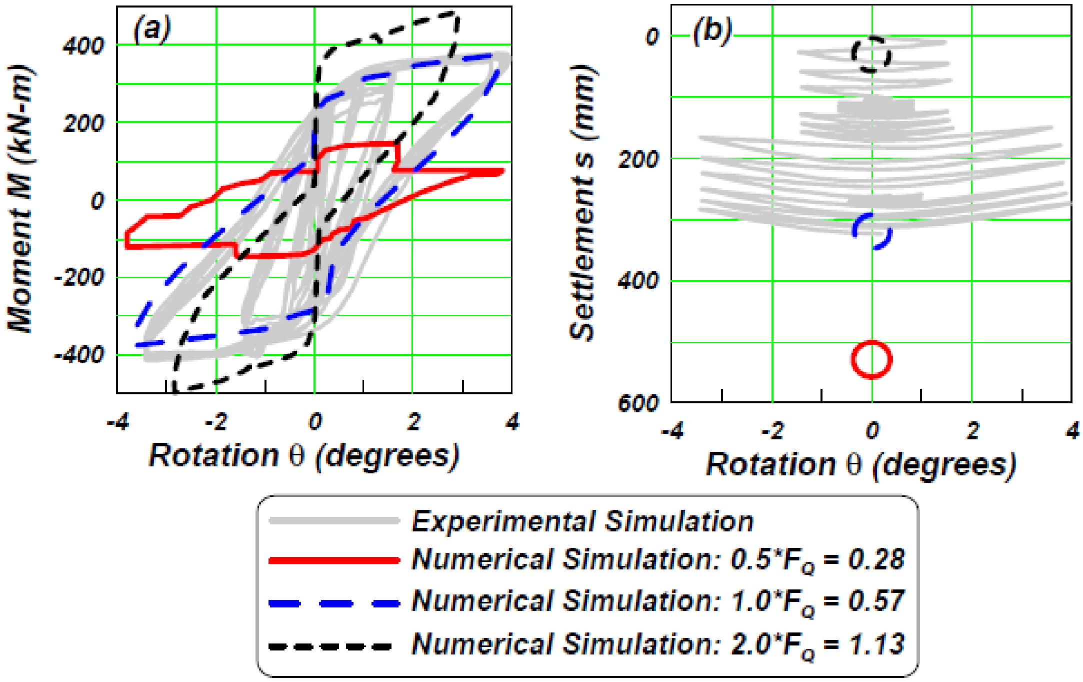

Figure 31. Sensitivity analysis results considering varying bearing-capacity factors F_Q: (a) moment-rotation behavior and (b) settlement-rotation behavior (KRR02-S21 Series data) (from Kutter et al. 2006).

Energy dissipation was evaluated from experimental datasets to quantify the amount of equivalent viscous damping for the foundations rocking on soil. Equivalent viscous damping as defined by Chopra (1995) for a single degree of freedom is the ratio of hysteretic energy dissipated during one cycle of loading to the elastic strain energy associated with that cycle of motion at a peak displacement. The total amount of hysteretic energy dissipation was actually the sum of all force-displacement areas (moment-rotation, lateral force-sliding, vertical force-settlement), but the investigators assumed moment-rotational rocking would dominate the system energy dissipation.

As part of their investigation, Kutter et al. (2006) also reviewed available macro-element modeling procedures for shallow foundations under monotonic, slow-cyclic, and dynamic loading conditions. The macro-element model considered the foundation and the soil as a macro-element for which the constitutive model was based on plasticity theory. The loading was treated using generalized stress variables while the foundation displacements were the corresponding generalized strain variables. The authors presented three macro-element models proposed by previous authors: Nova and Montrasio (1991), Houlsby and Cassidy (2002), and Cremer et al. (2001). Nova and Montrasio (1991) developed a macro-element model that evaluated displacements of rigid shallow foundations on sand under combined action of inclined and eccentric monotonic loading conditions. Houlsby and Cassidy (2002) developed a macro-element model to predict the behavior of rigid circular footings on sand when subjected to monotonic combined vertical, horizontal, and moment loading. Cremer et al. (2001) proposed a nonlinear soil-structure interaction macro-element model for shallow foundations under cyclic loading on cohesive soil. Kutter et al. (2006) reviewed the available macro-element approaches and suggested that an improved model could be derived by combining the features of Cremer et al. (2001) and Houlsby and Cassidy (2002).

Gajan et al. (2008), which included many of the same contributors to Kutter et al. (2006), further developed two numerical models of shallow foundations subjected to seismic loading. The first numerical model was the BNWF model which consisted of vertical springs distributed along the base of the footing to capture rocking, uplift, and settlement, while horizontal springs attached to the sides of the footing captured the resistance to sliding, as shown in Figure 32. The second numerical model was the contact interface model (CIM) which provided nonlinear constitutive relations between cyclic loads and displacements at the footing-soil interface of a shallow rigid foundation subjected to combined moment, shear, and axial loads.

The two-dimensional BNWF model was constructed using a mesh of elastic beam-column elements for footing behavior and zero-length soil elements to model soil-footing behavior. Nonlinear inelastic behavior of the soil was modeled using available material models implemented in OpenSees. These nonlinear inelastic material models included both far-field elastic stiffness and damping as well as local plastic response due to gap formation and closure. The BNWF schematic is shown in Figure 32.

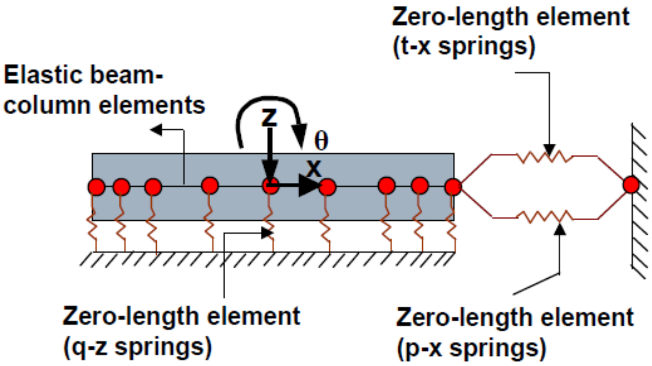

Figure 32. BNWF schematic (from Gajan et al. 2008).

The BNWF model accounted for behavior of the soil-foundation system due to nonlinear, inelastic soil behavior and geometric (uplifting) nonlinearity. Nonlinearity and permanent deformation were exhibited in moment-rotation, shear-sliding, and axial-vertical displacement modes. Thus, hysteretic energy dissipation was captured for these modes at the foundation base. Additionally, the BNWF model had the robustness to account for larger reactions that develop at the ends of stiff footings subjected to vertical loads by allowing stiffer vertical springs and finer spring distribution at the end regions of footings.

The user-defined input parameters of the model included soil type (sand or clay), load capacity (vertical bearing, horizontal passive, and horizontal sliding), vertical and lateral stiffness, radiation damping, tension capacity, distribution and magnitude of vertical stiffness, and spring spacing. Non-user-defined parameters included the elastic range and nonlinear region of the backbone stiffness curve. Limitations of the BNWF model were that vertical and lateral capacities of the foundation were not coupled in this model. Thus, if vertical or moment capacity was increased or decreased, there would be no affect to the shear capacity. Likewise, if there were any change in the lateral capacity or stiffness, the axial and moment capacity would not be affected. Also, the springs along the base of the footing were uncoupled, so the response of one spring would not influence neighboring springs.

The CIM was developed to provide nonlinear constitutive relationships between cyclic loads and displacements of the footing-soil system during combined cyclic vertical, shear, and moment loading. The footing of the CIM was rigid and considered a macro-element when combined with the soil in the zone of influence beneath the footing. The macro-element was modeled by keeping track of the geometry of the soil surface beneath the footing as well as the kinematics of the footing-soil system in order to account for moving contact areas and gaps. The concept of the CIM is shown in Figure 33.

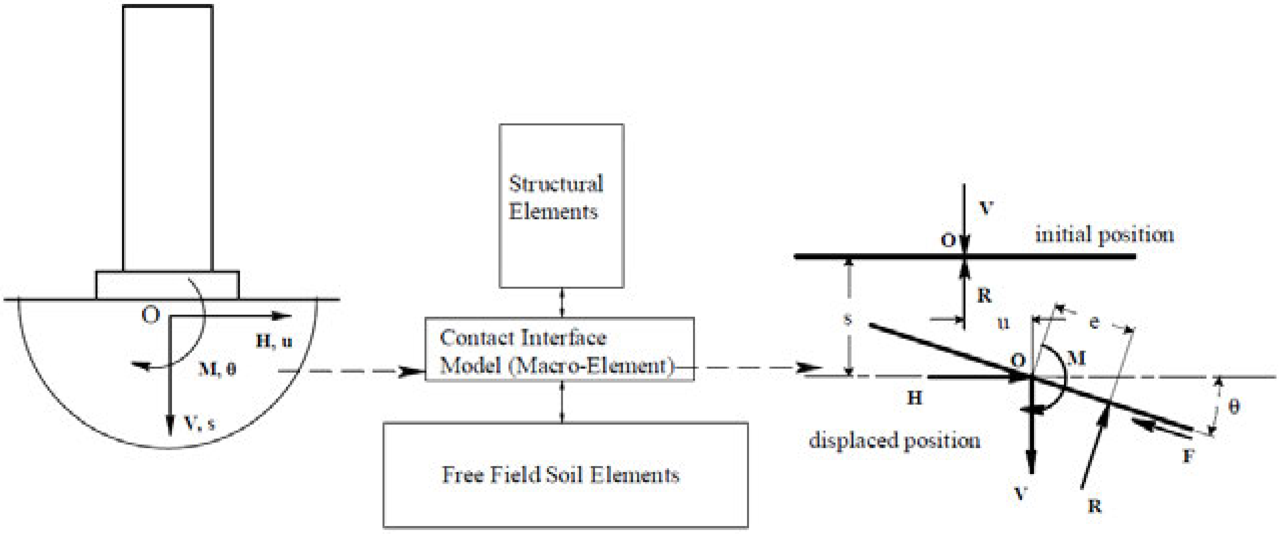

Figure 33. Concept of macro-element contact interface model and forces and displacements at footing-soil interface during combined loading (from Gajan et al. 2008).

When incremental displacements were given to the CIM as input, it returned the corresponding incremental loads and vice versa. As mentioned previously in Kutter et al. (2006), other researchers attempted macro-element approaches to model load-displacement behavior of structural elements and shallow foundations. The previous approaches described the constitutive relations based on yield surfaces, potential surfaces, and tracking the load path history in generalized load space. The CIM differed in the sense that constitutive relations were obtained by tracking the geometry of gaps and the contacts of the soil-footing interface. The loss of contact between the footing and soil and subsequent rounding of the soil surface was observed in Kutter et al. (2006). The CIM was able to capture the gap formation between the footing and underlying soil as well as the effect of the gap on the vertical and lateral foundation capacities. The foundation-soil contact was tracked by a parameter referred to as the critical contact area ratio, which is a ratio of total area of the footing to the area of the footing required to have contact with the soil to support vertical and shear loads. For a shear wall with a constant foundation width loaded in the plane of the wall, the critical contact area could be expressed as a footing length ratio. The critical contact length and rounded soil surface is shown in Figure 34.

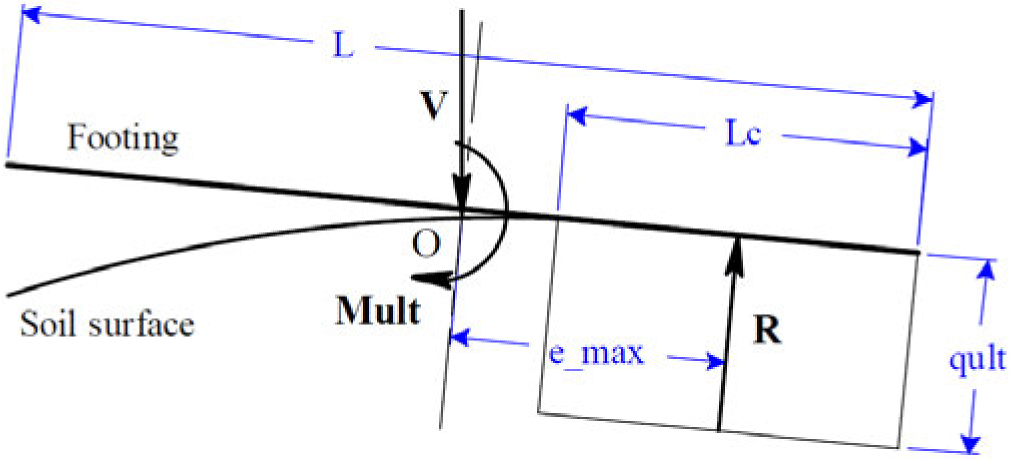

Figure 34. Critical contact length and ultimate moment (from Gajan et al. 2008).

Regarding rounding of the soil surfaces, the CIM also kept track of elastic rebound and bulging of soil as plastic compression in loaded areas occurred adjacent to gap formations. The authors described the position of the soil surface by using soil_min and soil_max parameters. The soil_max surface was the maximum instantaneous local settlement while soil_min represented the partially rebounded soil surface following gap formation, which is shown in Figure 35.

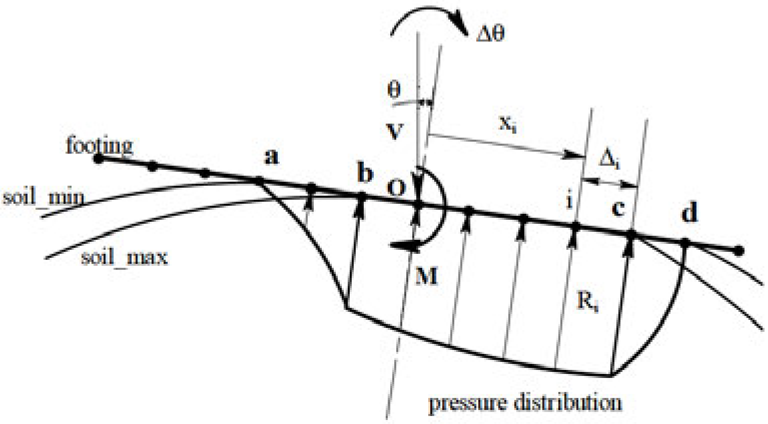

Figure 35. Contact interface model for cyclic moment loading (from Gajan et al. 2008).

The footing in Figure 35 was modeled with a finite number of nodes each of which corresponded to a node at soil_min and soil_max surfaces. The contact area of the footing with the soil, the contact points with soil surfaces, and the bearing pressure distribution along the contact area were updated for every increment of rotation as explained by Gajan and Kutter (2009). The following steps were given by Gajan and Kutter (2009), which detailed the computation procedure behind the CIM:

1) The computation began by an assumed point of rotation (i.e. point b for an incremental clockwise rotation in Figure 35) and proceeded to update the new location of the footing at each node.
2) The soil_max surface was updated according to the new position of the footing. If the footing settled more than the previous soil_max layer at any node, the soil_max layer was updated with the current footing location at that node; otherwise the soil_max layer remained as it was in the previous increment.
3) The user-defined rebounding ratio and footing position were then used to locate the soil_min surface. If a node on the footing was in contact with the soil in the previous increment and lost contact with the soil in the current increment, then the new soil_min surface was updated, otherwise the soil_min location remained as defined in the previous increment. The rebound ratio was related to the factor of safety of the footing against bearing capacity failure. A higher factor of safety footing would have a higher rebound ratio, which decreased the amount of permanent settlement. Based on the rebound ratio, the new end contact nodes of the footing and soil_min profile were updated.
4) The new bearing pressure distribution was calculated at every node in contact with

the soil_max surface.

5) The pressure distribution at nodes in contact with the soil_min layer, but not the soil_max layer, were modeled by a power law with zero pressures at the extreme contact points.

6) The new bearing pressures at all footing nodes in contact with the soil were updated. Nodes not in contact were set to zero pressure, as the soil provided no tension resistance.

7) The distribution of normalized bearing pressure along the contact length was integrated to obtain the total resisting vertical force. This resisting vertical force was checked against the applied vertical force. If vertical force equilibrium was achieved within a certain tolerance, the next step proceeded. If equilibrium was not achieved, a new point of rotation was assumed and steps 1-7 were repeated until equilibrium was found.

8) The moment at the base center point of the footing was calculated by integrating the product of bearing pressure and distance along the contact length of the footing.

9) The incremental vertical displacement (settlement or uplift) due to rotational loading was obtained from the incremental change in the vertical location of the middle node of the footing, which was a natural outcome of keeping track of the geometry of the footing-soil interface.

Unlike the BNWF model, the moment, shear, and vertical load capacities in the CIM were coupled. Gajan et al. (2008) explained that coupling was achieved through a proposed bounding surface for shallow foundations subjected to combined vertical, horizontal, and moment loads. The bounding surface at a constant vertical load is depicted in Figure 36.

The coupling effect of the bounding surface is realized, for example, when the moment capacity was reached after a gap formation, the horizontal capacity of the footing decreased correspondingly.

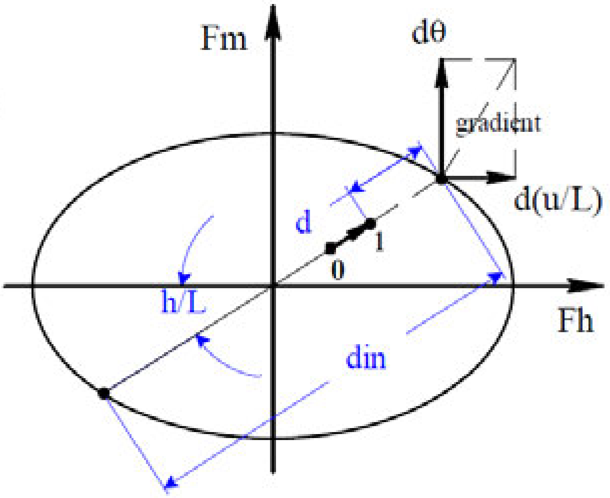

Figure 36. Cross section of bounding surface in normalized *M-H* plane and geometrical parameters used in interface model (from Gajan et al. 2008).

The user-defined input parameters for the CIM were the ultimate vertical load, the length of footing, the initial vertical stiffness, the initial horizontal stiffness, the elastic rotation limit, the rebound ratio, and the internal node spacing.

Gajan et al. (2008) used case studies of structures to directly compare the results from the BNWF model and CIM. Generally, moment and shear capacities agreed between both models. Both models exhibited similar hysteretic energy dissipation through the moment-rotation and horizontal-sliding modes. While rotations from both models were similar, the settlement and sliding estimations from the CIM were greater than the BNWF model. The lack of settlement and sliding agreement was attributed to the lack of moment-shear coupling in the BNWF model.

Gajan et al. (2008) used the two numerical models for comparison against the experimental centrifuge results described in Kutter et al. (2006). An example of comparison with one of the centrifuge tests on clay is given for the BNWF model and CIM in Figure 37 and Figure 38, respectively.

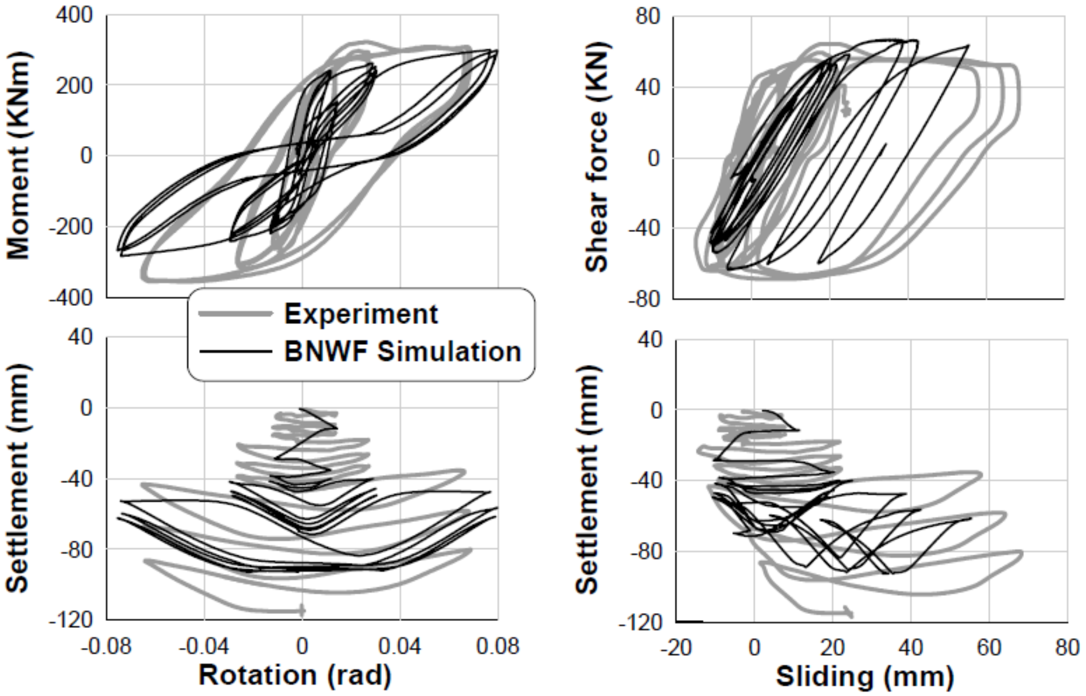

Figure 37. Comparison of load-deformation behavior of shear wall footing for BNWF simulation and KRR03_02 centrifuge test (C_u = 100 KPa, FS_V = 2.8, $M/(H\text{x}L)$ = 1.80) (from Gajan et al. 2008).

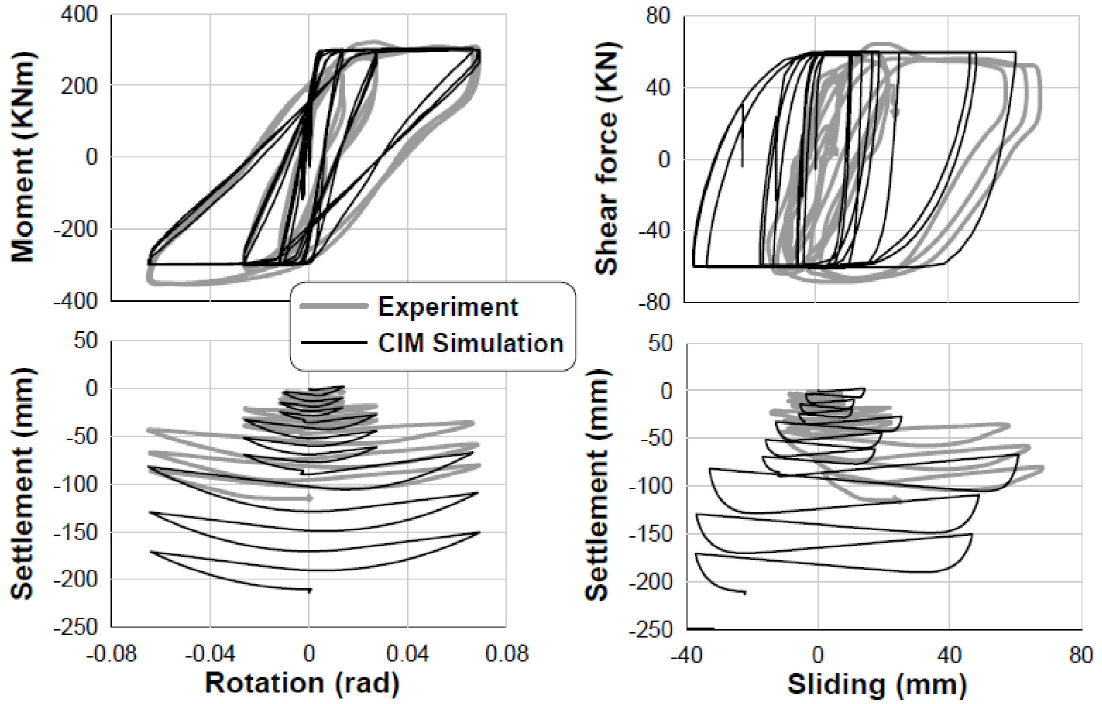

Figure 38. Comparison of load-deformation behavior of shear wall footing for CIM simulation and KRR03_02 centrifuge test (C_u = 100 KPa, FS_V = 2.8, $M/(H \mathrm{x} L)$ = 1.80) (from Gajan et al. 2008).

From the comparison with experimental centrifuge test results, the authors found that the most notable hysteretic features were well captured by both numerical tools. These features included shapes, peaks, and unloading and reloading of the footing response curves. The maximum moment was slightly under-predicted in both models which was attributed to neglecting increased soil capacity from previous loading cycles and the friction and passive pressure on the front and sides of the footing. The maximum sliding and settlement displacement was under-predicted by the BNWF model, while the CIM slightly over-predicted sliding displacement for structures with greater aspect ratios and under-predicted sliding displacement for those with smaller aspect ratios. Finally, the total energy dissipation from the experiments was well predicted by both models.

Gajan and Kutter (2009) further studied the effect of the proposed bounding surface for shallow foundations in sandy soil subjected to combined vertical, horizontal, and moment loads. The main focus of their study was to examine the effect of the moment-to-shear ratio applied at the base of the footing on load capacities, energy dissipation characteristics through rocking and sliding modes, and the cyclic and permanent displacements experienced by the footing. Centrifuge experiments on model shear wall-footing structures were performed and compared with available experimental results from previous studies. Each test was performed at 20g acceleration so that model footings would have prototype dimensions of 2.8m long by 0.65m wide.

Slow lateral cyclic loading was provided by an actuator. Load cells attached to the actuator measured applied lateral load while four linear potentiometers were attached to fixed locations of the centrifuge. The contact points of the linear potentiometers were allowed to slide along the structure during rigid body translation and rotation. These linear potentiometers were used in the calculations for settlement, sliding, and rotation at the base center point of the footing. This important distinction of measuring technique should be noted as it differed from the approach taken in Chapter 4 of this work.

Results from Gajan and Kutter (2009) showed that footings subjected to large moment-to-shear ratios tend to rotate more than they slide. Thus, 3 to 30 times more energy was dissipated by foundation rocking than by sliding for footings with factors of safety against bearing capacity between 2 and 15. Figure 39 illustrates this difference in mode energy dissipation for different moment-to-shear ratios.

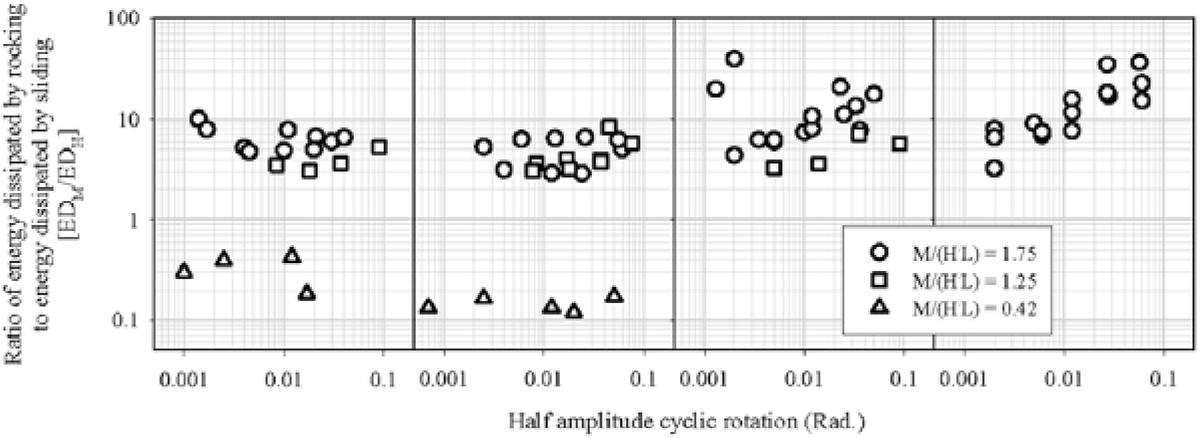

(a) $FS_V = 2 \sim 3$ (b) $FS_V = 3 \sim 5$ (c) $FS_V = 5 \sim 8$ (d) $FS_V = 10 \sim 15$

Figure 39. Effect of FS_V and M/(HL) on ratio of energy dissipated by rocking mode to energy dissipated by sliding mode (from Gajan and Kutter 2009).

Lower moment-to-shear loading ratio produced more sliding than rocking and dissipated more energy through the sliding mode than rocking. Generally, the moment-to-shear loading ratio greater than unity caused more energy dissipation and permanent settlement from rocking motion than sliding with the same normalized amplitude of rotation. It was also discovered that the ultimate moment and resulting permanent settlement of the foundation could be correlated to the critical contact area ratio, introduced by Gajan et al. (2008), regardless of the factor of safety against bearing capacity and moment-to-shear ratio. For example, a footing with a large critical contact area ratio dissipated more seismic energy due to rocking than sliding and resulted in less permanent settlement per cycle of rocking than that caused by the same normalized magnitude of sliding.

CHAPTER 3

FOOTING EXPERIMENTS FOR SMALL-STRAIN VIBRATION

3.1 Motivation for Study

Several geotechnical centrifuge studies have been pursued with the goal of characterizing the vertical, coupled lateral-rocking and multi-modal dynamic response of surface, embedded, and pile foundations subjected to small-amplitude vibrations (e.g., Pak and Guzina, 1995; Pak and Ashlock, 2000; Pak, Ashlock, and Abedzadeh, 2008; Ashlock and Pak, 2009; Pak, Ashlock, Kurahashi, and Soudkhah, 2010). These efforts were accompanied by analytical and computational investigations to develop improved three-dimensional homogeneous and inhomogeneous continuum models to more accurately capture the observed behavior. Results from an extensive program of dynamic centrifuge experiments including the vertical-centric (VC), horizontal-centric (HC), and vertical-eccentric (VE) test types were presented for surface foundations in Pak et al. (2010).

In the VC test, a dynamic force is applied vertically through the center of the foundation to elicit a symmetrical vertical response. In the HC test, a horizontal force is applied in the central plane of the foundation, which is equivalent to a horizontal force and moment at the centroid. The HC loading therefore results in coupled horizontal-rocking motions, and will not provoke the vertical response if the foundation is relatively symmetric. In the VE test, a vertical load is applied in the same vertical plane as the VC test, but at a horizontally eccentric location. VE forcing is equivalent to a vertical force and rocking moment at the foundation centroid, which activates the vertical and coupled horizontal-rocking modes of the foundation simultaneously to produce a more revealing multi-dimensional response.

Many of the aforementioned studies have demonstrated that the shear modulus required for the homogeneous half-space model to match a measured lateral-rocking response is typically 20-40% lower than that required for the vertical response of the same soil-foundation system (e.g. Pak and Ashlock, 2000; Pak, Ashlock, Kurahashi, and Soudkhah, 2010). This phenomenon has been confirmed for uniform dry sands under a range of footing sizes and contact pressures, both for the hybrid-mode VE tests as well as the combination of the traditionally separate VC and HC tests. As a practical remedy to the problem, the concept of Impedance Modification Factors (IMF) was introduced in Pak and Ashlock (2000).

In the IMF approach, frequency-independent factors, α_{ij} are applied to the components of the lateral-rocking impedance matrix to give the modified impedance matrix

$$\boldsymbol{K}(\omega)=\begin{bmatrix} K_{vv}(\omega) & 0 & 0 \\ 0 & \alpha_{hh}K_{hh}(\omega) & \alpha_{hm}K_{hm}(\omega) \\ 0 & \alpha_{mh}K_{mh}(\omega) & \alpha_{mm}K_{mm}(\omega) \end{bmatrix}. \tag{3.0}$$

For square surface foundations, Ashlock (2000) has shown that the coupling IMF α_{mh} can be taken as unity for simplicity. Despite their frequency-independence, the IMFs α_{hh} and α_{mm} can be calibrated for a homogeneous half-space to provide an improved match and prediction of experimental observations. Although it may be proposed that a reduced modulus be used for the lateral-rocking impedance matrix, such an alternative would not offer sufficient freedom to match the two response peaks commonly observed in experiments, whereas the IMF approach can readily handle the problem with its two independent degrees of freedom. Provided that experimental issues such as friction are handled sufficiently, calibration typically results in horizontal and rocking IMFs which are less than unity. This indicates an overestimation of the associated impedances by various elastic half-space models as a result of the simplifying assumptions made and the non-physical properties of the solutions (e.g. idealized soil property profiles, isotropy, singular stresses).

The goals of this investigation are to develop experimental techniques to study field-scale surface foundation vibration problems for the excitation types described above, to verify observed behavior from previous centrifuge studies which indicated a need for corrections by the IMF approach, and to perform the first field-scale calibration of IMFs for in-situ conditions of a natural soil deposit.

3.2 Foundation

In this study of field-scale dynamic tests of surface footings on a natural deposit of cohesive soil, a foundation with base dimensions of 55 x 55 cm and a height of 45 cm was constructed of concrete with two layers of steel wire mesh reinforcement. These dimensions were chosen such that one of the foundations used in centrifuge tests of Pak, Ashlock, Kurahashi, and Soudkhah (2010) would be a 1:10 scale model of the new foundation used in this study. Because the centrifuge models are constructed of aluminum, their prototype-scale inertial properties and contact pressure are greater than those of the concrete foundation. However, the large foundation offers an opportunity to examine many of the findings from the centrifuge studies under actual in-situ site conditions. The physical properties of the foundation are given in Table 1. Formwork was built out of oriented strand board with 2x4 sawn lumber frames (Figure 40a). The oriented strand board was coated with oil, and caulking compound was applied to the corners to aid in the removal of the formwork. An electric concrete mixer, Quikrete Concrete Mix, and water were used to procure the batch of concrete necessary to build the footing (Figure 40b). As concrete was poured, a vibratory wand was used to consolidate the concrete (Figure 40c). The foundation was left to cure (Figure 40d) and eventually transported to a prepared test site.

(a) (b)

(c) (d)

Figure 40. Construction of the test foundation. (a) formwork, (b) concrete mixer, (c) vibratory wand, (d) concrete curing.

Table 1. Physical properties of concrete foundation.

Width (m)	0.550	HC excitation height (m)	0.110
Height (m)	0.450	VE excitation eccentricity (m)	0.245
Mass (kg)	327.1	Vertical accel. eccentricity (m)	±0.18
Polar moment of inertia (kg m^2)	13.76	Upper horiz. accel. height (m)	0.200
Centroid height (m)	0.225	Lower horiz. accel. height (m)	0.020

3.3 Soil

3.3.1 Site Preparation

A natural soil deposit outside Spangler Geotechnical Laboratory at Iowa State University was selected and an area of approximately 6 x 6 m was leveled. A skid-steer loader was utilized to prepare the site area. The constructed foundation was transported from Town Engineering Building to Spangler and located in the center of the leveled area (Figure 41).

Figure 41. Spangler test site used for small-strain footing vibration experiments.

3.3.2 Physical Properties

During grading of the site, disturbed samples from the top 6” to 12” were obtained for classification and consistency tests. The soil near the surface is classified as a silty, clayey sand with group symbol SC-SM, since the physical properties were found to have 43% fines, $LL = 28$, $PI = 6$, $C_u > 200$, and $C_z = 2.21$. Tests were performed at the site in the months of May, August, September, and December of 2010. An experimental borehole was drilled adjacent to the graded site in August of 2010. The borehole was subsequently used as a groundwater monitoring station after installing a pvc well point backfilled with pea-gravel, with a bentonite cap. Depths to groundwater varied from 2.5 m in August to 3.2 m in December.

3.4 Excitation System

To provide dynamic forcing, a Labworks, Inc. ET-139 Electrodynamic Shaker was suspended from a surveying tripod using rubber straps. As depicted in Figure 42, the shaker was mounted in three orientations to achieve inertial mass shaker configurations for the VC, HC and VE tests described above. The elasticity of the rubber straps along with a slight offset of the tripod towards the foundation results in a horizontal prestress force, allowing the shaker to act as an inertial mass for dynamic excitation in the HC configuration. The excitation signal to the shaker was provided by an LDS Dactron Photon II signal analyzer in conjunction with a Labworks, Inc. PA-141 power amplifier and a portable generator.

(a) **(b)** **(c)**

Figure 42. Experimental setups for surface footing vibration tests. (a) VC test, (b) HC test, (c) VE test.

3.5 Measurement System

Epoxy adhesive was used to attach ceramic mounting pads to the concrete footing. The force sensor and accelerometers were attached at locations (see Table 1) which were selected through a parametric study of the theoretical accelerance functions for a range of force and response points. The experimental testing program included series of VC, HC, and VE tests as described above, using random and swept sine excitation. For each test, the applied force and acceleration at two to three points on the foundation surface were measured in the time-domain. To measure the force applied to the foundation, a PCB model 208 C05 force sensor with a 22.24 kN (5000 lb) range in compression was used. The force sensor is shown in Figure 43a.

Three types of accelerometers were used in the footing vibration tests. Initially, three PCB model 356 B08 triaxial high sensitivity accelerometers were used (Figure 43b) to record accelerations on the foundation surface. These accelerometers have a measurement range of ±490 m/s^2 pk (±50g pk) and a resonant frequency greater than 20 kHz. Eventually, a set of PCB model 353 B03 single axis general purpose accelerometers (Figure 43c) were purchased. These accelerometers have a measurement range of ±4905 m/s^2 pk (±500g pk) and a resonant frequency greater than 38 kHz. One program of tests was performed with these accelerometers, but it was determined that their resolution was too low. This set of accelerometers was replaced with PCB model 353 B33 single axis accelerometers (Figure 43d). These accelerometers proved to be more desirable because they had a resolution equal to that of the triaxial accelerometers. These accelerometers have a measurement range of ±491 m/s^2 pk (±50g pk) and a resonant frequency greater than 22 kHz.

(a) (b) (c) (d)

Figure 43. Measuring instruments used in surface footing vibration tests. (a) PCB model 208 C05 force sensor, (b) PCB model 356 B08 triaxial accelerometer, (c) PCB model 353 B03 single axis accelerometer, (d) PCB model 353 B33 single axis accelerometer.

3.6 Measurement Approach

The approach taken to acquire data from the instrumentation used throughout the experimentation phase of this study involved sampling and digitization of time domain signals. Once digitized, the time domain signal was then converted to the frequency domain via the Fast Fourier transform (FFT). As is common in analyses of frequency domain signals, the processed signals of greatest importance are the frequency response functions (FRF), the coherence functions (COH), and the auto/power-spectral density functions (ASD). For this study, the FRF is the ratio of directional acceleration at given points on the foundation surface to the dynamic load applied at a point of stimulus. In previous studies (e.g. Pak and Guzina, 1995), this FRF is referred to as accelerance. Consistent with previous studies, the accelerance functions of surface footings are composed of a combination of a vertical or horizontal force and a vertical or horizontal acceleration.

3.6.1 Data Digitization

As previously noted, data was measured by accelerometers and force sensors. These instruments are designed to produce a voltage proportional to the amount of imposed force or acceleration, respectively. A continuous measurement, such as voltage, is known as an analog signal. In order for an analog signal to be processed by a computer, it must first be digitized. A digitized signal is a close representation of the analog one. The analog data signals must first be sampled at a selected time interval Δt to be converted to the digitized representation. The sampling rate s is the inverse of the time interval and expressed in units of samples per second (Hz).

Aliasing is a common problem in the processing of time domain signals. Aliasing is dependent upon the Nyquist or Folding frequency f_c, which is a function of the sampling rate.

$$f_c = \frac{1}{2\Delta t} \tag{3.1}$$

Aliasing occurs when frequencies above f_c in the original data appear below f_c after application of the FFT. Anti-aliasing filters are typically used to combat this erroneous effect. These are analog low pass filters that remove frequency data above f_c before it converted to digital format. It would be typical for anti-aliasing filters to conservatively remove data above 70-80% of f_c in order to produce alias-free frequency lines.

The plug-and-play Dactron dynamic signal analyzer used in this study was programmed to use anti-aliasing filters with the cutoff frequency (f_{cutoff}) set to the selected bandwidth (B) of measurement. Substituting the sampling rate into Equation (3.1), the Nyquist frequency can be expressed as

$$f_c = \frac{s}{2}. \tag{3.2}$$

The desired measurement bandwidth B can then be related to the required sampling rate s as

$$B = f_{cutoff} = 0.78 f_c = \frac{0.78s}{2} \rightarrow s = 2.56B. \tag{3.3}$$

This simple relationship allows the Dactron analyzer to use a sampling rate that is a scaled multiplier of 2.56 times the chosen bandwidth of measurement to reduce the aliasing error. A bandwidth of 500 Hz and record length of N = 4,096 samples per window were used in this study, yielding a sampling rate of 1,280 Hz, sampling duration of T = 3.2 s per window with a sampling interval of Δt = 781.25 µs and a frequency resolution of Δf = 0.3125 Hz.

3.6.2 Fourier Transforms

The ability to analyze time domain signals in the frequency domain is based on the discovery that it is possible to resolve any periodic function into an equivalent infinite summation of sine and cosine waves. The frequencies of these sinusoidal components start at zero and increase in integer multiples of the function's base frequency, which results in an infinite series known as the Fourier series. For problems in this study in which the behavior is not necessarily periodic, the Fourier transform may be used to obtain a continuous spectral representation $X(f)$ of transient data $x(t)$

$$X(f) = \int_{-\infty}^{\infty} x(t) e^{-i2\pi ft} dt \tag{3.4}$$

where $i = \sqrt{-1}$. The inverse of this transform is given by

$$x(t) = \int_{-\infty}^{\infty} X(f) e^{i2\pi ft} df\ . \tag{3.5}$$

For a real valued function *x(t)*, *X(f)* is complex.

In order to evaluate a function sampled over a discrete time interval (0,*T*) at *N* equally spaced points which are a distance *Δt* apart, the discrete Fourier transform (DFT) must be used. The data sampling times are simply

$$t_n = n\Delta t, \qquad\qquad n = 0,1,2,...,N-1\ . \tag{3.6}$$

Typically, the discrete frequency values f_k are chosen such that

$$f_k = \frac{k}{T} = \frac{k}{N\Delta t}, \qquad\qquad k = 0,1,2,...,N-1 \tag{3.7}$$

Note that $k = N/2$ corresponds to the Nyquist frequency. Denoting $x(t_n)$ by x_n, the discrete forms of Equations (3.4) and (3.5) may be written as

$$X(f_k) = \Delta t \sum_{n=0}^{N-1} x_n e^{-i2\pi kn/N}, \qquad k = 0,1,2,...,N-1 \tag{3.8}$$

and by denoting $X_k = X(f_k)$

$$x(t_n) = \frac{1}{N\Delta t} \sum_{k=0}^{N-1} X_k e^{i2\pi kn/N}, \qquad n = 0,1,2,...,N-1\ , \tag{3.9}$$

where *Δf* has been replaced with $1/N\Delta t$ in Equation (3.9).

The discrete Fourier transform (DFT) from Equation (3.8) is applied through the FFT algorithm, which is most efficient when N is a power of two. The Dactron's user interface featured a menu to choose N by powers of two. To obtain the maximum possible resolution, N=4096 was chosen for all experiments in this study.

Spectral leakage occurs as a result of the limitation of sampling at a number of discrete times and frequencies, and is also related to discontinuities at the ends of the measurement records (Bendat and Piersol, 1986). Signal energy should be concentrated only at one frequency but the discontinuities contribute to the spreading of signal energy into all other frequencies. One common approach to evaluating a DFT over only a portion of the actual data signal $x(t)$ is to view $X(f_k)$ in Equation (3.8) as the Fourier transform of an unlimited time history record $v(t)$ multiplied by a rectangular time window $u(t)$, where

$$u(t) = \begin{cases} 1 & 0 \le t \le T \\ 0 & \text{otherwise} \end{cases} \tag{3.10}$$

so that

$$x(t) = u(t)v(t) \tag{3.11}$$

The Fourier transform of the actual data signal $x(t)$ becomes a convolution of the Fourier transforms of the time window $u(t)$ and the unlimited time history record $v(t)$. Hence,

$$X(f) = \int_{-\infty}^{\infty} U(\alpha)V(f-\alpha)d\alpha \tag{3.12}$$

while the Fourier transform of the rectangular time window is

$$U(f) = T\left(\frac{\sin(\pi fT)}{\pi fT}\right)e^{-i\pi fT} \quad . \tag{3.13}$$

The magnitude of Equation (3.13) can be seen in Figure 44. Spectral leakage of power at the large side lobes of |*U(f)*| may exist at frequencies away from the main lobe of the spectral window. Since this leakage of power could cause significant distortions of *X(f)*, *T* is chosen to be an integer multiple of T_p, the period of data *v(t)*. The Fourier components will not leak into the main lobe when *T* is an integer multiple of T_p because *U(f)* is zero at $f = kf_P = (k / T_P),\ k = 1, 2, \ldots$.

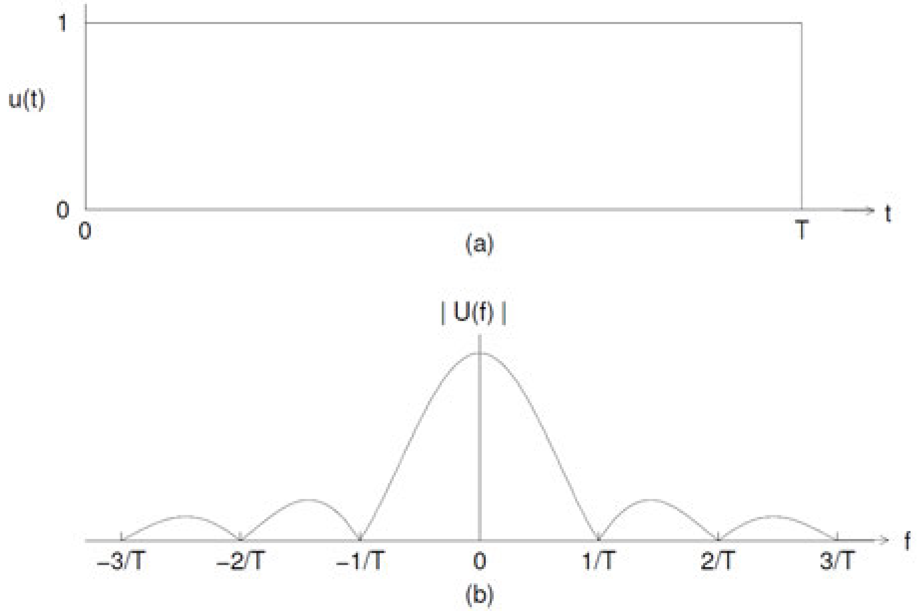

Figure 44. Rectangular window. (a) Time Window. (b) Spectral Window (from Ashlock, 2000).

Many windows have been developed to alleviate the leakage problem. One of the most commonly used windows is the Hanning window, which was used in this study. This window is defined by

$$u(t) = \begin{cases} 1 - \cos^2\left(\dfrac{\pi t}{T}\right) & 0 \le t \le T \\ 0 & \text{otherwise} \end{cases} \tag{3.14}$$

and is shown with the magnitude of its Fourier transform (see Bendat and Piersol, 1986) in Figure 45. Though side lobe leakage is reduced, use of a Hanning window also reduces the magnitude of the Fourier transform by a factor of $\sqrt{3/8}$. To correct for the magnitude adjustment from the Hanning window, the right hand sides of Equations (3.8) and (3.9) must be multiplied by $\sqrt{8/3}$ and $\sqrt{3/8}$, respectively.

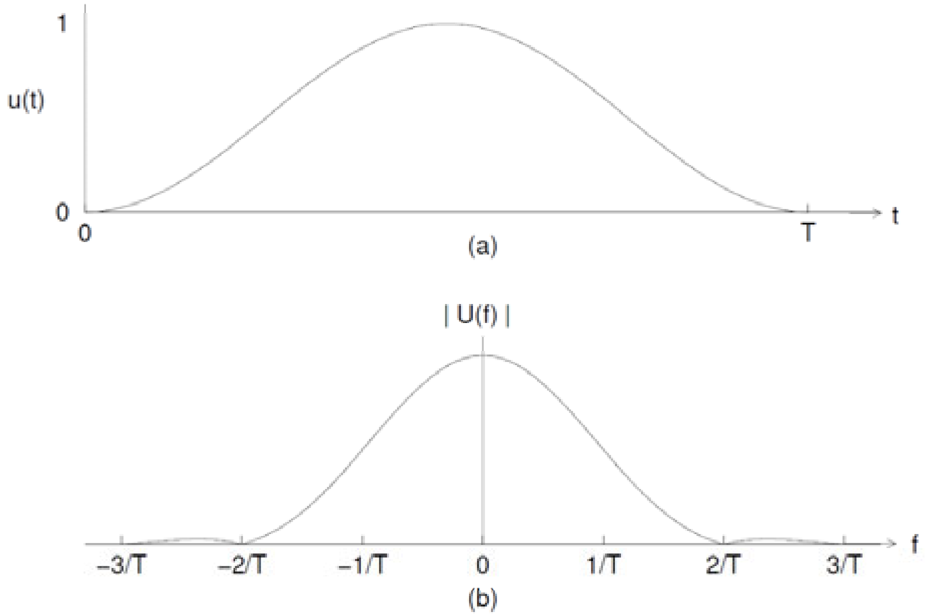

Figure 45. Hanning window. (a) Time Window. (b) Spectral Window (from Ashlock, 2000).

3.6.3 Frequency Response Function

The frequency response function is a complex valued transfer function that expresses the output of a linear, time invariant system to an applied input as a function of frequency. As mentioned previously, the focus of this investigation was the accelerance frequency response function, which is the ratio of acceleration to force. The dynamic characteristics of a constant parameter linear system with a single input and output may be described by a unit impulse response function *h(τ)*. The unit impulse response function *h(τ)* is the output of the system at any time due to a unit impulse applied at time $\tau = 0$. For an arbitrary input *x(t)*, the output *y(t)* is given by the convolution integral

$$y(t) = \int_{-\infty}^{\infty} h(\tau)x(t-\tau)d\tau \quad . \tag{3.15}$$

The frequency response function *H(f)* is found by taking the Fourier transform of the unit impulse response function:

$$H(f) = \int_{-\infty}^{\infty} h(\tau)e^{-i2\pi f\tau}d\tau \quad . \tag{3.16}$$

Taking the Fourier transform of both sides of the convolution integral given in Equation (3.15) yields

$$Y(f) = H(f)X(f) \quad . \tag{3.17}$$

Equation (3.17) is a linear algebraic expression in the frequency domain that relates the Fourier transforms of the input and output functions in terms of the frequency response function.

For a system with zero measurement noise, the frequency response function of a physical system may be solved in terms of the DFT of the input *x(t)* and output *y(t)* as

$$H(f_k) = \frac{Y(f_k)}{X(f_k)}, \quad k = 0,1,2,\ldots,N-1 \tag{3.18}$$

A statistical definition of Equation (3.18) to minimize the effect of inherent measurement noise in a least-square sense may be written as

$$H(f_k) = \frac{G_{xy}(f_k)}{G_{xx}(f_k)} \tag{3.19}$$

in which G_{xx} is the one-sided auto-spectral density function:

$$G_{xx}(f_k) = \frac{2}{N\Delta t} X^*(f_k) X(f_k), \quad k = 0,1,2,\ldots,N-1 \tag{3.20}$$

and G_{xy} is the one-sided cross-spectral density function:

$$G_{xy}(f_k) = \frac{2}{N\Delta t} X^*(f_k) Y(f_k), \quad k = 0,1,2,\ldots,N-1 \tag{3.21}$$

where $X^*(f_k)$ is the complex conjugate of $X(f_k)$(see Bendat and Piersol, 1986).

Averaging a set of auto-spectral and cross-spectral records from the input and output signals is also a way to minimize random experimental error on the measured FRF:

$$\overline{G}_{xx}(f_k) = \frac{2}{n_d N \Delta t} \sum_{i=1}^{n_d} X_i^*(f_k) X_i(f_k), \quad k = 0,1,2,\ldots,N-1 \tag{3.22}$$

$$\overline{G}_{xy}(f_k) = \frac{2}{n_d N \Delta t} \sum_{i=1}^{n_d} X_i^*(f_k) Y_i(f_k), \quad k = 0,1,2,\ldots,N-1 \tag{3.23}$$

where n_d is the number of averages. The small-strain vibration experiments described herein made use of the analyzer to measure 30 transfer function averages for each test. Substituting Equations (3.22) and (3.23) into Equation (3.19) gives the spectrally averaged transfer function as

$$H(f_k) = \frac{\overline{G}_{xy}(f_k)}{\overline{G}_{xx}(f_k)}. \tag{3.24}$$

The input *f(t)* for the small strain vibration experiments was the load cell signal, and the outputs $\ddot{x}_n(t)$ were the accelerometer signals at *n* points on the footing. The resulting system can be thought of as *n* separate single-input/single-output systems. The accelerance functions are

$$A_i(f_k) = \frac{\overline{G}_{f\ddot{x}_i}(f_k)}{\overline{G}_{ff}(f_k)}, \quad i = 1,2,\ldots,n \tag{3.25}$$

where *n* is the number of acceleration signals considered during a test.

The coherence function is a measure of the measurement quality. It is used to characterize the amount of noise and system linearity from the recorded data, and can be defined as

$$\gamma_{xy}^{2}(f_k) = \frac{\left|\overline{G}_{xy}(f_k)\right|^2}{\overline{G}_{xx}(f_k)\overline{G}_{yy}(f_k)} . \qquad (3.26)$$

A perfectly linear single-input/single-output system with constant properties and zero extraneous noise will produce a coherence of unity for all frequencies. Coherence will never be greater than unity. Coherence less than unity may indicate a change in the properties of a linear system, a non-linear system, or noise in the data signals.

Accelerance and coherence plots for tests of various forcing signals, loading configurations, and seasonal conditions are presented and analyzed later in this chapter.

3.6.4 Calculation of Theoretical Accelerance Functions

The formulation for theoretical accelerance functions of a rigid foundation on the surface of an elastic half-space in conjunction with various Boundary Element Formulations of impedance functions, both presented in Ashlock (2000), was used as a basis for comparing analytical and computational dynamic soil-structure interaction models with experimental results.

3.7 Experimental Discussion and Results

To gain an idea of the relevance and limitations of current methods of practice for the physical problem, experimental results were plotted together with theoretical accelerance functions calculated by consideration of the equations of motion and impedance functions for a rigid foundation on a homogeneous and a square root half-space. The impedance functions are complex valued force-displacement ratios in the frequency-domain, in which the real part represents the dynamic stiffness and the imaginary part reflects the out-of-phase component due to radiation and material damping (see, e.g. Gazetas, 1991). In this study, impedances were obtained from the rigorous 3D boundary element code BEASSI. This boundary element formulation featured a library of multilayered viscoelastic fundamental solutions for generalized soil profiles (see Pak and Guzina, 1999).

An inspection of various measurements indicates that the smoothest transfer functions with the best coherence are obtained when the armature of the electromagnetic shaker is allowed to impact the force sensor rather than remain in full contact. Impact loading also promotes better engagement of the shaker's inertia, which provides more energy at low frequencies. The excitation signals examined in this study therefore include random (pink noise) forcing with impacts, and a swept sine forcing which also contains a degree of randomness due to the impacts of the inertial mass shaker. One drawback of the inertial mass shaker configuration is the difficulty in consistently making flush impacts with the force sensor, since the coherence is sensitive to the quality of alignment between the exciter armature and force sensor. The use of 30 transfer function averages served to help limit the effects of loading misalignment. Figure 46 and Figure 47 illustrate typical measurements of vertical force and acceleration from VC tests with random and swept-sine excitation, respectively. A sharp reduction in coherence at approximately 64 Hz and 128 Hz is exhibited in Figure 46(d) and Figure 47(d). This phenomenon is likely due to harmonics of approximately 60 Hz AC electrical noise originating from the portable generator. Comparing Figure 46 and Figure 47, one can see that the swept-sine excitation helps secure a slightly improved coherence in the low frequency region due to the momentary concentration of the excitation energy at a given frequency during the sweep. However, a spurious peak in the accelerance is also observed near 25 Hz for swept-sine forcing (Figure 47).

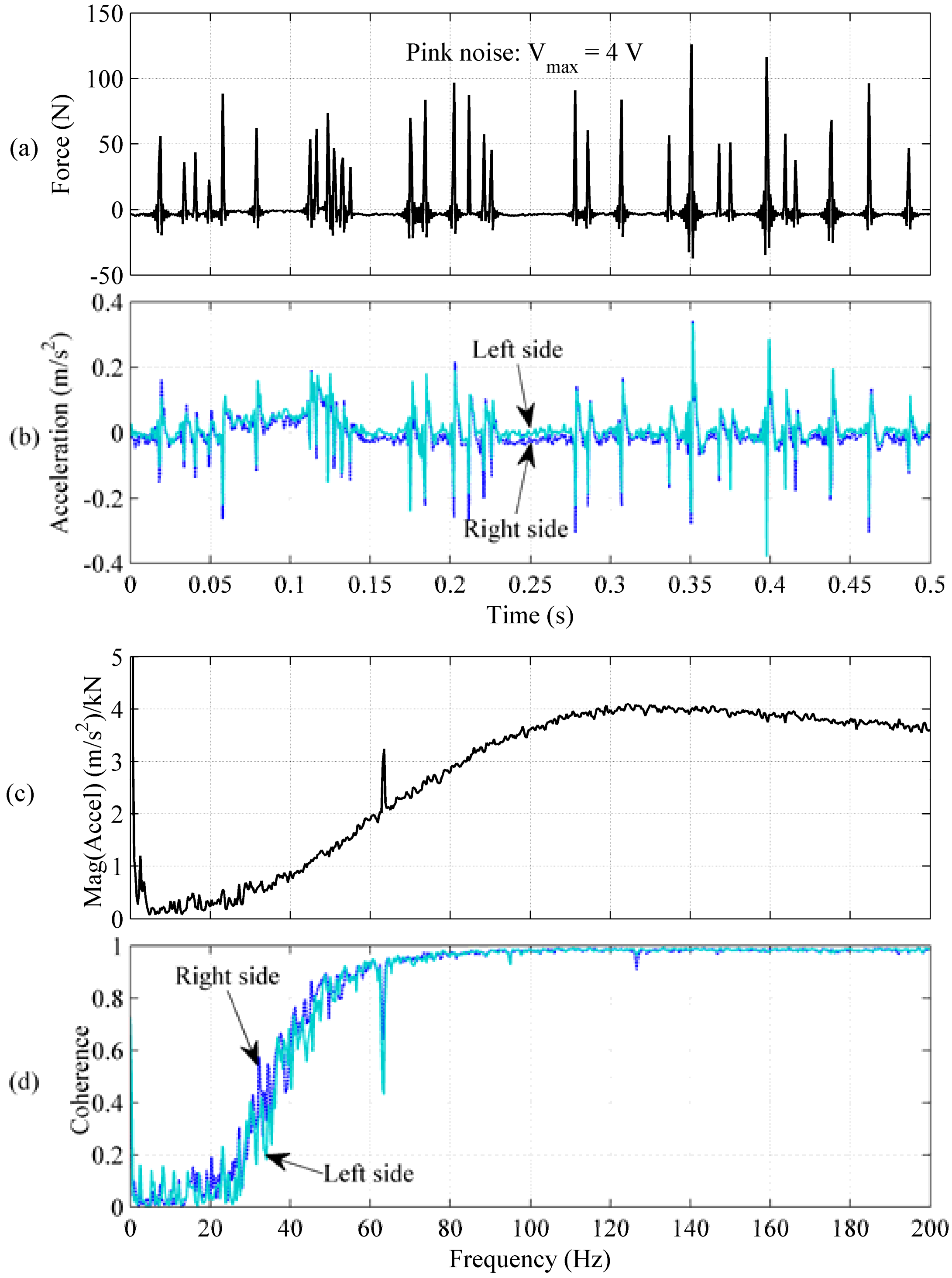

Figure 46. Typical vertical response from VC test using random excitation with impacts. (a) force, (b) acceleration (left and right sides), (c) averaged transfer function (d) coherence (left and right sides).

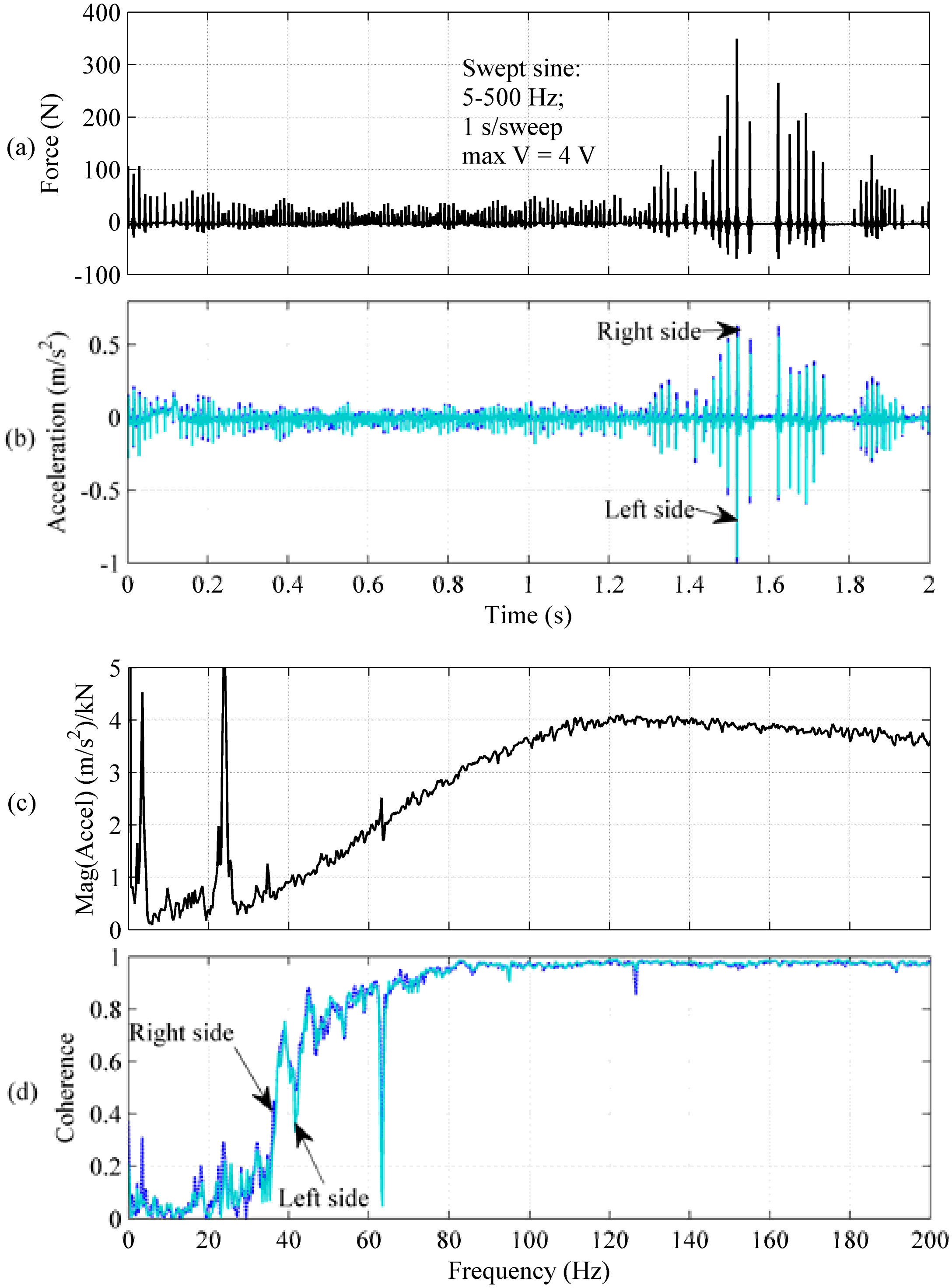

Figure 47. Typical vertical response from VC test using swept sine excitation with impacts. (a) force, (b) acceleration (left and right sides), (c) averaged transfer function (d) coherence (left and right sides).

For both vertical and coupled lateral-rocking modes of vibration, complex-valued theoretical accelerances were fit to experimental ones in a least-squares sense for a range of half-space shear moduli. That is to say the least-squares difference between measured and theoretical responses of the real and imaginary parts was computed over a frequency range of interest. In the following, modal vibration response and excitation types for each test will use the notation “AA/BB" where AA and BB denote the response and excitation types, respectively (VC, VE, or HC). Figure 48 illustrates the sensitivity of the theoretical VC/VC accelerance to variations of the equivalent homogeneous half-space shear modulus $G_{eq.hom.}$ and the assumed soil density ρ of 1922.2 kg/m^3 (120 lb/ft^3). Part (a) of this figure also illustrates the results of the matching procedure, in which the best-fit equivalent homogeneous shear modulus is seen to be 64 MPa for the given test.

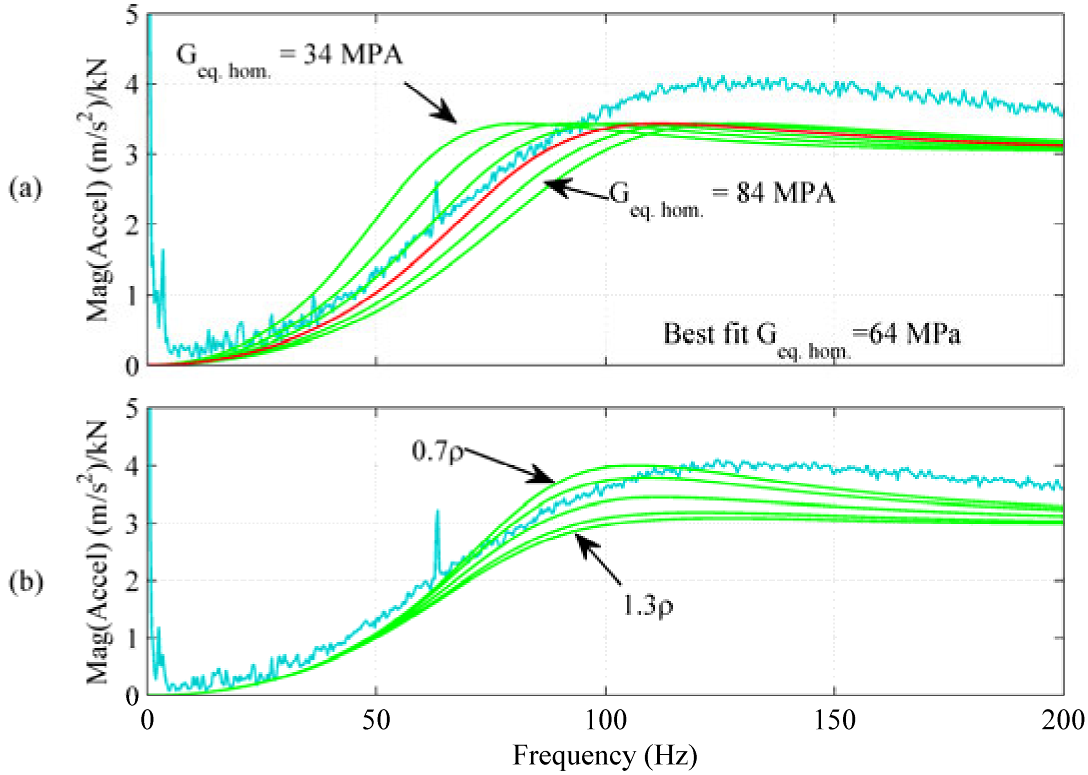

Figure 48. Sensitivity of VC/VC accelerance to homogeneous half-space parameters (a) shear modulus $G_{eq.hom.}$ = 34, 44, 54, 64, 74 and 84 MPa and (b) soil density 0.7, 0.8, 1.0, 1.2 and 1.3 times assumed value of ρ = 1922.2 kg/m^3.

Figure 49 illustrates the sensitivity of the theoretical VC/VC accelerance where the shear modulus of the half-space *G(z)* is defined in terms of a constant shear modulus $G_{eq.sqrt.}$, the soil depth *z*, and the footing half-width *b*

$$G(z) = G_{eq.sqrt}\sqrt{\frac{z}{b}}\ . \tag{3.26}$$

Part (a) of this figure illustrates the sensitivity of the theoretical VC/VC accelerance to the constant shear modulus $G_{eq.sqrt.}$ and part (b) shows the sensitivity of the assumed soil density ρ of 1922.2 kg/m^3 (120 lb/ft^3). Part (a) also gives results of the matching procedure, in which the best-fit equivalent square root shear modulus is seen to be 121 MPa for the given test.

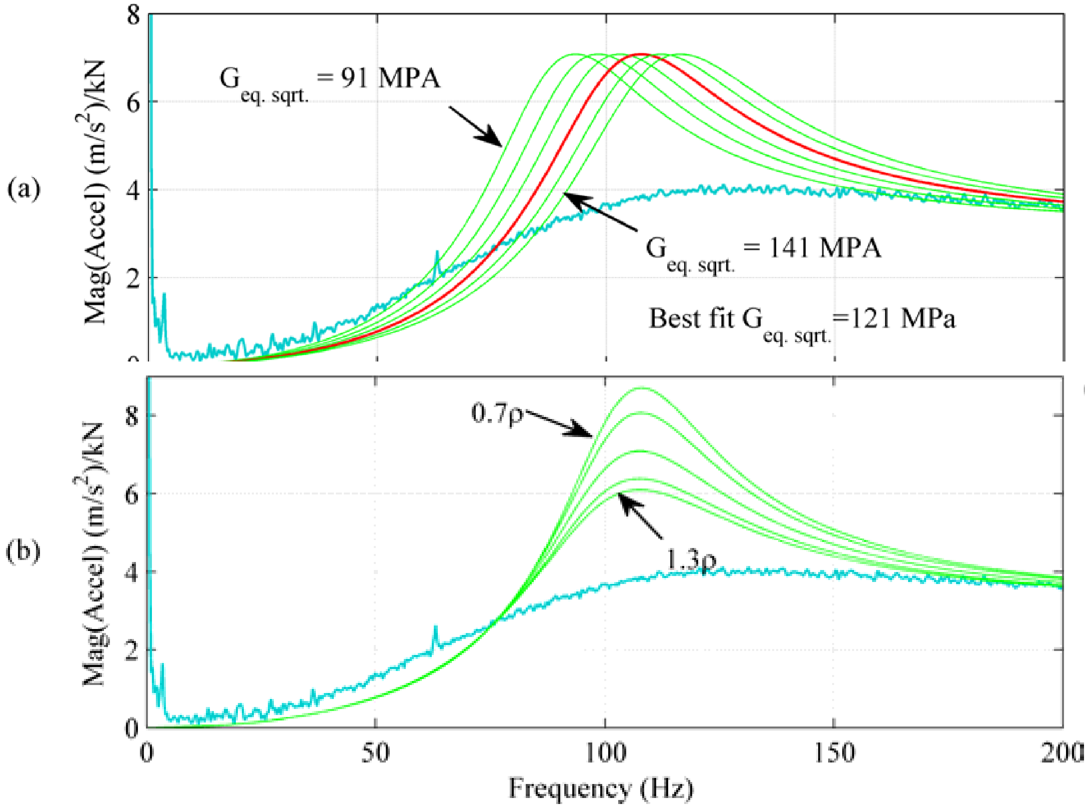

Figure 49. Sensitivity of VC/VC accelerance to square root half-space parameters (a) shear modulus $G_{eq.sqrt.}$ = 91, 101, 111, 121, 131 and 141 MPa and (b) soil density 0.7, 0.8, 1.0, 1.2 and 1.3 times assumed value of ρ = 1922.2 kg/m^3.

In the aforementioned centrifuge studies of dry, uniform, cohesionless soil, excellent agreement of measured and theoretical transfer functions was obtained without requiring consideration of material damping in the half-space. In this investigation, however, it was determined through inspection of the theoretical response that a value of 5% hysteretic damping was required to model the dynamic response of the system, likely due to the presence of fines and the elevated moisture conditions due to precipitation. Hysteretic damping was implemented by specifying a complex-valued shear modulus $G_{eq.hom} \cdot (1 + 2\xi i)$, in accordance with the elastic-viscoelastic correspondence principle (Christensen, 1971).

Figure 50 contains experimental responses for the vertical mode of vibration from a symmetric mode VC test and a hybrid-mode VE test. As shown in the figure, the best-fit equivalent homogeneous shear modulus was determined to be 64 MPa for both test types, illustrating that the multi-mode VE test can be used in place of the conventional VC test to characterize the vertical response. For a similar evaluation of the lateral-rocking mode, experimental HC responses obtained from an HC and a VE test are compared in Figure 51. Although the real and imaginary parts of the HC/HC and HC/VE accelerances are clearly not equal due to the differences in force and acceleration in the two tests, fitting the homogeneous half-space solution to these responses results in the same value of the best-fit modulus, $G_{eq.hom.}$ = 45 MPa.

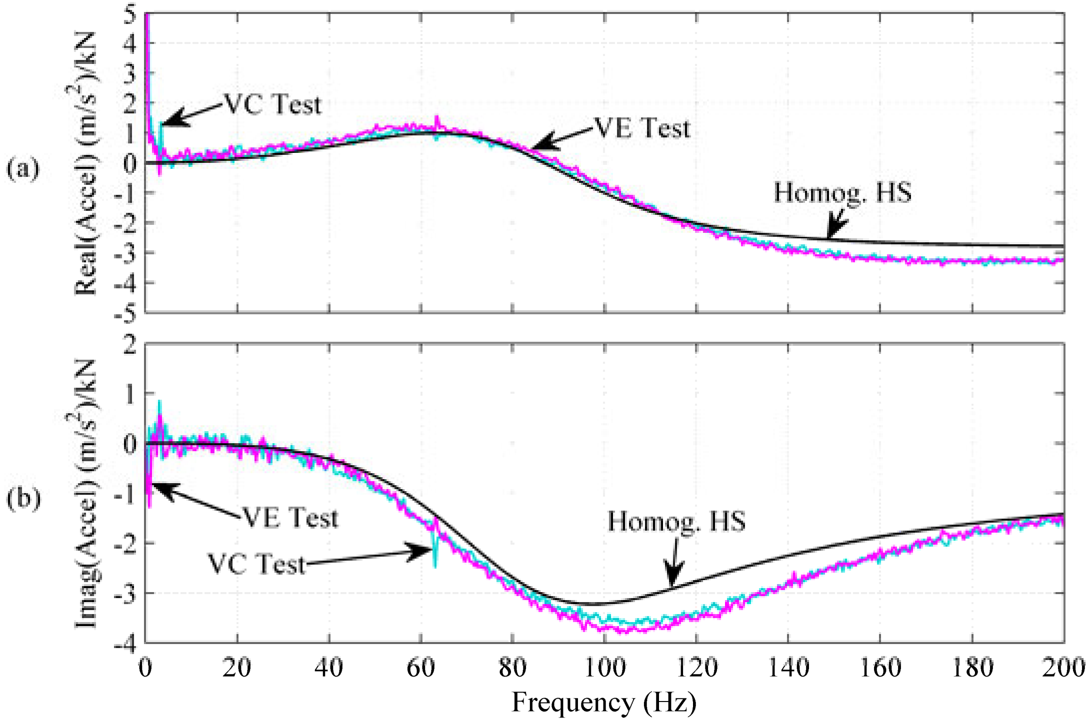

Figure 50. Best-fit homogenous half-space accelerance for vertical mode of vibration from VC and VE tests for (a) real and (b) imaginary parts. Equivalent homogeneous shear modulus = 64 MPa.

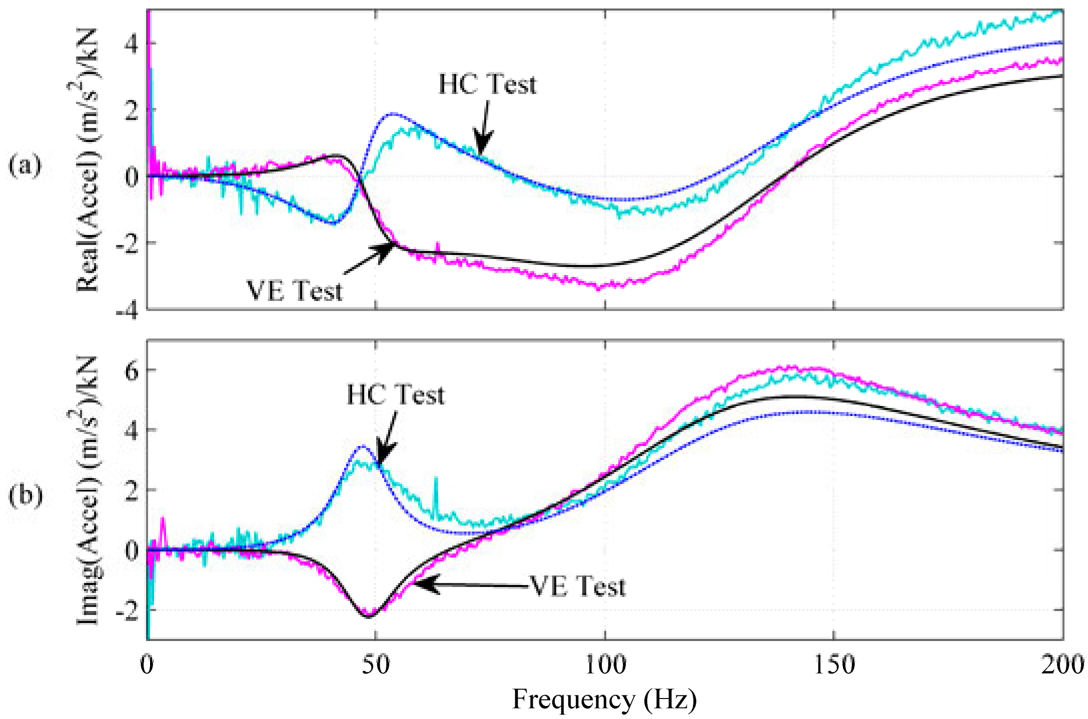

Figure 51. Best-fit homogenous half-space accelerance for lateral-rocking mode of vibration from HC and VE tests; (a) real and (b) imaginary parts. Equivalent homogeneous shear modulus = 45 MPa.

Together with the vertical mode, this demonstrates the equivalence of a single VE test to a combination of VC and HC tests. The efficacy of the dynamic VE test is an attractive alternative to the conventional VC and HC tests for surface foundations due to its ability to simultaneously engage the modes of vibration under consideration in realistic general planar motion. Along with the benefit of increased efficiency, the VE test also minimizes concerns over differences in contact conditions and load-history effects that are encountered in sequential VC and HC tests. The latter point is especially important in the case of large excitations or nonlinear responses, for which the results of VC and HC tests cannot be superimposed. As illustrated in Figure 50 and Figure 51, a reduction in shear modulus of about 30% from the vertical to the coupled lateral-rocking response is required for a suitable agreement when using the homogeneous half-space model. This result is consistent with previous centrifuge studies of scaled-model foundations as well as other model-scale and full-scale studies as discussed in Ashlock and Pak (2009).

As a consequence of the behavior typified by Figure 50 and Figure 51, the homogeneous half-space model will fail to capture the lateral-rocking behavior if one uses an equivalent homogeneous shear modulus determined from a VC test. This is illustrated directly in Figure 52, where the HC response using the vertical mode modulus of 64 MPa is shown. Likewise, if the shear modulus is determined from an HC test, the VC peak frequency will be under-predicted. As an engineering solution to the problem, the use of IMFs (see Equation 3.0) is also shown in Figure 52 to improve the predicted response of the measured accelerance for both real and imaginary parts. For the soil type and conditions tested, the experimentally calibrated IMFs are $\alpha_{hh} = 0.64$ and $\alpha_{mm} = 0.82$, which are similar to those reported for centrifuge tests of uniform, dry cohesionless soil (e.g. Ashlock, 2000; Pak and Ashlock, 2000).

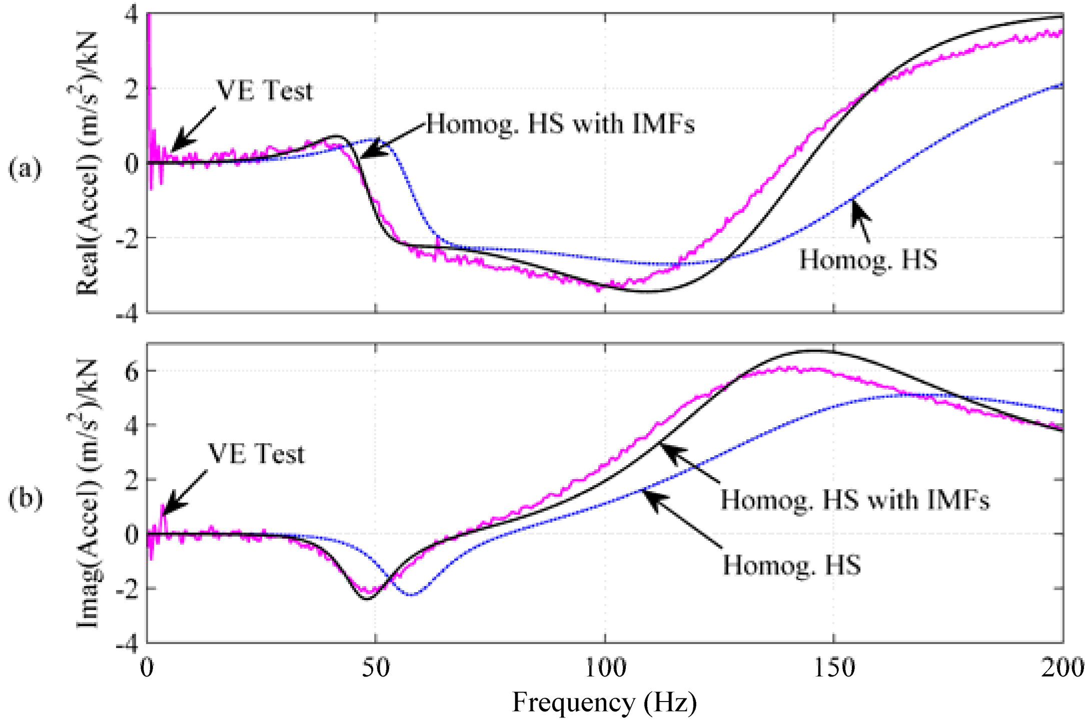

Figure 52. Best-fit homogenous half-space accelerance with IMFs for lateral-rocking mode of vibration from VE test for (a) real and (b) imaginary parts. $\alpha_{hh} = 0.64$, $\alpha_{mm} = 0.82$ using equivalent homogeneous shear modulus = 64 MPa.

Another aspect of the study was to observe the dependence of the dynamic response on temperature and moisture conditions by periodically measuring the accelerance functions through changing seasons. To this end, experimental tests were performed in May, August, September, and December. Local ambient temperatures were recorded at each test time and varied from 85°F in August to 29°F in December as shown in Figure 53.

Figure 53. Mean daily temperatures (°F) from May 14, 2010 to December 3, 2010.

Vertical responses from VC tests are presented in Figure 54 through Figure 58. A summary of these responses are shown in Figure 59, from which a envelope of responses is created.

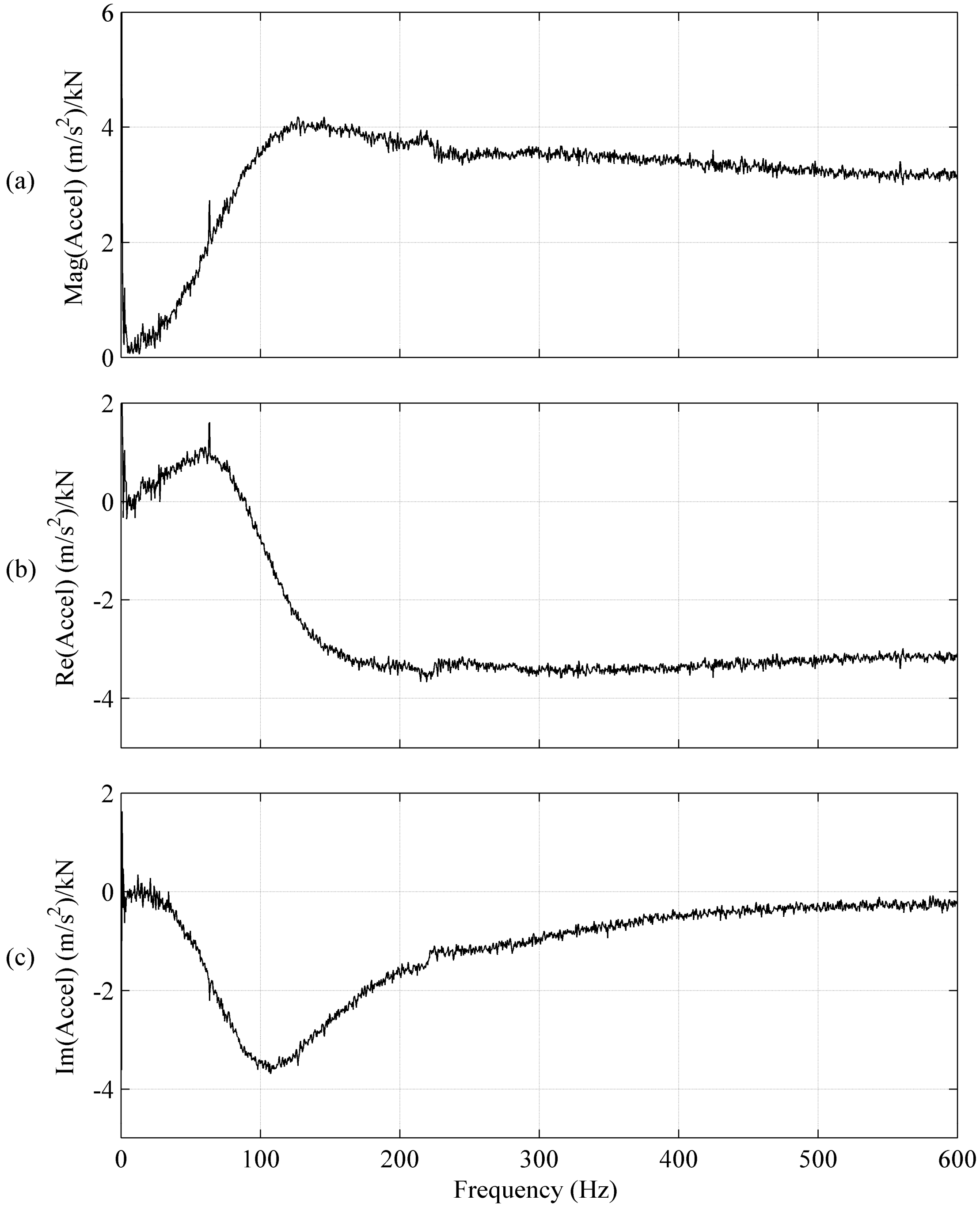

Figure 54. VC response (vertical) from May 14, 2010.

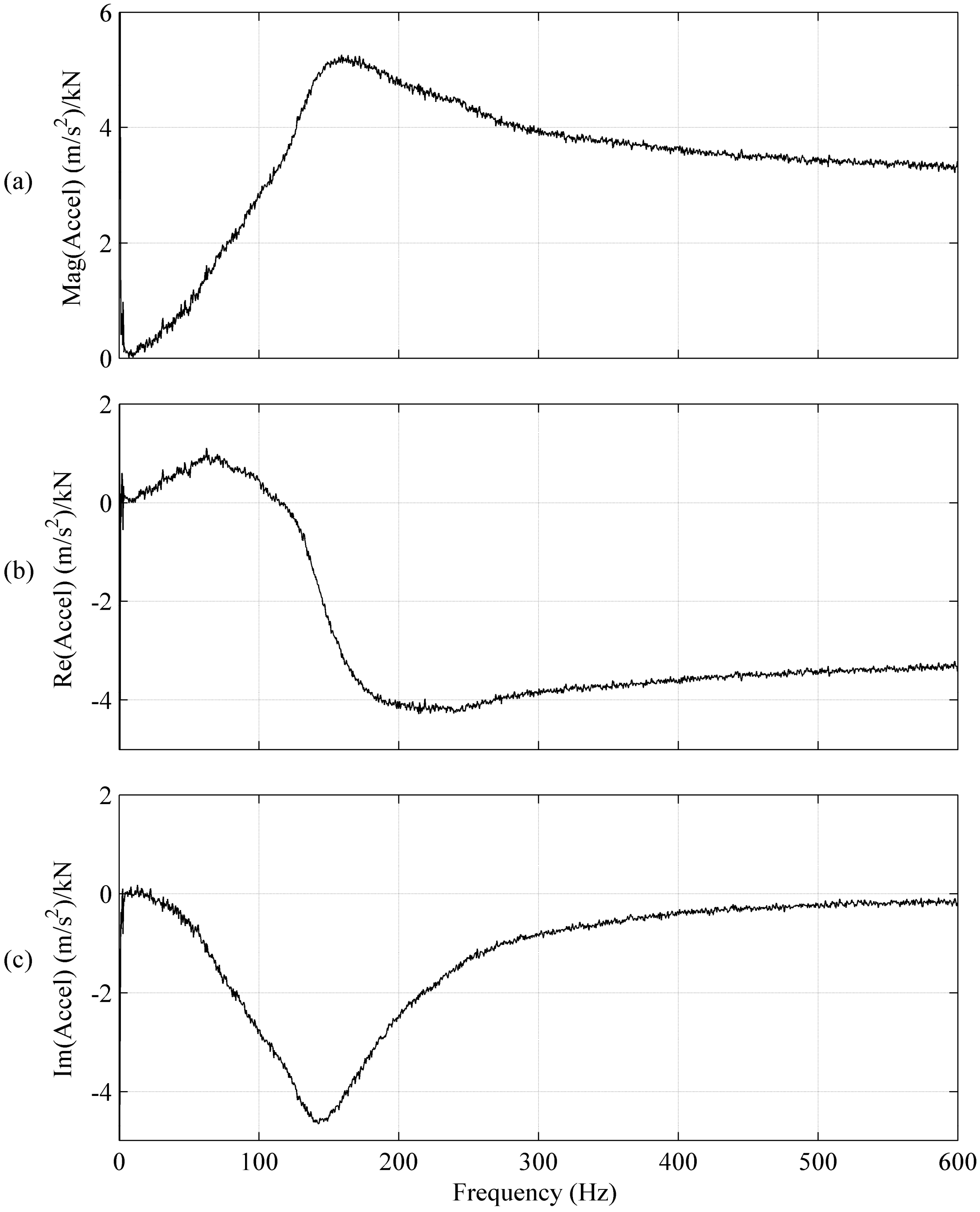

Figure 55. VC response (vertical) from August 27, 2010.

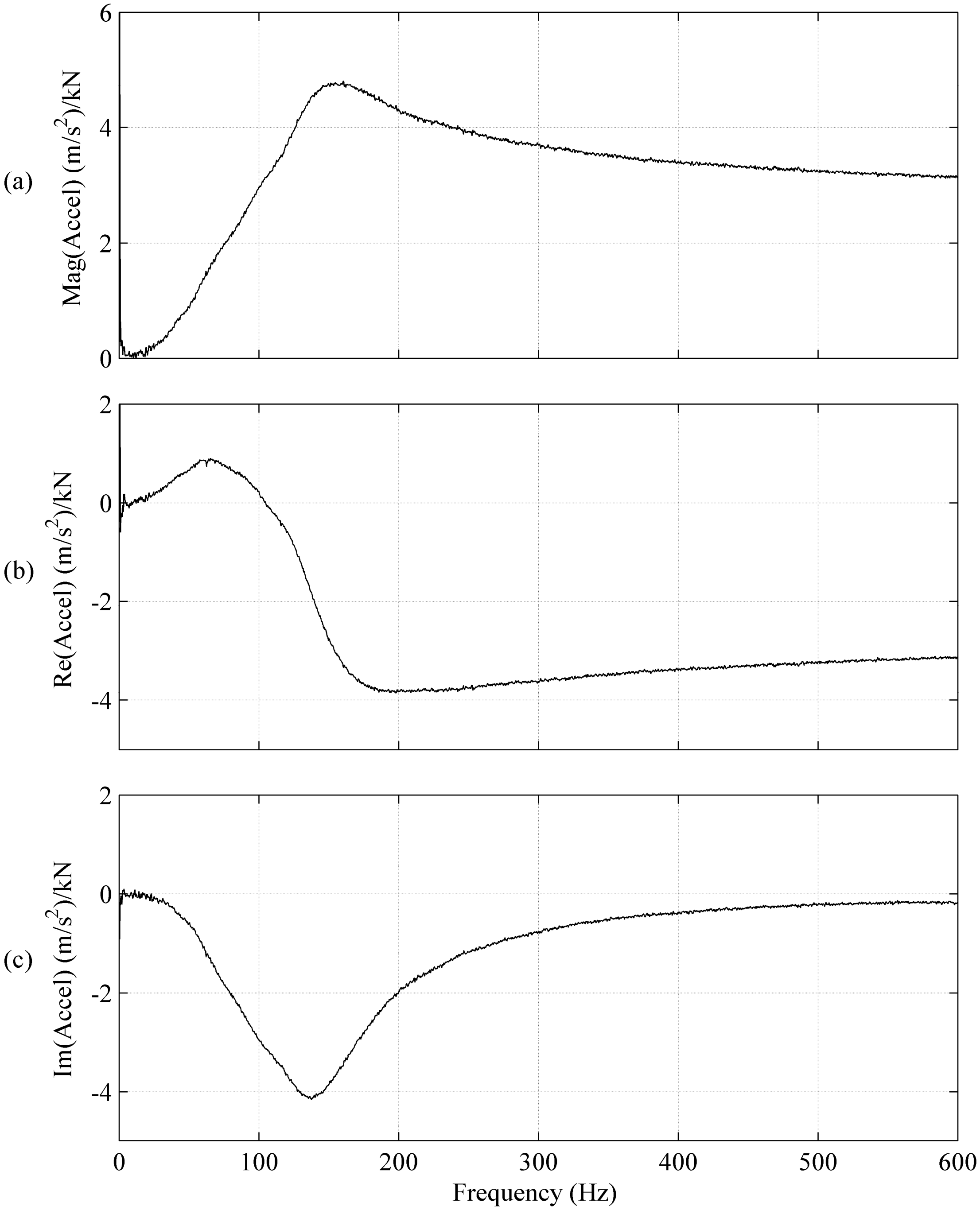

Figure 56. VC response (vertical) from September 17, 2010.

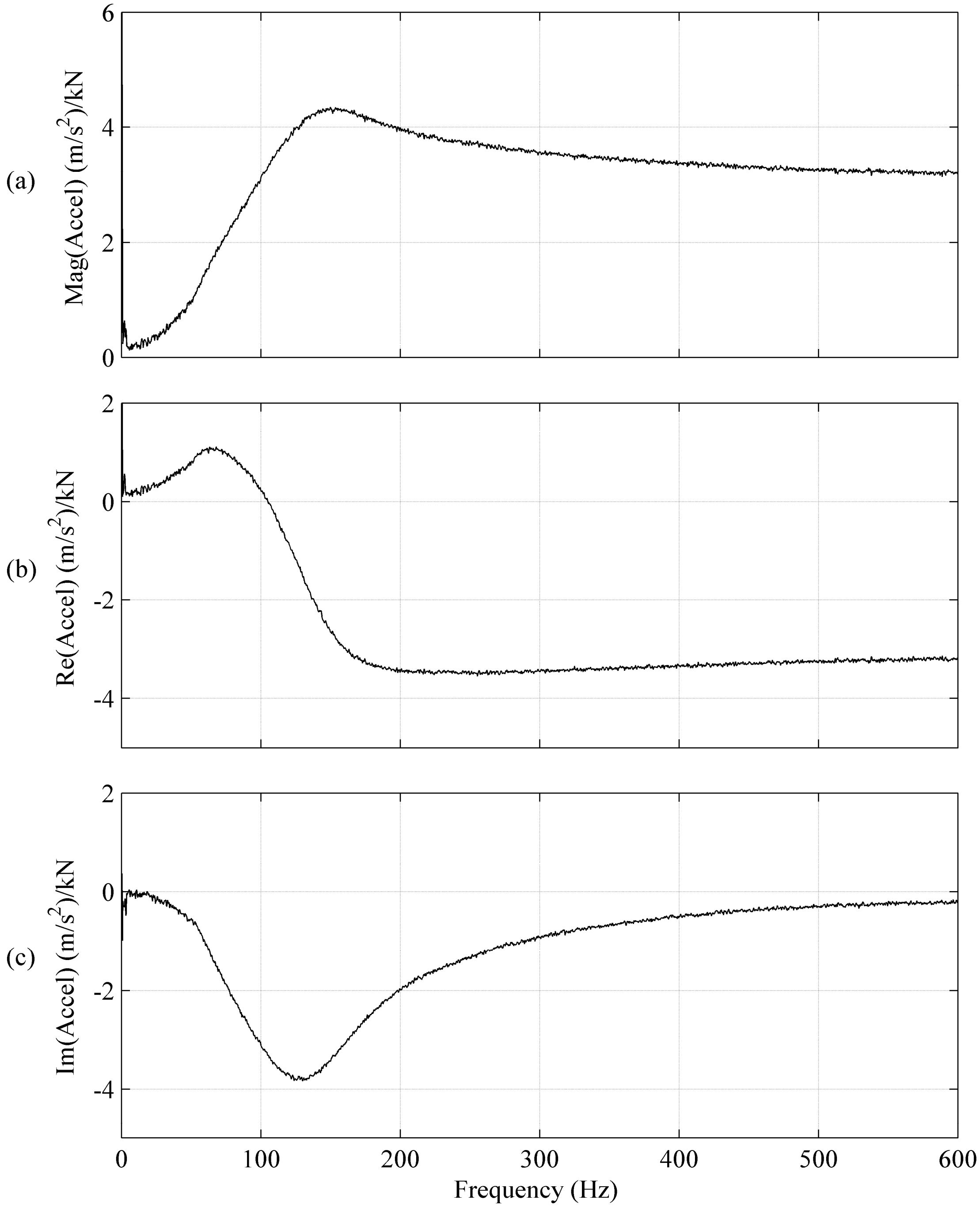

Figure 57. VC response (vertical) from September 24, 2010.

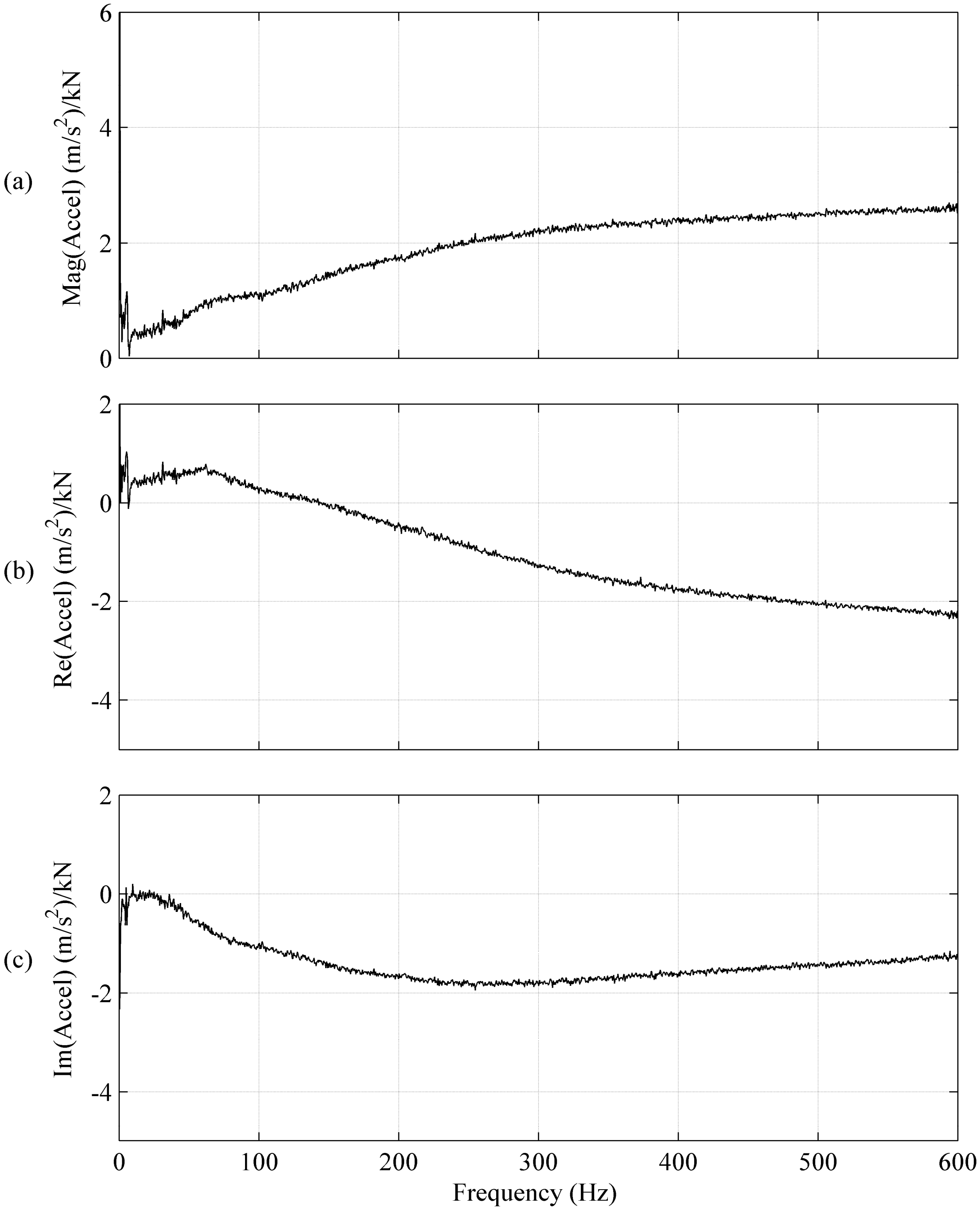

Figure 58. VC response (vertical) from December 3, 2010.

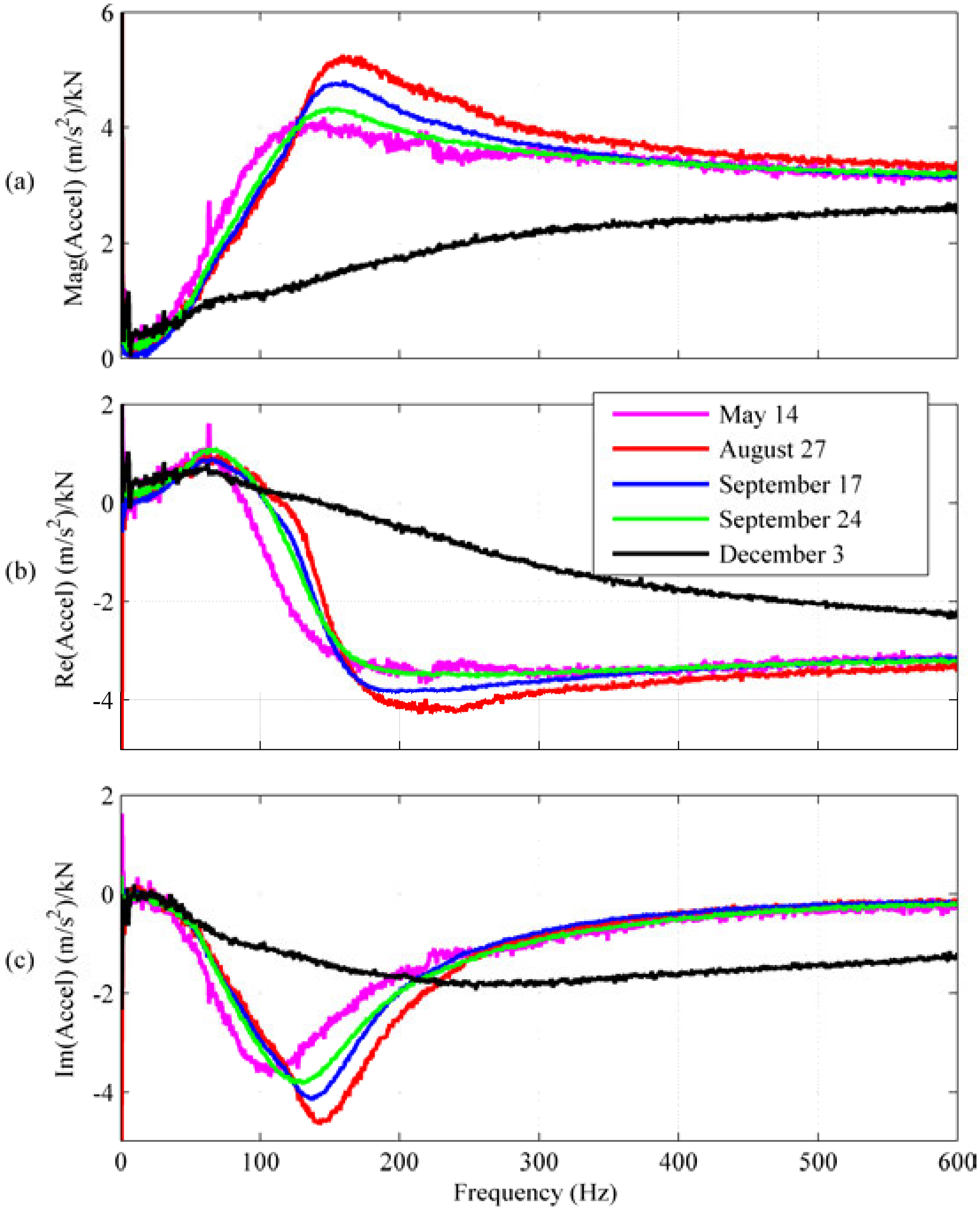

Figure 59. Summary of vertical VC responses.

Figure 59a shows that the peak magnitude of accelerance increased by 25% from May 14 to August 27, 2010. The characteristic trough in the imaginary response (Figure 59c) shows that the peak frequency increased 50% in the same duration, revealing that impedances can change drastically with seasonal temperature and moisture conditions. Even the tests of September 17 and September 24, 2010, which are only one week apart, have quite different responses in peak amplitude and frequency. The peak amplitude was reduced by about 10% as shown in Figure 59a and the peak frequency was reduced by about 5% as shown in Figure 59c. The test from December 3, 2010 exhibited a dramatically different response from the previous tests. This is presumably due to much different soil-footing contact conditions even though the footing was never moved from its original location of installation. A change in contact conditions could be attributed to a sufficiently frozen soil, time consolidation effects, disturbance from previous excitation experiments, or a combination of all of these.

One of the most important findings from this study was that a hybrid VE test was shown to be equivalent to VC and HC tests. This is significant because researchers interested in multi-modal response of vibrating surface footings need only perform one test rather than two separate tests. The convenience of the hybrid VE test equivalence is even more important when the researcher is concerned with experiments on virgin soil deposits. The hybrid VE test allows the researcher to engage both the vertical and lateral-rocking modes of vibration within a single test. This conclusion has been presented for scale model centrifuge tests, but the research in this work has verified its validity for field-scale tests on a natural soil deposit. Another important finding was that the homogeneous and square root half-space models were confirmed to capture individual modal dynamic responses of a square surface footing, but the half-space models were not able to accurately capture multi-modal response of a square surface footing. It was shown that a shear modulus fit to the vertical mode of vibration overestimated the lateral-rocking response. The multi-modal limitations of these models led to the first known field-scale validation of the IMF approach to relate shear moduli between vertical and lateral modes of vibration.

CHAPTER 4

LARGE STRAIN ROCKING FOOTING EXPERIMENT

4.1 Motivation for Study

A test program was implemented to further study the behavior of rocking soil-structure systems at large strain levels. A review of several small scaled-model centrifuge rocking experiments was described in Chapter 2. As typical for centrifuge testing, these studies benefitted from prepared soil specimens and a high level of parameter control. Laboratory research facilitates studying fundamental behaviors of a particular system through parametric control. Often times as research evolves into field-scale testing, fundamental behaviors once exhibited in the laboratory become compromised by the environment and factors associated with the scale of a project. This chapter describes field-scale tests of a rocking soil-structure system, an experimental approach to study large-strain foundation rocking, experimental results, and a simplified analytical model to capture the observed behavior.

4.2 Rocking Foundation System

To investigate the rocking behavior of a surface footing on a natural soil deposit, three types of rocking tests were investigated in the experimental program. The surface footing was square and represents an isolated column footing supporting a structural assembly. The structural assembly can be seen in Figure 60. Dimensions for the structural assembly can be found in Table 2. The structural assembly is made up of a concrete footing, threaded anchor rods, non-shrink grout, a steel base plate, an AISC HP shape steel column, a concrete pile cap, a hydraulic inertial shaker, and steel plate counterweights.

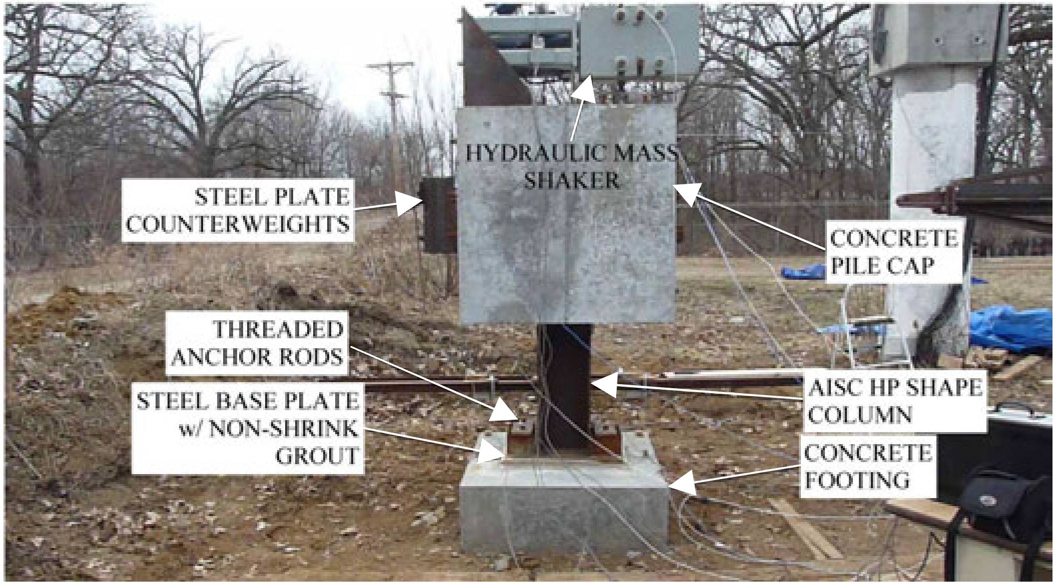

Figure 60. Structural assembly.

Table 2. Structural assembly dimensions.

Concrete footing width (m)	0.914
Concrete footing height (m)	0.308
AISC HP column	HP10x42
Column base plate thickness (m)	0.0191
Column base plate length (m)	0.508
Column base plate width (m)	0.254
Non-shrink grout thickness (m)	≈0.0381
Concrete pile cap width (m)	0.914
Concrete pile cap height (m)	0.914

4.2.1 Small-Strain Dynamic Forced Vibration Tests

Each type of rocking test offered a different level of soil strain and excitation type. The program started with small soil strain amplitudes resulting from forced vibration by the hydraulic mass shaker. The shaker was mounted at the top of the assembly in a horizontal orientation by means of a custom fabricated gusset-type steel plate connection. This configuration can be seen in Figure 61. A total of 14 steel inertial mass plates were used on the shaker. The mass of the shaker relative to the mass of the entire system was substantial, therefore the shaker and inertial mass plates remained present through the entire experimental program, due to the shaker's influence on the overall static and dynamic response. The shaker was connected to a signal control and to a hydraulic power supply. The hydraulic power lines were connected as seen in Figure 62. These lines were suspended from the top of the large reaction column to minimize their influence on the rocking system.

(a) (b)

Figure 61. Steel plate gusset connection between pile cap and shaker.

Figure 62. Hydraulic power lines suspended from reaction column.

4.2.2 Intermediate-Strain Free Vibration Tests

The second type of rocking that increased the level of soil strain by rotating the structural assembly to an initial rotation displacement using a tensioned cable. From the initial rotation displacement, the system was set into free rocking vibration by releasing the cable using a snap mechanism as pictured in Figure 63. The snap mechanism was built by fabricating two steel angles with a hole in the center of one of the legs. The two angles were field welded back to back with an inch of separation to a steel plate which was bolted to the concrete pile cap. The separated angles provided a space for a shackle rigging, which is pictured in Figure 64. The shackle rigging connects the pile cap to a come-along, which was anchored back to a 0.91 m diameter reinforced concrete reaction column continuous with a 11.88 m deep drilled shaft by a steel assembly. The reinforced concrete reaction column and steel assembly is discussed in further detail in the description of the slow cyclic lateral displacement tests. The come-along provided the tension to pull the structural assembly to an initial rotation displacement. The snap mechanism functioned by connecting the shackle rigging to the fabricated angles with a bullpin, which is a tapered steel shaft used by ironworkers to set structural steel. The bullpin was threaded between the angle holes and the shackle rigging. Upon connecting the come-along to the pile cap, the come-along was cranked to pull the structural assembly to an initial rotation displacement. A ball-peen hammer was used to strike the bullpin, which disengaged clear of the assembly, released the shackle, and set the structure into free vibration. Various bungee cords and a temporary pvc support tube were employed to catch the come-along and ensure it did not interfere with the structure or the measuring instrumentation post-release. Information on the measurement instrumentation types and locations can be found in Section 4.4.

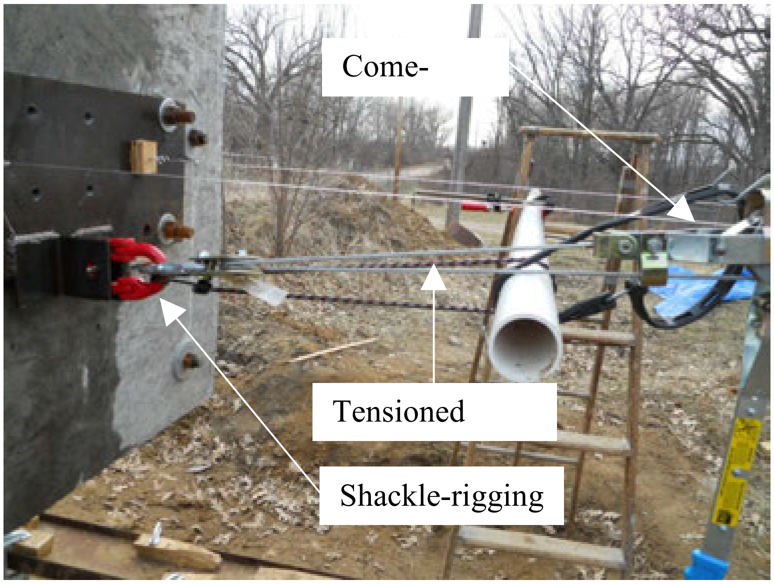

Figure 63. Quick-release cable “snap” mechanism for free-vibration tests.

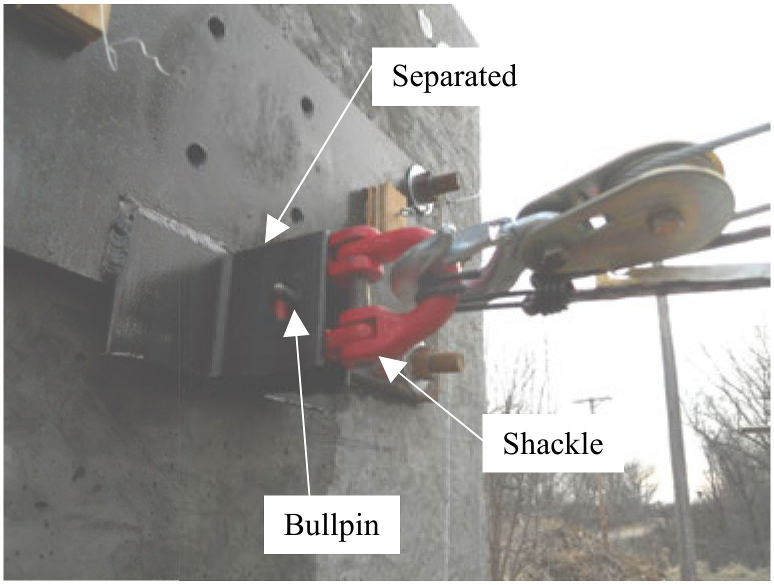

Figure 64. Quick-release shackle rigging.

4.2.3 Large-Strain Quasi-static Cyclic Tests

The third type of rocking tests used a doubly-hinged hydraulic jack to provide a slow cyclic lateral force to the concrete pile cap. The doubly-hinged hydraulic jack was attached to a steel plate which was mounted to the concrete pile cap. The pile cap was slowly pushed and pulled by the hydraulic jack in a pseudo-static manner so that the material dependent system response in the form of soil stiffness and hysteretic damping could be isolated from the inertial dynamic response. The hydraulic jack was anchored back to a large reinforced concrete reaction column which was installed for a previous study (Sritharan, et al. 2007; Suleiman, et al. 2006). A steel assembly was fabricated to mount the hydraulic jack to the large reaction column, as can be seen in Figure 65. The base of the assembly was secured around the large reaction column with steel chains.

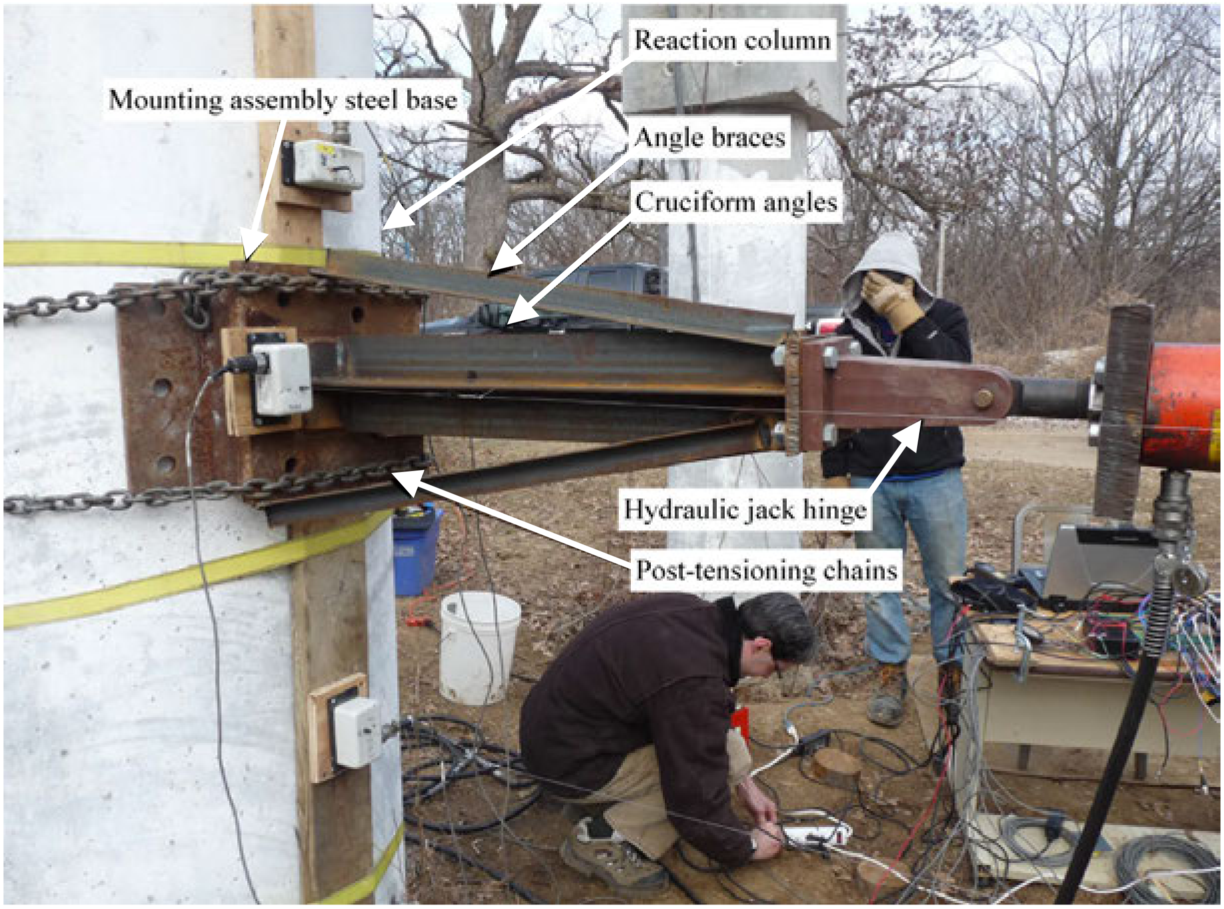

Figure 65. Steel assembly used to support the hydraulic jack.

Two steel angles were shop welded in a cruciform orientation with a steel mounting plate for the hydraulic jack's hinge. The cruciform angles were then field welded to the base of the post-tensioned assembly. Three smaller steel angles were field welded to brace the cruciform angles. The doubly hinged hydraulic jack was installed and connected to a load cell attached to the side of the concrete pile cap, as shown in Figure 66. Information on the measurement instrumentation types and locations can be found in Section 4.4.

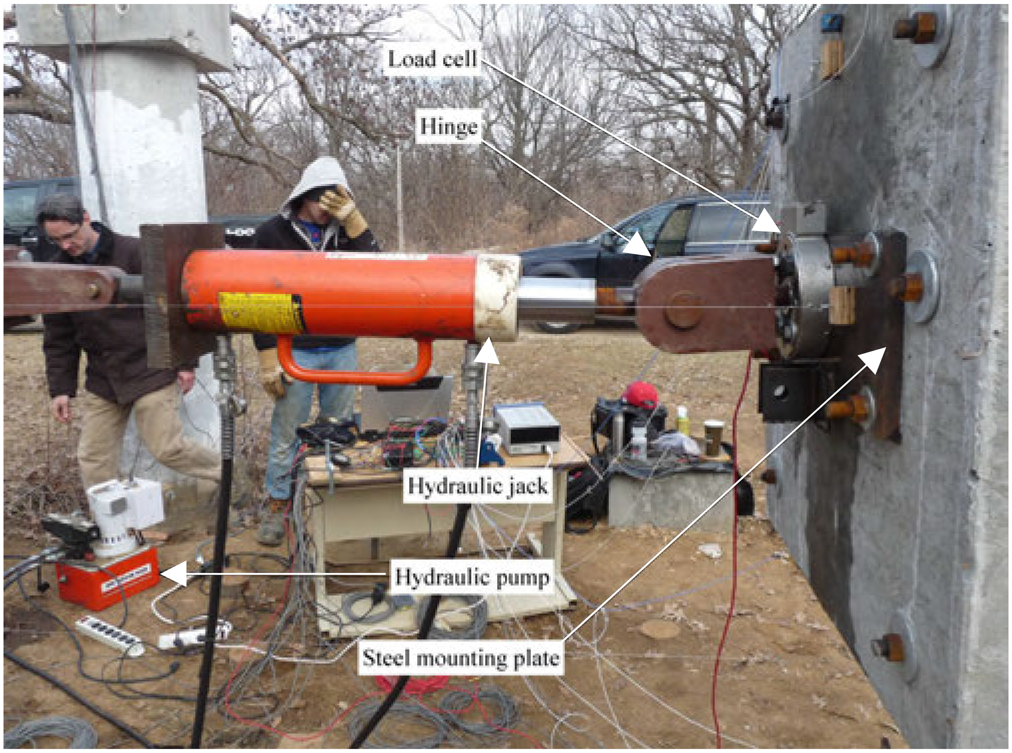

Figure 66. Hydraulic jack attached between steel assembly and pile cap.

4.3 Natural Soil Classification and Site Preparation

The rocking system was built and tested at Spangler Geotechnical Laboratory at Iowa State University. As noted, the outdoor test location was selected to be adjacent to available reaction columns from previous studies (see Sritharan, et al. 2007; Suleiman, et al. 2006; Shelman 2009). These studies classified the soil deposit as a low plasticity glacial till clay as defined by the Unified Soil Classification System. A skid-steer loader was used to level a test area of approximately 4 m x 4 m by removing the topsoil over a depth of 6 in. to 12 in. The low permeability of the clay coupled with inadequate drainage left the test site vulnerable to standing water, as depicted in Figure 67 following a snow melt. The area was dewatered 37 days before testing, resulting in a water table near the surface during testing.

Figure 67. Testing area under water on February 17, 2011.

4.4 Measurement System

Epoxy adhesive was used to attach ceramic accelerometer mounting pads to the shaker, concrete pile cap and concrete footing. PCB model 356 B08 triaxial high sensitivity accelerometers and PCB model 353 B33 single axis accelerometers were attached to the mounting pads. Both accelerometer types have a measurement range of ±490 m/s^2 pk (±50g pk). The triaxial accelerometers have a resonant frequency greater than 20 kHz and the single axis accelerometers have a resonant frequency greater than 22 kHz. A load cell within the hydraulic shaker and accelerometers attached to the moving mass were used to measure frequency domain response of the system under dynamic forced vibration. The accelerometers on the pile cap were also used to compute the inertial force and resulting base moment of the moving pile cap in free vibration in the time domain. Figure 68 shows the configuration and reference axis of the accelerometer measurements.

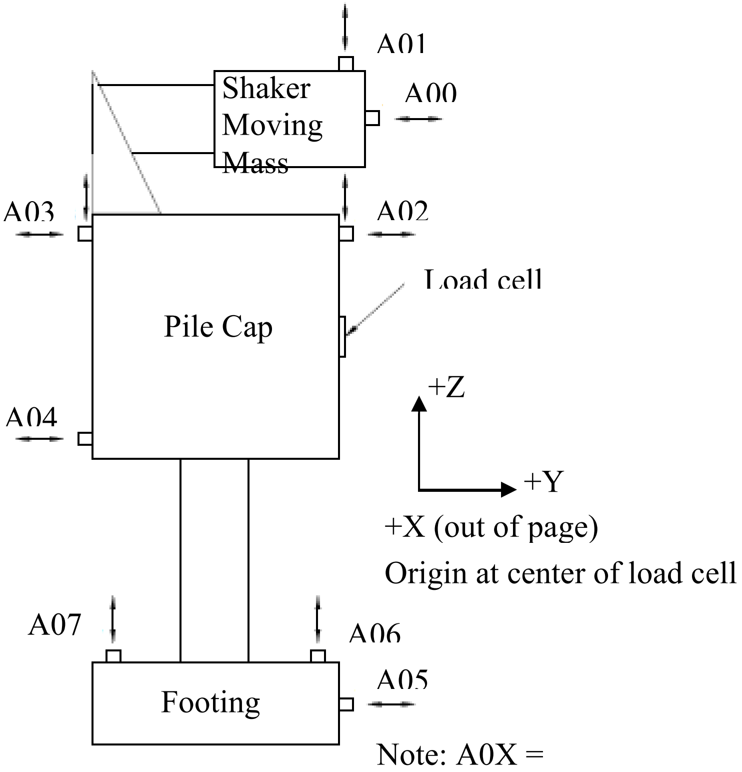

Figure 68. Accelerometer locations and measurement directions.

String potentiometers (string pots) were installed on the concrete pile cap and concrete footing for the free vibration and quasi-static cyclic tests. The string pot signals were measured in the time domain and used to triangulate/track the motion of the system in the rocking analysis as described in Section 4.5.2. Figure 69 shows the string pot layout used for the rocking tests.

A National Instruments LabVIEW signal analyzer with custom dynamic signal analyzer and time-record capture programs was used to collect and process signal data for each of the tests. Refer to Table 3 and Table 4 for the positions of the accelerometers, string pots, and other instruments at the conclusion of testing.

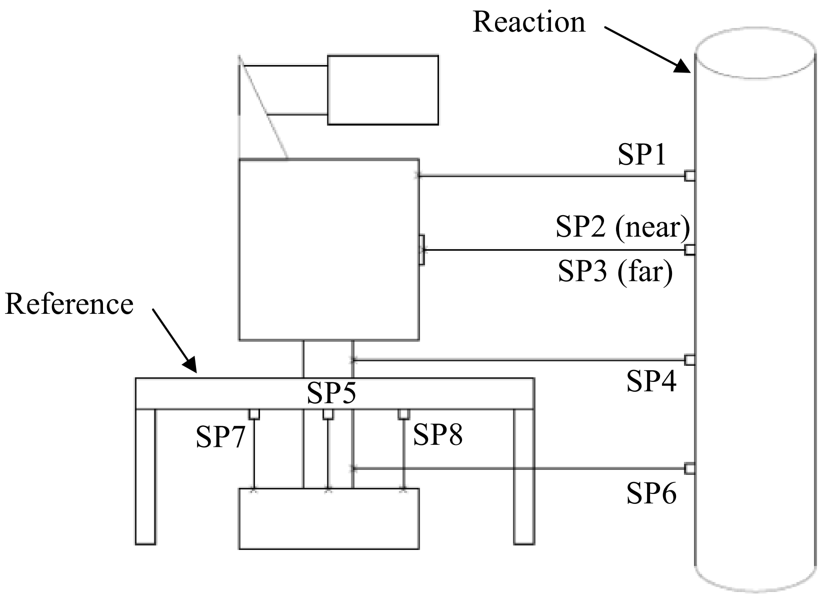

Figure 69. String pot locations.

Table 3. Instrument locations on rocking system at the conclusion of experimentation.

Instrument type	Tag	X (m)	Y (m)	Z (m)
Single axis	A00	0.000	0.000	0.597
Single axis	A01	N/A	N/A	N/A
Triaxial accelerometer	A02	0.000	0.000	0.232
Triaxial accelerometer	A03	0.000	-0.914	0.232
Single axis	A04	0.000	-0.914	-0.606
Single axis	A05	0.000	0.000	-1.527
Single axis	A06	0.000	-0.051	-1.375
Single axis	A07	0.000	-0.864	-1.375
String pot	SP1	0.000	0.000	0.184
String pot	SP2	-0.152	0.000	-0.141
String pot	SP3	0.152	0.000	-0.148
String pot	SP4	0.000	0.000	-0.714
String pot	SP5	-0.406	-0.457	-1.375
String pot	SP6	0.000	0.000	-1.194
String pot	SP7	-0.406	-0.864	-1.372
String pot	SP8	-0.406	-0.051	-1.378
Load cell	N/A	0.000	0.000	-0.140

Table 4. Locations of instruments or other items on the rocking system.

Instrument/Item	Location	X (m)	Y (m)	Z (m)
Bullpin	Pile cap	0.000	-0.051	-0.279
shaker top	Shaker	0.000	0.000	0.756
shaker bottom	Shaker	0.000	0.000	0.438
SP1	Reaction	0.000	0.000	0.214
SP2	Reaction	N/A	0.000	-0.114
SP3	Reaction	N/A	0.000	-0.124
SP4	Reaction	0.000	0.000	-0.692
B/SP 5	Reference	-0.402	-0.476	-1.162
SP6	Reaction	0.000	0.000	-1.178
B/SP 7	Reference	-0.386	-0.881	-1.162
B/SP 8	Reference	-0.406	-0.067	-1.162
DCDT	Reaction	0.000	0.000	0.864

4.5 Excitation and Measurement Approach

4.5.1 Small-Strain Dynamic Forced Vibration Tests

Each type of rocking test required different instrumentation. The first type of rocking test focused on measuring the dynamic response of the system under small strain lateral loading provided by an inertial mass shaker. Two types of excitation signals were used for these tests. The first was a swept sine signal to measure the frequency response of the system over a specified range of frequencies. Accelerometers were installed on the hydraulic shaker, concrete pile cap, and concrete footing (Figure 68). Table 3 provides Cartesian coordinates for the accelerometers used in the rocking tests.

Table 5 provides detailed technical specifications for the accelerometers used. The signal analyzer was used to compute the Fast Fourier Transform (FFT) of each signal. A transfer function of the concrete footing acceleration divided by the shaker's acceleration was then plotted as the frequency response of the footing. Natural frequencies of the system could then be determined from the transfer function peaks.

Table 5. Accelerometer technical specifications.

Accelerometer model	Sensitivity (±10%)	Measurement range	Frequency range (±5%)	Resonant frequency	Weight
PCB 356 B08	10 mV/(m/s^2)	±490 m/s^2 pk	0.5 to 5000 Hz	≥20 kHz	20 gm
PCB 353 B33	10.19 mV/(m/s^2)	±491 m/s^2 pk	1 to 4000 Hz	≥22 kHz	27 gm

Once the natural frequencies of the system were determined from the transfer functions from small-strain vibration tests with random forcing, dynamic time domain response was investigated for harmonic excitation. In order to take advantage of dynamic amplification to achieve larger strain levels, harmonic sinusoidal signals were prescribed to the shaker at the previously measured natural frequencies. The amplitudes of the sinusoidal signals were progressively increased throughout the testing program. For an SDOF system, the dynamic amplification, *D*, is a magnification of the static displacement under harmonic forcing at frequency, ω, and depends on the damping ratio, ξ, and natural frequency, ω_n, of the system. Figure 70 illustrates the effects of dynamic amplification for lightly damped systems ($0\% < \xi \leq 20\%$). Note that amplification is maximized when the forcing frequency ratio, β, is at a resonant condition near unity. The classical dynamic amplification factor is given in Equation (4.1)

$$D = \frac{1}{\sqrt{\left[\left(1-\beta^2\right)^2 + \left(2\xi\beta\right)^2\right]}} \tag{4.1}$$

where

$$\beta = \frac{\omega}{\omega_n}. \tag{4.2}$$

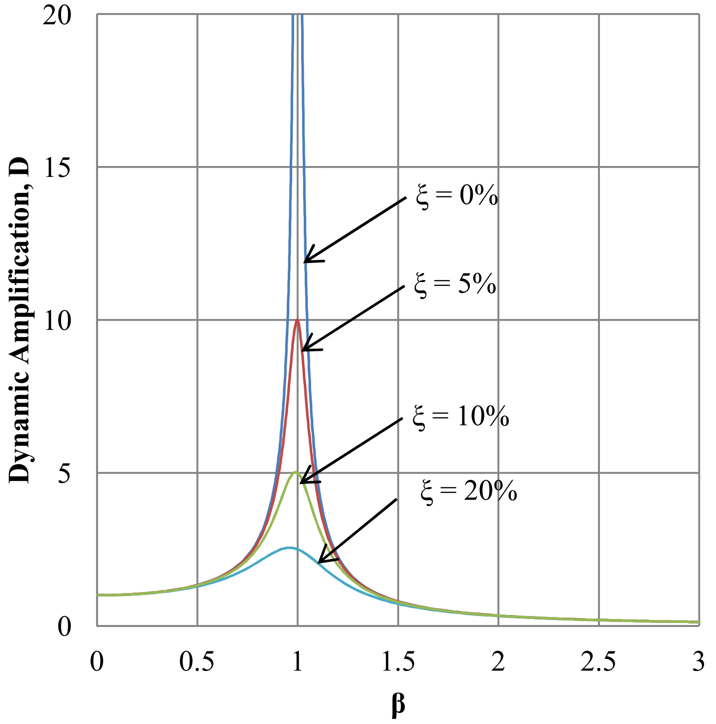

Figure 70. Dynamic amplification factor for forced vibration of a SDOF system.

4.5.2 Free Vibration Tests

The second type of rocking test investigated the dynamic time domain response of the system in free vibration. The accelerometer instrumentation described in Sections 4.4 and 4.5.1 was used for these tests. Knowing the centroid of the entire rocking system along with accelerations at discrete points, rigid body kinematics were used to calculate the accelerations and rotations of the centroid. Similar to the rocking studies reviewed in Chapter 2, the motion of the footing is typically characterized by the displacement of the bottom center point of the footing. However, one of the main concerns in using string pots to capture the motion of the system is that large rotations of the footing result in significant rotations of the string pots about their reference points. Therefore, string pot measurements during the tests give only the distance between the reference point and the attachment point, but the angles of the strings are unknown. Table 3 provides Cartesian coordinates for the string pot connection points used in the rocking tests. Table 6 provides detailed technical information for the string pots used. Because displacements at the bottom center point of the footing were not directly measured, measurements from three string pots along with a simultaneous nonlinear system of equations were used to triangulate the displacement and rotation of the footing control point. Key assumptions for this formulation are that the footing is a rigid body and no out of plane displacement or rotation takes place during the tests. As seen in Figure 69, additional string pots were installed for measurement redundancy and to track the motion of the pile stem and cap.

The displacement formulation at the bottom center of the footing assumes three known string pot reference positions, three string pot length measurements, and simultaneous position equations for three points on the footing. The three reference points on the footing are shown in Figure 71. After the test begins, the measurements on the displaced rigid footing are shown in Figure 72.

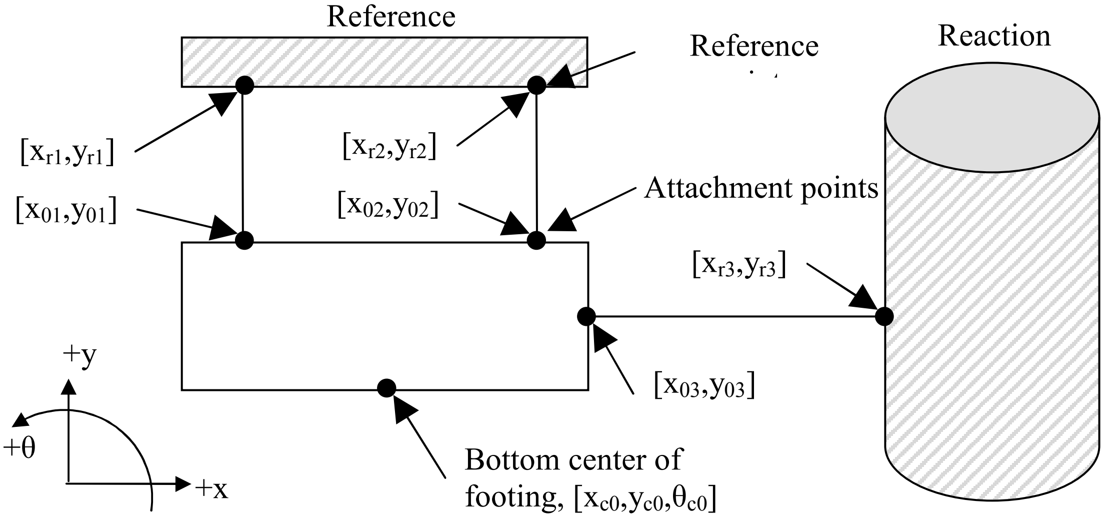

Figure 71. Initial testing position of footing and string pot reference positions.

Table 6. Displacement measurement technical specifications.

Model number	Full stroke range	Resolution	Tension (± 20%)	Max. acceleration
Celesco PT101	0 – 0.508 m	infinite	12 oz.	11 g
DCDT	0 – 0.051 m			

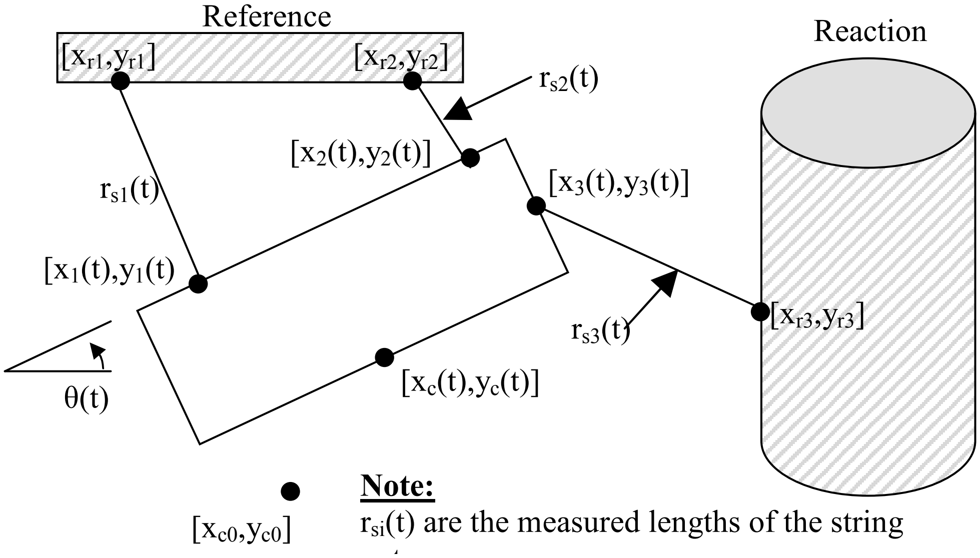

Figure 72. Displaced position of footing during test.

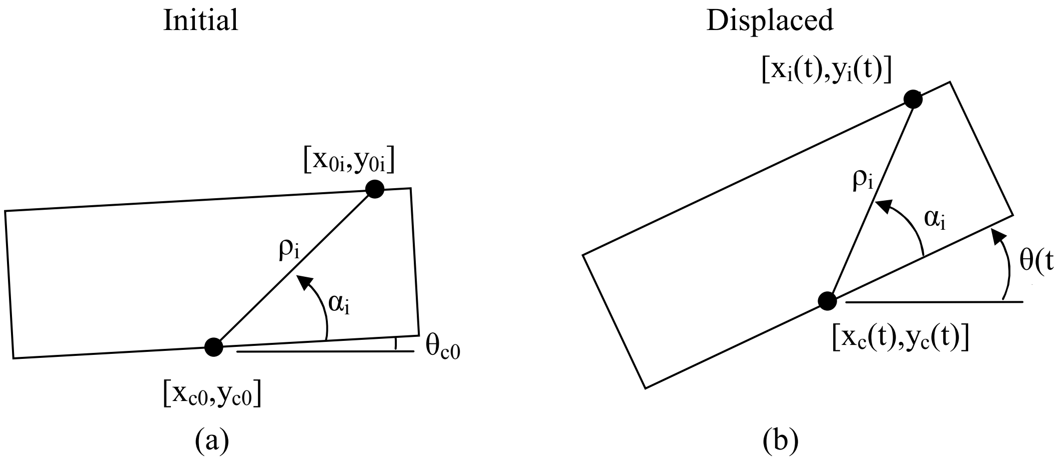

Figure 73. Polar string pot attachment points relative to control point. (a) Initial position, (b) displaced position during test.

Before position equations for the three discrete points are formulated, it is useful to define the polar coordinates (ρ_i, θ_i) of these points relative to the bottom center of the footing, as illustrated in Figure 73. Using Figure 73, the distance and angle between the two points can be expressed in Equations (4.3) and (4.4).

$$\rho_i = \sqrt{\left(x_{0i} - x_{c0}\right)^2 + \left(y_{0i} - y_{c0}\right)^2} \tag{4.3}$$

$$\alpha_i = \tan^{-1}\left(\frac{y_{0i} - y_{c0}}{x_{0i} - x_{c0}}\right) - \theta_0 \tag{4.4}$$

Referring to Figure 72 and Figure 73b, the current position of a point on the footing at any time can be expressed as

$$x_i(t) = x_c(t) + \rho_i \cos\left(\alpha_i + \theta(t)\right) \tag{4.5}$$

$$y_i(t) = y_c(t) + \rho_i \sin\left(\alpha_i + \theta(t)\right)$$

$$. \tag{4.6}$$

The string pot measurement only indicates the change in distance between its attachment and reference points, but the angle of the string is unknown. However, one may determine the string pot's instantaneous length $r_{si}(t)$ from the measurement, which can be related to the position ($x_i(t), y_i(t)$) of the attachment point on the foundation by Pythagoras' theorem as

$$(x_i(t) - x_{ri})^2 + (y_i(t) - y_{ri})^2 = r_{si}^2(t)\,. \tag{4.7}$$

Substituting Equations (4.5) and (4.6) into Equation (4.7) gives

$$\left[x_c(t) + \rho_i \cos(\alpha_i + \theta(t)) - x_{ri}\right]^2 + \left[y_c(t) + \rho_i \sin(\alpha_i + \theta(t)) - y_{ri}\right]^2 = r_{si}^2(t)$$

$$. \tag{4.8}$$

Equations (4.3) to (4.8) can be applied to the three attachment locations shown in Figure 72 to give three Equations (4.8) (i = 1,2,3) in three unknowns $x_c(t)$, $y_c(t)$, and $\theta(t)$. The resulting simultaneous nonlinear system of equations was formed and efficiently solved for each measurement point in time using Matlab. The solution was verified against measurements from a redundant fourth string pot. Since the free vibration rocking tests involved the use of the reaction column as shown in Figure 71 and Figure 72, the lateral displacement at the top of the reaction column was also monitored by a DC displacement transducer (DCDT). Very small displacements were measured by the DCDT, confirming that displacements of the reaction column were negligible. For more information on the DCDT, refer to Table 6.

4.5.3 Quasi-Static Cyclic Loading Tests

The third type of rocking test involved slow cyclic lateral displacement and rotation of the system. The time domain response of the system was captured using the same instrumentation from the free vibration tests described above. A load cell was used in addition to the accelerometers, string pots, and DCDT. The load cell was attached between the hydraulic jack and concrete pile cap as seen in Figure 66, to measure the lateral force applied to the pile cap.

4.6 Experimental Results and Discussion

4.6.1 Dynamic Forced Vibration Tests

A frequency analysis of the footing response was performed to identify resonant frequencies of the footing-soil system. The forcing signal and footing response in the time domain for one of the tests is shown in Figure 74. Accelerometers attached to the top surface of the footing were used to form transfer functions relative to the horizontal acceleration of the hydraulic shaker's inertial mass. This transfer function will henceforth be referred to as the accelerance. Figure 74 shows the accelerance of two of the points on the footing. A number of potential accelerance peaks emerge from the test. The coherence measurement is also plotted in Figure 74 as a measure of linearity in the system. Perfectly linear systems have a coherence of unity. As Figure 74 illustrates, the small strains from the test result in a coherence close to unity. Three frequencies (4, 9, and 68 Hz) from this analysis were chosen as forcing frequencies to be used in the subsequent harmonic excitation tests. The rocking impedance K_{mm} most strongly influences the peak seen at about 9 Hz in Figure 74, while the impedance K_{hh} has a stronger effect on a second peak at around 68 Hz. Thus, each of the frequencies selected for harmonic excitation are less than 100 Hz.

A representative harmonic test is presented in Figure 75 and Figure 76. These figures show two of the time domain tests with sinusoidal loading. While these figures clearly show the acceleration response out of phase by π/2 radians (rocking), the horizontal acceleration and dynamic amplification provided by the hydraulic mass shaker was not enough to overcome the system's resistance to overturning. The concrete footing was unable to be uplifted in the small strain dynamic tests with the hydraulic shaker. The log of tests from the first class of rocking is presented in Table 7.

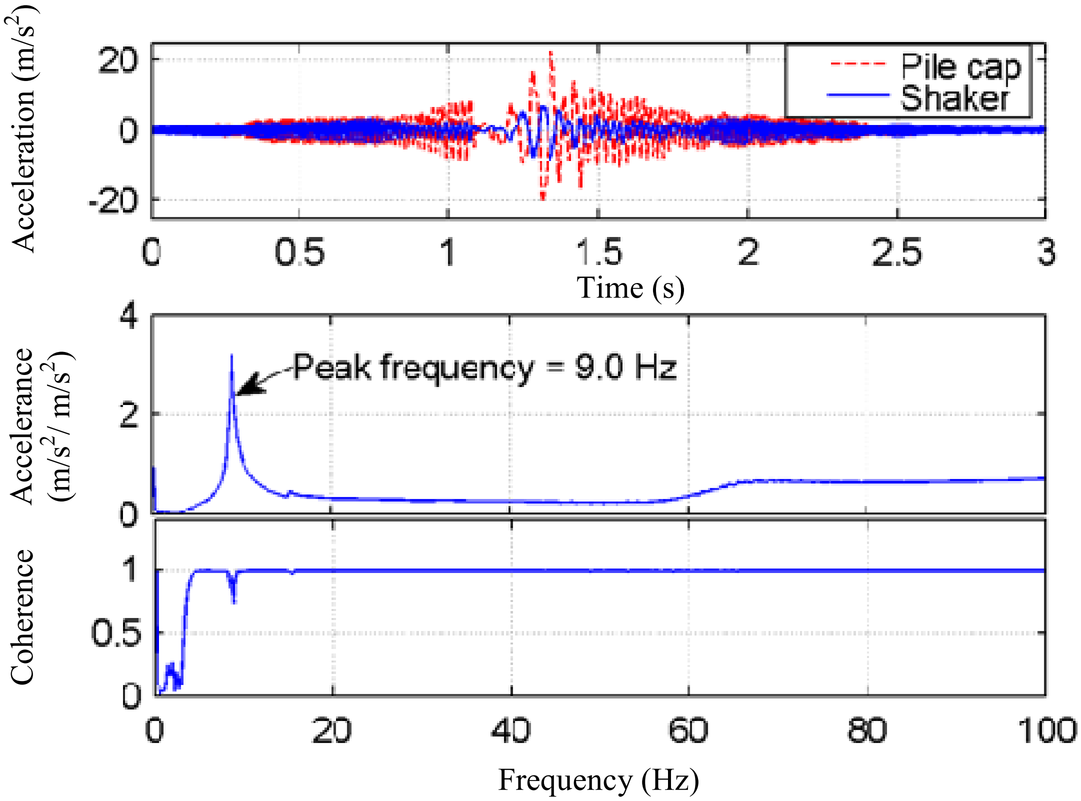

Figure 74. Footing response from dynamic forced vibration test HC-S4 with 9 Hz excitation frequency.

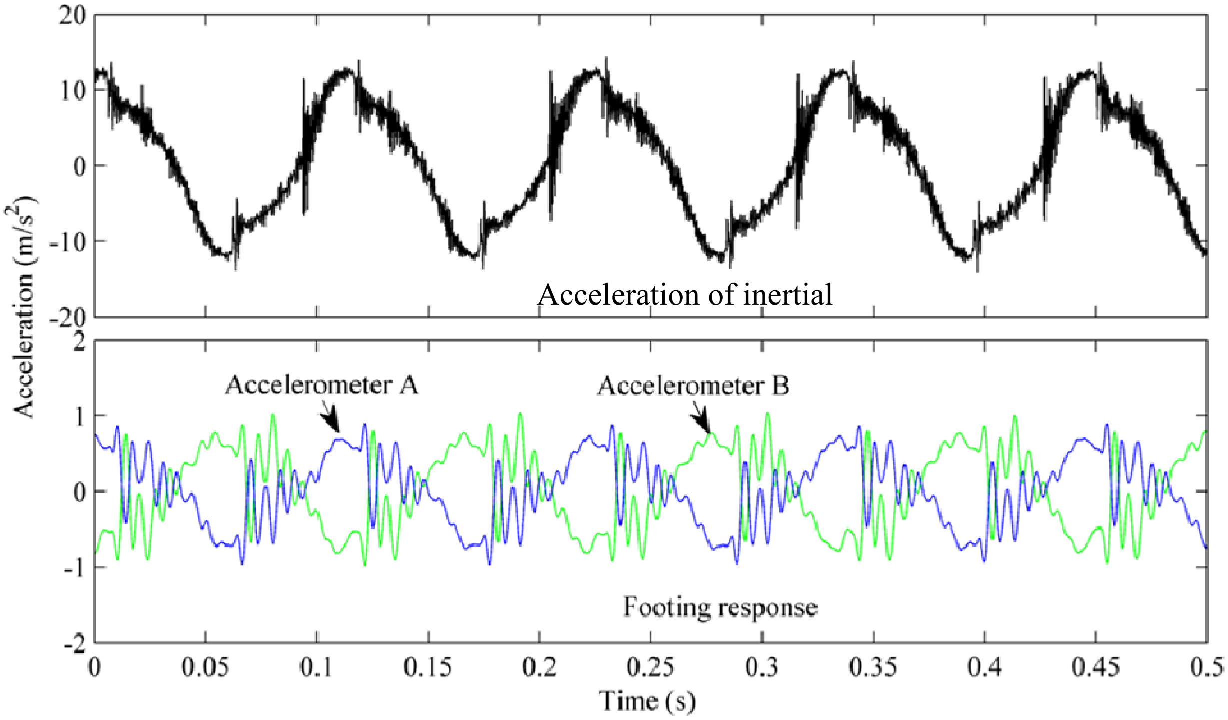

Figure 75. Time domain response of footing in harmonic excitation test LR14 with 9 Hz excitation frequency.

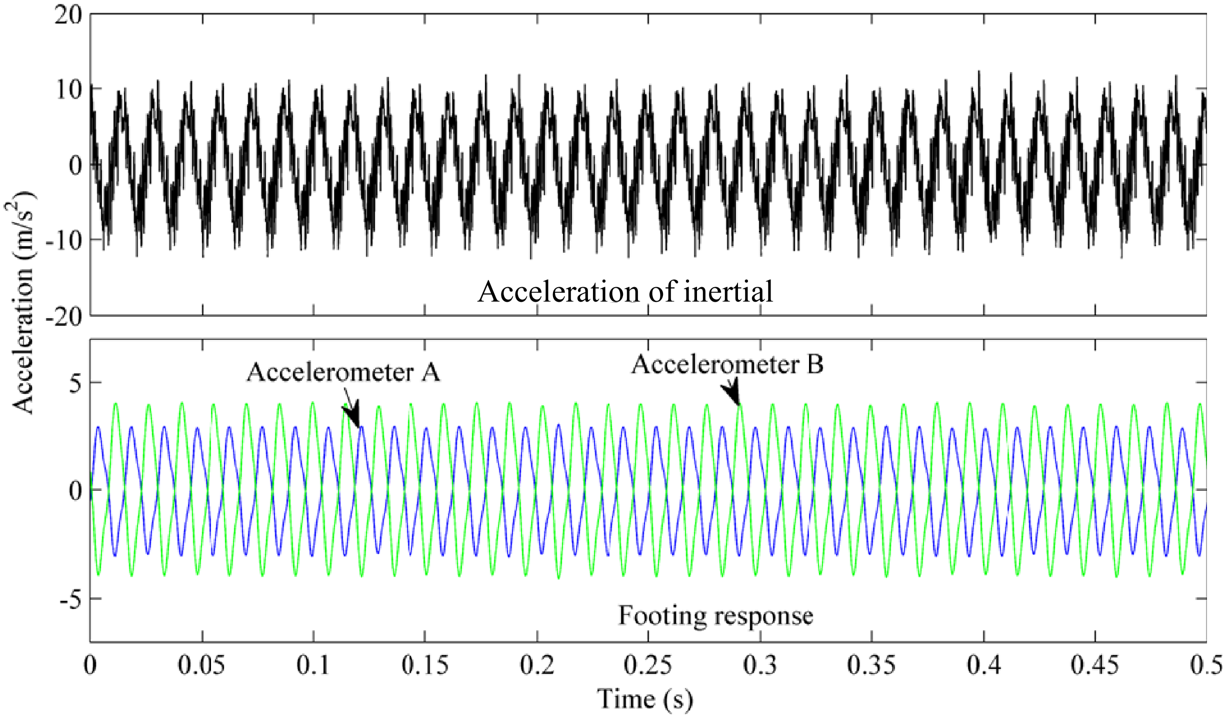

Figure 76. Time domain response of footing in harmonic excitation test LR16 with 68 Hz excitation frequency.

Table 7. Log of small-strain dynamic tests using hydraulic inertial mass shaker.

Data file	Measurement domain	Notes		
		Shaker controller settings	Hydraulic power supply @ 10 GPM	Signal settings
HC-Amb1	Frequency	N/A	N/A	Ambient test
HC-S1	Frequency	Gain 1.7; Span 2.0	2000 psi	1 V pk; 250 Hz test; 3 second sweep; 1-250 Hz sweep
HC-S2	Frequency	Gain 1.7; Span 5	2000 psi	1 V pk; 250 Hz test; 3 second sweep; 1-250 Hz sweep
HC-S3	Frequency	Gain 1.7; Span 4	2000 psi	1 V pk; 250 Hz test; 3 second sweep; 1-250 Hz sweep
HC-S4	Frequency	Gain 1.7; Span 5	2000 psi	1 V pk; 250 Hz test; 3 second sweep; 1-250 Hz sweep
LR01	Time	N/A	N/A	Ambient test
LR02	Time	Gain 1.7; Span 2	2000 psi	1 V pk; 9 Hz sine
LR03	Time	Gain 1.7; Span 4	2000 psi	1 V pk; 9 Hz sine
LR04	Time	Gain 1.7; Span 5	2000 psi	1 V pk; 9 Hz sine
LR05	Time	Gain 1.7; Span 10	2000 psi	1 V pk; 9 Hz sine
LR06	Time	Gain 1.7; Span 2	2000 psi	1 V pk; 68 Hz sine
LR07	Time	Gain 1.7; Span 4	2000 psi	1 V pk; 68 Hz sine
LR08	Time	Gain 1.7; Span 5	2000 psi	1 V pk; 68 Hz sine
LR09	Time	Gain 1.7; Span 10	2000 psi	1 V pk; 68 Hz sine
LR10	Time	Gain 1.7; Span 10	3000 psi	1 V pk; 5 Hz sine
LR11	Time	Gain 1.7; Span 5	3000 psi	5 V pk; 4 Hz sine
LR12	Time	Gain 1.7; Span 8	3000 psi	5 V pk; 4 Hz sine
LR13	Time	Gain 1.7; Span 6	2000 psi	1 V pk; 9 Hz sine
LR14	Time	Gain 1.7; Span 10	2000 psi	1 V pk; 9 Hz sine
LR15	Time	Gain 1.7; Span 5	2000 psi	1 V pk; 68 Hz sine
LR16	Time	Gain 1.7; Span 10	2000 psi	1 V pk; 68 Hz sine

4.6.2 Free Vibration Tests

A series of free vibration snap tests were performed on the rocking system following the dynamic forced vibration tests. As shown in f the quasi-static cyclic tests. Figure 77 to Figure

87 present the motion and moment-rotation relationship of the footing at the bottom center control point from the free vibration snap tests.

Table 8, tests Snap01 to Snap08 were performed prior to the quasi-static cyclic tests (Cyclic01 to Cyclic09) of increasing strain and plastic deformation. Following the quasi-static cyclic tests, free vibration tests Snap09 to Snap11 were performed to observe the effects from the large plastic deformations of the quasi-static cyclic tests. Figure 77 to Figure 87 present the motion and moment-rotation relationship of the footing at the bottom center control point from the free vibration snap tests.

Table 8. Chronological order of Free Vibration (snap) and Quasi-static cyclic tests.

Data File	Test Type	Notes
Snap01	Free Vibration	Initial uplift at edge of footing = ~1/2"
Snap02	Free Vibration	Initial uplift at edge of footing = ~1"
Snap03	Free Vibration	Initial uplift at edge of footing = ~1.25"
Snap04	Free Vibration	Initial uplift at edge of footing = ~1.5"
Snap05	Free Vibration	Initial uplift at edge of footing = ~1.5"
Snap06	Free Vibration	Initial uplift at edge of footing = ~2"
Snap07	Free Vibration	Initial uplift at edge of footing = ~2"
Snap08	Free Vibration	Initial uplift at edge of footing = ~2"
Cyclic01	Quasi-static	Push/Pull = ~ +/- 1", 3 cycles
Cyclic02	Quasi-static	Push/Pull = ~ +/- 2", 3 cycles
Cyclic03	Quasi-static	Push/Pull = ~ +6/- 5.25", 3 cycles, data lost; out of memory
Cyclic04	Quasi-static	Push/Pull = ~ +6/- 5.25", 6 cycles
Cyclic05	Quasi-static	Push/Pull = ~ +/- 1"
Cyclic06	Quasi-static	Push/Pull = ~ +/- 4"
Cyclic07	Quasi-static	Push/Pull = ~ +6/- 5.5"
Cyclic08	Quasi-static	Push/Pull = ~ +8/-5.5"
Cyclic09	Quasi-static	Push/Pull = ~ +8.5/-5.5"
Snap09	Free Vibration	Initial uplift at edge of footing = ~1.5"
Snap10	Free Vibration	Initial uplift at edge of footing = ~2"
Snap11	Free Vibration	Initial uplift at edge of footing = ~3.75"

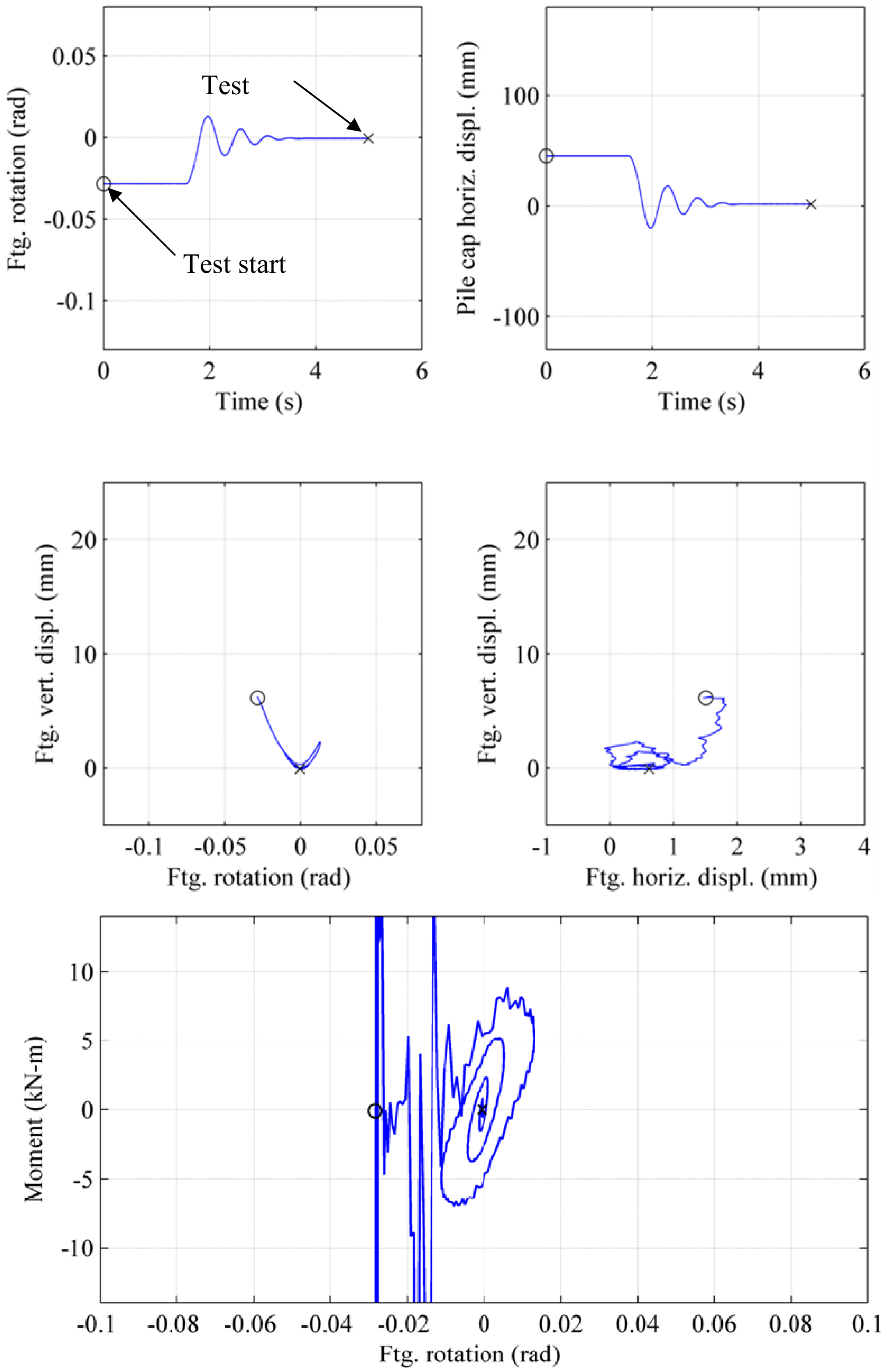

Figure 77. Response of footing at bottom center control point in free vibration test Snap01.

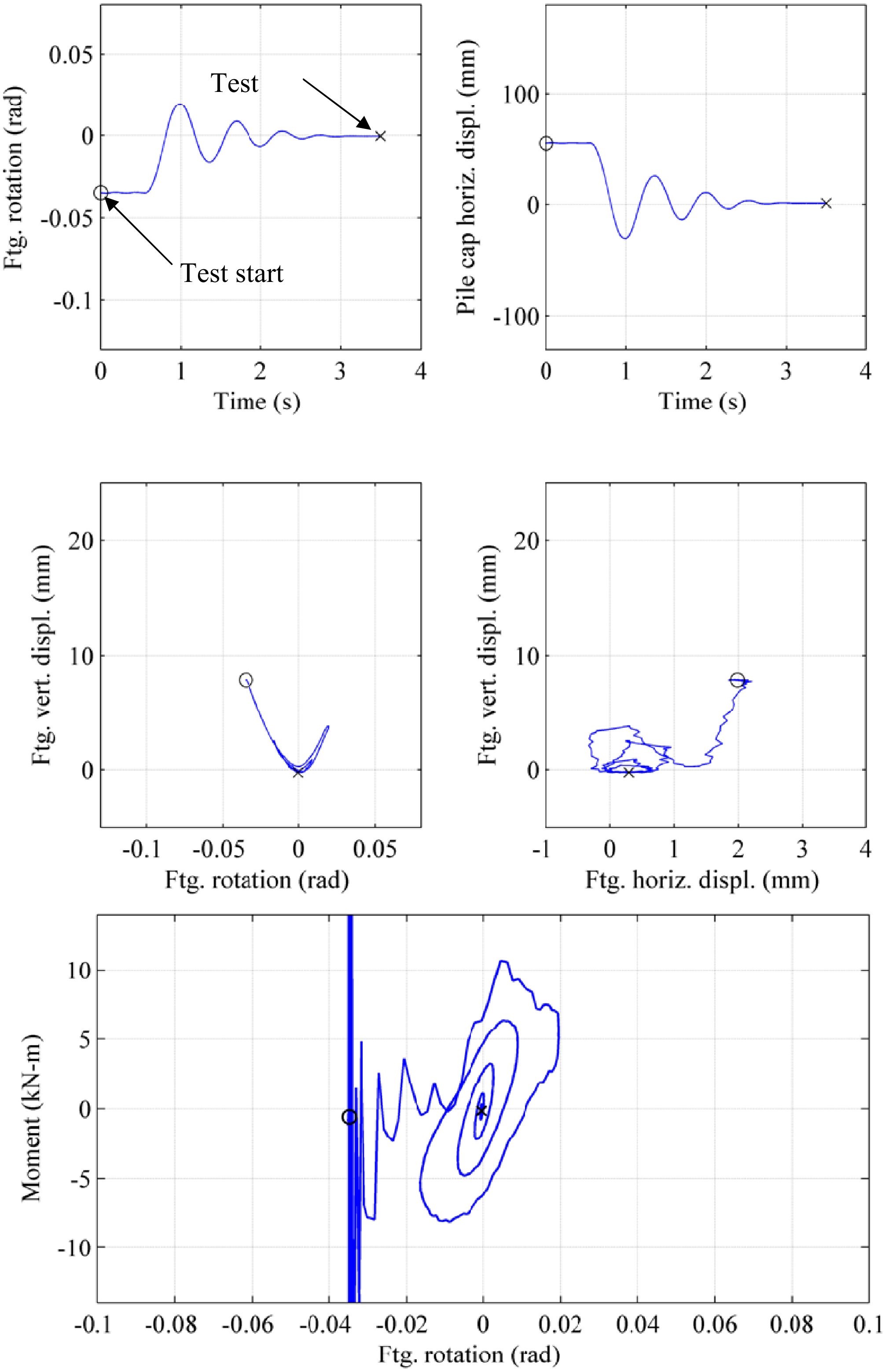

Figure 78. Response of footing at bottom center control point in free vibration test Snap02.

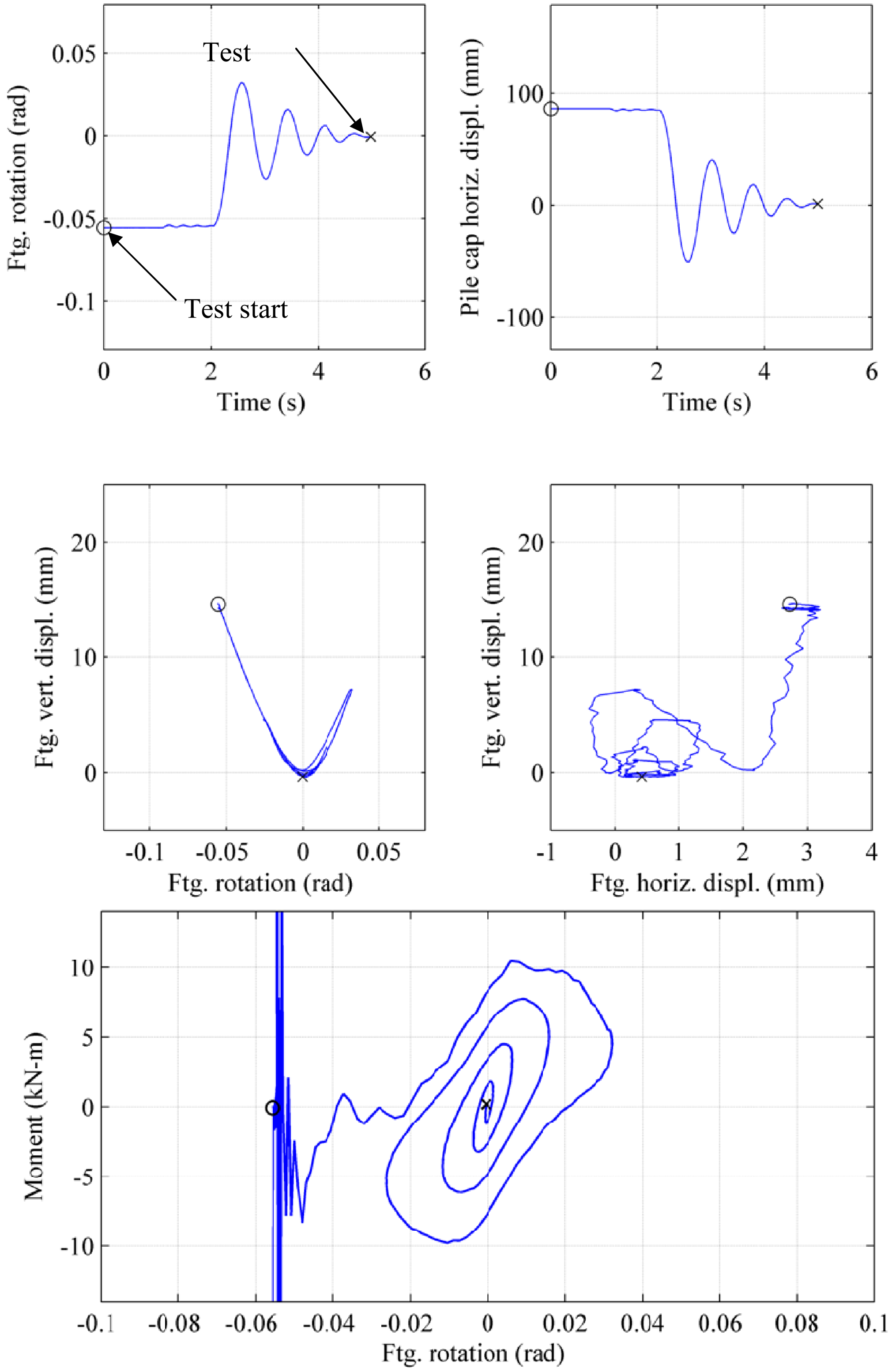

Figure 79. Response of footing at bottom center control point in free vibration test Snap03.

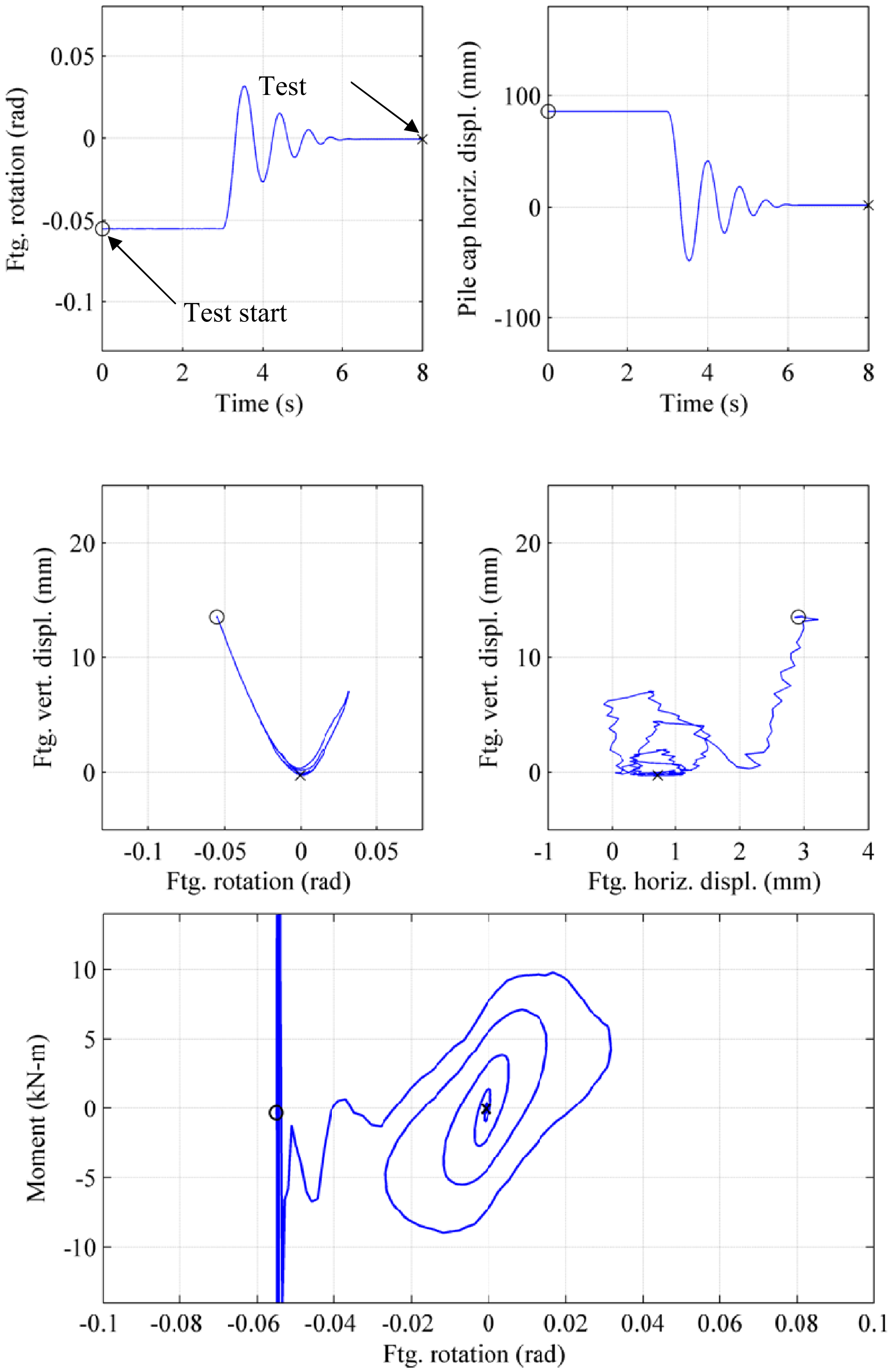

Figure 80. Response of footing at bottom center control point in free vibration test Snap04.

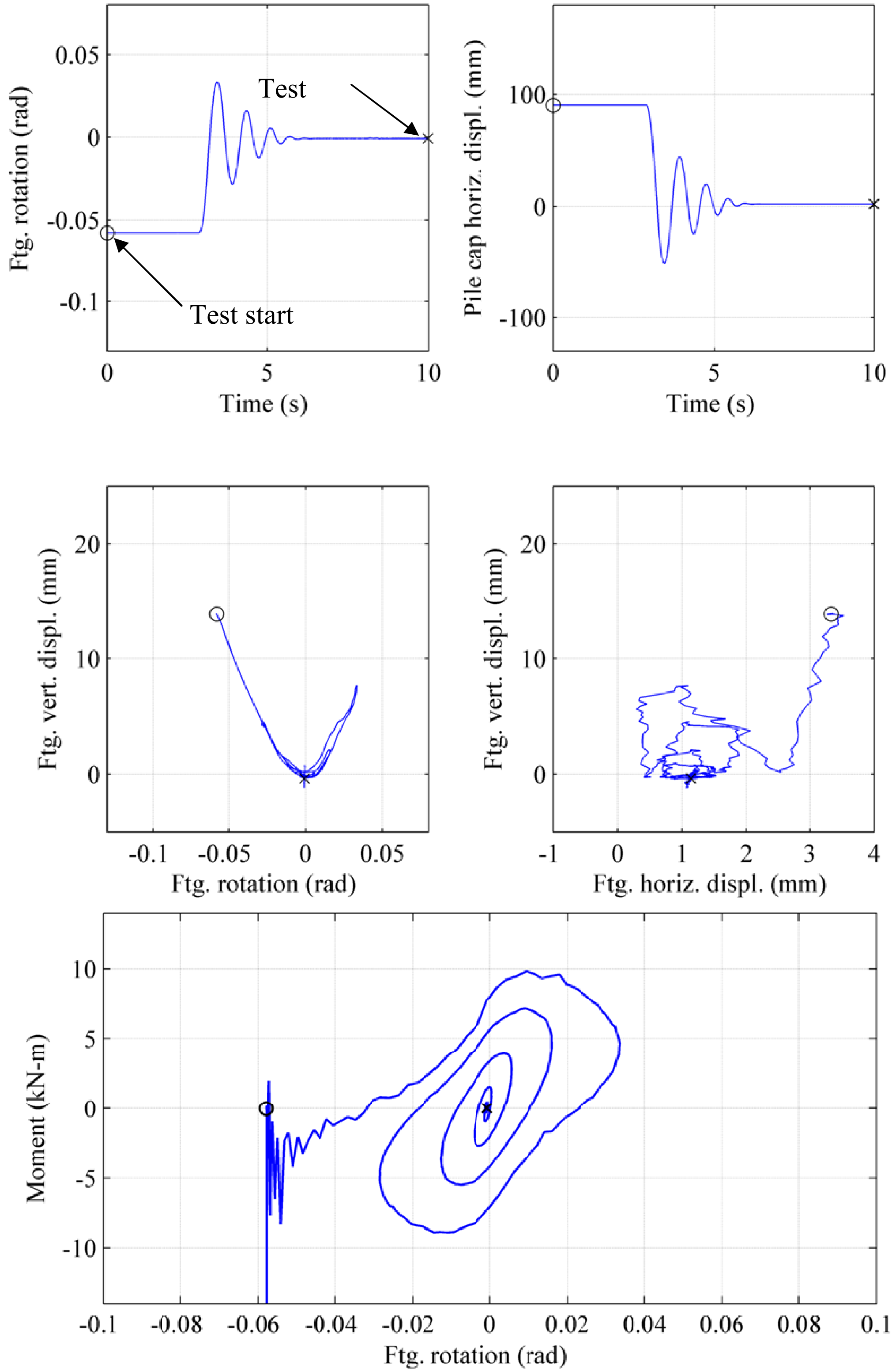

Figure 81. Response of footing at bottom center control point in free vibration test Snap05.

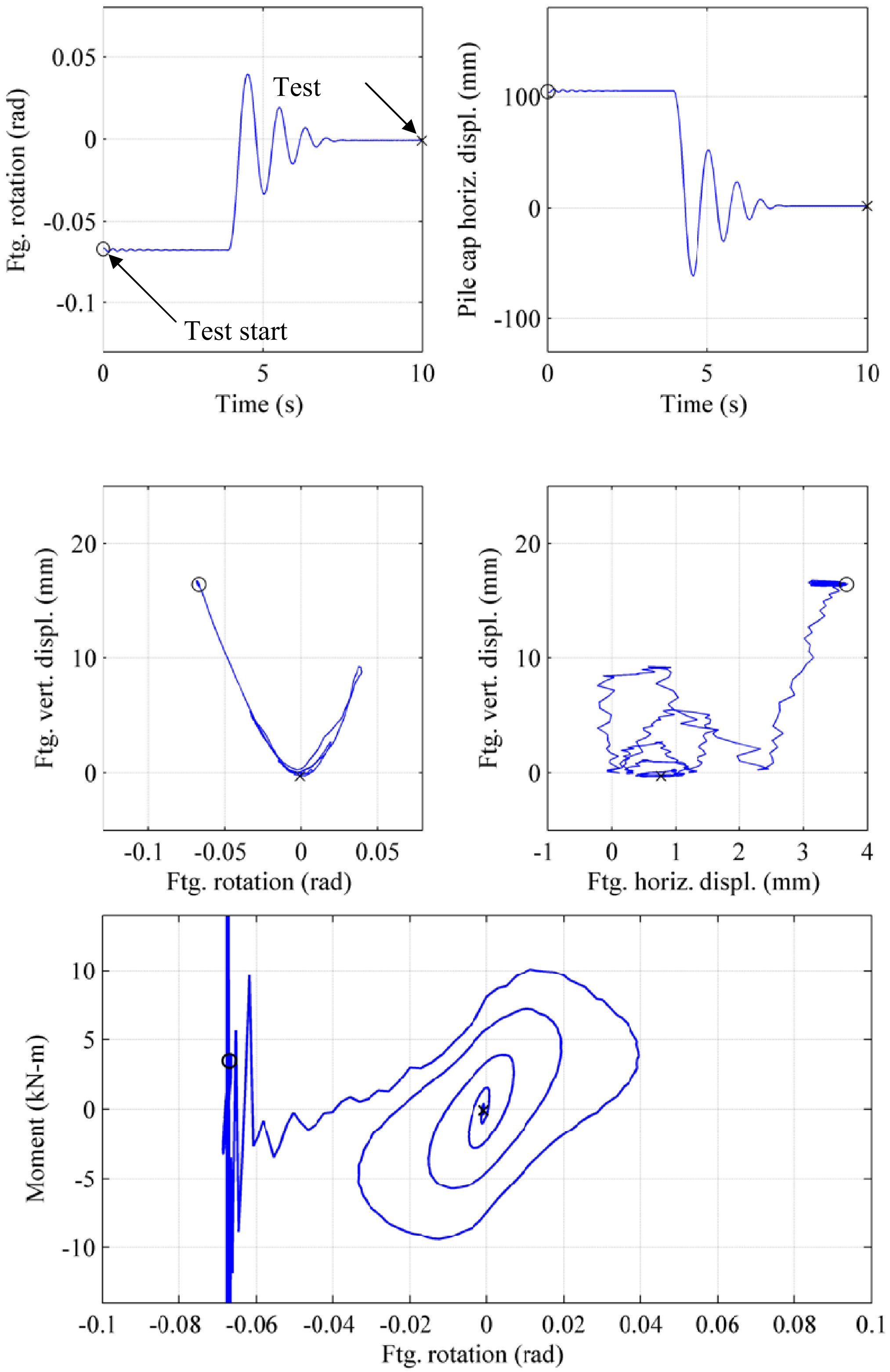

Figure 82. Response of footing at bottom center control point in free vibration test Snap06.

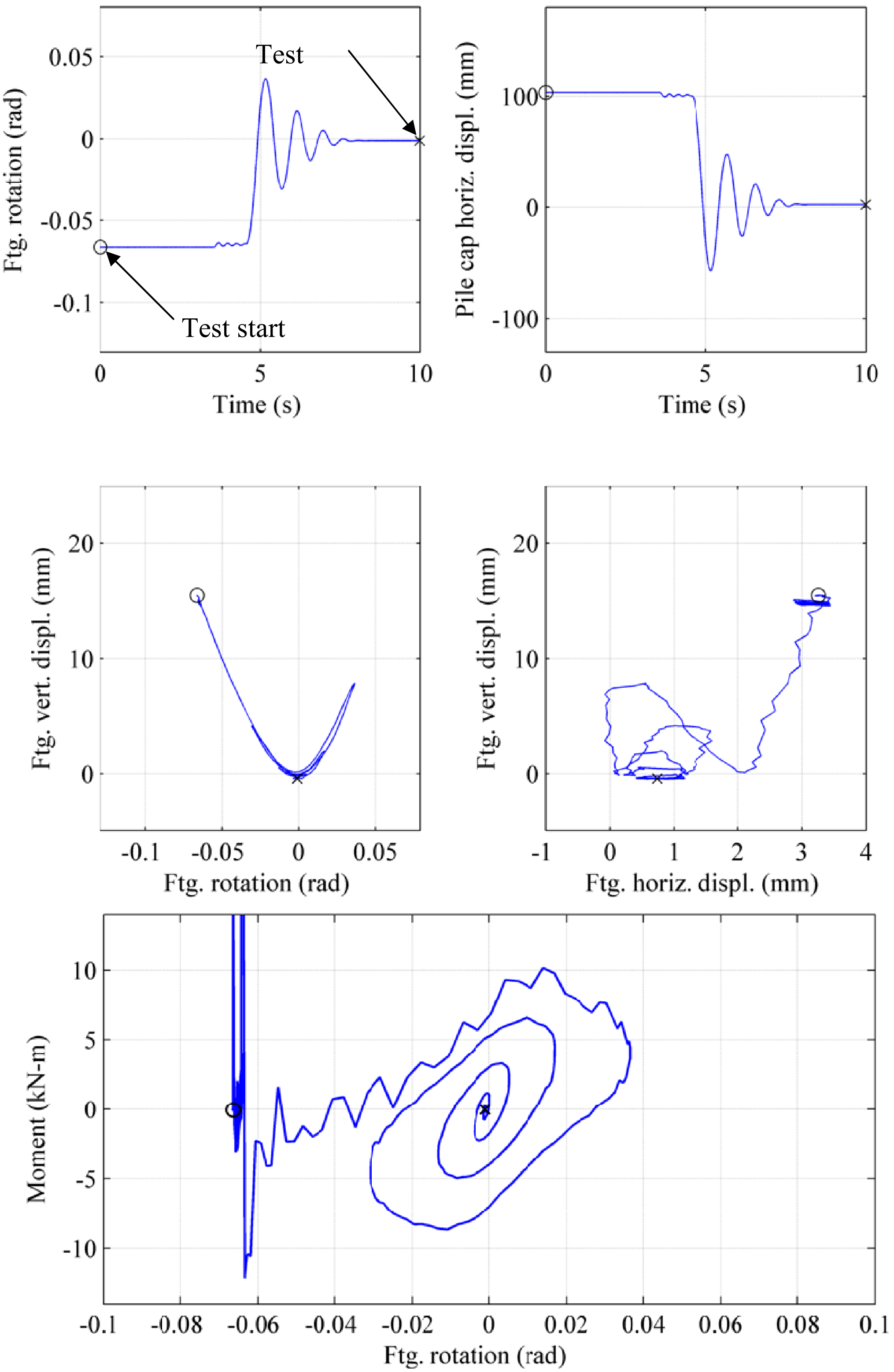

Figure 83. Response of footing at bottom center control point in free vibration test Snap07.

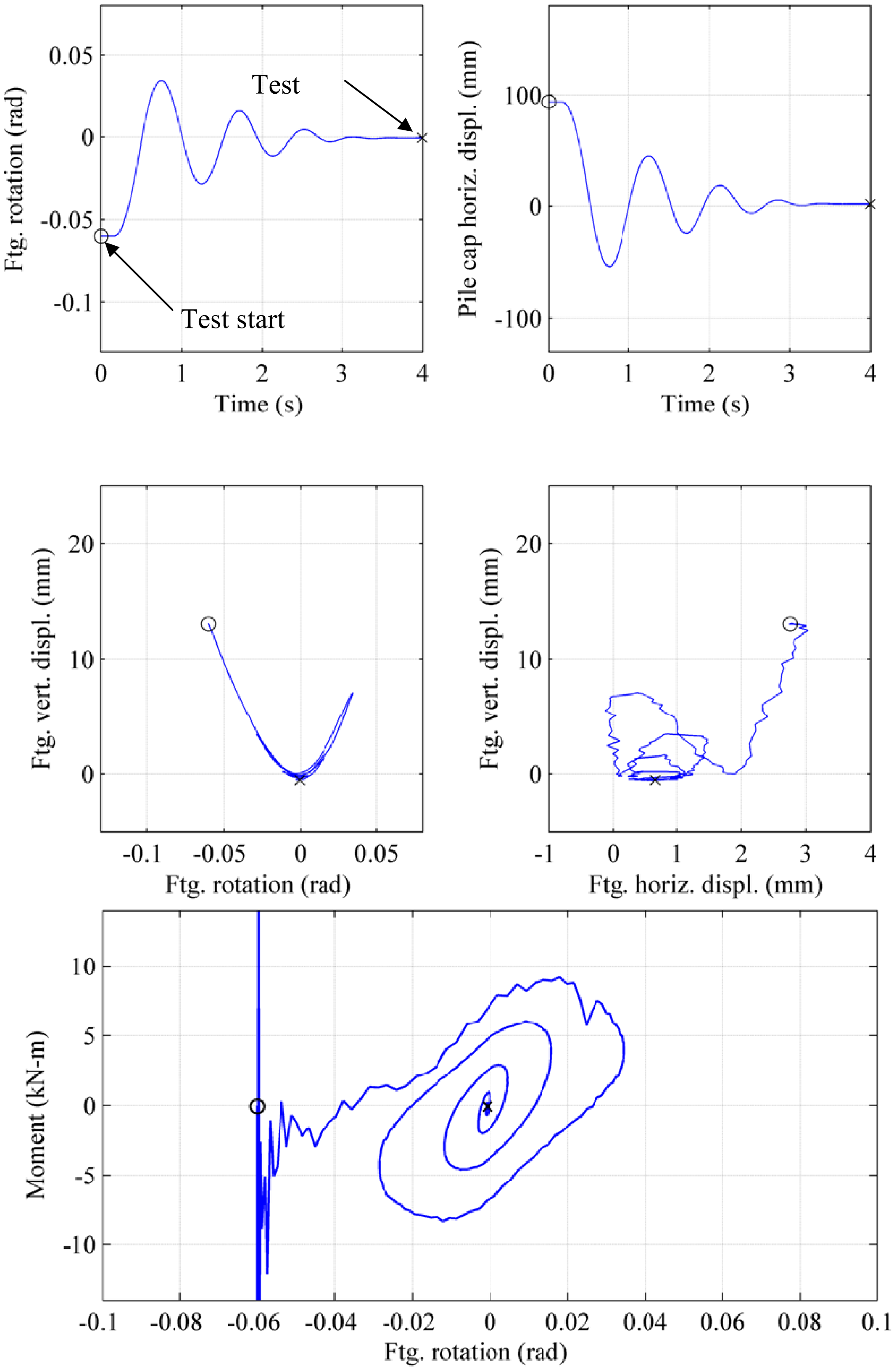

Figure 84. Response of footing at bottom center control point in free vibration test Snap08.

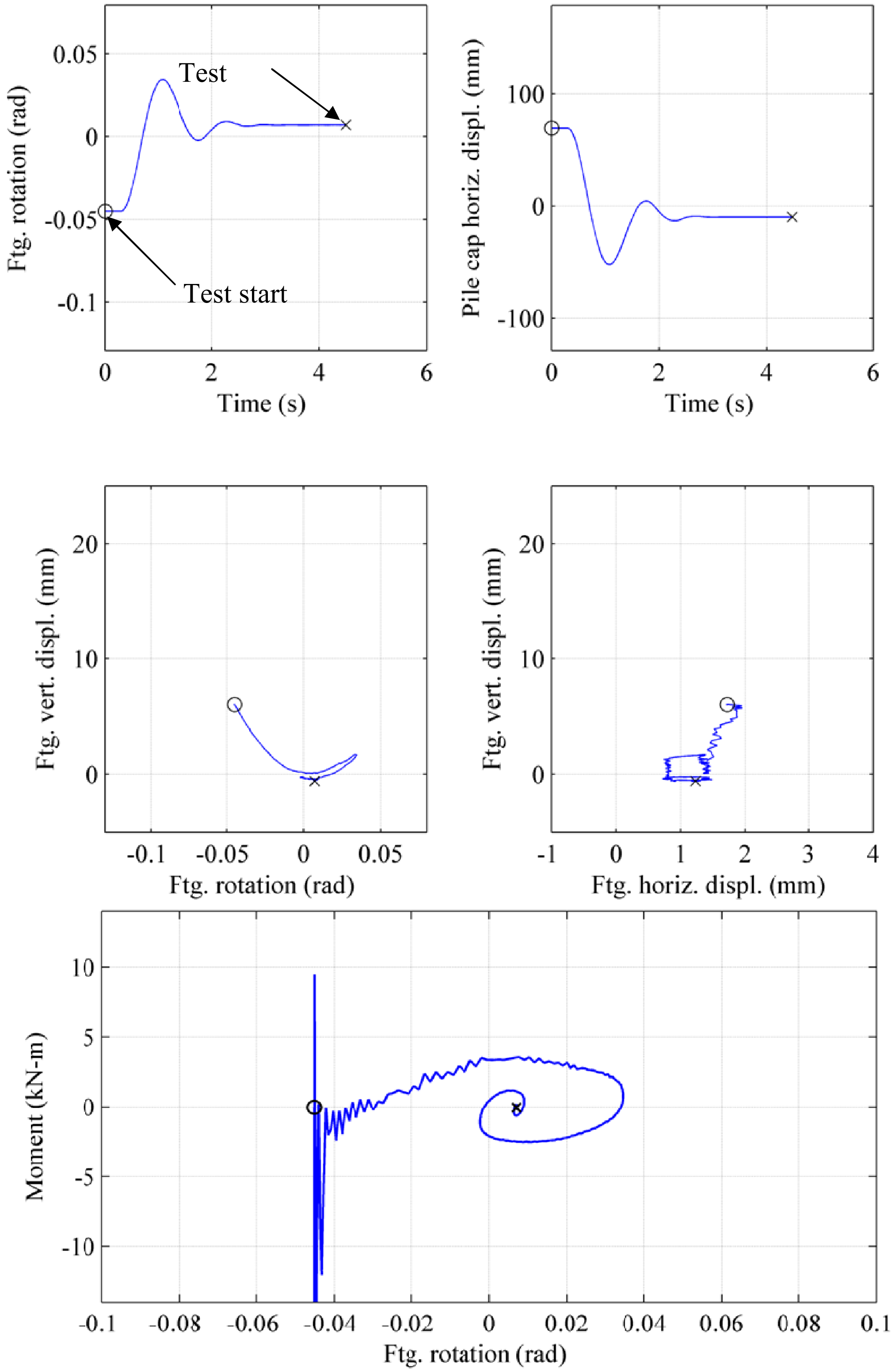

Figure 85. Response of footing at bottom center control point in free vibration test Snap09.

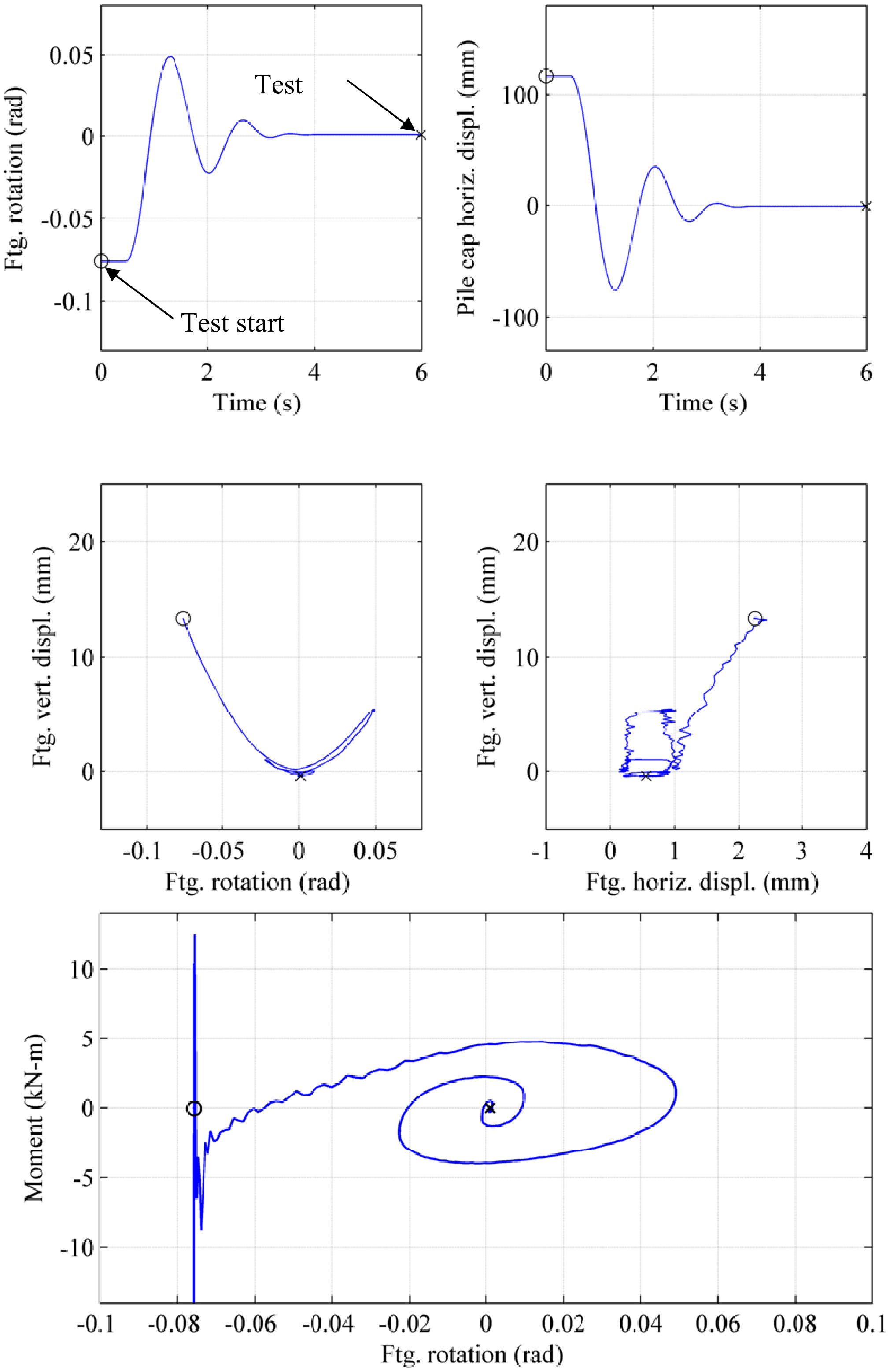

Figure 86. Response of footing at bottom center control point in free vibration test Snap10.

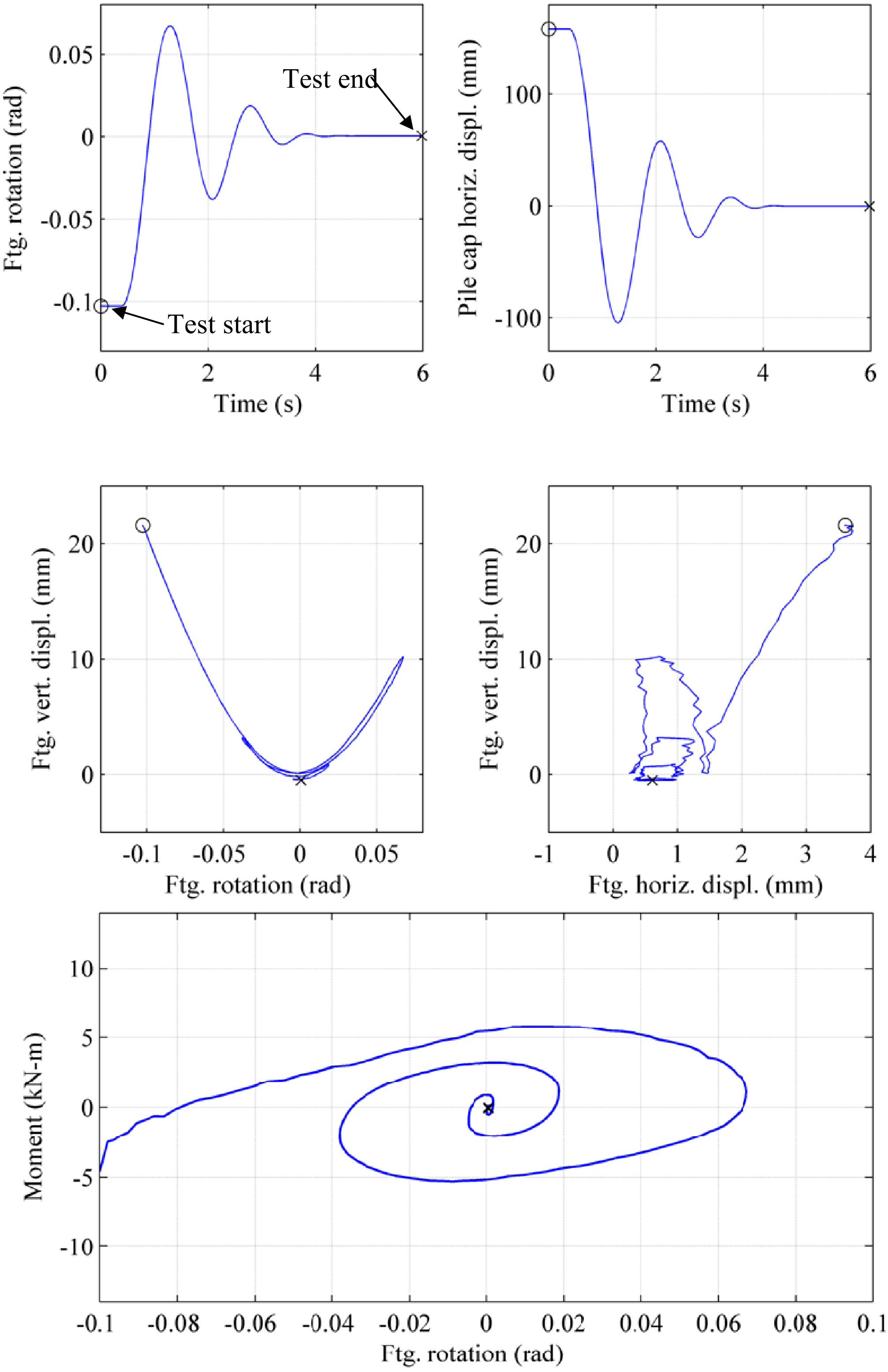

Figure 87. Response of footing at bottom center control point in free vibration test Snap11.

The moment in these plots are due to the inertial rotation of the rocking system. The moment was computed by using accelerometer measurements and the calculated inertial properties of the system. The spurious peaks near the start of the moment-rotation plots from Figures 77 - 87 are likely due to the sudden disengagement of the "snap" mechanism, which was described in Section 4.2.2.

Figure 88 shows that initial rotations of the footing's bottom center control point from free vibration snap tests generally increased as the test program progressed.

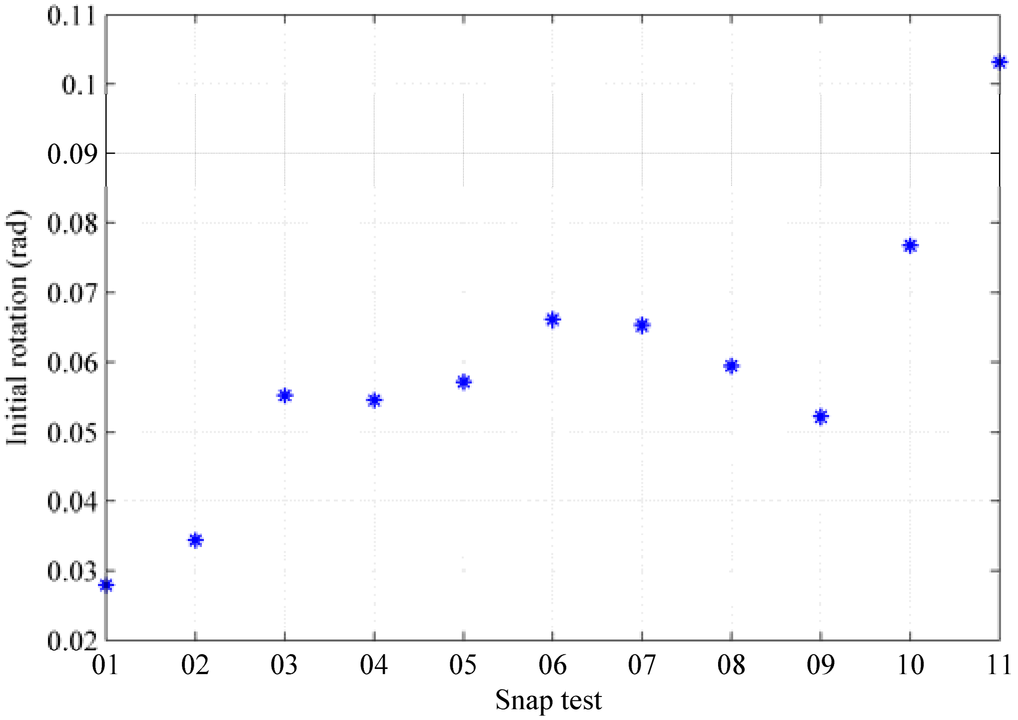

Figure 88. Initial rotation of footing's bottom center control point from snap tests.

Figure 90 and Figure 91 show the reduction of the rocking system period from the first to second peaks in free vibration under snap test loading. The decrease in the period of the system can be attributed to a softer soil-structure interface at larger initial rotations due to more soil yielding which also causes rounding of the loaded soil surface. The rounding of the soil surface is the basis for a recently developed rocking model known as the Contact Interface Model (CIM, Gajan and Kutter 2009), which was designed to provide nonlinear relations between cyclic loads and displacements at the footing-soil interface as described in Chapter 2. This model tracks the plastic deformations of a soil surface due to kinematics of the footing-soil system. Examination of the soil surface after both free vibration and slow lateral cyclic tests confirmed that the soil indeed adopted a rounded surface. A simple free body diagram helps capture this intuitive phenomenon, as in Figure 89a, and supported in the testing photos of Figure 89b and c. Figure 89a is a free body diagram taken from Gajan and Kutter (2010) depicting footing length *L*, vertical load *V*, ultimate moment *Mult*, critical contact length *Lc*, resultant force *R*, bearing pressure *qult*, and resultant eccentricity *e_max*.

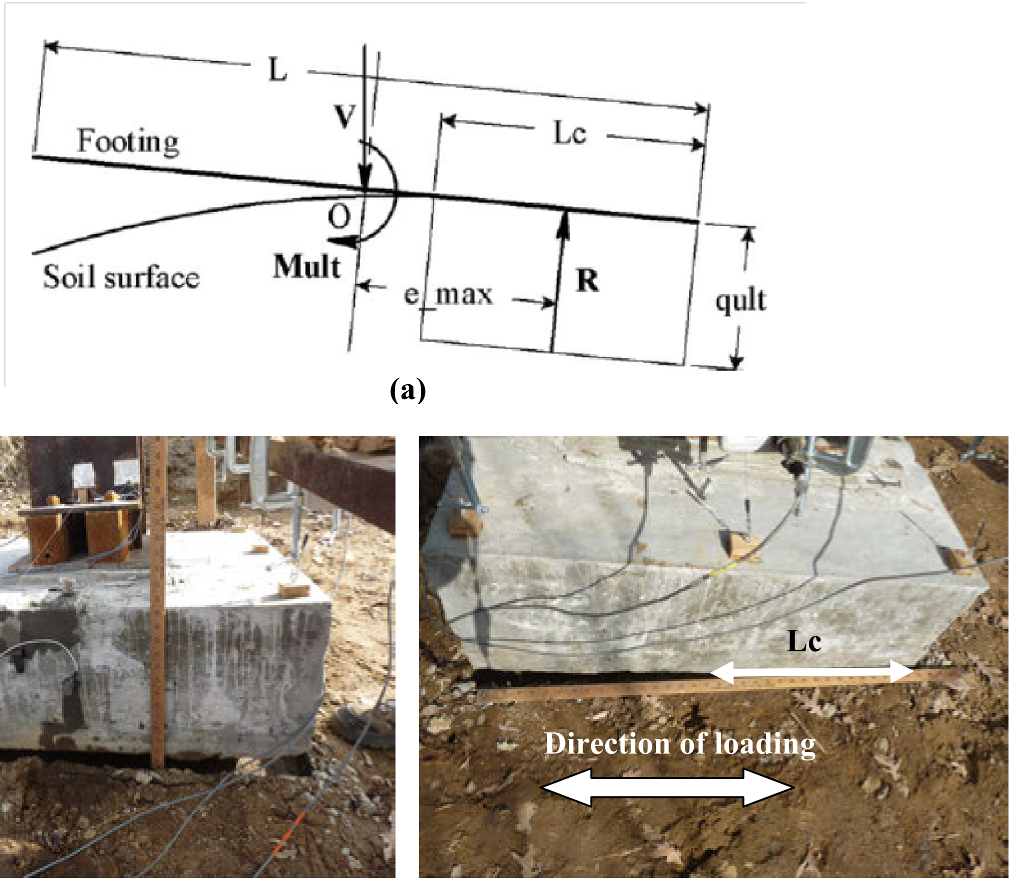

(a)

(b) **(c)**

Figure 89. Soil rounding. (a) Parameters of CIM; (b), (c) Measurement of uplift amplitude and contact length during testing.

While the CIM is conceptually simple, the implementation of the model OpenSees is not as straight forward. For this study, much time and effort was invested in an attempt to recreate analyses presented in published works utilizing the CIM with little to no success. This hurdle perhaps illustrates the need for a more simplified method to analyze load-deformation behavior of soil-footing systems in rocking due to cyclic loading.

In a broad sense, as free-vibration snap testing progressed from smaller to larger initial rotations (see Figure 88), the damped period of the system increased for the first period as illustrated in Figure 90. Increased period duration of rocking footings suggests that force demands imposed on a structure would likely be reduced (Bartlett 1976). Not only does the period change from test to test under various initial rotations, but also from initial to subsequent cycles within a test as illustrated in Figure 91. In fact, the period of the second cycle of a test was shown to have decreased by as much as 30 to 50% from the first cycle. Figure 90 shows the dramatic change in period from tests Snap01 to Snap08 and Snap09 to Snap11. Tests Snap01 to Snap08 were run consecutively as described inf the quasi-static cyclic tests. Figure 77 to Figure 87 present the motion and moment-rotation relationship of the footing at the bottom center control point from the free vibration snap tests.

Table 8. The period of the first cycle of Snap09 had increased by approximately 20% from that of Snap08, indicating that the stiffness of the system had been decreased due to plastic yielding and rounding of the contact interface.

The stiffness of the soil is affected by localized yielding, thus the natural frequency and period of the rocking footing-soil system are also affected. Assigning a period to the system is further clouded because the rocking footing makes impacts with soil at two rotation peaks. Since this is a field study on a heterogeneous natural soil deposit, each impact zone uniquely affects the dynamic properties of the rocking system.

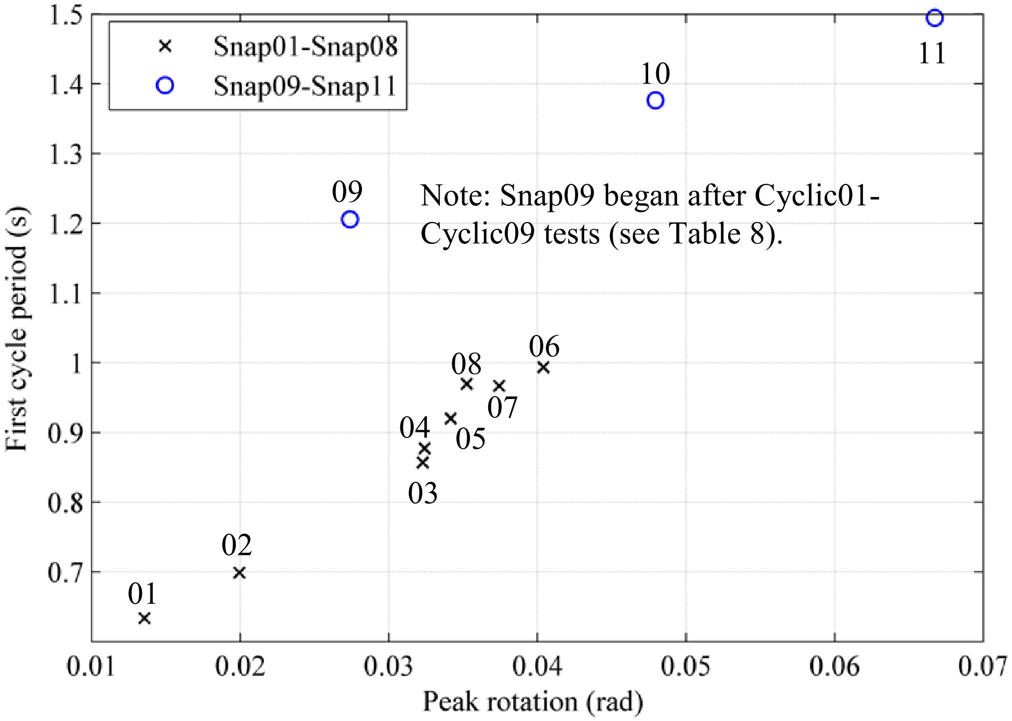

Figure 90. Period during first cycle of snap tests.

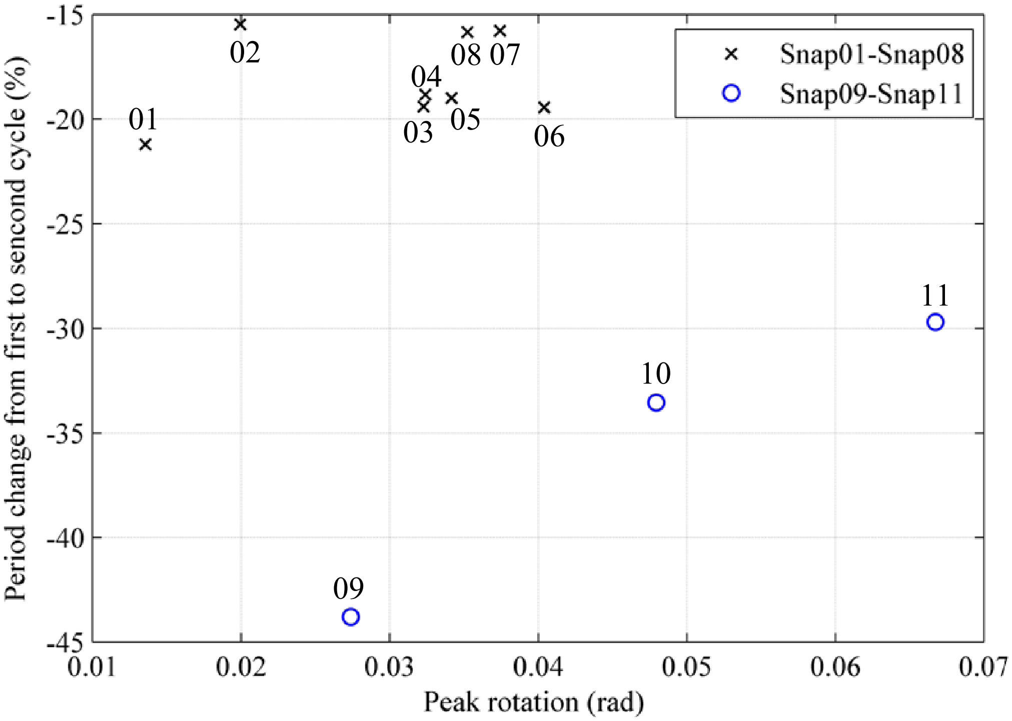

Figure 91. Period change from first to second cycles of snap tests.

Analysis from the snap test free vibration response also sheds light on the effects of damping on the rocking response of the system. Figure 77 to Figure 87 nearly shows straight lines between peak envelopes of the rotation-time or horizontal displacement-time curves, which indicate that the response of the system generally does not follow the logarithmic decrement of decay. Figure 92 gives the logarithmic ratio of initial peak rotation amplitude, x_0, to n^{th} peak rotation amplitude, x_n for a representative free vibration test to examine the decay of the rotational peaks. If the response was a true logarithmic decrement of decay, the curve in Figure 92 would be linear.

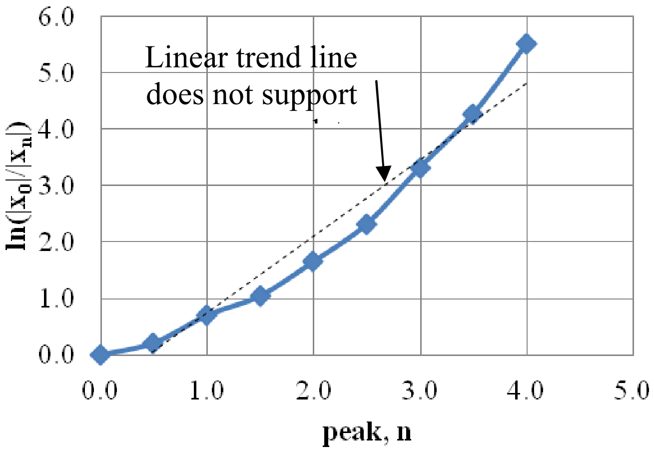

Figure 92. Peak footing rotation decay for test Snap06.

Classical equations of motion for free vibration can be used to estimate the amount of equivalent viscous damping in a system (see Figure 107 in Chapter 4). Though free vibration problems are free from external forcing, release from an initial displacement will cause inertial forces to develop as the system rocks. Damping can be calculated from the moment-rotation curves from each free vibration snap test shown in Figure 77 to Figure 87.

4.6.3 Quasi-static Cyclic Loading Tests

Figure 93 to Figure 100 present the data from the quasi-static cyclic tests in terms of moment-rotation, horizontal force-horizontal displacement, vertical displacement-rotation, and vertical displacement-horizontal displacement.

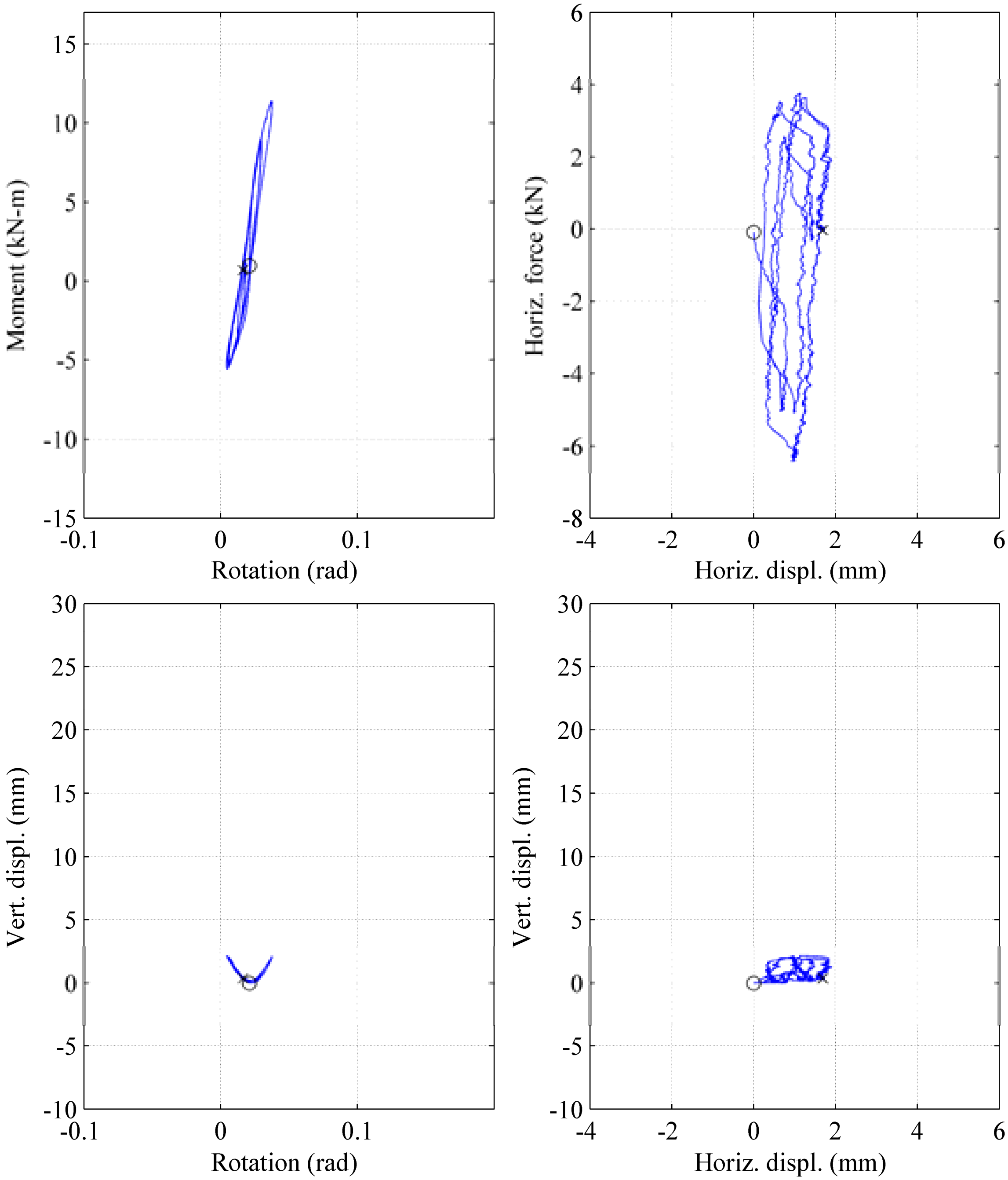

Figure 93. Footing at bottom center control point in quasi-static cyclic test Cyclic01.

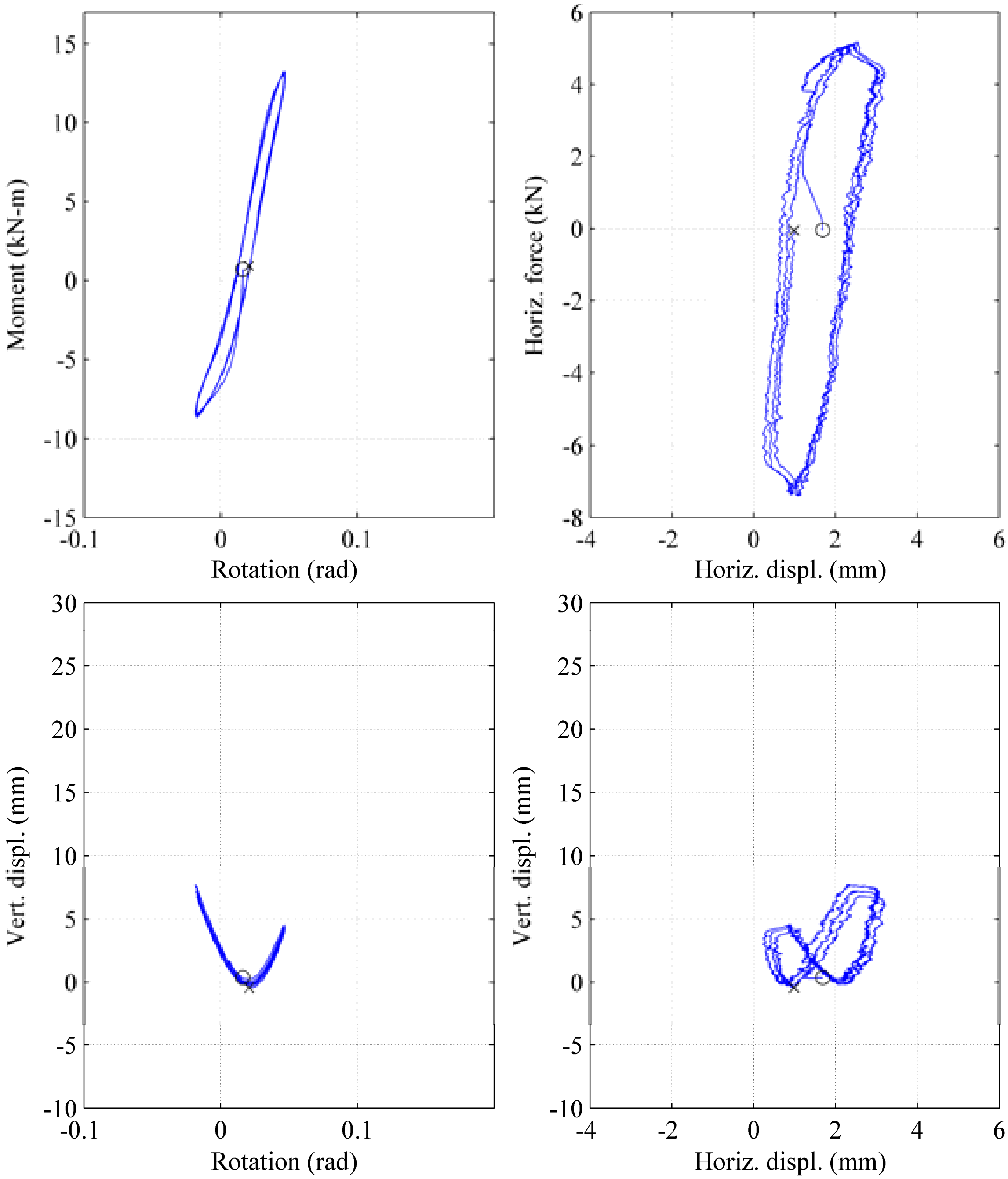

Figure 94. Footing at bottom center control point in quasi-static cyclic test Cyclic02.

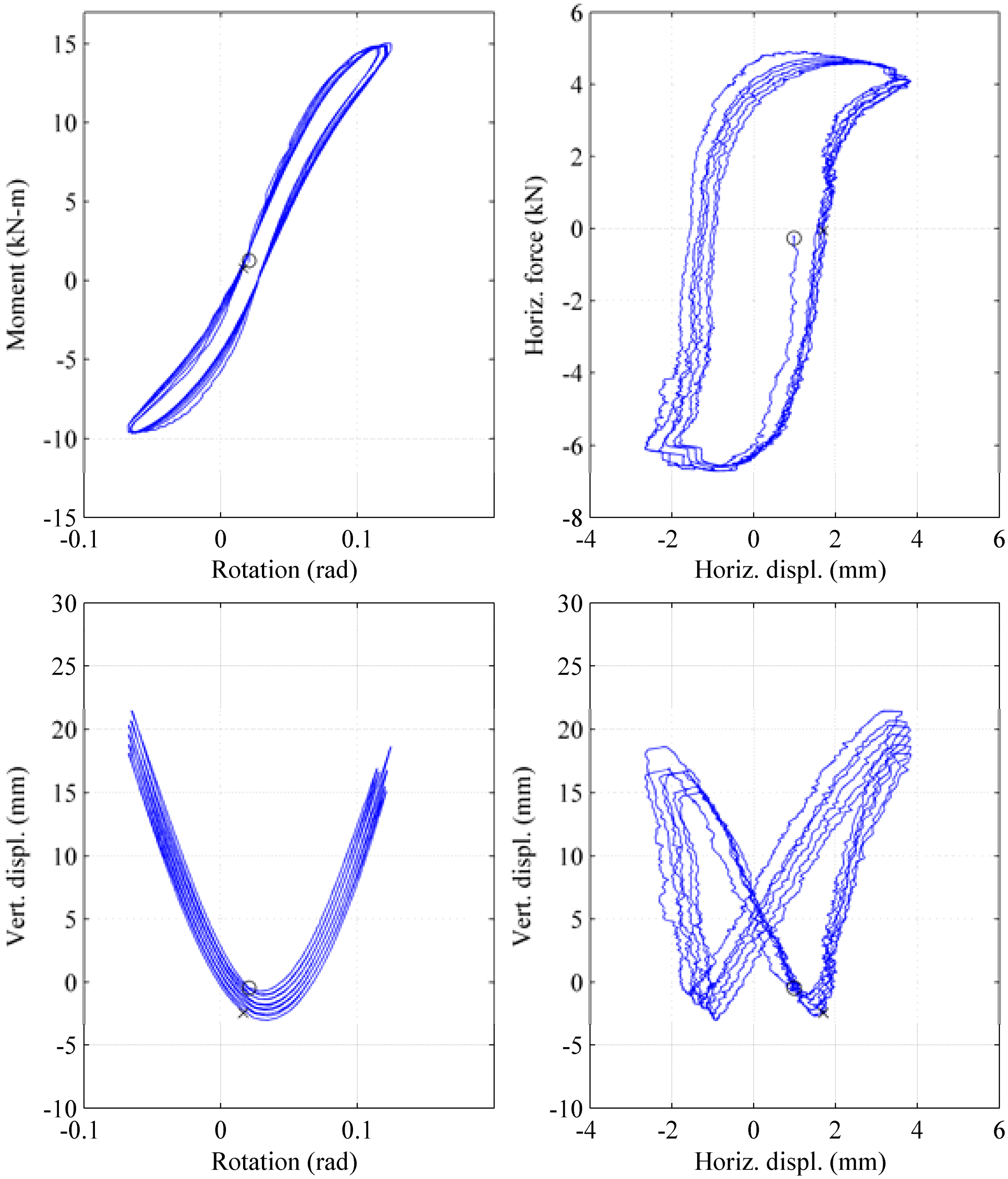

Figure 95. Footing at bottom center control point in quasi-static cyclic test Cyclic04.

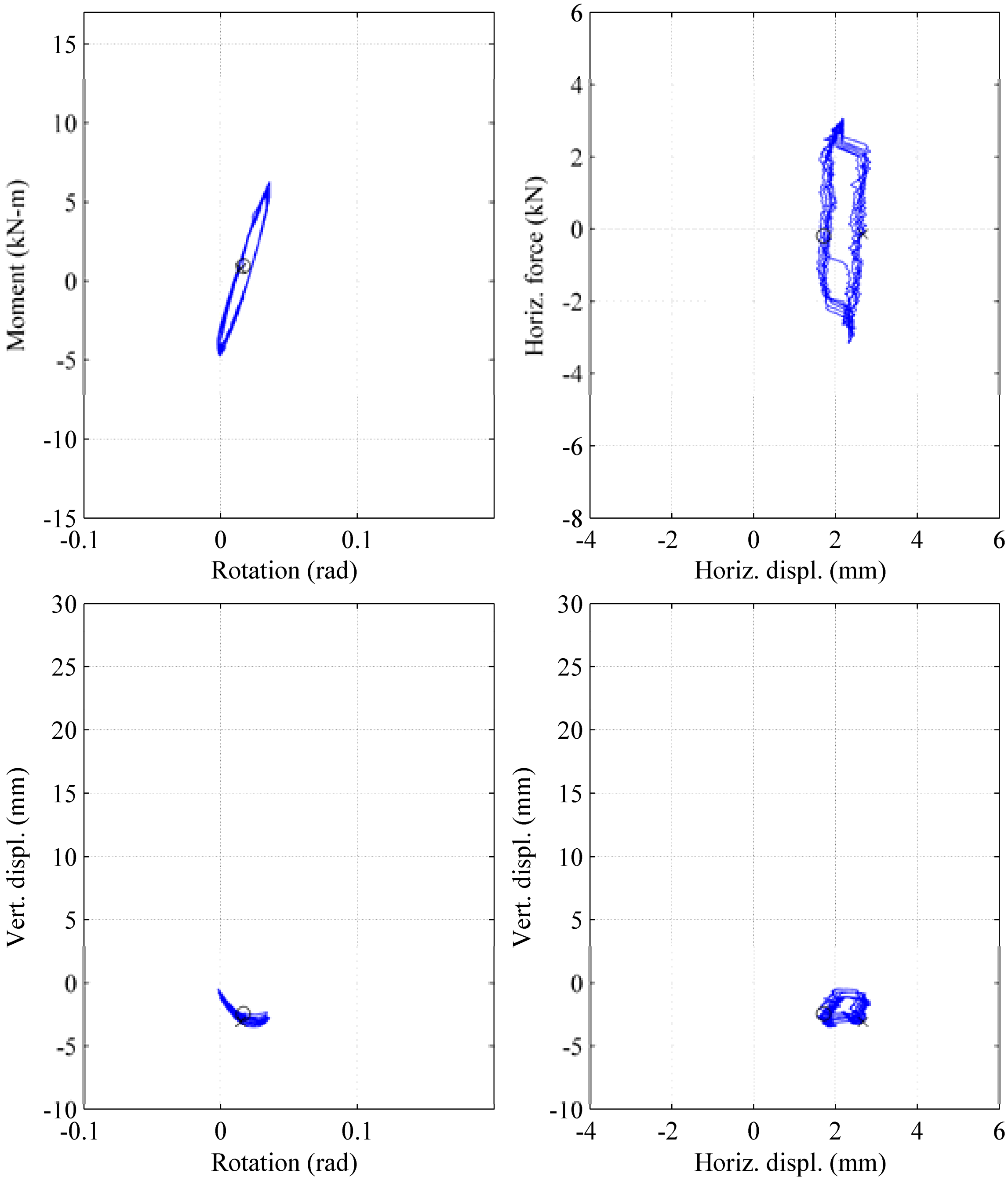

Figure 96. Footing at bottom center control point in quasi-static cyclic test Cyclic05.

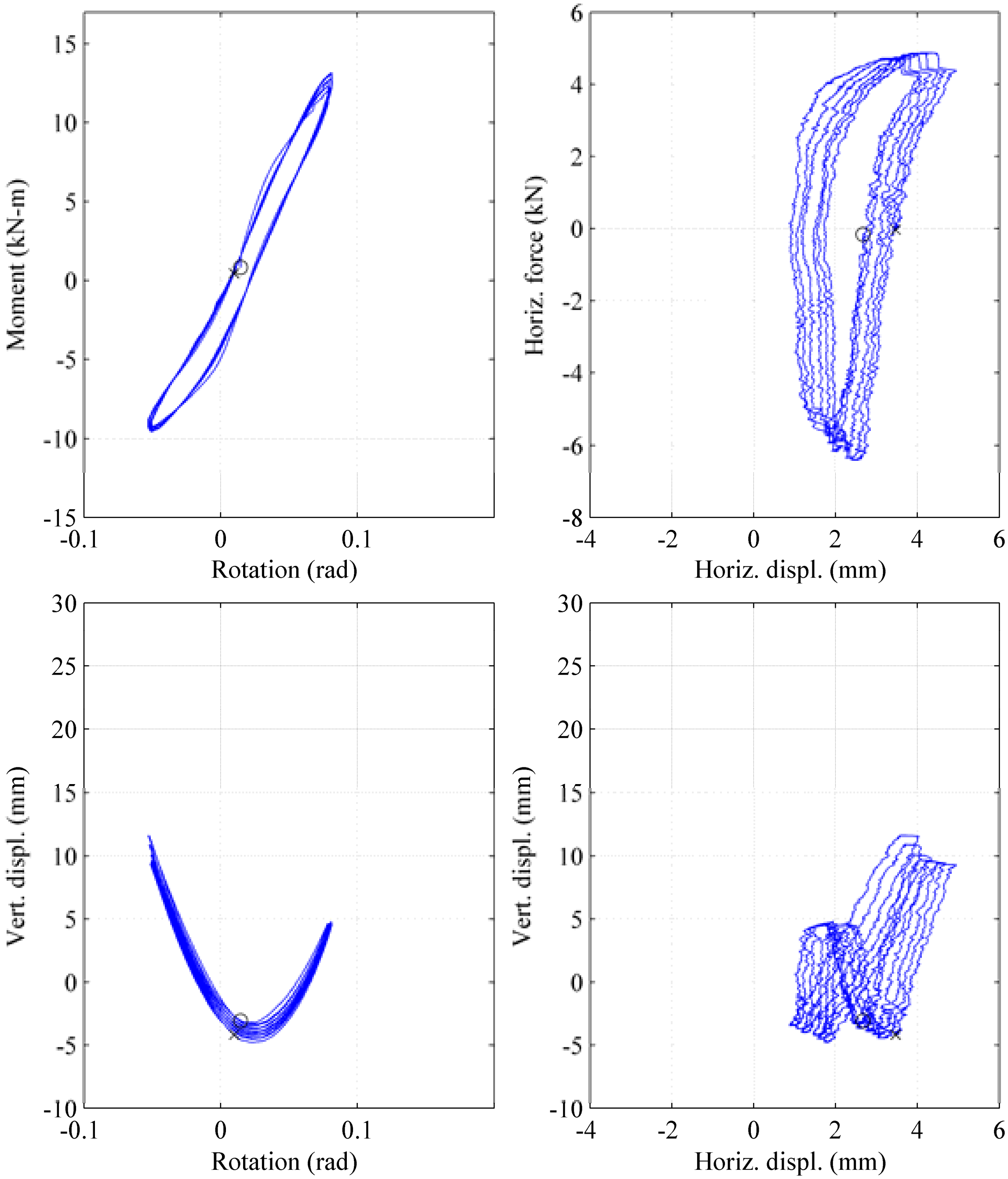

Figure 97. Footing at bottom center control point in quasi-static cyclic test Cyclic06.

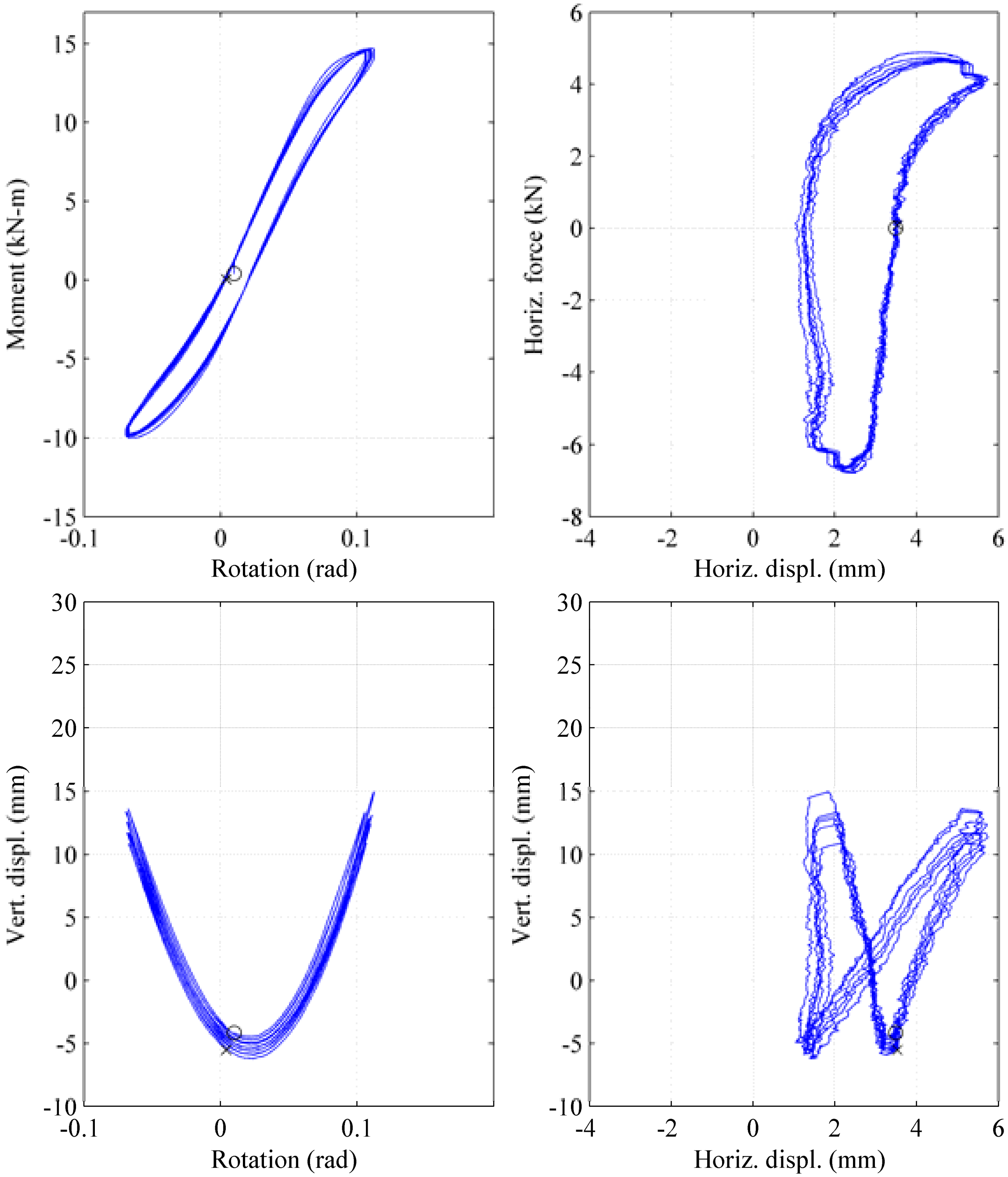

Figure 98. Footing at bottom center control point in quasi-static cyclic test Cyclic07.

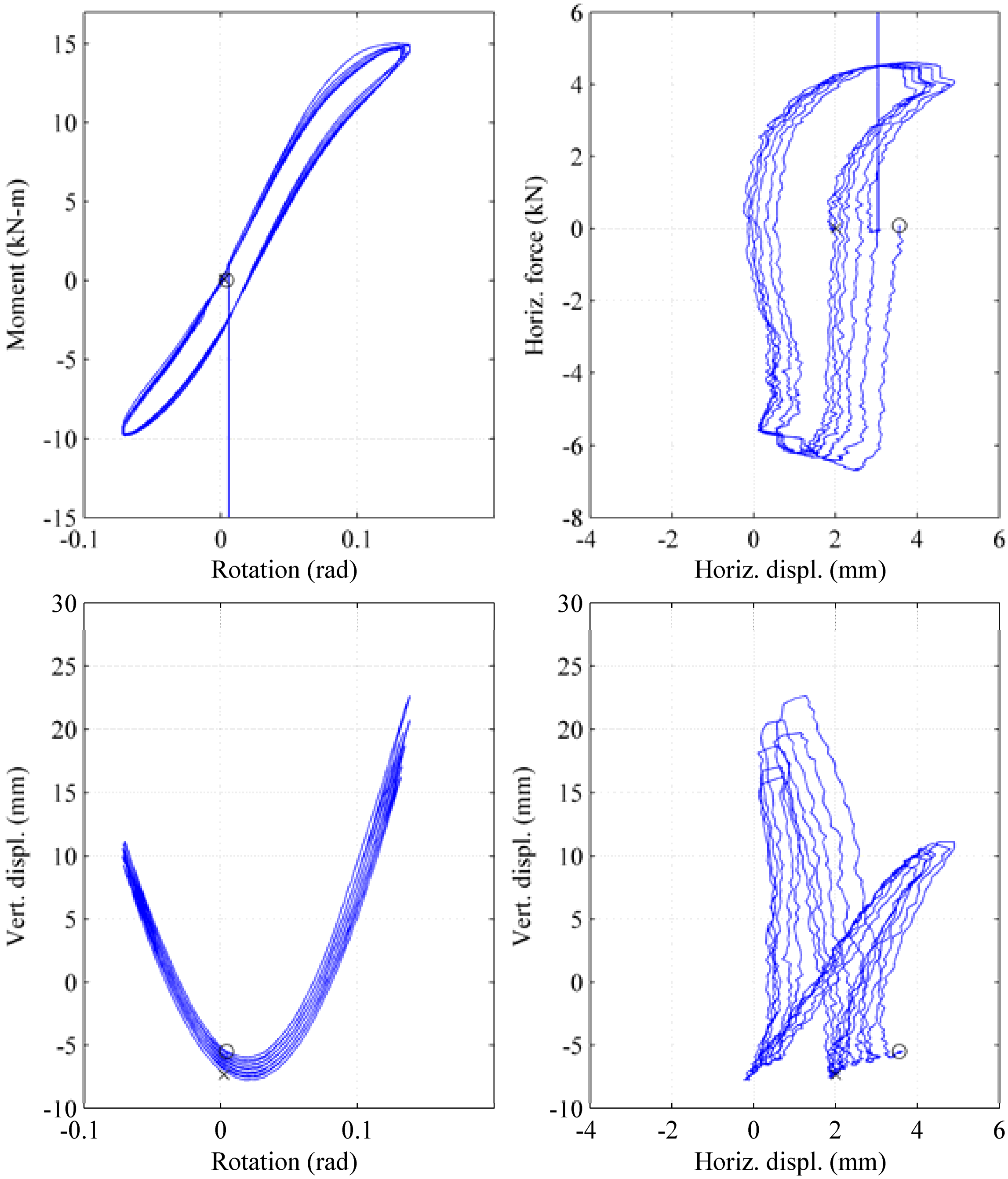

Figure 99. Footing at bottom center control point in quasi-static cyclic test Cyclic08.

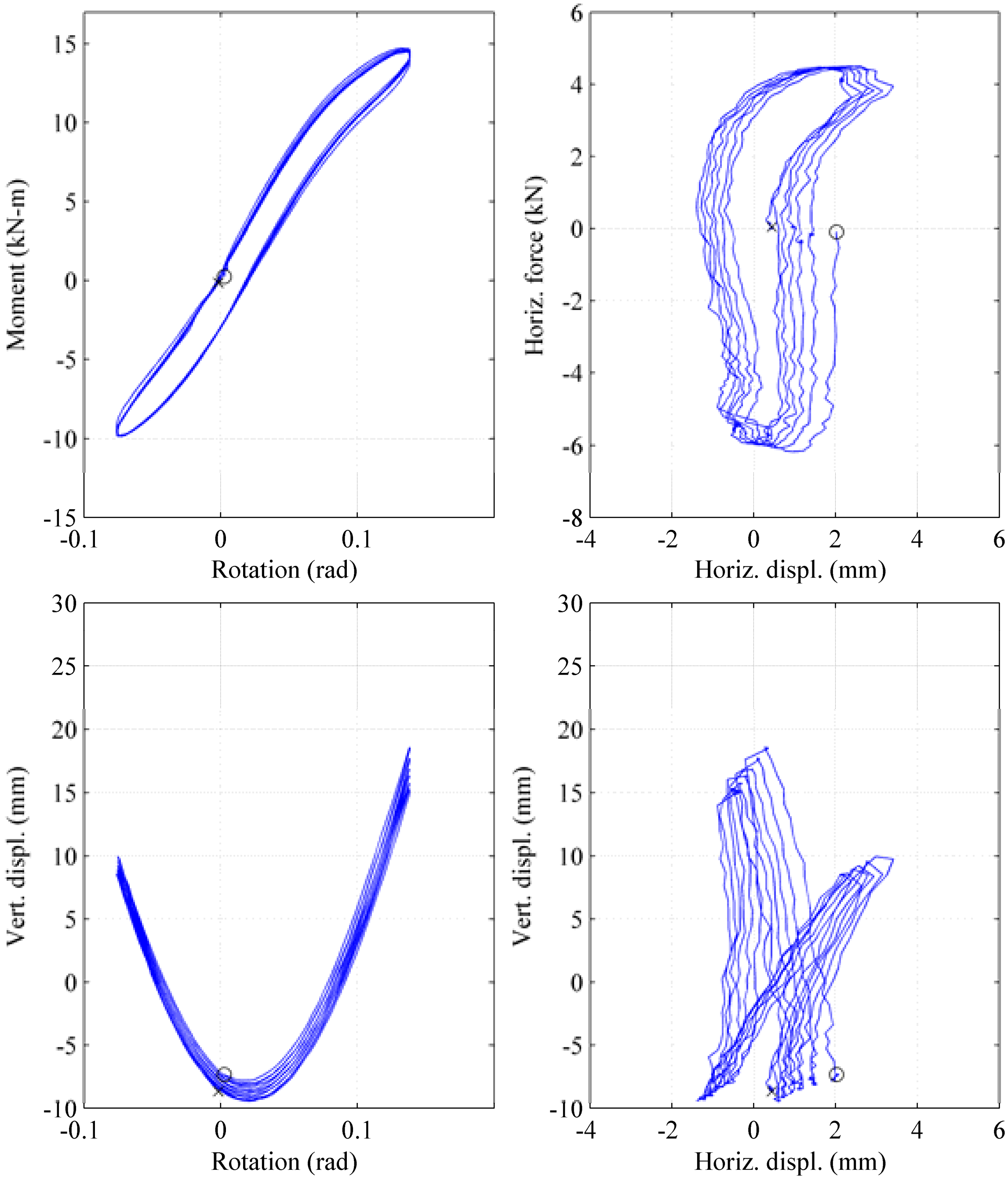

Figure 100. Footing at bottom center control point in quasi-static cyclic test Cyclic09.

It is useful to estimate the rotational stiffness from the initial elastic portion of the moment-rotation loops from the quasi-static cyclic tests herein. For reference, these stiffness values can then be compared with design methods such as the elastic stiffness given by Gazetas (1991) for the rotation of a surface footing;

$$k_{\theta,\max} = \frac{G_{MAX}}{1-\nu} I^{0.75} \left[3\left(\frac{L}{B}\right)^{0.15} \right] , \tag{4.9}$$

where *I* is the moment of inertia computed about the centroid of the footing base normal to the direction of loading, *v* is the Poisson's ratio of the soil (approximated as 0.25 for stiff clays, Gazetas 1991), *L* is the length of the footing, and *B* is the width of the footing. From Seed and Idriss (1970), the initial shear modulus, G_{max}, can be approximated to

$$G_{MAX} \simeq (1000 \text{ to } 2500) S_u \tag{4.10}$$

for a very stiff clay. Based on previous cone penetration tests at the Spangler test site by Shelman (2009), the undrained shear strength, S_u, is about 1000 kPa at the "equivalent" depth of the zone of influence for a square footing on an inhomogeneous soil deposit. Gazetas (1991) shows that the "equivalent" depth of the zone of influence for the rocking mode of vibration can be approximated as

$$\bar{z} = \frac{B}{6} , \tag{4.11}$$

where *z* is the "equivalent" soil depth and *B* is the footing width.

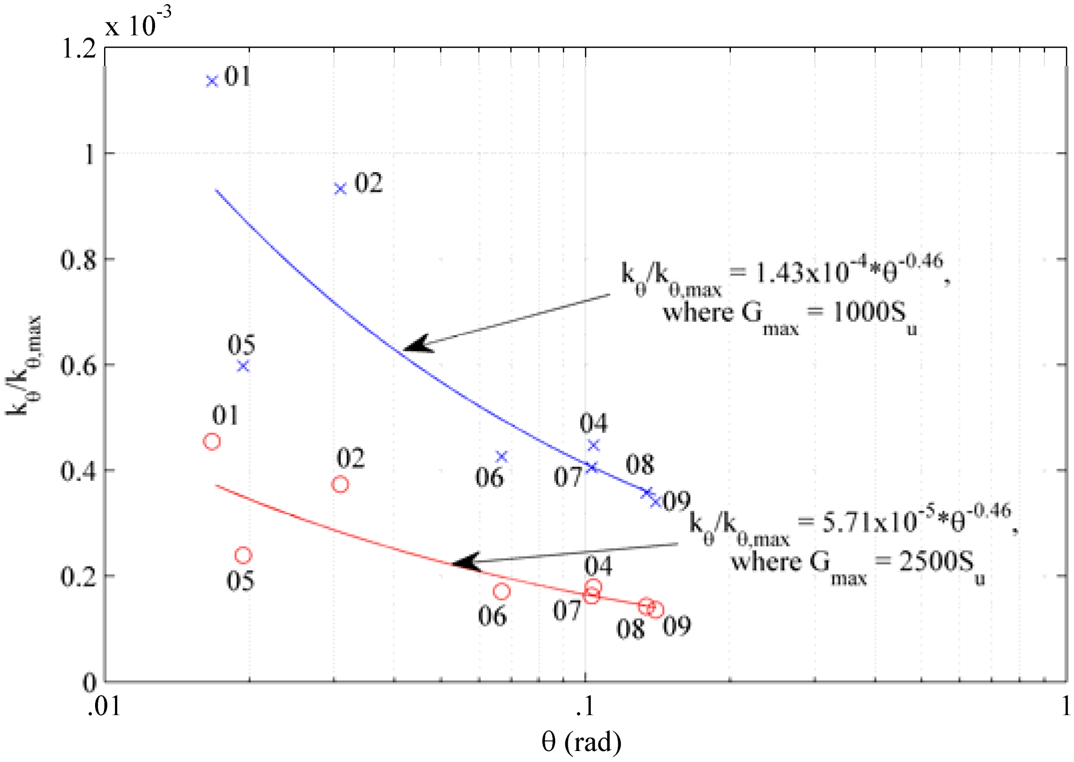

Figure 101. Rotational stiffness degradation.

Figure 101 shows k_θ normalized by $k_{\theta,max}$ of Equation (4.9) for each cyclic test performed (data for Cyclic03 was lost). The data from the cyclic tests were normalized against two levels of $k_{\theta,max}$, according to the limits of the estimated correlation of G_{max} with regard to S_u. A mean stiffness reduction trend was computed for each level of rotational stiffness, giving

$$\frac{k_\theta}{k_{\theta,\max}} = 1.43\times10^{-4}\left(\theta^{-0.46}\right), \quad G_{\max} = 1000 S_u \tag{4.12}$$

and

$$\frac{k_\theta}{k_{\theta,\max}} = 5.71\times10^{-5}\left(\theta^{-0.46}\right), \quad G_{\max} = 2500S_u \quad . \tag{4.13}$$

These initial elastic rotational stiffness degradation relationships for stiff clay should be used cautiously, as the database of experimentation is currently limited. The rotational stiffness degradation for stiff clays is a topic worthy of further study and experimentation, where different types of clays, rotation levels, footing sizes, and embedment configurations could be explored. A similarly broad study has already been performed for shallow footings on sand by Gajan, et al. (2004), where a recommended stiffness reduction trend was shown to be

$$\frac{k_\theta}{k_{\theta,\max}} = 3.0\times10^{-3}\left(\theta^{-0.6}\right) \quad . \tag{4.14}$$

Figure 102 presents the failure envelopes for all cyclic tests performed in this study. These curves represent the moment-rotation and horizontal force-horizontal displacement relationships as the quasi-static cyclic tests subjected the soil-footing system to increasing rotations/displacements.

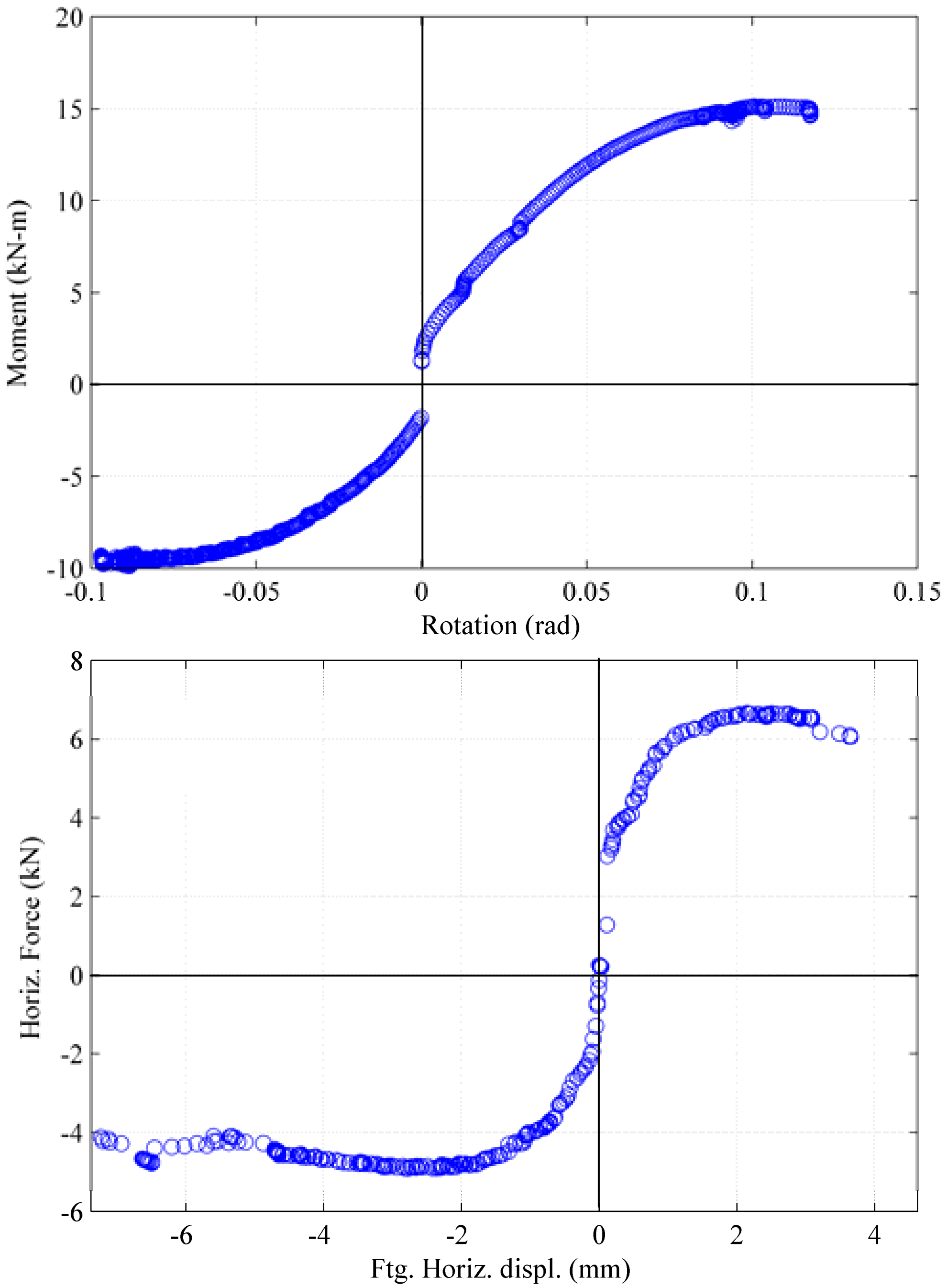

Figure 102. Failure envelopes for all cyclic tests performed in this study.

From Figure 93 to Figure 100, the moment-rotation plots show the amount of hysteretic energy dissipated at the interface of the footing with the soil. The results from the figures indicate that each test maintained moment capacity. Moment capacity did not reduce with regard to number of cycles or amplitude of rotation. As Figure 103 reveals, the initial elastic secant rotational stiffness decreases as amplitude of rotation increases. This degradation in rotational stiffness is associated with the inelastic soil response as testing progresses to higher rotation levels.

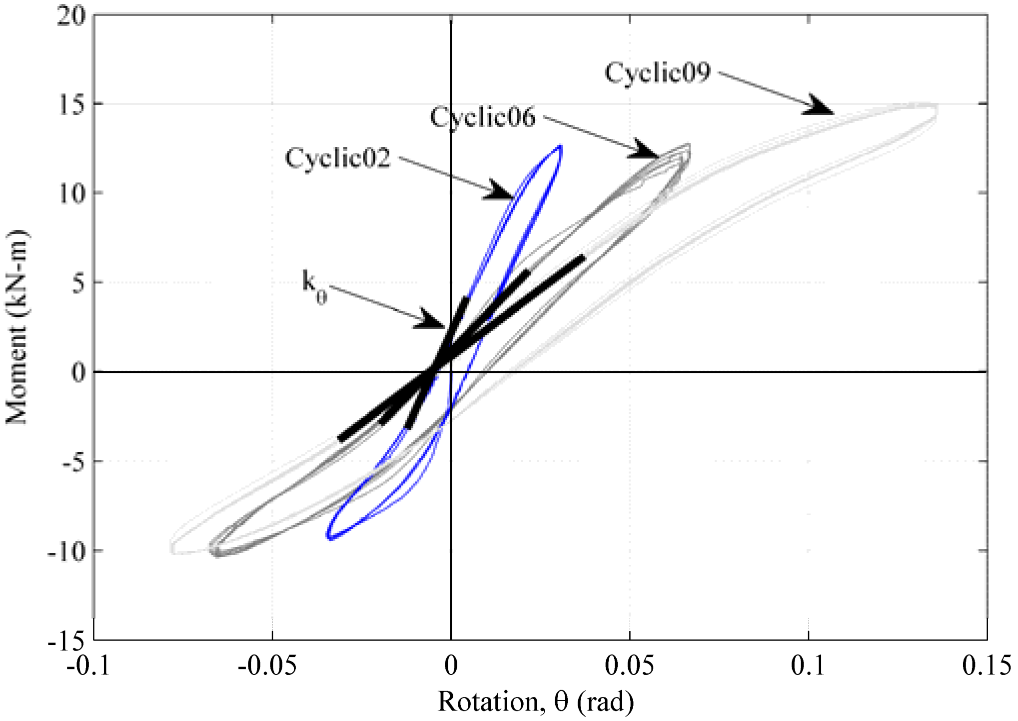

Figure 103. Moment-rotation plot at footing base control point showing rotation stiffness degradation due to cumulative rounding and plastic yielding.

The vertical displacement-rotation plot, as shown in Figure 104, helps illustrate the contact problem with rocking foundations. The rocking footing experiences uplift near peak rotations and a portion of the footing base loses contact with the soil. Yielding of the soil takes place as the footing loses contact with the soil while the remaining portion in contact attempts to maintain static equilibrium. As the footing uplifts and soil yielding continues to work in tandem, the cyclic lateral loading causes rounding of the soil surface. Rounding of the soil surface implies that gaps form near both pivot points of the rocking footing. These gaps contribute to the nonlinear moment-rotation relationship and the degradation of rotational stiffness. The vertical displacement-rotation relationship also shows the amount of permanent vertical settlement accumulated throughout a test. Each quasi-static lateral cyclic test lasted between three and six cycles, which does not provide opportunity for much vertical deformation to be witnessed from a single test. However, as shown in Figure 104, the rate of vertical deformation decreases as the footing settles deeper. As the footing settles, the vertical stiffness is increasing as the embedment depth and compaction increase.

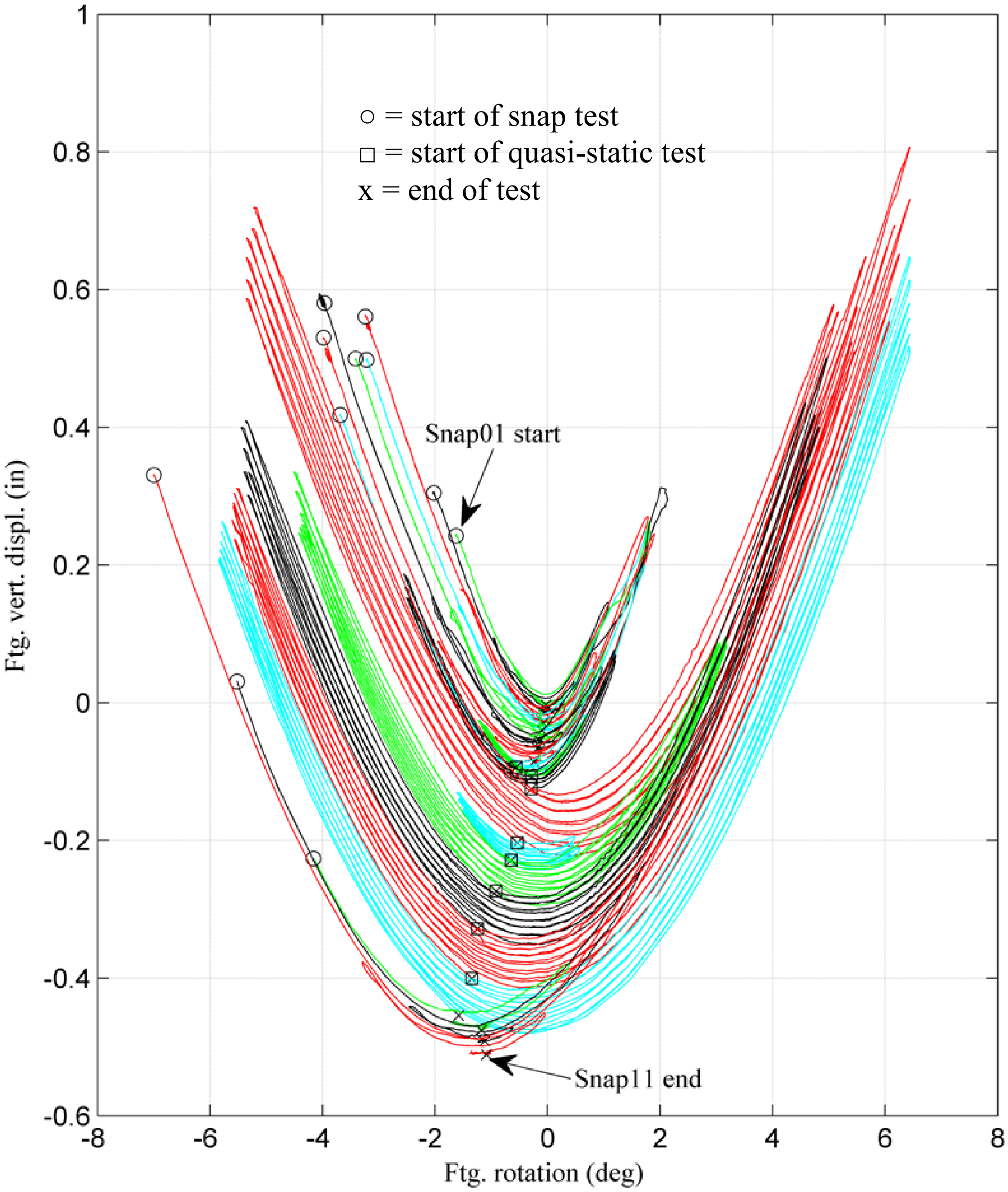

Figure 104. Cumulative vertical displacement-rotation plot throughout all free vibration (snap) tests and quasi-static cyclic tests performed in this study.

Similar to the maintaining of moment capacity, the horizontal force-horizontal displacement relationship clearly shows that horizontal force does not reduce relative to number of cycles or amplitude of displacement. Another interesting observation is that horizontal displacement remains relatively unchanged until the peak shear capacity is reached, at which point the footing began to slide.

The butterfly shapes of the vertical displacement-horizontal displacement plot shows the coupling relationship of uplift and sliding. The base of the butterfly shows the two points at which the base-center control point of the footing lands, depending on which side is being uplifted.

4.7 Analytical Model

As mentioned previously, several analytical models have been developed to capture the dynamic force-displacement behavior of rocking at the soil-structure interface. Researchers such as Gajan, et al. (2005) have investigated the use of experimental data to develop beam-on-nonlinear-Winkler-foundation models (BNWF) and contact interface models (CIM). These models each have their own advantages, disadvantages, and limitations. The BNWF is based on Emil Oskar Winkler's work from the 19th century. This approach approximates the soil-structure interface as a series of discrete, nonlinear elements composed of springs and dashpots. The CIM takes a finite element approach by defining a soil-structure macro-element that tracks the soil stress distribution and footing displacements at discrete points along a footing. Both models are dependent upon defining the stiffness of the soil for shallow foundation systems. As with many theoretical models of soil systems, researchers and design professionals are ever striving to strike a balance between accuracy and practicality. The common thought is that a more rigorous model with detailed representation of all observed physical mechanisms would lead to better overall system response. However, the uncertainty of defining such input parameters can often cloud the behavior of the system. For example, using the CIM in OpenSees could not be recreated even when using identical inputs as detailed in the Appendices of the reports (e.g., Gajan et al. 2008).

As a simpler alternative, an Experimental Nonlinear Spring and Dashpot (ENSD) model will be presented in this section to offer a more practical approach to the rocking foundation system compared to the CIM and BNWF. As the name suggests, the ENSD develops a nonlinear stiffness model of the rotational and horizontal displacement degrees of freedom calibrated from experimental virgin quasi-static cyclic tests. The hysteretic damping of the system response is approximated as equivalent viscous damping. The mass of the system represents the inertial term of the equation of motion and can be closely approximated, if not directly measured, by knowing the weights and geometries of the components of the system.

The first step to using the ENSD model is to express the rotational and horizontal stiffness in terms of nonlinear springs. For this purpose, Figure 105 shows a virgin backbone curve for the rotational and horizontal stiffness, assembled from all eight slow cyclic tests.

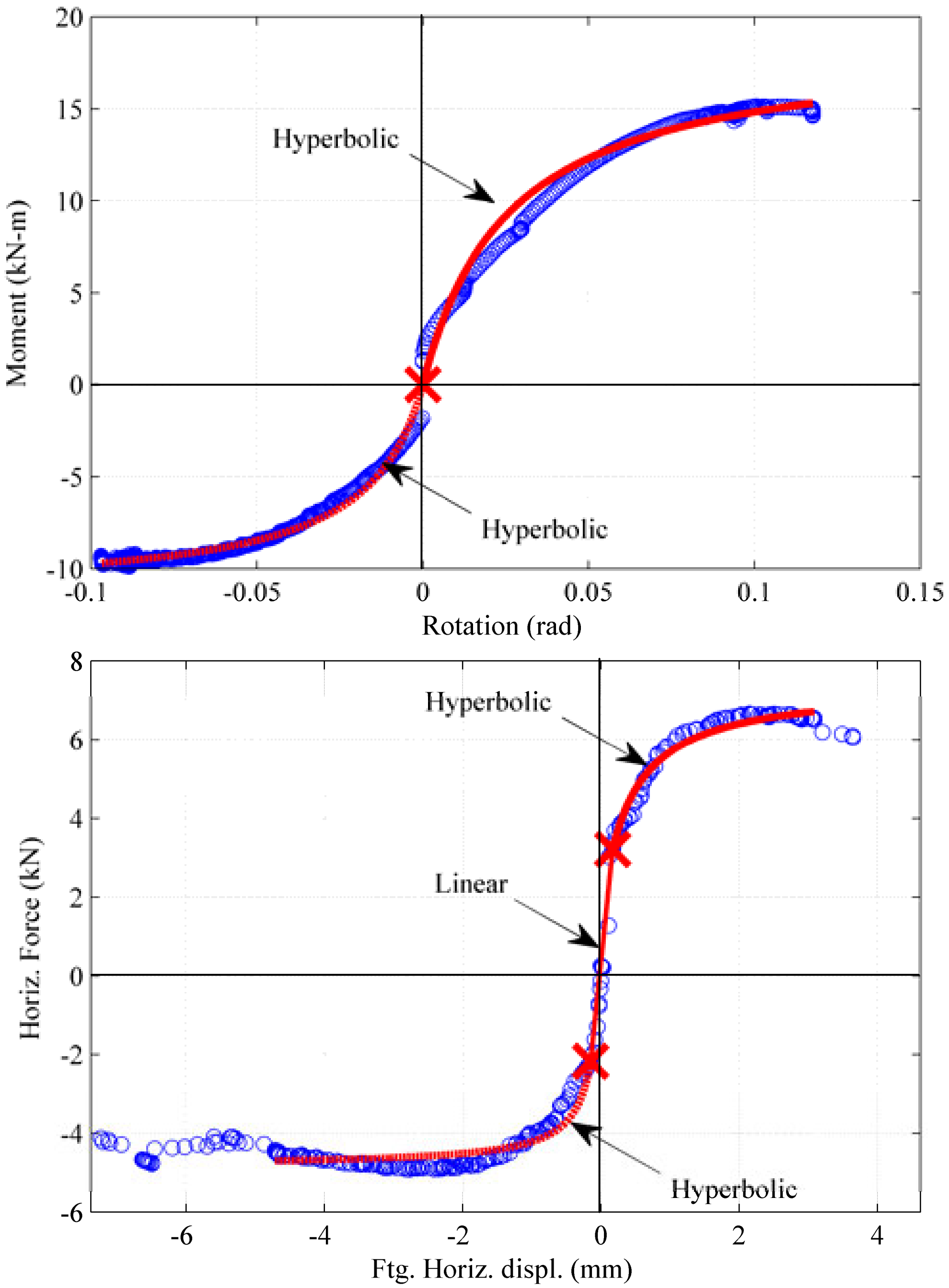

Figure 105. Soil-structure stiffness model (March 27, 2011).

Inspection of the rotational stiffness curve revealed that the experimental data could approximately be described in terms of a hyperbolic fit of the following form:

$$M = \frac{\theta}{m\theta + b}, \tag{4.14}$$

where *m* and *b* are slope and intercept regression coefficients when the experimental data is transformed to the linearly trending *θ*/*M* against *θ*, as shown in Figure 106.

The shape of the horizontal stiffness backbone curve clearly shows that a simple hyperbolic fit would be insufficient to capture the actual behavior. At small displacements, the horizontal stiffness appears to be approximately linear. The hyperbolic fit becomes more appropriate outside small displacements as the soil begins to yield, then eventually slide. Thus, a nonlinear spring was defined by a linear trend line linking two hyperbolic fits. The yield points were determined by inspection of the experimental backbone curve and represent the transition from hyperbolic to linear behavior, as shown in Figure 105. The hyperbolic segments of the horizontal stiffness could approximately be described as:

$$H = \frac{(u - u_y)}{m(u - u_y) + b}, \tag{4.15}$$

where $(u - u_y)$ is the horizontal displacement beyond the yield point, *m*, and *b* are slope regression coefficients when the experimental data is transformed to the linearly trending $(u - u_y)/H$ against $(u - u_y)$ as shown in Figure 106.

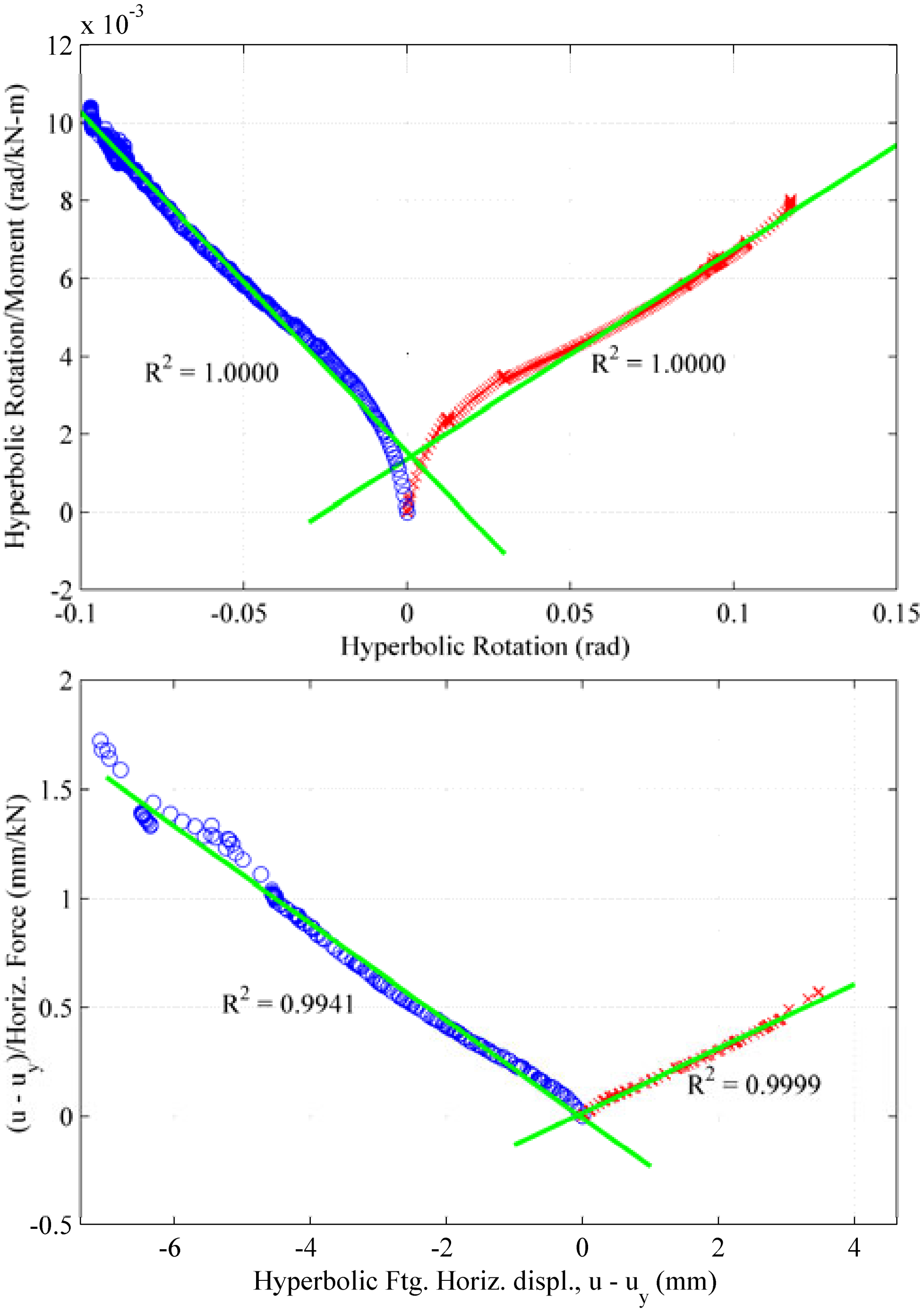

Figure 106. Quality of hyperbolic fit to rotational and horizontal stiffness curves.

This hyperbolic fit is analogous to the stress-strain relation of soils outlined by Hardin and Drnevich (1972). Because the rocking footing rotates about two different contact points (i.e. $\pm\theta$), a hyperbolic fit was computed for both directions of loading.

The damping characteristics of the ENSD model are expressed as a viscous dash pot, defined in terms of an equivalent viscous damping ratio. Equivalent viscous damping can be calculated using the classical approach of the ratio of area under experimental slow cyclic hysteresis loops to the area under the secant modulus triangle, see Figure 107. A number of techniques and approaches with varying complexity exist to express the type and amount of damping present in a system. The equivalent viscous damping approach was chosen for its wide acceptance with hysteresis curves from slow cyclic tests, such as those from cyclic triaxial or cyclic simple shear tests. The simplicity of the equivalent viscous damping approach is also consistent with the relatively practical nature of the ENSD model.

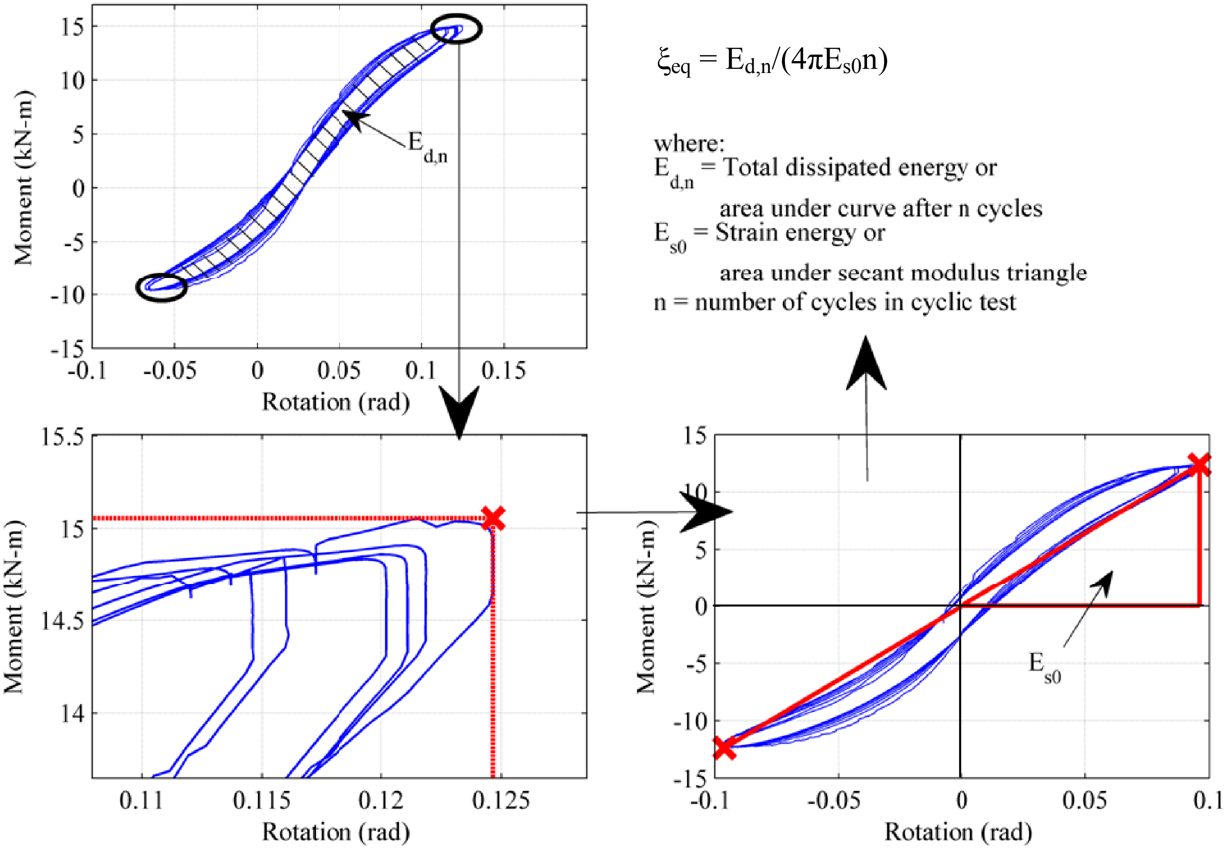

Figure 107. Calculation of Equivalent viscous damping from quasi-static cyclic tests.

Once the equivalent viscous damping terms have been defined by the moment-rotation and horizontal force-horizontal displacement hysteretic loops, a numerical method can be applied to solve the free vibration equations of motion for the dynamic free vibration snap tests. The free vibration equation of motion is shown in Equation (4.16).

$$m\ddot{x}(t) + c\dot{x}(t) + kx(t) = 0 \tag{4.16}$$

One of the simplest methods for numerical integration in time is the central difference method. The central difference method is based on finite difference expressions for the time derivatives of Equation (4.16). The time derivatives for velocity and acceleration are given in terms of constant time step *Δt*.

$$\dot{x}(t) = \frac{x(t+\Delta t) - x(t-\Delta t)}{2\Delta t} \tag{4.17}$$

$$\ddot{x}(t) = \frac{x(t+\Delta t) - 2x(t) + x(t-\Delta t)}{(\Delta t)^2} . \tag{4.18}$$

Equations (4.17) and (4.18) can be substituted into Equation (4.16) to give

$$m\frac{x(t+\Delta t) - 2x(t) + x(t-\Delta t)}{(\Delta t)^2} + c\frac{x(t+\Delta t) - x(t-\Delta t)}{2\Delta t} + kx(t) = 0 \tag{4.19}$$

where *x(t-Δt)* and *x(t)* are assumed to be known from implementation of the previous time step. Rearranging Equation (4.19) gives

$$\left[\frac{m}{(\Delta t)^2}+\frac{c}{2\Delta t}\right]x(t+\Delta t)=-\left[\frac{m}{(\Delta t)^2}-\frac{c}{2\Delta t}\right]x(t-\Delta t)-\left[k-\frac{2m}{(\Delta t)^2}\right]x(t) \quad . \tag{4.20}$$

The next time step can then be solved by

$$x(t+\Delta t)=\frac{-\left[\frac{m}{(\Delta t)^2}-\frac{c}{2\Delta t}\right]x(t-\Delta t)-\left[k-\frac{2m}{(\Delta t)^2}\right]x(t)}{\left[\frac{m}{(\Delta t)^2}+\frac{c}{2\Delta t}\right]} \tag{4.21}$$

Equation (4.21) shows how to solve for the displacement at the next time step *t+Δt* in terms of known displacements at previous time step *t-Δt* and current time step *t*. To solve for the displacement at the first time step t_1, displacements from time steps t_0 and t_{-1} are required. Displacement at t_0 is given as part of the initial conditions. To determine displacement at t_{-1} Equations (4.17) and (4.18) are written for time step t_0 in Equations (4.22) and (4.23)

$$\dot{x}(t_0)=\frac{x(t_1)-x(t_{-1})}{2\Delta t} \tag{4.22}$$

$$\ddot{x}(t_0)=\frac{x(t_1)-2x(t_0)+x(t_{-1})}{(\Delta t)^2} \quad . \tag{4.23}$$

Solving for $x(t_1)$ in Equation (4.22) and substituting it into Equation (4.23) gives

$$x(t_{-1}) = x(t_0) - \Delta t\left[\dot{x}(t_0)\right] + \frac{(\Delta t)^2}{2}\ddot{x}(t_0) \quad . \tag{4.24}$$

Since the initial velocity $\dot{x}(t_0)$ is also given, Equation (4.24) can be rearranged to solve for the acceleration at time 0 ($t_0 = 0$);

$$\ddot{x}(t_0) = \frac{-c\dot{x}(t_0) - kx(t_0)}{m} \quad . \tag{4.25}$$

An equation of motion can be written to include both rotation and horizontal displacement following the form of Equation (4.16),

$$\begin{bmatrix} m & 0 \\ 0 & J \end{bmatrix}\begin{Bmatrix} \ddot{x} \\ \ddot{\theta} \end{Bmatrix} + \begin{bmatrix} c_x(x) & 0 \\ 0 & c_\theta(\theta) \end{bmatrix}\begin{Bmatrix} \dot{x} \\ \dot{\theta} \end{Bmatrix} + \begin{bmatrix} k_{xx}(x) & k_{x\theta}(\theta) \\ k_{\theta x}(x) & k_{\theta\theta}(\theta) \end{bmatrix}\begin{Bmatrix} x \\ \theta \end{Bmatrix} = \begin{Bmatrix} 0 \\ 0 \end{Bmatrix} \quad , \tag{4.26}$$

where *m* and *J* are the mass and mass moment of inertia, respectively, of the rocking system shown in Figure 60. The inertial components of the system were not directly measured but computed based on the geometry of the components and widely accepted material densities for steel and concrete. The inertial components of the hydraulic mass shaker were provided by the manufacturer. The computed inertial properties of the rocking system are shown in Table 9. It should be noted that coupling terms $k_{\theta x}$ and $k_{x\theta}$ should be small for surface footings due to lack of lateral and overburden soil resistance and were therefore neglected in the ENSD model predictions Allowing for coupling terms in the stiffness and damping matrices by analyzing the hysteresis loops of moment-horizontal displacement and horizontal force-rotation might improve the predictions of the free-vibration tests.

Table 9. Computed inertial properties of rocking system.

Property	Value
Mass, *m*	3057.22 kg
Radius of gyration, *R*	1.341 m
Mass moment of inertia, *J*	5497.74 kg-m^2

The central difference method can be implemented in computer programs rather simply to solve for the footing's rotation and horizontal displacement in time, while allowing for the nonlinear moment-rotation and horizontal force-horizontal displacement relations shown in Figure 105. The ENSD model calibrated to the cyclic tests was then used to predict the responses of the free vibration snap tests. The measured displacement at time of release ($t = 0$) was prescribed as the initial displacement in the model, with zero velocity. Figure 108 to Figure 118 show simulations of experimental tests using the ENSD model.

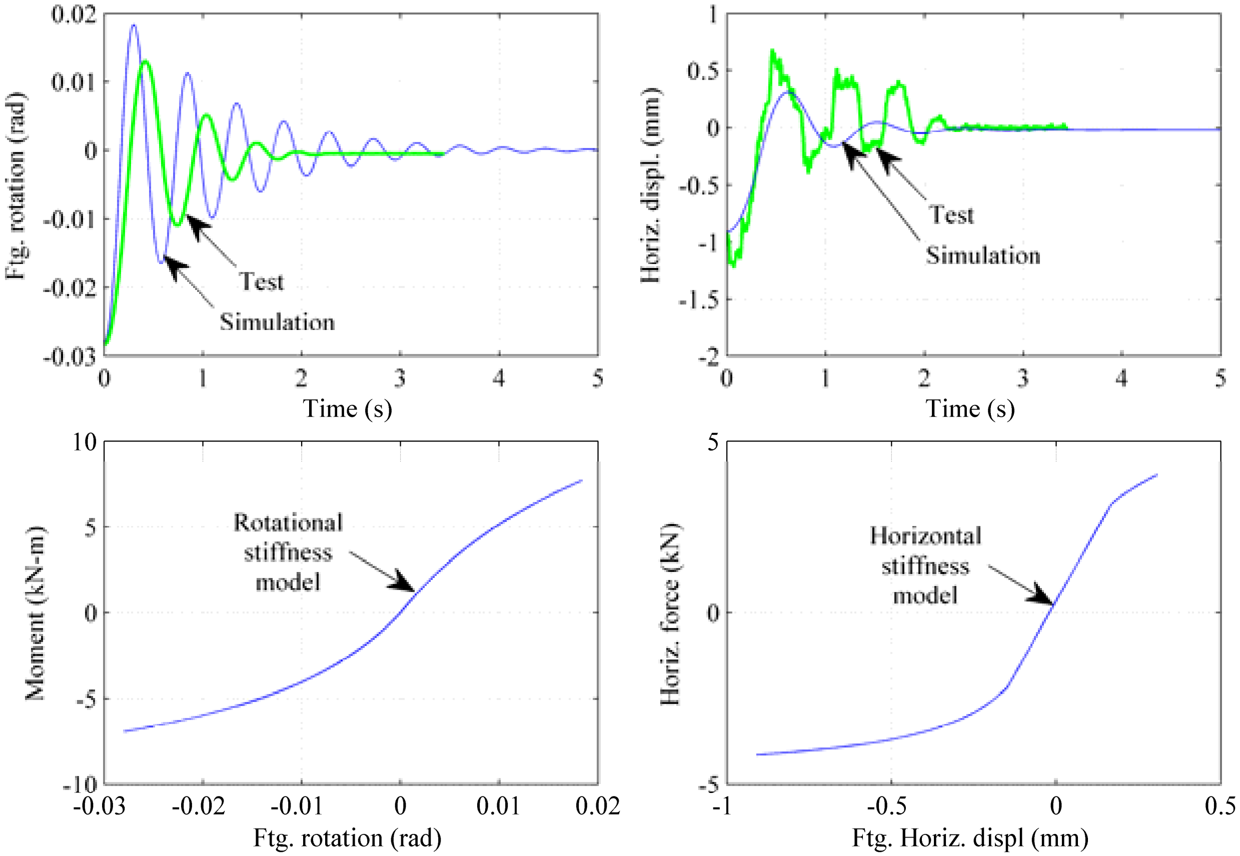

Figure 108. Analytical model simulation of free vibration snap test Snap01.

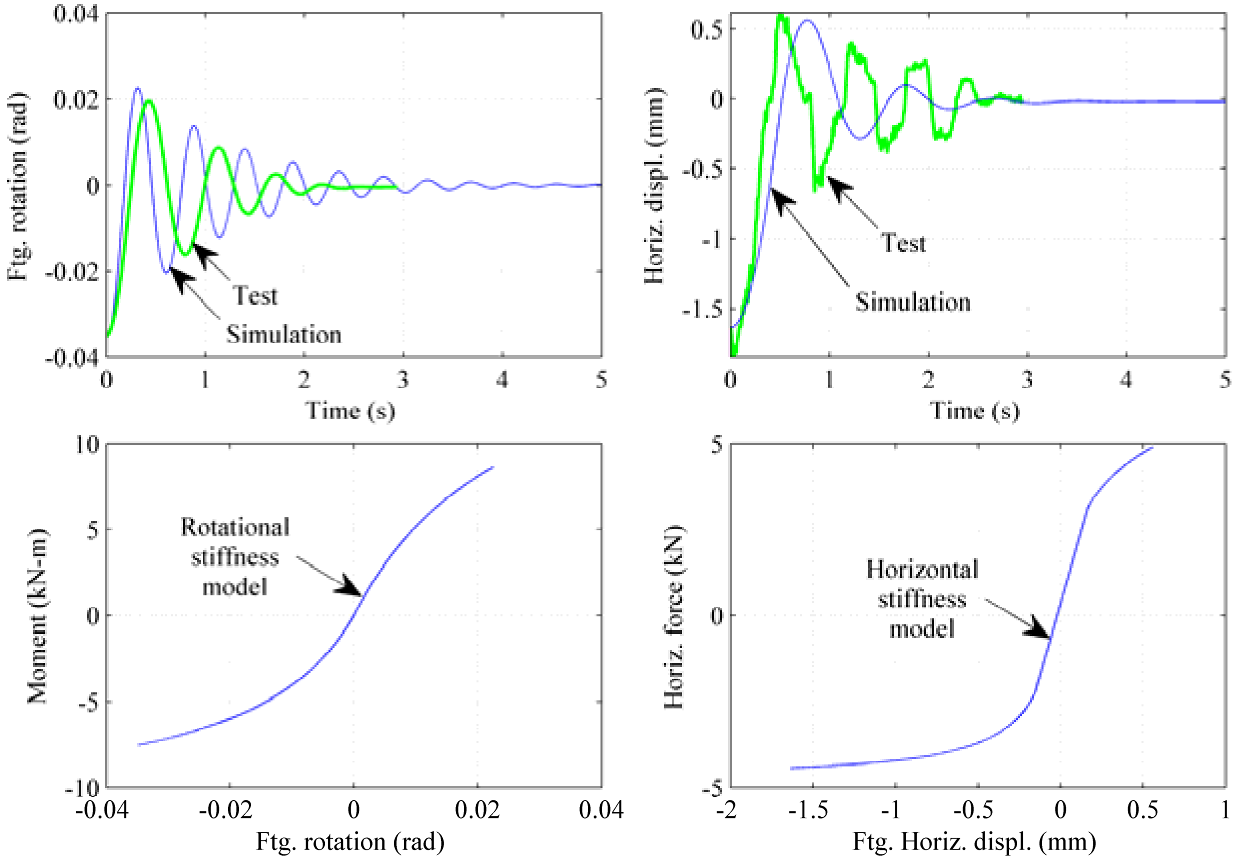

Figure 109. Analytical model simulation of free vibration snap test Snap02.

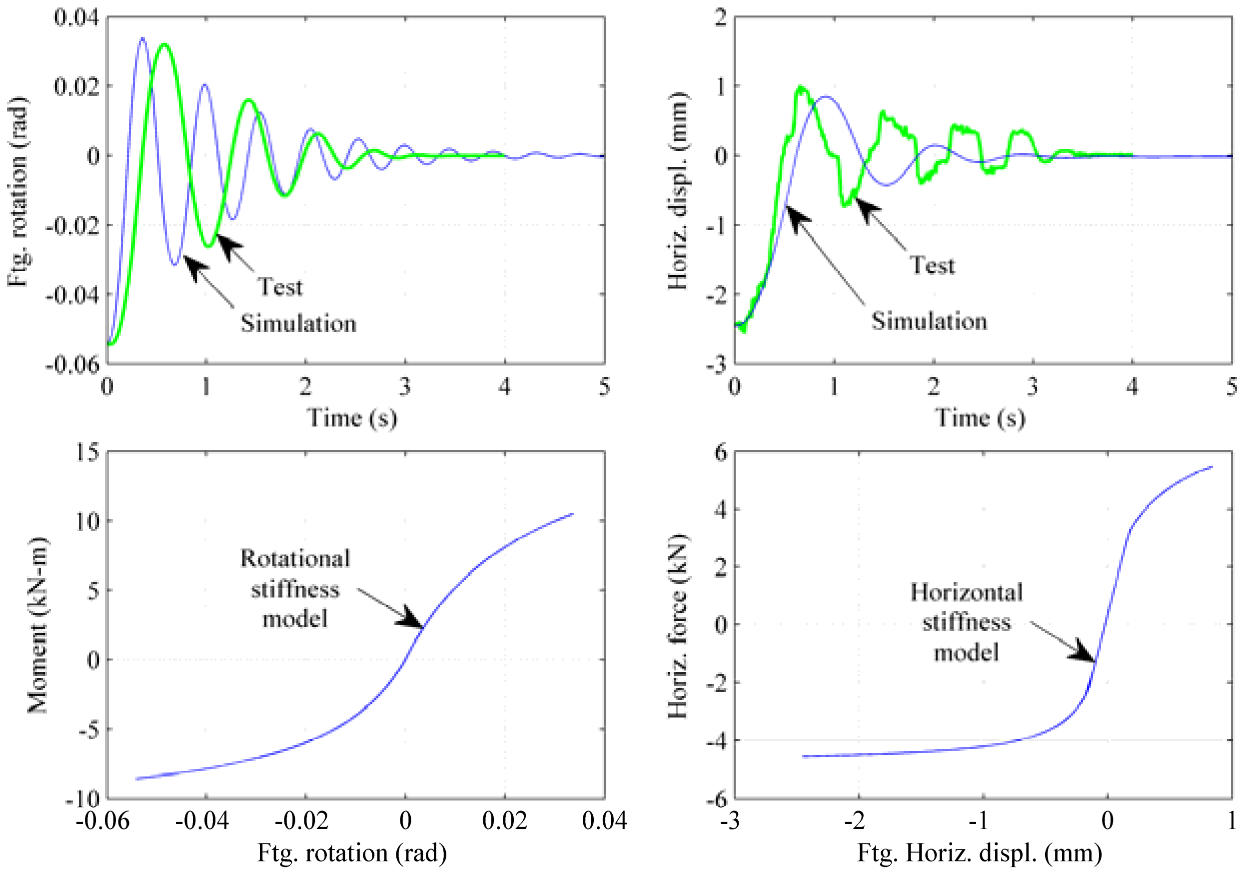

Figure 110. Analytical model simulation of free vibration snap test Snap03.

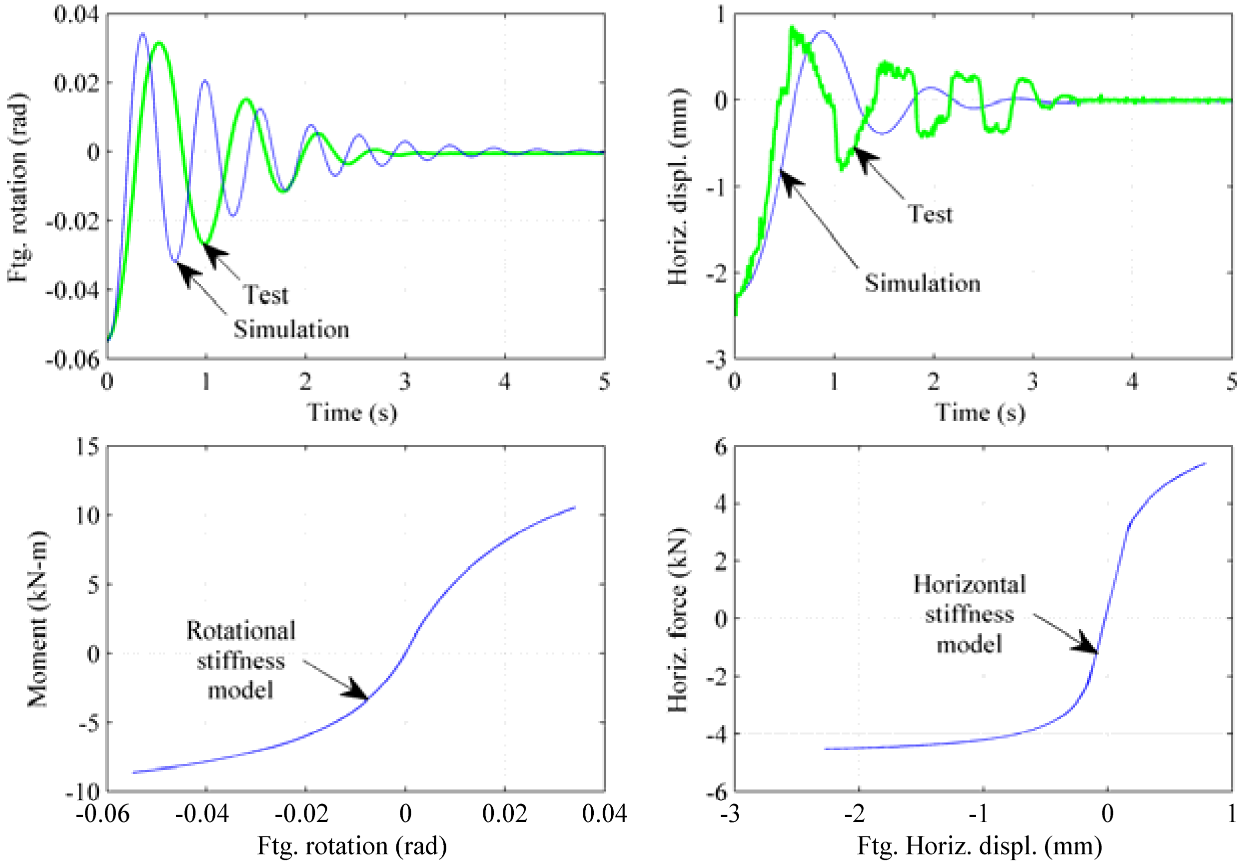

Figure 111. Analytical model simulation of free vibration snap test Snap04.

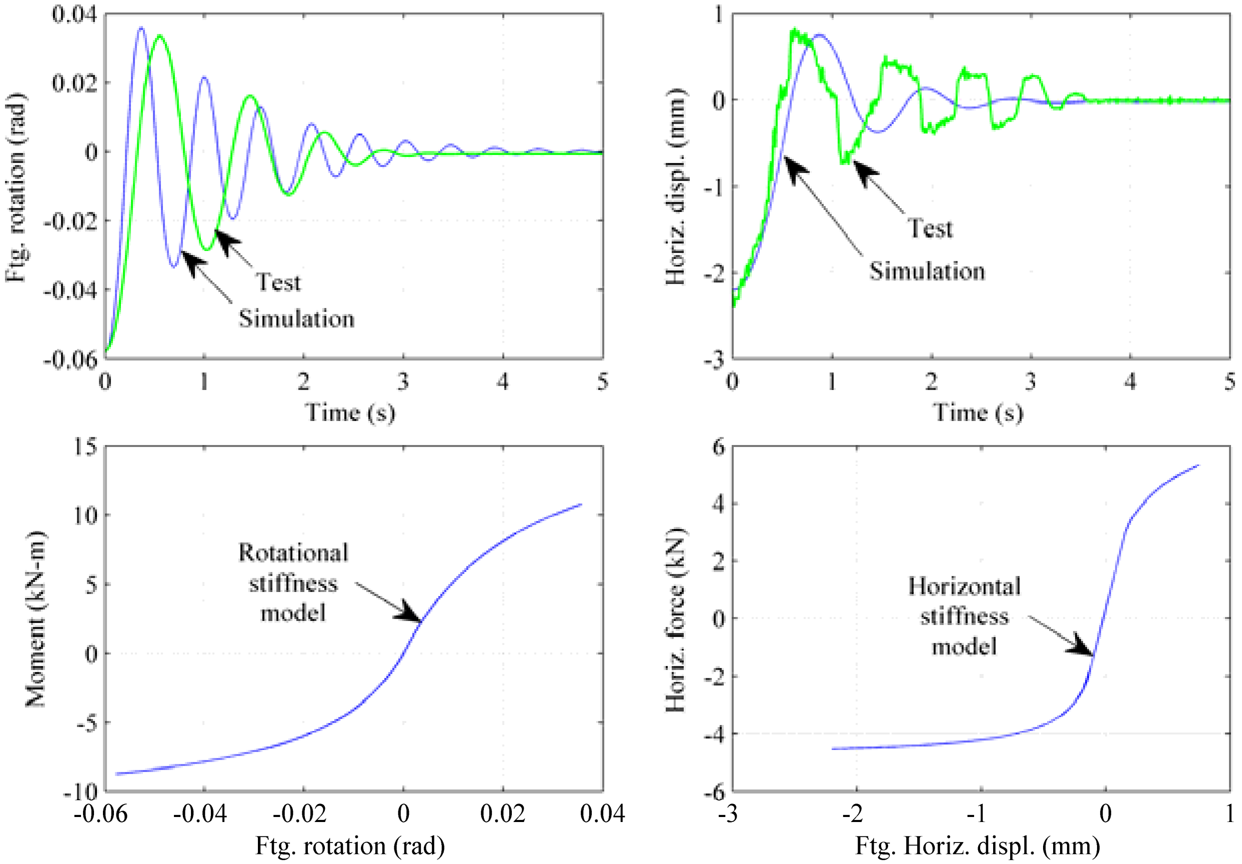

Figure 112. Analytical model simulation of free vibration snap test Snap05.

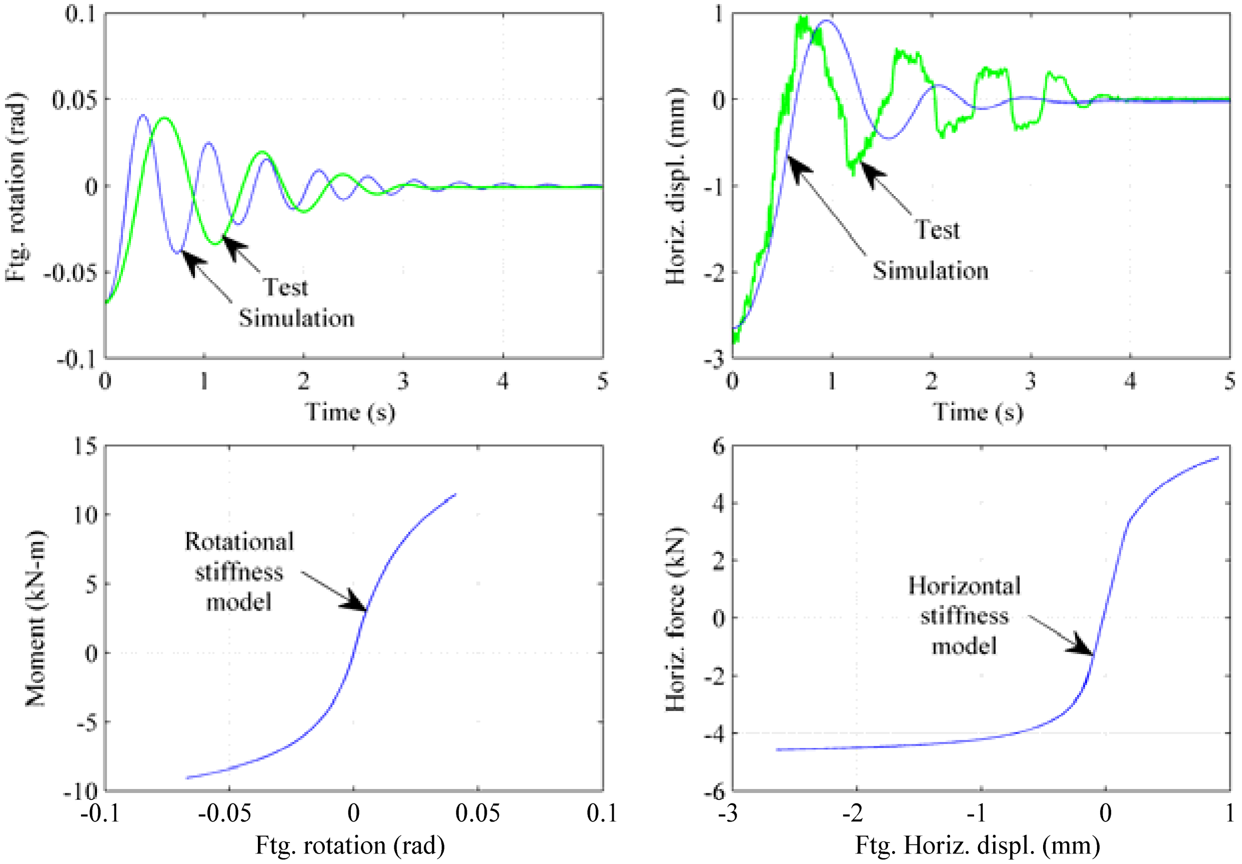

Figure 113. Analytical model simulation of free vibration snap test Snap06.

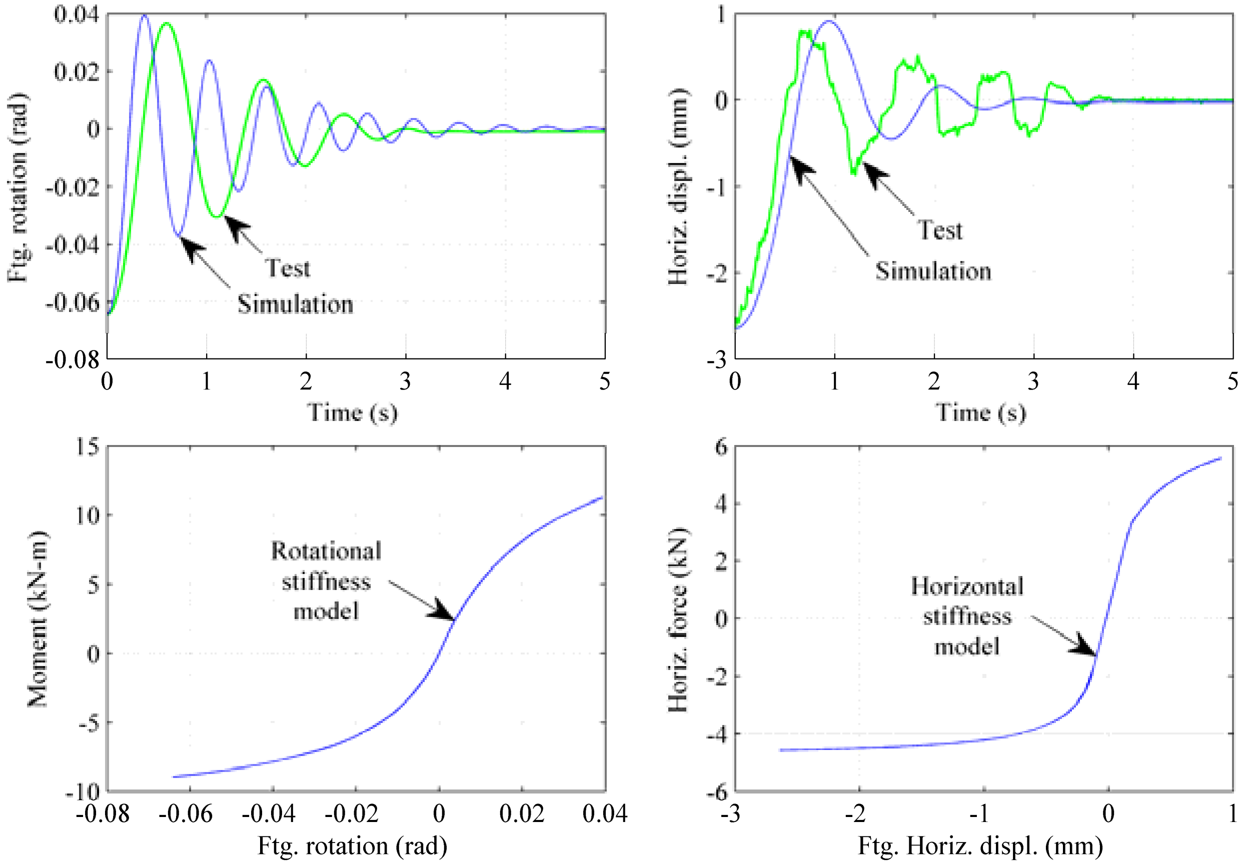

Figure 114. Analytical model simulation of free vibration snap test Snap07.

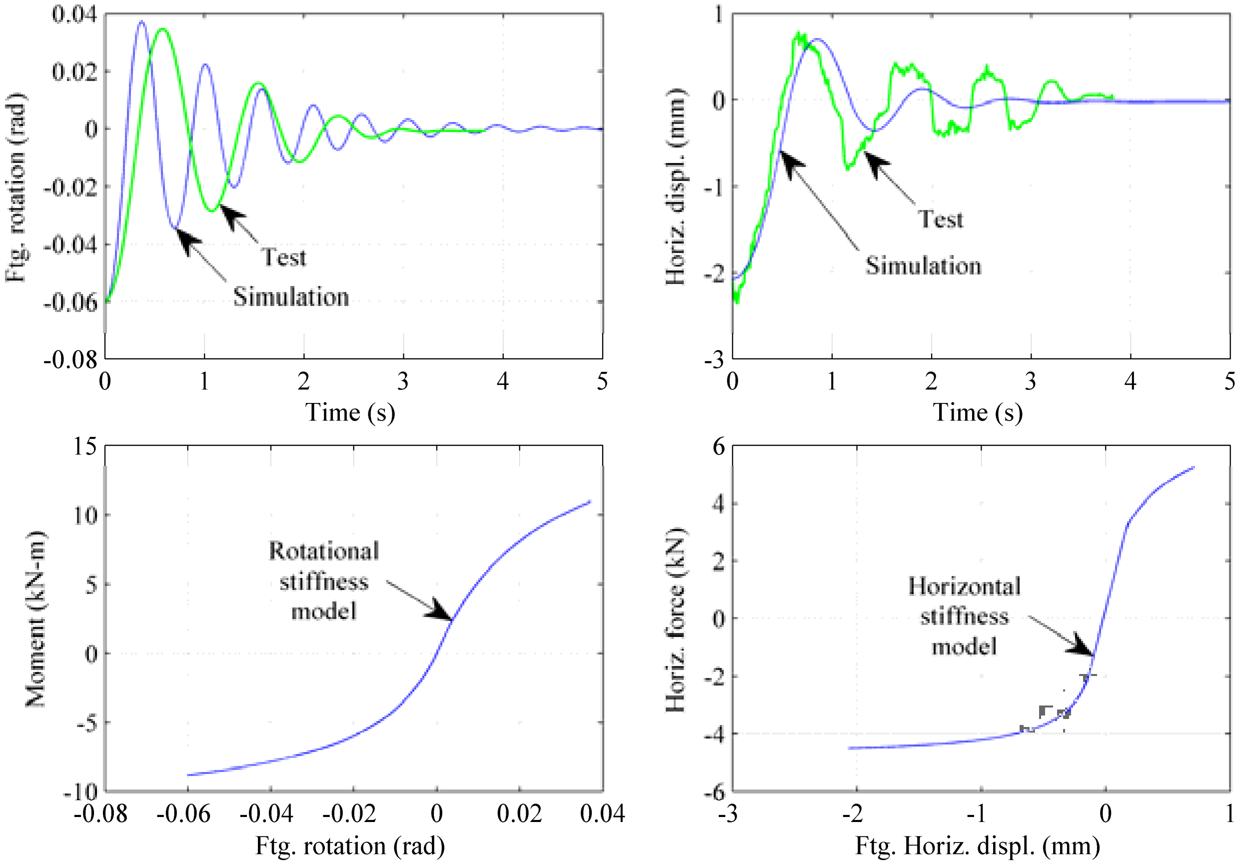

Figure 115. Analytical model simulation of free vibration snap test Snap08.

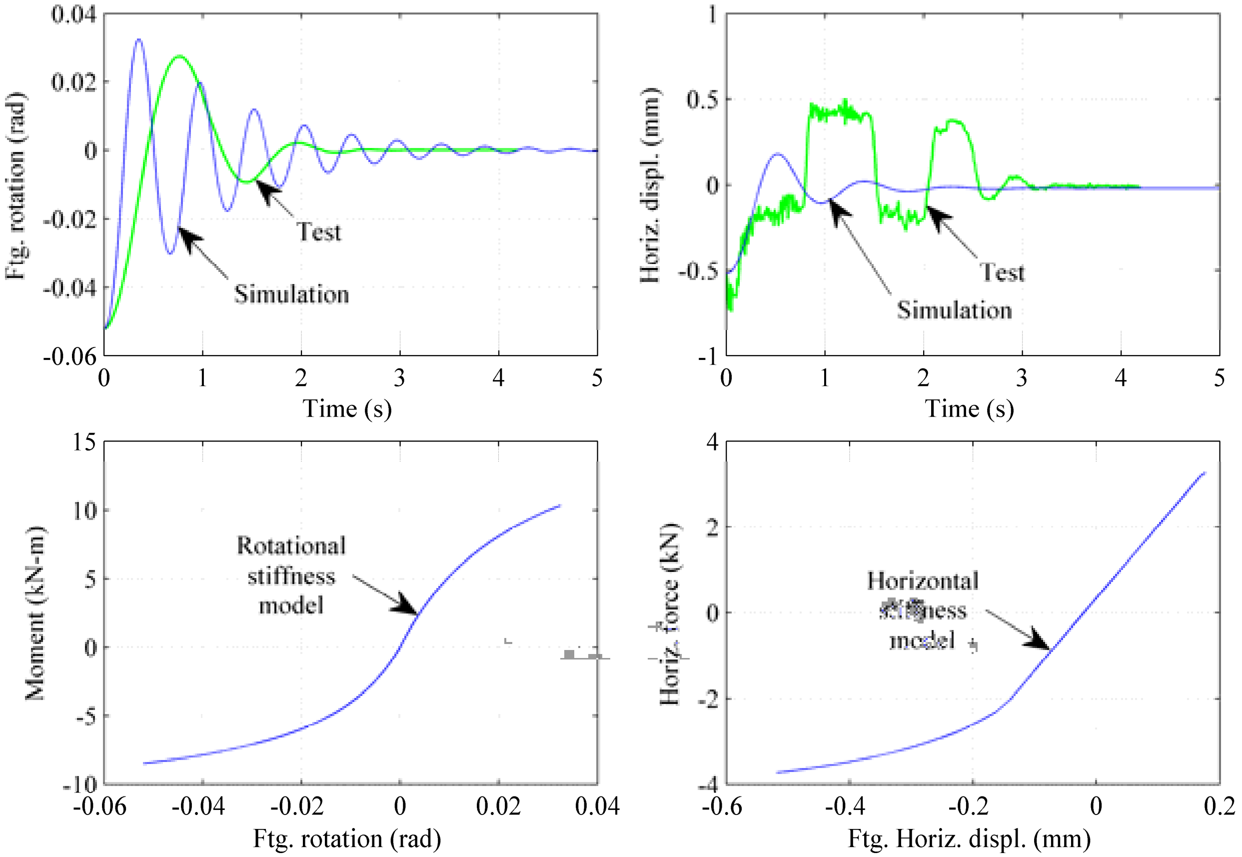

Figure 116. Analytical model simulation of free vibration snap test Snap09.

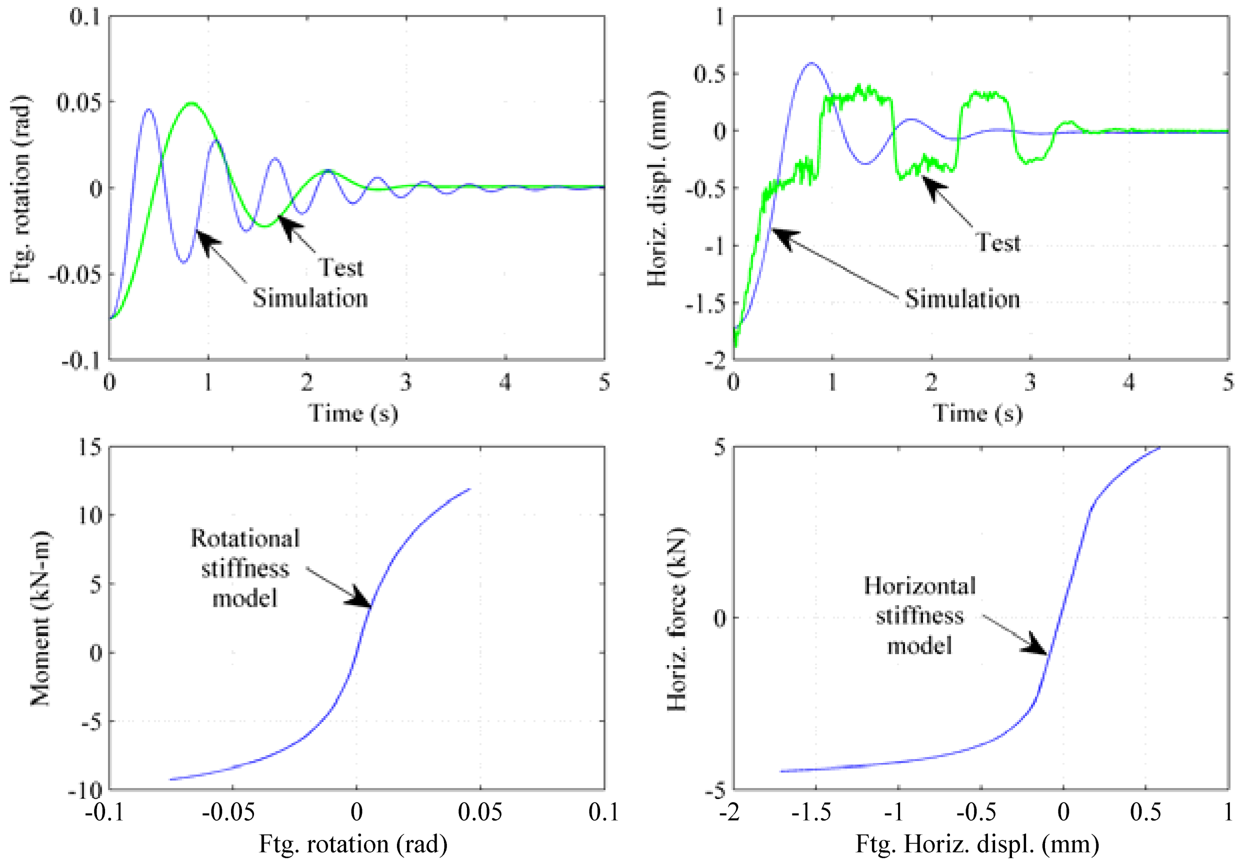

Figure 117. Analytical model simulation of free vibration snap test Snap10.

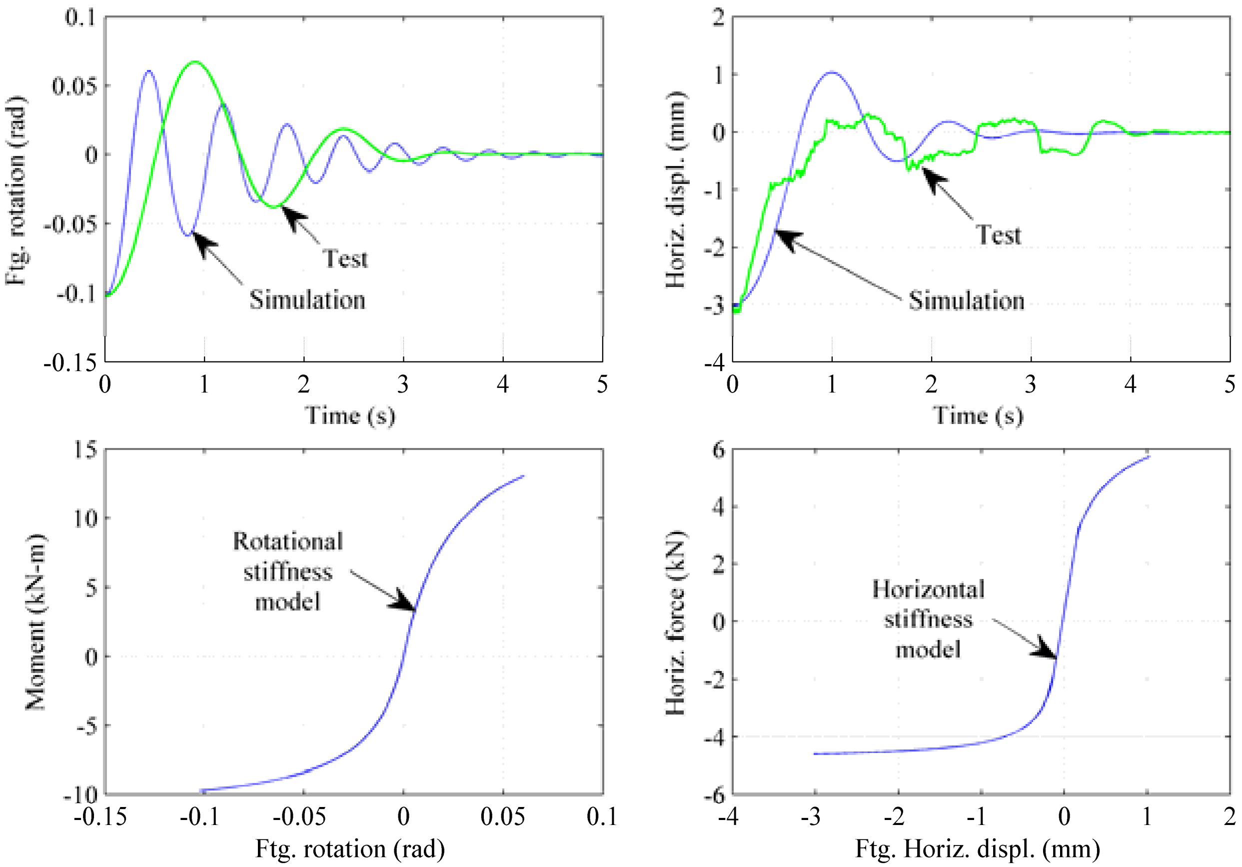

Figure 118. Analytical model simulation of free vibration snap test Snap11.

As seen from the simulations, the ENSD model does a sufficiently accurate job capturing the displacement amplitude from the experimental tests. The period of the simulation tends to be under-predicted in the rotational mode of vibration and over-predicted in the horizontal mode of vibration. As can be seen from the experimental tests, the period in the rotational mode of vibration should be the same as the horizontal mode of vibration. The period in the ENSD model is dictated from the approximated stiffness curves and equivalent viscous damping coefficients for each mode of vibration. Thus, periods for moment and horizontal force will not necessarily be the same. Alternatively, period could be the same if the backbone stiffness curve and equivalent viscous damping was approximated for one of the modes of vibration. Knowing the mass of the system, the dynamic period could be computed. This period could then be used to back-calculate the stiffness for the other mode of vibration.

The sensitivity of the ENSD model was tested with regard to mass in Figure 119. The mass of the system should be easily obtained within ±25% of the actual mass. Figure 119 reveals that the effect of mass mostly influences the period of the system. The amplitude of displacement at each peak is not significantly affected by mass of the system.

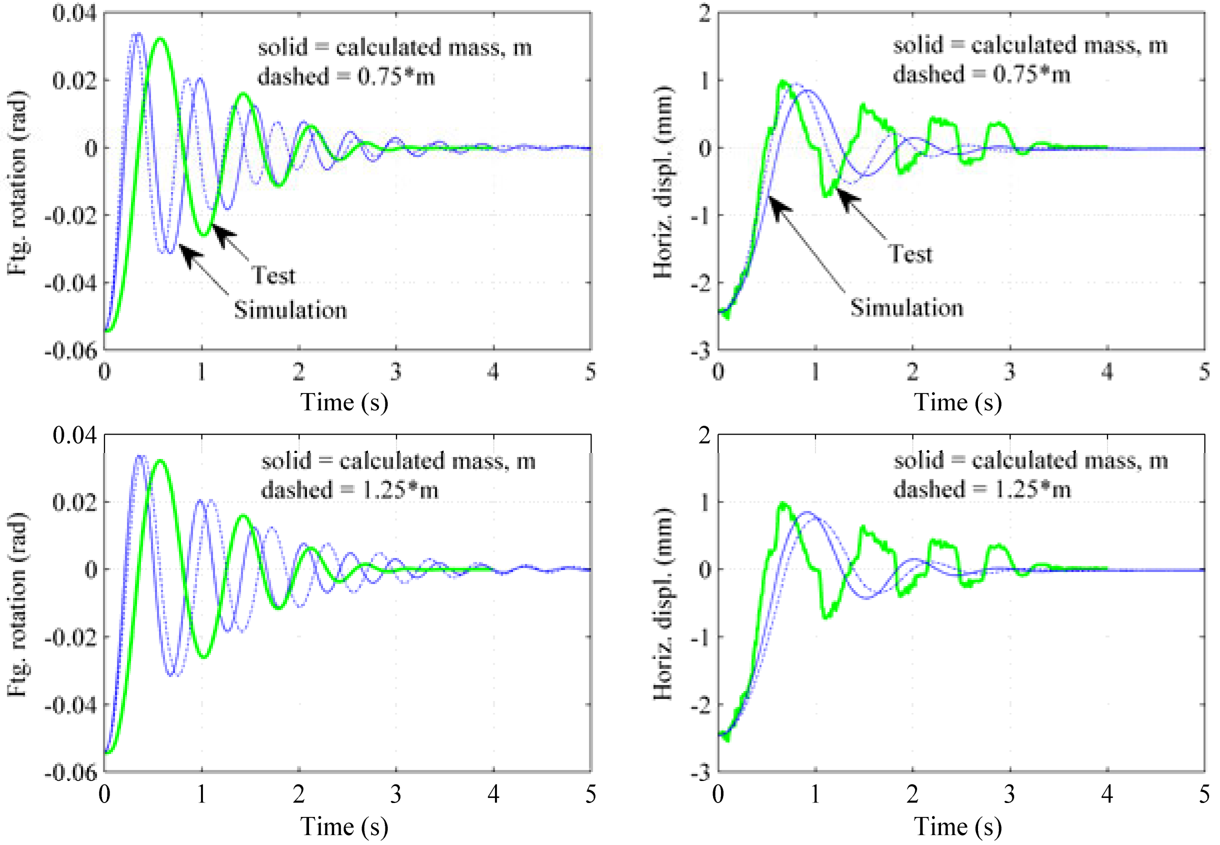

Figure 119. Mass sensitivity for analytical model simulation of free vibration snap test Snap03.

The sensitivity of the ENSD model was also tested with regard to equivalent viscous damping in Figure 120. The equivalent viscous damping was varied by ±25% of that used in the ENSD model simulations above. As expected, Figure 119 and Figure 120 reveals that the effect of equivalent viscous damping mostly influences the displacement amplitude. The effect on the period is noticeable, but only after the first two or three peaks.

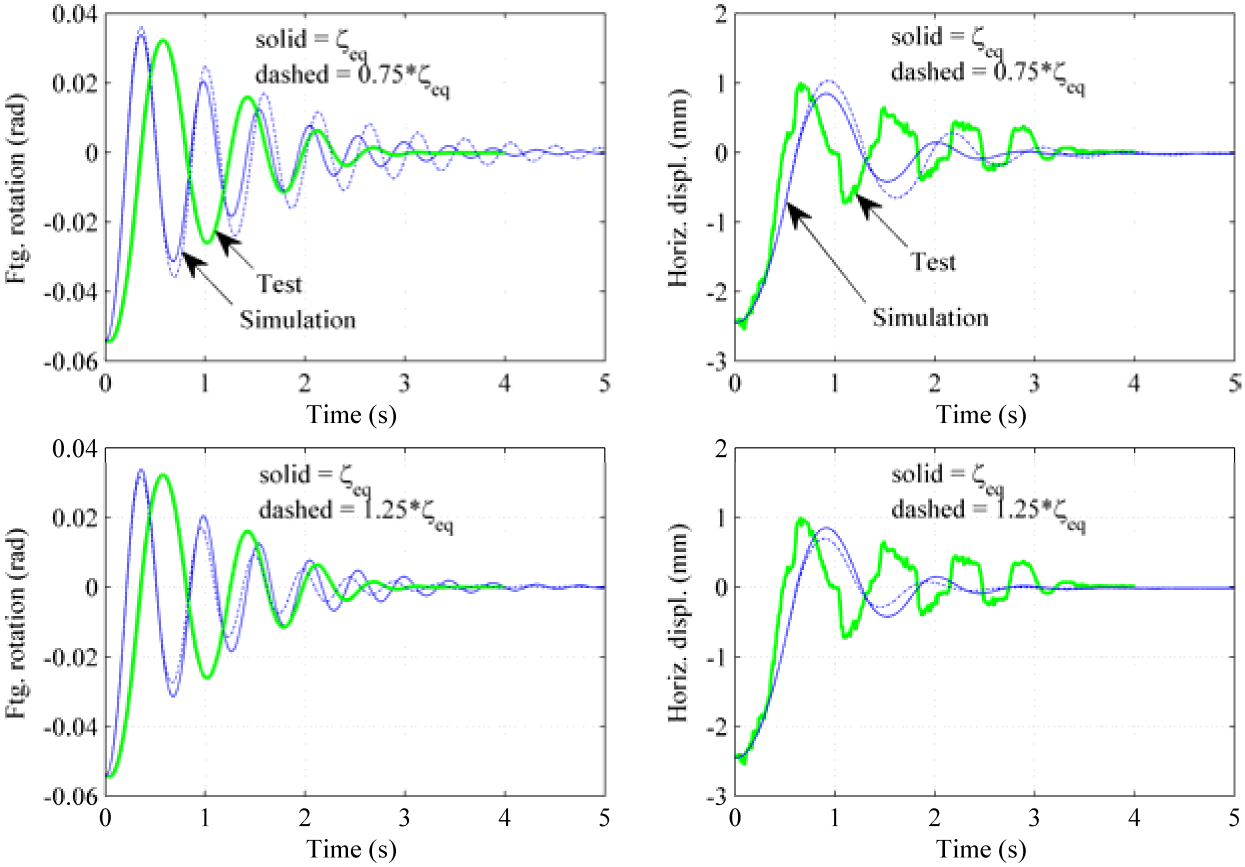

Figure 120. Damping sensitivity for analytical model simulation of free vibration snap test Snap03.

Certainly, the ENSD model relies on the availability of experimental quasi-static test results. However, the attractive part of the ENSD model is that little computational effort is required to produce sufficiently accurate displacement predictions of the free vibration dynamic response of rocking surface footings. When compared with cumbersome finite element contact model approaches, like the CIM, the ENSD model could be a much simpler analytical tool for foundation designers that are trying to work with as much efficiency as possible.

CHAPTER 5

CONCLUSIONS

5.1 Small-Strain Vibration Conclusions

In this study, experimental techniques were developed for performing field-scale small-strain wave propagation tests of surface foundations using an electromagnetic exciter in an inertial shaker configuration. A footing was constructed on a natural loamy soil deposit and tested under vertical and coupled lateral-rocking vibrations using random and swept-sine excitation types. The validity and efficiency of the hybrid-mode VE test was demonstrated via its equivalence to separate modal vertical and lateral-rocking tests. This is significant because researchers interested in multi-modal response of vibrating surface footings need only perform one test rather than two separate tests. The convenience of the hybrid VE test equivalence is even more important when the researcher is concerned with experiments on virgin soil deposits. The hybrid VE test allows the researcher to engage both the vertical and lateral-rocking modes of vibration within a single test. This conclusion has been presented for scale model centrifuge tests, but the research in this work has verified its validity for field-scale tests on a natural soil deposit. Critical insights from numerous past centrifuge scaled-model studies on dry cohesionless soils were verified and extended to field-scale as well as natural soil and moisture content conditions. Specifically, previously demonstrated limitations of the homogeneous half-space model commonly used in engineering practice were verified for the case of foundations undergoing realistic multi-modal vibrations. Homogeneous half-space models were confirmed to capture individual modal dynamic responses of a square surface footing, but the half-space models were not able to accurately capture multi-modal response of a square surface footing. It was shown that a shear modulus fit to the vertical mode of vibration overestimated the lateral-rocking response. To address the multi-modal limitations of the theory, a set of Impedance Modification Factors was calibrated for the soil type and in-situ conditions encountered in this study. This was the first known field-scale validation of the IMF approach to relate shear moduli between vertical and lateral modes of vibration. To extend the usefulness of current half-space theories in engineering practice, it is recommended that IMFs be calibrated for a range of natural soil types and moisture conditions encountered in geotechnical engineering projects, and the effects of foundation size and contact pressure be examined parametrically. Based on the successful application of the IMF technique to centrifuge pile-vibration results (Pak et al. 2006), the experimental techniques and insights developed in this study are apt to be useful for the cases of full-scale tests of embedded and deep foundations as well. Seasonal effects of the foundation response were also observed as the footing was tested from May 2010 to December 2010. Peak magnitudes of accelerance were shown to vary as much as 25% and resonant vibration peak frequencies shifted as much as 50%. These results led to the conclusion that soil-footing impedaces can change drastically with seasonal temperature and moisture conditions. The test from December 3, 2010 exhibited a dramatically different response than the previous tests. This was presumably due to much different soil-footing contact conditions even though the footing was never moved from its original location of installation. A change in contact conditions could be attributed to a sufficiently frozen soil, time consolidation effects, disturbance from previous excitation experiments, or a combination of all of these.

5.2 Large-Strain Rocking Conclusions

Depending on the level of soil strain and loading type, rocking foundations may be able to dissipate large amounts of seismic energy through soil hysteresis. This understanding has led to recent research into the effectiveness of seismic energy dissipation by designing shallow footing foundations to rock when subjected to dynamic loading. A field investigation of a rocking system experimental program was performed and described in Chapter 4. This description presented the physical aspects of the soil-structure rocking system, the measurement system, the various types of tests performed, a discussion of the experimental results, and an analytical model to predict the dynamic response of a rocking system from results of quasi-static rocking footing tests.

The ENSD analytical model is a much simpler approach for the foundation designer than other finite element methods that track displacements of the foundation-soil interface (i.e. CIM, see Chapter 2). The displacement results of the foundation were reasonably accurate with the ENSD model, and the computational effort required to simulate the dynamic response was dramatically reduced in comparison to the CIM. The importance of the simplicity of the model cannot be overstated. It is critical for engineering designers to have reliable and accurate analytical tools available. Typically designers do not have the luxury to spend great amounts of time troubleshooting cumbersome analytical models that may or may not provide accurate results. The ENSD model provides sufficiently accurate rotational and translational displacements of a rocking surface footing in free vibration.

5.3 Suggestions for Further Research

5.3.1 Small-strain vibrations

It would be useful to examine further field-scale and full-scale dynamic tests of surface footings on different types of natural soil deposits. Using the IMF approach to relate vertical and lateral-rocking responses of surface footings, it would be valuable to calibrate IMFs for a variety of soil and foundation types. This would assist foundation designers with the prediction of multi-modal responses of foundations subjected to small-strain vibrations.

5.3.2 Large-strain vibrations

It would be valuable to test field-scale rocking systems on virgin soil deposits to eliminate disturbance effects from previous dynamic load history. The ENSD model could be calibrated for a number of soil types and footing configurations. It would also be valuable to calibrate the ENSD model with centrifuge testing to verify observed behavior from field-scale testing.

The premise of allowing foundations to rock on soil as a means to dissipate energy will continue to meet resistance in the structural engineering community. For an infrastructure that is funded by taxpayers, construction and maintenance costs to provide safe infrastructure is of primary importance. When a seismic event occurs on a bridge bent, for example, a compelling study would be to look at the costs associated with the rehabilitation of a bridge that has plastic hinges designed to develop within the piers versus rocking systems that use soil yielding as the mechanism that dissipates energy. In the case of bridge bents, which are essential civil structures, researchers could study mechanisms that govern or limit the amount of rotational displacement to ensure against overturning failure.

The results of the field investigation generally supported the claim that energy may be dissipated at the soil-structure interface. Rounding of the soil surface due to rocking-induced plastic deformations would require great care when identifying dynamic properties of these systems. Furthermore, the yielding soil will introduce nonlinearities into the response of the soil-foundation system, directly influencing the periods of vibration. A degradation of rotational stiffness was exhibited as soil was strained due to increasing amplitudes of rotation. Prior to implementing rocking foundations into practice for seismic loading, additional field-scale experiments are recommended to study the effects of soil type, foundation size, and foundation shape, and calibrate computational models such as the nonlinear contact interface model of Gajan and Kutter (2009) or the Experimental Nonlinear Spring and Dashpot model developed herein.

BIBLIOGRAPHY

Ashlock, J.C. (2000). “Experimental and theoretical modeling of dynamically loaded surface foundations on granular soils", Master's thesis, University of Colorado at Boulder.

Ashlock, J.C. and Pak, R.Y.S. (2009). “Experimental response of piles in sand under compound motion", *Journal of Geotechnical and Geoenvironmental Engineering*, 135 (6), 799-808, ASCE.

Bendat, J.S. and Piersol, A.G. (1986). *Random Data*. Wiley-Interscience Publications, New York.

Chopra, A.K. (1995). *Dynamics of Structures: Theory and Applications to Earthquake Engineering*. Prentice-Hall.

Christensen, R.M. (1971). *Theory of Viscoelasticity*, Academic Press, New York.

Cremer, C., Pecker, A., and Davenne, L. (2001). “Cyclic macro-element for soil-structure interaction: Material and geometrical non-linearities”, *International Journal for Numerical and Analytical Methods in Geomechanics*, 25 (13), 1257-1284.

Crouse, C.B., Hushmand, B., Luco, J.E., and Wong, H.L. (1990). “Foundation impedance functions: theory versus experiment", *Journal of Geotechnical Engineering*, 116 (3), 432-449.

Crouse, C.B., Liang, G.C., and Martin, G.R. (1985). “Experimental foundation impedance functions", *Journal of Geotechnical Engineering*, 111 (6), 819-824.

Dobry, R. and Gazetas, G. (1986). “Dynamic response of arbitrarily shaped foundations", *Journal of Geotechnical Engineering*, 112.2.

Gajan, S., Hutchinson, T.C., Kutter, B.L., Raychowdhury, P., Ugalde, J.A., and Stewart, J.P. (2008). “Numerical models for analysis and performance-based design of shallow foundations subjected to seismic loading”, Pacific Earthquake Engineering Research Center. PEER 2007/04.

Gajan, S. and Kutter, B.L. (2009). “Contact interface model for shallow foundations subjected to combined cyclic loading”, *Journal of Geotechnical and Geoenvironmental Engineering*, 135 (3), 407-419.

Gajan, S. and Kutter, B.L. (2009). “Effects of moment-to-shear ratio on combined cyclic load-displacement behavior of shallow foundations from centrifuge experiments”, *Journal of Geotechnical and Geoenvironmental Engineering*, 135 (8), 1044-1055.

Gajan, S., Kutter, B.L., Phalen, J.D., Hutchinson, T.C., and Martin, G.R. (2005). “Centrifuge modeling of load-deformation behavior of rocking shallow foundations”, *Soil Dynamics and Earthquake Engineering*, 25 (7-10), 773-783.

Gazetas, G. (1991). “Chapter 15: Foundation Vibrations." in *Foundation Engineering Handbook*, 2nd Ed., H.Y. Fang, Ed., Van Nostrand Reingold.

Hardin, B.O. and Drnevich, V.P. (1972). “Shear modulus and damping in soils: design equations and curves", *Journal of the Soil Mechanics and Foundation Division, Proc. ASCE*, 98 (SM7), 667-692.

Houlsby, G.T. and Cassidy, M.J. (2002). “A plasticity model for the behaviour of footings on sand under combined loading”, *Géotechnique*, 52 (2), 117-129.

Housner, G.W. (1963). “The behavior of inverted pendulum structures during earthquakes”, *Bulletin of the Seismological Society of America*; 53 (2), 404-417.

Kutter, B.L., Martin, G., Hutchinson, T., Gajan, S., and Phalen, J. (2006). “Workshop on modeling of nonlinear cyclic load-deformation behavior of shallow foundations”, Pacific Earthquake Engineering Research Center. PEER 2005/14.

Luco, J.E. and Mita, A. (1987). “Response of a circular foundation on a uniform half-space to elastic waves", *Earthquake Engineering Structural Dynamics*, 15, 105-118.

Luco, J.E. and Westman, R.A. (1971). “Dynamic response of circular footings", *Journal of the Engineering Mechanics Division, ASCE*, 97 (EM5), 1381-1395.

Luco, J.E. and Wong, H.L. (1992). “Identification of soil properties from foundation impedance functions", *Journal of Geotechnical Engineering*. 118 (5), 780-795.

Luco, J.E., Wong, H.L., and Trifunac, M.D. (1975). “A note on the dynamic response of rigid embedded foundations", *Earthquake Engineering and Structural Dynamics*. 4, 119-127.

Miklowitz, J. (1984). “Reflection and refraction of time harmonic waves at an interface", *The Theory of Elastic Waves and Waveguides*. Amsterdam: North-Holland. 119-35.

Nova, R. and Montrasio, L. (1991). “Settlements of shallow foundations on sand”, *Géotechnique*, 41 (2), 243-256.

Novak, M. (1970). “Prediction of footing vibrations", *Journal of the Soil Mechanics and Foundation Division, Proc. ASCE*, 96 (SM3), 837-861.

Pak, R.Y.S. and Ashlock, J.C. (2000). “Fundamental dynamic behavior of foundations on sand", Soil Dynamics and Liquefaction 2000, *Proc. Sessions of Geo-Denver 2000*, Geotechnical Special Publication Number 107, Geo-Institute, ASCE.

Pak, R.Y.S. and Guzina, B.B. (1995). “Dynamic characterization of vertically loaded foundations on granular soils", *Journal of Geotechnical Engineering*, ASCE, 121 (3), 274-286.

Pak, R.Y.S. and Guzina, B.B. (1999). “Seismic soil-structure interaction analysis by direct boundary element methods", *Int. J. Solid. Struct.*, Vol. 36 (31-32), 4743-4766.

Pak, R.Y.S., Ashlock, J.C., Abedzadeh, F., and Turner, N. (2006). “Dynamic hybrid-mode test of a pile on a centrifuge", *Physical Modeling in Geotechnics, 6th Int. Conf. on Physical Modeling in Geotechnics*, 1037-1042.

Pak, R.Y.S., Ashlock, J.C., and Abedzadeh, F. (2008). “Parametric Gmax sounding of granular soils by vibration methods", *Géotechnique*, 58 (7), 571-580, ICE.

Pak, R.Y.S., Ashlock, J.C., Kurahashi, S., and Soudkhah, M. (2010). “Physical characteristics of dynamic vertical-horizontal-rocking response of surface foundations on cohesionless soils", *Géotechnique*, ICE, accepted.

Quinlan, P.M. (1953). “Dynamic testing of soils: the elastic theory of soil dynamics", (symposium), *Special Technical Publication No. 156, American Society for Testing and Materials*, 3-34.

Reissner, E. (1936). “Stationäre, axialsymmetrische durch eine schüttelnde Masse erregte Schwingungen eines homogenen elastischen Halbraumes", *Ingenieur-Archiv*, 7 (6), 381-396.

Reissner, E. (1937). “Freie und erzwungene Torsionschwingungen des elastischen Halbraumes", *Ingenieur-Archiv*, 8 (4), 229-245.

Richart, F.E. and Whitman, R.V. (1967). “Comparison of footing vibration tests with theory", *Journal of the Soil Mechanics and Foundation Division, Proc. ASCE*, 93 (SM6), 143-168.

Shelman, A.T. (2009). “Seismic design of drilled shafts in clay”, MS Thesis. Iowa State University.

Shi, B., Anooshehpoor, A., Zeng, Y., and Brune, J.N. (1996). "Rocking and overturning of precariously balanced rocks by earthquake", *Bull. Seism. Soc. Am.*, 86 (5), 1364-1371.

Sritharan, S., Suleiman, M. T. and White, D. J. (2007). "Effects of seasonal freezing on
bridge column-foundation-soil interaction and their implications." *Earthquake spectra.* 23(1): 199-222.

Suleiman, M. T., Sritharan, S. and White, D. J. (2006). "Cyclic lateral load response of
bridge column-foundation-soil systems in freezing conditions." *Journal of structural engineering* 132(11): 1745-1754.

Sung, T.Y. (1953). "Dynamic testing of soils: vibrations in semi-infinite solids due to periodic surface loading", (symposium), *Special Technical Publication No. 156, American Society for Testing and Materials*, 35-64.

Svinkin, M.R. (2002). "Predicting soil and structure vibrations from impact machines", *Journal of Geotechnical and Geoenvironmental Engineering*, 128 (7), 602-612.

Velestos, A.S. and Wei, Y.T. (1971). "Lateral and rocking vibration of footings", *Journal of Soil Mechanics and Foundation Division, ASCE*, 97, 1227-1248.

Winkler, E. (1867). "Die lehre von elasticitat und festigkeit", Verlag H. Dominikus, Prague, 182-184.

Wong, H.L. and Luco, J.E. (1978). "Tables of impedance functions and input motions for rectangular foundations", *Report CE-78-15*, Department of Civil Engineering, University of Southern California.

Wong, H. and Luco, J. (1985). "Tables of impedance functions for square foundations on layered media.", *International Journal of Soil Dynamics and Earthquake Engineering*, 4.2, 64-81.